Deutsches Elektronen-Synchrotron
Universität Hamburg

FROM LINEAR TO NON-LINEAR X-RAY SPECTROSCOPY ON MATERIALS USING SASE-FELS

DISSERTATION
ZUR ERLANGUNG DES DOKTORGRADES

AN DER FAKULTÄT FÜR MATHEMATIK, INFORMATIK UND NATURWISSENSCHAFTEN
FACHBEREICHS PHYSIK
DER UNIVERSITÄT HAMBURG

VORGELEGT VON

ROBIN YOËL ENGEL

AUS HAMBURG

HAMBURG, 2023

Supervisors

Dr. Martin Beye
Deutsches Elektronen-Synchroton
Universität Hamburg

Prof. Dr. Nils Huse
Universität Hamburg

Gutachter der Dissertation:	Dr. Martin Beye Prof. Dr. Nils Huse
Zusammensetzung der Prüfungskommission :	Dr. Martin Beye Prof. Dr. Nils Huse Priv. Doz. Dr. Tim Laarmann Prof. Dr. Markus Gühr Prof. Dr. Daniela Pfannkuche
Vorsitzende der Prüfungskommission :	Prof. Dr. Daniela Pfannkuche
Datum der Disputation:	28.02.2023
Vorsitzender Fach-Promotionsausschuss PHYSIK:	Prof. Dr. Günter H. W. Sigl
Leiter des Fachbereichs PHYSIK:	Prof. Dr. Wolfgang J. Parak
Dekan der Fakultät MIN:	Prof. Dr.-Ing. Norbert Ritter

DEUTSCHES ELEKTRONEN-SYNCHROTRON

Abstract

From Linear to Non-Linear X-ray Spectroscopy on Materials using SASE-FELs

by Robin Yoël Engel

The key feature of X-ray Free Electron Lasers (XFELs) is their capability to generate ultrashort and at least partially coherent X-ray pulses with extreme intensity. This capability holds the promise to revolutionize X-ray physics in a way similar to how lasers have revolutionized optics, as the non-linear and coherent interactions known from the optical regime combined with the properties of X-ray radiation could enable techniques with unprecedented analyzing power. This thesis summarizes several contributions to the development from linear to non-linear X-ray spectroscopies at XFELs.

To begin with, I address the technical challenge of normalizing the spectral intensity fluctuations of XFEL-radiation by presenting several versions of the split-beam normalization scheme. Versions suitable for both monochromatic and broadband measurements, either in transmission through liquids or metal films or in reflection from bulk-supported samples are demonstrated and their capabilities and performance are compared.

Moving to non-parametric high-fluence studies, we present a non-linear absorption study at the nickel L_3-edge using a monochromatic split-beam normalization scheme. We interpret the fluence-dependent spectral changes by characterizing the evolution of the electronic system during interaction with the X-ray pulse using a rate model that quantifies the photon absorption and electronic scattering processes.

Further, we show a similar non-linear absorption experiment that utilizes a broadband split-beam normalization scheme. While we observe a comparable evolution of the electronic system, the broadband incident radiation leads to a strong contribution of stimulated inelastic scattering that is up to six orders of magnitude stronger than the spontaneous contribution that is exploited in conventional Resonant Inelastic X-ray Scattering (RIXS). Finally, we demonstrate sum and difference frequency generation between core-resonant XFEL-photons with two infrared photons for the first time. The observed photon-energy dependence of the third-order non-linear susceptibility suggests an enhancement through coupling between the 1s2p and 1s2s excited states, thus demonstrating a key capability of wave-mixing spectroscopy methods.

In summary, the presented work contributes to the development of non-linear X-ray spectroscopy on various fronts, but further developments will be needed to bring X-ray wave-mixing techniques into their preconceived position to deliver unprecedented insights into molecular and solid-state dynamics.

Zusammenfassung

Die wichtigste Eigenschaft von Röntgen-Freie-Elektronen-Lasern (XFELs) ist ihre Fähigkeit, ultrakurze und zumindest teilweise kohärente Röntgenpulse mit extrem hoher Intensität zu erzeugen. Daraus ergibt sich die Hoffnung, die Methoden der Röntgenphysik in ähnlicher Weise zu revolutionieren wie man es mit optischen Messmethoden durch die Einführung des Lasers vermochte, da die aus dem optischen Bereich bekannten nichtlinearen und kohärenten Wechselwirkungen kombiniert mit den Eigenschaften von Röngenstrahlung nie dagewesene Messungen ermöglichen könnten. In dieser Doktorarbeit werden mehrere Beiträge zur Entwicklung von linearer zu nicht-linearer Röntgenspektroskopie an XFELs zusammengefasst.

Zunächst behandle ich die technische Herausforderung, die inhärenten spektralen Intensitätsfluktuationen von XFEL-Strahlung zu normalisieren, indem ich verschiedene Realisierungen des Split-Beam Normalisierungsprinzips vorstelle. Die verschiedenen Aufbauten benutzen jeweils monochromatische und breitbandige Strahlung und sind jeweils für Transmissionmessungen durch dünne Filme und für Reflexionsmessungen von massiven Proben konzipiert. Ihre jeweiligen Vor- und Nachteile sowie die erreichte Sensitivität werden verglichen.

Daraufhin stelle ich eine nicht-parametrisch nichtlineare Absorptionsstudie an der Nickel L_3 Absorptionskante vor, für welche ebenfalls monochromatische Split-Beam-Normalisierung genutzt wurde. Wir interpretieren die fluenzabhängigen spektralen Veränderungen anhand der Evolution des elektronischen Systems während der Interaktion mit dem Röntgenpuls durch ein Ratenmodell, das die Absorption von Photonen und die Raten der elektronischen Streuprozesse quantifiziert.

Des Weiteren zeigen wir ein ähnliches nichtlineares Absorptionsexperiment mit einem breitbandigem Split-Beam Normalisierungsschema. Während eine vergleichbare Evolution des elektronischen Systems beobachtet wird, ermöglicht die breitbandig einfallende Strahlung einen wesentlichen Beitrag von stimulierter inelastischer Streuung, der bis zu sechs Größenordnungen stärker ist als der spontane Beitrag, welcher in konventionellen Messungen von Resonanter Inelastischer X-ray Streuung (RIXS) genutzt wird.

Schließlich demonstrieren wir zum ersten Mal Summen- und Differenzfrequenzgenerierung zwischen XFEL-Photonen und zwei Infrarotphotonen. Die beobachtete Photonenenergie-Abhängigkeit der nichtlinearen Suszeptibilität deutet auf eine Verstärkung des Signals durch die Kopplung zwischen den exzitonischen Konfigurationen 1s2p und 1s2s hin, was ein wesentliches Alleinstellungsmerkmal von Wellenmischungs-Experimenten demonstriert.

Zusammenfassend tragen die vorgestellten Arbeiten auf mehreren Wegen zur Forschung an nichtlinearer Röntgenspektroskopie bei. Allerdings werden weitere Entwicklungen benötigt um das Potential von Röntgenbasierten Wellenmischungs-Techniken für regelmäßige neue Einblicke in die Dynamik von Molekülen und Festkörpern zu umzusetzen.

Acknowledgements

The publications contained within this thesis are the collaborative work of many people, so my first and most important thanks go to the many outstanding colleagues without whom the research presented in this thesis would not have been possible.

From the long hours at the various beamlines to the discussions in seminars, at lunch, or during coffee, I have always enjoyed working with you and learned so much in the meantime!

A special thanks goes to my wonderful colleagues at FLASH and especially my small team with Simon, Markus, Piter and Jan. Foremost in this team I want to thank Martin, who has, from day one, been not only a supervisor, but a mentor who was always actively concerned with where we stand and how to best teach and prepare us for our research-life ahead.

I also want to thank Nils, who has been very helpful and supportive in his role as a secondary supervisor.

Thank you to all my friends, both on and off campus, who made my last years a very enjoyable time!

Finally, thanks to Nina for supporting me and being by my side all the way, thanks to my mother who has brought me to be who I am, and to my father who convinced me early on that I can do anything at all if I only set my mind to it.

Publications

The following publications are printed as part of this cumulative thesis in this order. My contribution to each is detailed below.

[1] **Shot noise limited soft X-ray absorption spectroscopy in solution at a SASE-FEL using a transmission grating beam splitter**,
Structural Dynamics 8, 014303 (2021)
Contributions: I participated in the experiment, was a main contributor to the online analysis and responsible for the final analysis of the data. I was also responsible for writing the manuscript and the review process.

[2] **Parallel broadband femtosecond reflection spectroscopy at a soft X-ray free-electron laser**,
Applied Sciences 10, 6947 (2020)
Contributions: I participated in the experiment, was a main contributor to the online analysis and responsible for the final analysis of the data. I was also responsible for writing the manuscript and the review process.

[3] **Ultrafast manipulation of the NiO antiferromagnetic order via sub-gap optical excitation**,
Faraday Discussions 237, 300-316 (2022)
Contributions: I participated in the experiment, was a main contributor to the online analysis and assisted in the final analysis of the data, and made minor contributions to the manuscript.

[4] **Electron dynamics at high-energy densities in nickel from non-linear resonant X-ray absorption spectra**,
arXiv 2211.17008 (2022)
Contributions: I participated in the experiment, was a main contributor to the online analysis and I was responsible for the final analysis of the data. I was also responsible for writing the manuscript and the review process.

[5] **A rate model of electron populations for non-linear high-fluence X-ray absorption near-edge spectra**,
arXiv 2211.17144 (2022)
Contributions: I developed the mathematical model together with Martin Beye and was responsible for its implementation. I was also responsible for writing the manuscript and the review process.

[6] **Stimulated resonant inelastic X-ray scattering in a solid**,
Communications Physics 5, 83 (2022)
Contributions: I performed a statistical analysis of the spectra to derive estimates of the minimum FEL pulse duration and made minor contributions to the manuscript.

[7] **Probing electron and hole colocalization by resonant four-wave mixing spectroscopy in the extreme ultraviolet**,
Science Advances 8, eabn5127 (2022)
Contributions: I participated in the experiment, was a main contributor to the online analysis, and was responsible for the final analysis of the data. I made major contributions to writing the manuscript and the review process.

Apart from these, my work at DESY further resulted in the following publications which are not printed in this cumulative thesis.

[8] **Photon-shot-noise-limited transient absorption soft X-ray spectroscopy at the European XFEL**,
Journal of Synchrotron Radiation 30, 2, 284-300 (2023)
Contributions: I participated in the experiment and the online analysis and made minor contributions to the manuscript.

[9] **Non-linear soft x-ray methods on solids with MUSIX — the multi-dimensional spectroscopy and inelastic x-ray scattering endstation**,
Journal of Physics: Condensed Matter 31, 014003 (2018)
Contributions: I participated in the experiment and made minor contributions to the manuscript.

[10] **The TRIXS end-station for femtosecond time-resolved resonant inelastic X-ray scattering experiments at the soft X-ray free-electron laser FLASH**,
Structual Dynamics 7, 054301 (2020)
Contributions: I participated in the experiment, was one of the main contributors to the online analysis, and made minor contributions to the manuscript.

[11] **The interplay of local electron correlations and ultrafast spin dynamics in fcc Ni**,
arXiv 2210.13162 (2022)
Contributions: I participated in the experiment, was one of the main contributors to the online analysis, and made minor contributions to the manuscript.

[12] **Ultrafast modification of the electronic structure of a correlated insulator**,
Physical Review Research 4, L032030 (2022)
Contributions: I participated in the experiment, assisted in the online analysis, and made minor contributions to the manuscript.

[13] **Optical control of 4f orbital state in rare-earth metals**,
arXiv 2106.09999 (2021)
Contributions: I participated in the experiment, was one of the main contributors to the online analysis, and made minor contributions to the manuscript.

[14] **Soft X-ray imaging spectroscopy with micrometer resolution**,
Optica 8, 2, 156-160 (2021)
Contributions: I participated in the experiment, was one of the main contributors to the online analysis, and made minor contributions to the final analysis as well as the manuscript.

[15] **Microstructure effects on the phase transition behavior of a prototypical quantum material**,
Scientific Reports 12, 10464 (2022)
Contributions: I participated in the experiment, was one of the main contributors to the online analysis, and made minor contributions to the final analysis as well as the manuscript.

Contents

Chapter 1

Introduction

The XFEL represents the culmination of three technologies that have each been transformative to the way in which we can observe the world of matter around us:
First, discovered by Konrad Röntgen in 1895 and cause for the first-ever awarded Nobel prize, X-rays are known in medicine for their ability to look through our opaque bodies. But the arguably greater impact of X-rays on our society was due to their scientific impact: The short wavelength of X-rays allows them to probe matter down to the atomic length scale, which helped us to analyze the fundamental structure of matter and the wondrous molecular mechanisms in our cells. Our digital age was enabled by advances in the material science of silicon. Material science is particularly fruitful with X-ray analysis tools since all chemical elements have unique electronic energy levels which can be specifically targeted by suitable X-ray wavelengths, so that tunable X-ray sources allow researchers to probe the chemical and structural properties of specific elements even in complex materials.
Second, the ability to create intense beams of coherent, fundamentally identical photons via <u>L</u>ight <u>A</u>mplification by <u>S</u>timulated <u>E</u>mission of <u>R</u>adiation (laser) enables us to manifest the quantum-physical wave-like nature of light in macroscopic observables. Thus, modern advances in quantum physics would be unthinkable without coherent laser beams. Lasers also enabled the field of non-linear optics[1], where multiple photons interact with matter at the same time and thus modify the interaction of the material with light. Non-linear processes are not only central to modern laser technology and drive much of the flexibility and ubiquity of laser sources, but also allow deep physical insights into the materials in which they occur. Today, lasers are ubiquitous from information technology to medicine, enabling countless sensory devices in our everyday lives, and have been instrumental to many Nobel prizes in physics (at least 1964, 1966, 1981, 1997, 2018, and 2022).
Third, the technology to build particle accelerators that can accelerate electron bunches to billions of electron volts of kinetic energy and compress them into bunches with high brilliance. Accelerator technology has been instrumental to particle physics in developing the standard model, which constitutes our most fundamental understanding of the universe around us. To compress particle pulses as well as laser pulses to extremely short bursts as short as a femtosecond, i.e. 10^{-15} s or the quadrillionths part of a second, allows us to make observations on the same timescale. This "ultra-fast" timescale reveals the movement of individual electrons around atoms and molecules, which in turn

---

[1] The demonstration of the first working laser by Maiman in 1960 [16] was soon followed by the discovery of second-harmonic generation by Franken et al. (1961) [17].

determines the chemical, electronic, and physical properties of materials.

The XFEL combines these developments by creating femtosecond-long bursts of laser-like X-ray radiation of freely tunable wavelength with a brightness unmatched by any other man-made X-ray source. This suggests that XFELs should naturally combine the transformative aspects of these technologies into new scientific insights. Indeed, XFEL-based science is already contributing to several of the most urgent scientific needs of modern civilization: The harvesting of sunlight as renewable energy, the storage of energy in form of batteries or synthesized fuels or gases generated by heterogeneous catalysis, as well as new basic components for computing electronics - all these hinge on our ability to design complex materials to achieve specific pathways for electronic excitations that lead to the desired chemical reactions or electric currents [18, 19]. In the one and a half decades since the first XFELs became operational and open to the scientific community, great advances have been made by exploiting their extreme pulse energies and the short pulse duration [20, 21]: The intense, focused radiation of XFELs enabled the study of matter at conditions of extremely high excitation densities which cannot be reached on earth in steady-state conditions [22–35]. Likewise, pump-probe experiments where a material system is probed with an XFEL pulse in a stroboscopic manner at a specific time-delay after exciting it with another (often optical laser) pulse are routinely performed and provide insight into electronic, magnetic, or chemical dynamics triggered by the pump pulse [36–47]. Despite their many merits, these studies still heavily rely on the principles of linear X-ray spectroscopy methods developed at synchrotrons, albeit utilizing a pulsed source. Furthermore, many material excitations can only be driven indirectly by optical pump lasers through the thermal response of the system, as opposed to a coherence-conserving direct excitation through photon absorption. In this aspect, the development of XFEL experiments still lags behind the implied promise of XFEL sources, since their coherence and brilliance in principle allows for non-linear X-ray spectroscopy methods: Non-linear spectroscopy exploits the effect of the simultaneous interaction of several photons with a given scattering center so that the response to each individual photon changes depending on the number and properties of all the photons involved. While generally more challenging to perform and interpret than linear spectroscopy, non-linear methods can on the one hand probe some states which are not accessible with linear spectroscopy due to dipole selection rules [48–50], and on the other hand probe more specific attributes of a sample, e.g. how certain excitations within the sample couple to each other. Figuratively speaking, each interacting photon whose properties can be restrained experimentally, provides the experimentalist an additional handle to constrain and determine the non-linear light-matter interaction process [51]. Combining such methods with the natural selectivity and localization of X-rays to electronic core levels is therefore highly attractive, as evidenced for example by the recently formed WavemiX network with the involvement of about 150 scientists and accepted or scheduled (long-term) proposals at most XFEL facilities (LCLS, SACLA, EuXFEL, SwissFEL, Fermi, and FLASH) [52].

1.1 Research Context

In the following paragraphs, I give a brief outline of the research development from linear to non-linear X-ray spectroscopy within the last two decades to contextualize the publications presented in this thesis.

The most straightforward implementation of non-linear X-ray spectroscopy is a high-fluence study, where the X-ray fluence is increased to the level where individual atoms may interact with multiple incoming photons. As later parts of the pulse thus find an already excited sample, the overall interaction becomes non-linearly dependent on the incident fluence. The first years of user operation of the first X-ray Free-Electron Lasers (FELs), the Free-electron LASer in Hamburg (FLASH) and the Linac Coherent Light Source (LCLS), saw a wave of quite successful non-linear X-ray studies that utilized ion time-of-flight spectrometers to investigate the multiple ionizations occurring upon intense X-ray irradiation of atoms [53, 54], molecules [55–57] and atomic clusters [58–60]. However, this thesis largely focuses on the study of solid samples, and techniques based on the detection of ions or electrons are challenging for high-density samples past a certain fluence because the strongly ionized matter affects the flight paths of charged particles (space-charge effects) [61, 62]. Thus, non-linear X-ray studies on solids generally utilize photon-in-photon-out techniques. As spectroscopic methods are concerned, this suggests studying either the absorption of the incident X-rays or the X-ray emission due to radiative core-hole decay (fluorescence or inelastic scattering). Because the absorption of focused FEL-pulses deposits a large amount of energy in the sample within a timescale that does not allow for significant expansion, the resulting plasma is created at the density of the original solid. This exotic state has seen significant research interest and was studied with much success by analyzing the X-ray emission of such plasmas [22–25, 28–35]. Other studies focused on the transmission in forward direction and found that the core-valence transition saturates, leading to induced transparency of the material [26, 27, 63–70], as well as evidence for multi-photon absorption processes [24, 25].

Most of these transmission studies investigated the X-rays at discrete, often non-resonant photon energies, rather than collecting full X-ray Absorption Near-Edge Spectroscopy (XANES) spectra around a core resonance. One reason for this is likely the experimental difficulty of collecting high-resolution transmission spectra while working with the inherent spectral intensity fluctuations of Self Amplified Spontaneous Emission (SASE) radiation. This is where the work presented in this thesis comes in, starting with an experimental scheme where the incident beam is split into two parts, one of which is used to probe the sample and the other to measure the unaltered incident spectrum. Based on experiences from earlier FEL experiments [71–73], we developed three different versions of a split-beam normalization scheme, suitable for transmission measurements through a liquid flat-jet [1], reflection from solid samples [2] and transmission through thin membranes [4, 8].

We use the reflection spectroscopy setup presented in [3] for a pump-probe experiment, wherein the transient reflection spectra are used to diagnose the reaction of the electronic system after absorbing an 800 nm infrared pulse. While one might describe such a pump-probe experiment overall as a non-linear process because the resulting spectra depend on the interaction of two separate photon pulses with the sample, care is typically taken to limit the fluence of the probe pulse to be non-disturbing. This way, the interaction with the probe pulse is purely linear, and the effects of changing the pump fluence as well as the incidence delay between the pump and probe pulse can be disentangled. This makes pump-probe schemes popular for the study of excited state dynamics at FELs [20, 21, 36–47, 74]. In the context of the development of non-linear spectroscopy, this pump-probe study [3] is included primarily to demonstrate the scientific value of the setup.

With adequate setups for measuring XANES spectra using focused SASE-radiation in hand, we performed a high-fluence transmission study on thin nickel films, presented in [4]. In contrast to earlier studies [26, 63–69], we measured continuous spectra of the nickel L_3-edge using varying fluences of monochromatic X-rays, covering over three orders of magnitude in fluence from mostly undisturbing, linear absorption to highly non-linear absorption where the excitation density reached several tens of eV per atom.

As XANES spectra encode the distribution of unoccupied electronic states around the Fermi-edge, this dataset allows for conclusions on the development of the electronic valence system during the absorption of the X-ray pulse. Rate models have been established as a useful phenomenological tool for describing saturable absorption at individual photon energies [66, 75, 76]. This led us to develop a classical finite-element rate model to quantify the rates of photon absorption and emission, electron thermalization and scattering as well as core-hole decays within the sample during interaction with the X-ray pulse [5]. As this model resolves the energetic distribution of electrons within the valence band and also accounts for fast photo- and Auger-electrons scattering with the valence system, it allowed us to reproduce the non-linearities of the spectra measured and presented in [4] to a large degree. On the one hand, this result is surprising since, among many other approximations, the model fundamentally operates in a single-electron picture and thus cannot account for any collective electronic effects or changes to the ground-state density of states. On the other hand, it is an encouraging result as it provides a tractable model, at least for the major effects in simple materials, for a highly non-linear process that is very challenging to capture in more a complete, quantum-physical description [77, 78].

The high-fluence studies discussed above are dominated by non-parametric effects, wherein the non-linearity of the overall process arises from the excitation energy that the pulse deposits in the sample while probing it. And while these studies are certainly crucial as they enable the understanding of highly excited systems and the excitation dynamics themselves, the greater part of the diagnostic advantages of non-linear spectroscopy hinted at earlier comes into play with the direct (coherent) interaction between multiple photons, i.e. in wave-mixing techniques.

As a first step towards X-ray wave-mixing, one may consider stimulated emission, which duplicates a photon interacting with an atom by drawing on the excitation energy that the atom absorbed from an earlier photon. Stimulated X-ray emission was identified early on as a promising tool to amplify the otherwise critically low signal level of RIXS [79–81]. The first spectroscopic experiments demonstrating stimulated X-ray experiments in this context followed as early as 2013 [82–84].

Technically, stimulated X-ray emission occurs in any high-fluence study such as [4]. However, since monochromatic X-rays were used, only elastic stimulated emission could occur, so that any signal gain due to stimulated emission was mathematically indistinguishable from the transmission gain due to saturation. Only when the bandwidth of the incident pulse is increased significantly to allow for inelastic stimulated emission, absorption of the higher-energy part of the pulse can create a population inversion that enables detectable amplification of the lower-energy part of the pulse through stimulated emission. This experiment is presented in [6]. Here, we demonstrated that the detected stimulated RIXS signal was six orders of magnitude stronger than the spontaneous signal observed in regular RIXS experiments. The largest part of this enhancement stems from the directed nature of the stimulated emission, which assumes the divergence of the stimulating pulse, as opposed to the spontaneous emission which is emitted more or less isotropically. Nevertheless, the signal still overlaps both in photon energy and in space with the incident beam, making the method not background-free.

As the next step in complexity one may consider X-ray second harmonic generation [85, 86] and Sum-Frequency Generation (SFG) [87], wherein two incident photons combine into one.[2] A relevant note about these second-order non-linear processes is that they are constrained to sites in the sample with broken inversion symmetry. This property can be exploited: As an example, second harmonic generation with photons resonant to the carbon K-edge has been demonstrated to specifically probe the electronic structure of the first 1-3 atomic layers of carbon in a graphite sample [86]. Nevertheless, it constitutes a major limitation to the applicability of the process, as inversion symmetry applies to a great number of sample systems.

For this reason, Four-Wave Mixing (FWM), a third-order non-linear process, has led to several very successful modalities in the optical regime [51, 88–93]. While the schemes vary, one common capability of wave-mixing spectroscopies is that they allow disentangling of how the excitations resonant with the respective waves are coupled within the material.[3] This would be particularly attractive to perform with a mixture of core-resonances (due to their local and element-specific character) and valence-transitions (due to their relevance to the material functionality) [80, 94–99]. This however requires that these methods can be translated to the Extreme Ultraviolet (XUV) and/or X-ray regime, which has proven a significant challenge to experiment development.

One group of FWM-schemes that have already seen significant experimental success are transient grating experiments [100–104]. Here, two degenerate XFEL pulses coincide at an angle so as to interfere on the sample surface, creating an excitation grating that develops over time and is probed by a delayed third optical pulse. The temporally varying diffraction from the excitation grating experienced by the probe pulse reveals the spatio-temporal development of the excitation pattern, which allowed significant insights into the propagation of acoustic excitations at the *mesoscale*, the range of many nanometers and hundreds of femtoseconds (as determined by the wavelengths, pulse durations and relative angles of the pulses involved). Note that in the common transient grating scheme, only the two degenerate waves forming the transient grating interfere coherently, while the third pulse simply diffracts from the excitation pattern they formed, and no new wavelength of light emerges from the interaction.

That changes in the case of SFG or Difference-Frequency Generation (DFG), which requires a fully coherent interaction between waves of different photon energy. One approach on this front is mixing XFEL pulses of different photon energy, which has come into reach of experiments recently due to the introduction of two-color FEL-operation schemes, and is seeing first successes in [105–109]. The other important approach is wave-mixing between XUV or X-ray waves and optical or Infrared (IR) waves. Here, the

---

[2] Note that the ordering may be disputable since these processes are second-order non-linear interactions, while stimulated inelastic scattering discussed above can be described as a third-order process [80].

[3] The dimensionality of the resulting coupling-plots coined the term *multidimensional spectroscopy.*

SFG between one optical and one X-ray wave demonstrated by Glover et al. in diamond has for several years been the only successful demonstration [87]. Very recently, Gaynor et al. have shown a coherent mixing between one 33 eV XUV pulse and two IR pulses in NaCl, achieving a wave-mixing signal separated in angle (but not in photon energy) and were able to constrain the coherent lifetime of the core-excitonic state [110]. In this context, we performed a wave-mixing experiment on LiF [7], where we for the first time observed both SFG and DFG signals between one XUV and two infrared photons from a solid sample, separated in energy on a spectrometer. A systematic variation of the incident XUV photon energy revealed a strong dependence of the generated signals on the core-resonance. Our quantitative interpretation suggests that the excitonic character of the core-resonance as well as an intermediate valence excitation drastically increased the third-order susceptibility. This way, the measurement allowed insights about the colocalization of the 1s2p and 1s2s core-excited states, which could not be probed with linear spectroscopy due to dipole selection rules.

In summary, I believe that the work presented in this thesis contributes significantly to the development of non-linear X-ray spectroscopy on various fronts, from the development of suitable normalization schemes [1, 2, 8] over the understanding of the relevant mechanisms in non-linear X-ray absorption around resonances [4, 5] to the exploitation of stimulated emission [6] and finally XUV-IR-wave-mixing [7]. Nevertheless, further experimental developments will be needed to establish that X-ray-wave-mixing techniques can deliver the significant scientific advancement in molecular and solid-state dynamics that they promise [80, 94–96].

Chapter 2

Fundamental Concepts

This chapter aims to equip a non-specialist reader with the concepts and terminology required to understand the remainder of this thesis. The chapter starts with an overview of the working principle and relevant properties of SASE-FELs. Second, the relevant terminology to describe X-rays propagating through matter is introduced and then expanded to discuss several interaction mechanisms between X-rays and matter. On this basis, I proceed to provide an overview of core hole spectroscopies in general with an emphasis on those techniques that are used in the publications presented in this thesis.

2.1 Free-Electron Lasers

While the first X-ray light sources were X-ray tubes, the development of synchrotron light sources dominated scientific X-ray applications with the need for highly brilliant X-rays as soon as they became available.

The term brilliance (photons/s/mrad^2/mm^2/0.1% spectral bandwidth) is a useful characterization of the brightness of a beam for analytic applications. As shown in Figure 2.1 this development advanced over the last 50 years even faster than the development of the number of transistors on a single microprocessor, which is famously termed *Moore's Law*. XFELs represent the culmination of this development since their extremely short and bright pulses reach a peak brilliance[1] unparalleled by any other man-made X-ray source. This is enabled by a non-linear gain of X-ray intensity in the undulator section using a mechanism called SASE.

This section aims to elucidate the generation and characteristics of radiation from SASE FELs, which are relevant for most measurements presented in this thesis. This section is based on [114–116] and a lecture on X-ray physics by P.D. Dr. Michael Martins [117]. For a more in-depth discussion of XFEL physics than presented here, see [115, 118–120].

Figure 2.2 shows a schematic Layout of FLASH, the XFEL at which the majority of the experiments within this thesis were performed. An electron bunch, created via the photoelectric effect by absorption of an optical laser pulse, is released from a cathode in

---

[1] Notably, the peak brilliance refers to the highest momentary value of brilliance. When it comes to average brilliance over time, synchrotrons can perform similarly or even better than XFELs, since they typically produce many more pulses per second.

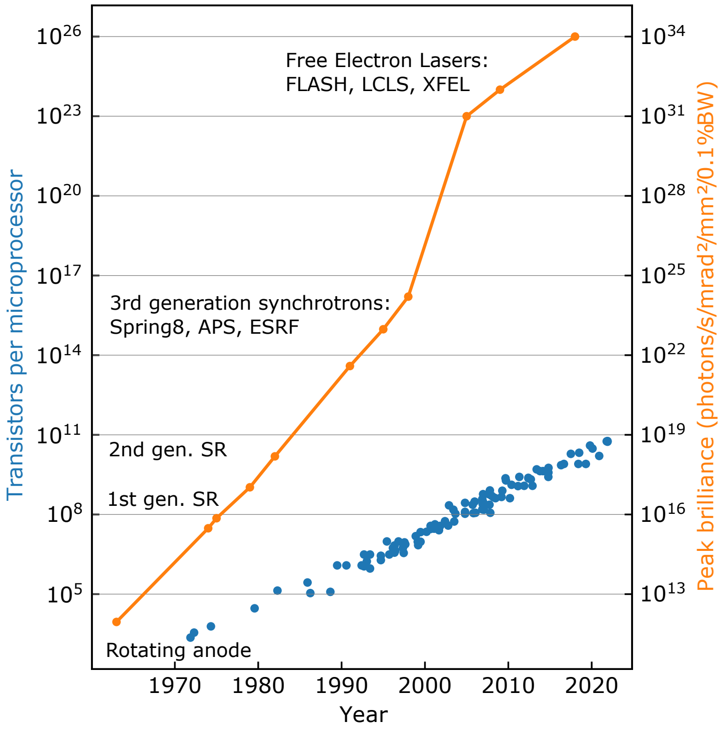

FIGURE 2.1: **Development of X-ray sources compared to microprocessors:** In the last 50 years, the number of transistors per microprocessor has increased by 10 orders of magnitude. In a co-enabling development, the peak brilliance available from X-ray sources developed in the same time increased by 22 orders of magnitude. For adequate comparison, the same relative scaling was chosen for both axes. Data assembled from [111–113].

the Radio Frequency (RF) gun and accelerated in superconducting accelerating modules towards the undulator section. In between, bunch compressors are inserted to reduce the electron bunch length to about 100 fs. In the undulator section, the electrons radiate X-rays as per the SASE process described below. The electrons act as a gain medium to allow an exponentially growing X-ray intensity, which leads to an even shorter photon pulse, typically of some tens of femtoseconds in duration. The photon pulse is then directed through one of the X-ray beamlines to the active experiment.

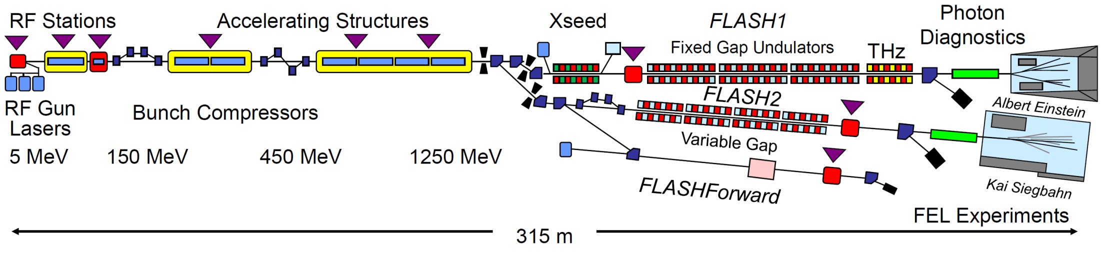

FIGURE 2.2: **Schematic layout of FLASH**. The electron beam is generated at the RF gun to the left and accelerated to 1250 MeV, and then directed in the undulators of FLASH1 or FLASH2, where the X-ray beams are generated and then used in the Albert Einstein and Kai Siegbahn experimental halls. Shown is the state before the upgrades performed in 2022. The components are not to scale; the total length is 315 m. Figure kindly provided by Siegfried Schreiber.

2.1.1 Synchrotron Radiation

To understand the SASE-process, we must first consider the general functionality of the magnetic structures where synchrotron radiation is produced, which holds for all synchrotron sources. These are called insertion devices, but specifically, wigglers or undulators, depending on their undulator parameter (see below). Let us consider a one-dimensional electron bunch traveling with a relativistic speed of v_e (and a Lorentz-factor of $\gamma = 1/\sqrt{1-(v_e^2/c^2)}$) through an insertion device on the optical axis as schematically laid out in Figure 2.3.

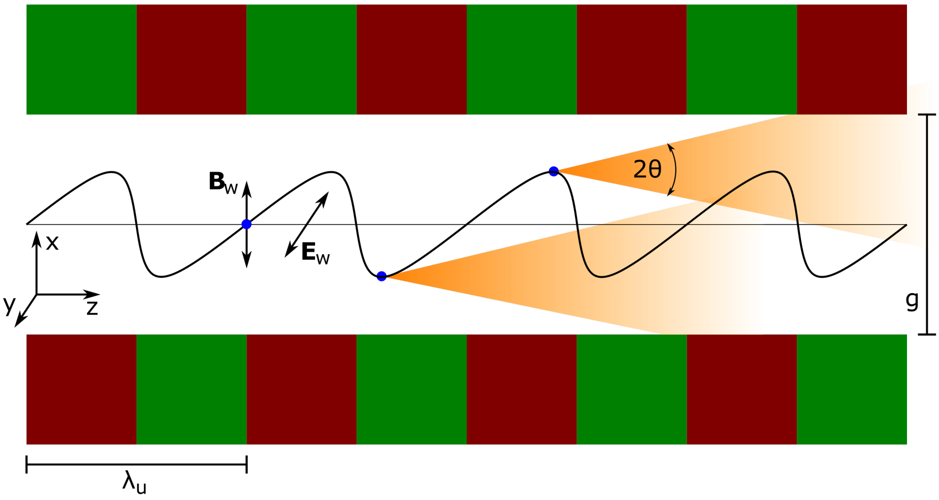

FIGURE 2.3: **Electrons traveling through an undulator.** The electrons enter the undulator from the left and are forced by the undulator's magnetic field onto a sinusoidal path on the yz-plane. This movement causes them to emit electromagnetic radiation into a cone with the opening angle 2θ. $\boldsymbol{E_w}$ and $\boldsymbol{B_w}$ indicate the electric and magnetic field vectors of the emitted wave.

The electrons experience the magnetic field of the undulator's magnets:

$$B_x(z) = B_{\text{eff}} cos\left(\frac{2\pi}{\lambda_u}z\right), \tag{2.1}$$

which can be tuned by varying the undulator gap g, so that the effective magnetic field becomes

$$B_{\text{eff}} = B_0/cosh(\frac{\pi g}{\lambda_u}),$$

where λ_u is the undulator period. Via the Lorentz force, the electrons are thus forced by the undulator magnetic field onto a sinusoidal path in the horizontal plane:

$$v_y = \frac{eB_{\text{eff}}\lambda_u}{2\pi\gamma m_0} sin\left(\frac{2\pi}{\lambda_u}z\right) \tag{2.2}$$

$$= \frac{Kc}{\gamma} sin\left(\frac{2\pi}{\lambda_u}z\right) \tag{2.3}$$

$$K = \frac{eB_{\text{eff}}\lambda_u}{2\pi m_0 c}, \tag{2.4}$$

where v_y is the horizontal velocity component and K is called the *undulator parameter*, which is characteristic for the type of insertion device: For values of $K \gg 1$, the insertion device is called a *wiggler* and is usually built with electromagnets and $\lambda_u > 20\,\text{cm}$, while for values of $K < 1$, it is called an *undulator* and is usually built with permanent magnets and $\lambda_u \sim 2\,\text{cm}$ [116, 117].

The oscillating movement of the electrons causes them to emit dipole radiation. For the sake of brevity, let us consider a simplified argumentation for this paragraph [114]: In the electron's frame of reference, ignoring for a moment that the longitudinal velocity (v_z) of the electrons is not quite constant, the emission happens with a dipole-typical cos^2 (dumbbell) emission character and an emitted wavelength of $\lambda = \lambda_u/\gamma$, which is the wavelength of the undulator's magnetic field seen from the electron's perspective. Seen from the laboratory frame of reference, the relativistic Doppler shift reduces this wavelength to $\lambda = \frac{\lambda_u}{2\gamma^2}$, and the emission character becomes a cone in forward direction with a half opening angle of $\theta = 1/\gamma$. In a wiggler, the amplitude of the electron's oscillation is so large that these emission cones do not overlap; in an undulator, however, the overlap is significant, so that the waves emitted by an individual electron emitted anywhere in the undulator interfere with each other and create coherent radiation within the bandwidth of constructive interference. As a consequence, the spectral intensity created in a wiggler increases linearly with the number of periods, while it can rise quadratically in an undulator.

Since the transverse movement of the electrons necessarily subtracts from their longitudinal velocity v_z, their path, which may be perfectly sinusoidal in space, is distorted in time. Since the emitted spectrum can be described as a Fourier transform of their oscillation in time, this distortion leads to contributions at higher harmonics of the fundamental wavelength in the emitted spectrum [116].

If we return to a more thorough analysis and account for the fact that not v_z, but γ is the conserved quantity, as well as allow for radiation deviating at an angle θ from the optical axis, the resonance condition of the undulator becomes [116]:

$$\lambda = \frac{\lambda_u}{2\gamma^2}\left(1 + \frac{K^2}{2} + \gamma^2\theta^2\right) \tag{2.5}$$

The spectral bandwidth of the undulator radiation is limited by the number of emission cones from individual electrons that interfere, which corresponds to the number of undulator periods N_u:

$$\frac{\Delta\lambda}{\lambda} = \frac{1}{N_u} \tag{2.6}$$

2.1.2 Self-Amplified Spontaneous Emission

While even in a storage ring-based synchrotron light source, the individual electrons in the undulator radiate coherently, different electrons still emit at a random relative phase. This changes at XFELs because of the SASE process or alternatively due to *seeding*[2]. Both processes imprint a *microbunch* structure onto the electron bunch and thus lead to coherence between the emission of the typically $\sim 10^{10}$ electrons within the bunch; as the brightness of coherent radiation scales quadratically instead of linearly with the number of emitters, XFELs can reach a peak brilliance which is higher than that of storage rings by about 10 orders of magnitude, as shown in Figure 2.1.

The SASE process begins as the electron bunch enters the first undulator. The initial distribution of electrons within the bunch is only modulated by random shot noise in the electron density. This bunch now begins to spontaneously emit photons from anywhere within the bunch, as described in the section above. The co-evolution of the electron bunch and the emitted radiation power is qualitatively shown in Figure 2.4, showing a slow initial growth of radiated power. The emitted radiation propagates forward together with the electron bunch at the speed of light. The field of this light wave, indicated as $\boldsymbol{B}_w$ and $\boldsymbol{E}_w$ in Figure 2.3, now causes additional Lorentz forces on the moving electrons. While a full derivation of the forces involved is beyond the scope of this introduction and can be found in [114, 115, 118] (in this order of complexity), generally speaking, the transverse oscillation of the electrons in the additional magnetic field $\boldsymbol{B}_w$ creates a force depending on the relative phase of the light wave and the undulator period, which results in the electron density being modulated in z-direction with a periodicity of λ. This effect is called *microbunching.* The more pronounced the microbunching structure of the electron bunch, the greater the coherently emitting fraction of electrons and thus the emitted radiation power. The analysis of the development of microbunching over time is not reproduced here but results in the *XFEL equation* (Eq. 2.7), which shows that the transfer of energy from the electron bunch to the emitted radiation is proportional to the already existing field strength $\boldsymbol{E}_w$. This manifests in the exponential increase shown in Figure 2.4.

$$\frac{d\gamma}{dt} = \frac{e\boldsymbol{E}_w K}{2\gamma mc} \left(cos[(k + k_u)z - \omega t] + cos[(k - k_u)z - \omega t]\right) \tag{2.7}$$

Here, $k_u = 2\pi/\lambda_u$ is the wave vector of the undulator and $\omega = 2\pi c/\lambda = kc$ is the angular frequency of the radiation. The exponential gain continues until the electromagnetic wave has drawn so much energy from the electron bunch that γ is reduced so far that it no longer fulfills the resonance condition for the original radiation. This causes the relative phase between the undulator's magnetic field and the radiation to invert so that energy begins to flow back from the radiation to the electron bunch, thus ultimately limiting further growth of the radiation power[3]. This is called the saturation regime.

---

[2] A discussion of seeding schemes is beyond the scope of this thesis. See [121–125] for further information.

[3] A common technique to increase the amount of energy extracted from the bunch is to adjust the undulator gap with the undulator distance to account for the lost electron energy and sustain the same resonance condition over a longer distance. This is called undulator *tapering* and can significantly increase the ultimate FEL pulse energy.

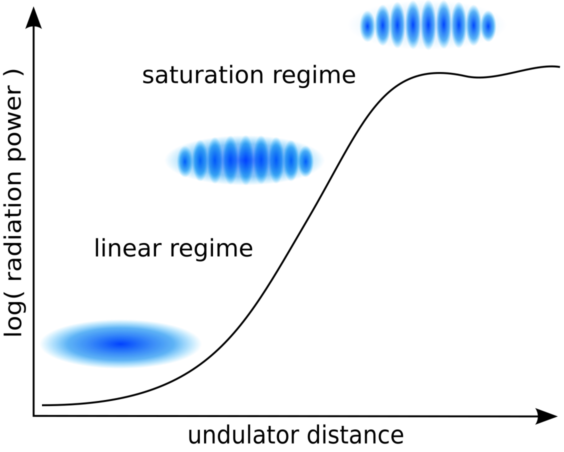

FIGURE 2.4: **Microbunching during the FEL gain process**. The SASE process begins with spontaneous radiation at the beginning of the undulator, which co-propagates with the electron bunch and imprints a *microbunching* modulation with its own wavelength on the bunch, which increases the coherently radiating fraction of electrons, thus enabling an exponential growth in radiation power (linear regime) until the electron kinetic energy is sufficiently reduced so far that the resonance condition no longer matches the microbunch structure and the energy transfer between electrons and photons changes direction.

Overall, this makes SASE a non-linear gain process that amplifies the initial shot noise in the electron bunch by transferring energy from the electron bunch into the electromagnetic wave [119]. It requires a very low emittance of the electron bunch, which cannot be sustained in a storage ring, which is why XFELs strictly require linear accelerators to operate. Even then, under typical experimental conditions, only a part of the electron bunch in phase space actually contributes to the SASE process, so that electron bunches on the order of 100-200 fs duration may produce photon pulses on the order of tens of femtoseconds.

One may draw some parallels to the gain process in optical lasers, where an ensemble of atoms is prepared in an excited, population-inverted state (corresponding to the accelerated electron bunch of the FEL) in a cavity with a resonance condition (corresponding to the undulator resonance condition), and initial spontaneous emission from individual atoms is amplified by stimulating coherent emission into the same modes from the remaining gain medium. These parallels motivate the term free electron *laser*, together with the laser-like properties of the resulting radiation.

Properties of SASE radiation

In the average over many pulses, SASE spectra are ideally Gaussian distributed in both time and energy, and may be characterized by their envelope pulse duration Δt and bandwidth ΔE. These parameters emerge from the phase space volume of the lasing part of the average electron bunch. Individual SASE pulses develop several modes. These modes manifest in their structure as "spikes", both in the time domain and in the spectral (photon energy) domain. Figure 2.5 demonstrates this on two pairs of simulated spectra with different pulse durations.

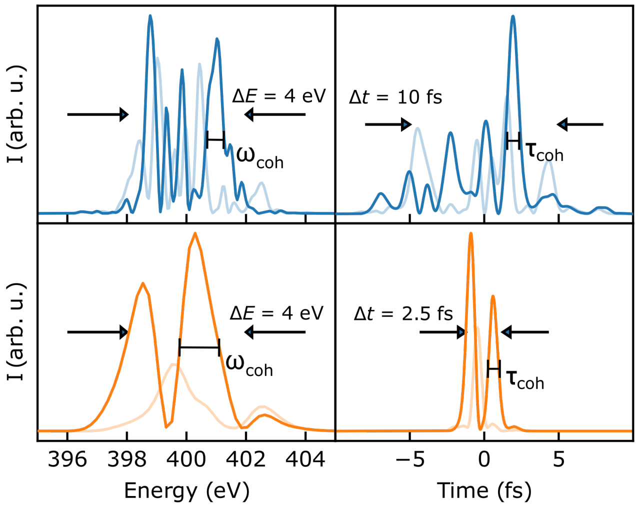

FIGURE 2.5: **Examples for SASE pulse structure** in the domains of time and photon energy. Pulses are simulated with the partial coherence method [126]. To demonstrate the stochastic nature of SASE, each panel shows simulations for two independent pulses (solid and transparent lines, respectively). The upper panels show pulses with a pulse duration of Δt=10 fs and the lower panels with Δt=2.5 fs. The bandwidth (FWHM) was chosen to be $\Delta E/E = 1\%$, which is a typical value for FLASH [119].

While the structure of the electric field in the time and energy domain is connected by the Fourier transform, this relation cannot be trivially exploited for temporal characterization because the information about the electric field's phase is lost in measurements of intensity. However, some relations can be derived: The individual modes are fully coherent and bandwidth-limited. This means that generally, the width of spectral and temporal spikes represents the spectral and temporal coherence of the pulse, respectively. By the Fourier relation, the envelope or average bandwidth is thus proportional to the inverse coherence time, and the pulse duration is proportional to the inverse spectral coherence [127]. Based on this principle, analysis of SASE-spectra measured with sufficient resolution also allows for statistical deductions about the pulse duration [128–131][4].

An often relevant consideration is the pulse energy delivered either within the entire SASE pulse or, in cases where a monochromator is used, a specific interval of the spectrum. Because SASE is a stochastic process, this pulse energy W_p fluctuates from shot to shot.

Integrating over the full SASE-spectrum of each shot from an XFEL operating in the saturation regime, the pulse-to-pulse energy fluctuations tend to approximate a normal distribution with limited spread in the order of some of tens of percent in deviation from the mean. However, these fluctuations increase dramatically when considering pulses that are very narrow either in the time domain (short pulses) or in the spectral domain (monochromatic pulses), as well as when the XFEL is operated in the linear regime.

---

[4] I performed such an analysis for the data-set which lead to our publication with Higley et al. [6]. While this analysis was my main contribution to that paper, the algorithms used were developed and published before I started my Ph.D. research [130, 131] and are therefore not discussed in this thesis.

In the extreme case of an XFEL operating in the linear regime and using a narrowband monochromator, the pulse energy probability approaches a negative exponential distribution

$$p(W_p) = \exp\left(-\frac{W_p}{\langle W_p \rangle}\right), \tag{2.8}$$

where most pulses contain very little energy, but occasional high-energy pulses occur [120]; $\langle\rangle$ denotes the ensemble-average.

For many FEL experiments, the quantity of interest manifests in a relationship between the intensity incident on the sample and the one measured after sample-interaction. Considering the pulse energy fluctuations of SASE radiation, normalizing the observed effect only by an average incident intensity becomes viable only when a large number of pulses are averaged. This makes it useful to measure the (spectral) intensity of every pulse before it interacts with the sample. Chapter 3.3 discusses this in detail.

For a more detailed discussion of the statistical properties of SASE-radiation, the interested reader may be referred to [119, 120, 127].

2.2 Light Propagation through Matter

This section establishes fundamental terminology for X-rays traversing through matter, such as the parameters to quantify absorption and transmission, as well as the refractive index.

2.2.1 Absorption

In the simplest case, a light wave with an intensity[5] $I(\omega)$ and an angular frequency ω traversing a distance x of homogeneous material is absorbed by the material at a rate proportional to its own intensity. This rate can be characterized by the attenuation length $\lambda_A(\omega)$; the resulting differential equation may be solved to describe the attenuation of a light wave within a uniform sample after irradiation with an intensity I_0, leading to a simple form of the Lambert-Beer law[6]:

$$\frac{dI(\omega)}{dx} = -\frac{I(\omega)}{\lambda_A(\omega)} \qquad \Rightarrow \qquad I(x,\omega) = I_0(\omega) e^{-x\frac{1}{\lambda_A(\omega)}} \tag{2.9}$$

Experimentally, one may observe an intensity of I_T after transmission through a sample of thickness d. In this case, the terms transmittance $T(\omega)$, absorbance $A(\omega)$, and the the attenuation length $\lambda_A(\omega)$ are used later on in this thesis.

$$T(\omega) = \frac{I_T(\omega)}{I_0(\omega)} = e^{-\frac{d}{\lambda_A(\omega)}}, \tag{2.10}$$

---

[5] I here refer to intensity as the number of photons irradiated per unit time and per unit area.

[6] In its complete form, the Lambert-Beer law also considers the concentrations c of various absorbing species and their attenuation coefficient ϵ, where in case of a single species $\epsilon c = 1/\lambda$.

$$A(\omega) = \log_{10} \frac{I_T(\omega)}{I_0(\omega)} \qquad \lambda_A(\omega) = \frac{1}{\ln{(10)}} \frac{d}{A(\omega)} \tag{2.11}$$

In order to relate these macroscopic quantities to individual atoms, we may consider N_g as the number of atoms in the ground state that the light interacts with while traversing a unit volume. In this case, we may for the first time in this chapter assign each atom an absorption cross section $\sigma_a(\omega)$:

$$\sigma_a(\omega) = \frac{1}{N_g \lambda(\omega)} \tag{2.12}$$

2.2.2 Index of Refraction

The index of refraction $n_r = \sqrt{\epsilon_r \mu_r}$ is a useful parameter to characterize how the propagation of light changes in matter in comparison to the vacuum, and is thus defined in terms of the relative permittivity ϵ_r and permeability μ_r of a material.

There are several notation conventions to denote the real and imaginary parts of the refractive index: While in visible optics is $n_r = n + i\kappa$ is frequently used, $n_r = 1 - \delta - i\beta$ is customary in the X-ray regime, owing to the fact that the real part of n_r is typically smaller than unity for X-ray wavelengths. In a description of atoms scattering as dipoles, the index of refraction can also be expressed in terms of the atomic forward scattering factor $f = f_1 + i f_2$, which has been tabulated for most chemical elements by Henke et al. [132]:

$$n_r = 1 - \frac{r_0}{2\pi} \lambda^2 \sum_q n_q (f_{1q} + i f_{2q})$$

Here, n_q is the number density and f_{1q} and f_{2q} form the atomic forward scattering factors of the element indexed q; r_0 is the classical electron radius and λ the wavelength.

An absorption measurement can be used to derive the attenuation length λ_A, which relates to the imaginary part of the refractive index with $Im(n_r) = \lambda(4\pi\lambda_A)^{-1}$.

Kramers-Kronig Relation

The real and imaginary parts of the refractive index can furthermore be related by the Kramers-Kronig transform. This transform can be expressed in terms of atomic scattering factors [133]:

$$f_1 = Z^* - \frac{2}{\pi} P \int_0^\infty \frac{x f_2}{x^2 - E^2} dx$$

Here Z^* is a relativistic correction introduced by Henke et al. [132] and P denotes the Cauchy principal value. Since this integral is not trivial to evaluate, an algorithm by B. Watts is used later on in this thesis (specifically in publications [2, 3]) to perform this transformation [133].

2.3 Light-Matter Interaction

Let us now also establish a description of how light affects the electronic structure of materials it is traversing and vice versa. I begin this introduction by describing matter as an abstract two-level system, which already enables many important insights, such as the origin of natural linewidths and the balance between absorption and emission processes. After that, I move to a more precise description of the absorption cross-section in the form of Fermi's golden rule and introduce the dipole approximation and the concept of the oscillator strength as a link between the theoretical description and experimental observables. Finally, I will introduce the basics of non-linear light-matter interactions.

2.3.1 Absorption and Emission in a Two-Level System

In a most simple description, we may assume a number of atoms in a vacuum that are all initially in a ground state g, but also exhibit an excited state f which can be reached from state g by absorbing a photon with a photon energy of

$$E_{phot} = \hbar\omega_{fg}, \tag{2.13}$$

corresponding to the energy difference between state g and state f, where $\hbar$ is the reduced Planck's constant and ω_{fg} is the resonance frequency of the transition. In the inverse process, the excited atom may also relax back to the ground state by emitting an equivalent photon. It will do so if the atom is excited and a coherence between both states is stimulated by another resonant photon. If this stimulating photon is merely a result of the fluctuating electromagnetic field in a vacuum [134], the process is referred to as *spontaneous emission.* If the stimulating photon is the result of a specific irradiated light field, it is called *stimulated emission*, and the stimulated photon will match the exact properties (energy, polarization, and direction of propagation) of the stimulating photon. This simple model already has profound implications of great practical relevance, which are qualitatively discussed below.

Even in a perfect vacuum, the excited state will eventually decay spontaneously with a constant probability. Thus, if we observe the spontaneous decay of an ensemble of excited atoms, we should expect a rate of spontaneous emission events that is proportional to the number N_f of excited atoms. This forms again a linear differential equation (eq. 2.14) with the excited state lifetime τ_{SE} as a characteristic constant, resulting in an exponentially decaying time-evolution of the excited state (eq. 2.15)[7].

---

[7] Real systems can also decay non-radiatively by losing the excitation energy to another particle. Most relevant in the soft X-ray regime is the Auger decay process, where the excitation energy of a core excitation accelerates an electron that is consecutively emitted from the atom. This alternative decay pathway affects the excited state lifetime in the same way as spontaneous emission. Thus, in the following consideration of the natural line shapes, a more general τ can instead be used to describe the effective lifetime in order to account for all relevant decay channels, i.e. $\frac{1}{\tau} = \frac{1}{\tau_{SE}} + \frac{1}{\tau_{Auger}} + ...$ [135, 136].

$$\frac{dN_f}{dt} = -\frac{dN_f}{\tau_{SE}} \tag{2.14}$$

$$N_f(t) = N_f e^{-\frac{t}{\tau_{SE}}} \propto I(t) \tag{2.15}$$

Excited State Lifetime and Linewidth

Each event of spontaneous emission results in an emitted photon with an energy corresponding to the excitation energy. However, the exact time at which a given photon was emitted cannot be known beyond characterizing of the lifetime of the emitting excited state, so that the uncertainty relation [135, 136] between time and energy in turn limits the precision with which the energy of the resulting photon can be known. This results in the *natural line width* Γ (specified as Full Width Half Maximum (FWHM)) of the resulting radiation.

$$\Gamma = 2\hbar/\tau_{SE} \tag{2.16}$$

We can characterize this more precisely by translating the temporal behavior of each atom shown in eq. 2.15 into the frequency domain using a Fourier transform, which leads to:

$$I(t) \propto e^{-\frac{t}{\tau_{SE}}} \xrightarrow{\mathfrak{F}} I(\omega) \propto \frac{1}{\pi\tau_{SE}} \frac{1}{(1/\tau_{SE})^2 + \omega^2} := g(\omega) \tag{2.17}$$

so that the natural line shape $g(\omega)$ emerges, which takes the form of a Lorentz (or Cauchy) distribution. The Lorentzian line shape is characteristic of homogeneous broadening, where all emitting atoms are affected in the same way.[8]

Einstein Coefficients

The description of a two-level system was also used by Albert Einstein in his work "Strahlungs-Emission und -Absorption nach der Quantentheorie" [137], where he connects the rate of spontaneous emission, absorption and stimulated emission in an ensemble of atoms using the thusly named *Einstein coefficients* A_{fg}, B_{gf} and B_{fg}, respectively. Within the earlier discussed unit volume of atoms (N_g in the ground state, N_f in the excited state), one may expect a total rate of spontaneous emission events equal to:

$$W^s_{fg} = \frac{N_f}{\tau_{SE}} = A_{fg} N_f \tag{2.18}$$

In the additional presence of photons with an energy density ρ_ω per unit angular frequency[9], we can additionally expect a rate W^i_{gf} of absorption events and a rate W^i_{fg} of

---

[8] Real measurements are typically also affected by various additional broadening effects, such as collisional broadening, where the lifetime of the emitting state is reduced due to collisions with other molecules, as well as Doppler broadening, where the relative thermal motion of the radiating atoms broadens the spectral line due to the Doppler effect. Using a Boltzmann distribution for the atom velocities, this leads to a Gaussian line shape and is referred to as inhomogeneous broadening, since in this case, each atom radiates at a distinct frequency.

[9] As discussed in [138], the choice of units can change the relations 2.21 and 2.22.

stimulated emission events:

$$W_{gf}^{i} = B_{gf}^{\omega}\rho_{\omega}N_{g} \tag{2.19}$$

$$W_{fg}^{i} = B_{fg}^{\omega}\rho_{\omega}N_{f} \tag{2.20}$$

Under this premise, while treating ρ_{ω} as constant within the frequency range relevant for the absorption and emission between levels g and f, Einstein connected these coefficients by [138]:

$$B_{fg}^{\omega} = \frac{\pi^2 c^3}{\hbar\omega_{fg}^3}A_{fg} \tag{2.21}$$

$$\frac{B_{gf}^{\omega}}{B_{fg}^{\omega}} = \frac{g_f}{g_g} \tag{2.22}$$

where g_g and g_f are the degeneracy factors (i.e. the respective number of equivalent states) of the two levels. The Einstein coefficients that emerge from this very simple quantized description can be related back to the absorption cross section $\sigma_a(\omega)$ [138] which we introduced based on the phenomenological picture of absorption in the previous chapter:

$$\sigma_a(\omega) = \hbar\omega B_{gf}^{\omega}g(\omega)/c \tag{2.23}$$

$$= \frac{1}{2}\frac{g_f}{g_g}\frac{\pi c}{\omega_{fg}}g(\omega)A_{fg} \tag{2.24}$$

Equation 2.22 elegantly demonstrates the symmetry between the resonant processes of stimulated emission and absorption.

It also implies that in any optical two-level system, even with such high photon densities that spontaneous decay becomes negligible, the occupation of the final state f cannot exceed the degeneracy ratio g_f/g_g and the rate of stimulated emission can only ever match but never exceed the rate of absorption. At this point, the material appears effectively transparent - the transition is *saturated*. Note that the cross section for absorption (Eq. 2.24) and for stimulated emission only differs in terms of the degeneracy ratio, which will become relevant in chapter 4 of this thesis.

Rabi Oscillations

The description given above applies for the limit of incoherent radiation, which applies well to the studies presented in this thesis due to the small longitudinal/temporal coherence of the SASE-pulses used. When considering the interaction with a coherent field, the states of a two-level system become coherently coupled by the driving field. This can lead to an oscillation of the population density between the two fields that is eventually damped due to dephasing of the excited state[10].

For a more detailed quantum physical discussion of the two-level system exposed to a coherent electromagnetic field and the non-linear optical susceptibility emerging from this description, I recommend chapter 6 of R.W. Boyd's book on non-linear optics [51].

---

[10] In this context, it is common to refer to the relaxation time of the population, i.e. the excitation lifetime, as T_1 and the relaxation time of the precessing dipole moment as the dephasing time T_2.

2.3.2 Fermi's Golden Rule

Having characterized the absorption process as a macroscopic phenomenon and then in terms of the very general picture of a two-level system, we now look at a more complete, semi-classical description of the absorption process.

Fermi's golden rule uses a classical description of electromagnetic waves but a quantum-mechanical description of its perturbation on the wave functions of initial and final states. Here, I briefly rehearse this rule based on [139]. The rule quantifies the probability P_{gf} that an atom irradiated by an electromagnetic wave transitions from an initial ground state $|g\rangle$ to a final state $|f\rangle$ within a unit of time.

$$P_{gf} = \frac{2\pi}{\hbar} \left|\langle f|\, \bar{V}\, |g\rangle\right|^2 \rho_f(E) \tag{2.25}$$

This equation follows from Schrödinger's Equation when treating the effect of the incident wave as a harmonic time-dependent first order perturbation to the Hamiltonian. The term $\langle f|\, \bar{V}\, |g\rangle$ is referred to as the transition matrix element.

Using the Coulomb gauge so that $\boldsymbol{E} = -\frac{1}{c}\frac{\partial A}{\partial t}$, a plane incident wave can be written in terms of its vector potential:

$$\boldsymbol{A} = \boldsymbol{e}\frac{A_0}{2}\left(e^{i(\boldsymbol{k}\cdot\boldsymbol{x}-\omega t)} + e^{-i(\boldsymbol{k}\cdot\boldsymbol{x}-\omega t)}\right) \tag{2.26}$$

If we consider the perturbation that such a field will have on the electrons of an atom with linear momentum operators $\boldsymbol{p_i}$, totaling to $\boldsymbol{p} = \sum_i \boldsymbol{p_i}$, we can write the dominant term of the time-dependent perturbation as

$$V(t) = \frac{e}{mc}\boldsymbol{A}\cdot\boldsymbol{p} \tag{2.27}$$

By substituting 2.27 and 2.26 into 2.25, we arrive at the following transition probability caused by a plain wave:

$$P_{gf} = \frac{\pi e^2}{2\hbar m^2 c^2} A_0^2 \left|\langle f|\, e^{i\boldsymbol{k}\cdot\boldsymbol{x}}\boldsymbol{e}\cdot\boldsymbol{p}\, |g\rangle\right|^2 \rho_f(E) \tag{2.28}$$

Note that here only the negative time dependent exponential term $e^{-i\omega t}$ of 2.26 is considered as contributing to absorption. The same description can be used with the other term to describe a stimulated emission into an empty core hole.

$|g\rangle$: Ground state
$|f\rangle$: Final State
$\rho_f(E)$: Energy-dependent final state density
$\boldsymbol{E}(t)$: Electric field vector
$\boldsymbol{A}(t)$: Vector potential
A_0: Vector potential amplitude
$\boldsymbol{e}$: Unit vector
$\boldsymbol{k}$: Wave vector
$\boldsymbol{x}$: Space vector
ω: Radial frequency
e: Electron charge

2.3.3 The Dipole Approximation

Calculating equation 2.28 is still difficult due to the exponential function in the operator. Instead, the exponential function can be written as a power series. Neglecting the terms beyond the first order of this series is referred to as the *dipole approximation*. This cutoff is a good approximation if $\boldsymbol{k} \cdot \boldsymbol{r} \ll 1$, i.e. $2\pi|\boldsymbol{r}| \ll \lambda$.

If we describe electrons in atomic potentials, $\boldsymbol{r}$ is limited to the size of the atom, so that the dipole approximation yields good results up to wavelengths in the soft and tender X-ray regimes, where the wavelength begins to be comparable to the localization length scale of the electrons. With the dipole approximation, equation 2.28 reduces to:

$$P_{gf} = \frac{\pi e^2}{2\hbar m^2 c^2} A_0^2 \left|\langle f|\, \boldsymbol{e} \cdot \boldsymbol{p}\, |g\rangle\right|^2 \rho_f(E) \tag{2.29}$$

This probability can be normalized to the incident flux $F_{ph} = \frac{A_0^2 \omega}{8\pi\hbar c}$ to arrive at the absorption cross-section:

$$\sigma_{Abs}(E) = \frac{4\pi^2 e^2}{m^2 c\omega} \left|\langle f|\, \boldsymbol{e} \cdot \boldsymbol{p}\, |g\rangle\right|^2 \rho_f(E) \tag{2.30}$$

2.3.4 Oscillator Strength

Since the cross-section is a function of photon energy, experimental measurements usually observe an integrated value of σ_{Abs} over some range in E. This makes it useful to describe the intensity of resonances as an integral of the absorption cross-section in form of the dimensionless *optical oscillator strength* f, so that:

$$\sigma_{Abs} = \frac{2\pi^2 e^2 \hbar}{mc} \frac{df}{dE} \tag{2.31}$$

For transitions between two bound states, it is also called the *f-number* and can be described with the derivation above as [139]:

$$f = \frac{2}{m\hbar\omega} \left|\langle f|\, \boldsymbol{e} \cdot \boldsymbol{p}\, |g\rangle\right|^2 \tag{2.32}$$

2.3.5 Non-Linear Light-Matter Interaction

In most optical effects which we encounter on a day-to-day basis, the optical response of materials is proportional to the strength of the optical fields applied to it; this leads us to describe it as linear optics. The term non-linear optics thus encapsulates any effect where the optical response of a material is non-linearly dependent on the driving fields. This section follows R.W. Boyd [51] and his notation of using the tilde accent to denote quickly varying quantities.

To describe the non-linear optical response of a material, one considers the strength of the dipole moment which the electric field of a wave induces per unit volume. This is characterized as a polarization vector $\tilde{\boldsymbol{P}}$:

$$\tilde{\boldsymbol{P}} = \epsilon_0 \sum_n \boldsymbol{\chi}^{(n)} \tilde{\boldsymbol{E}}^n \equiv \sum \tilde{\boldsymbol{P}}^{(n)} \tag{2.33}$$

Expanding $\tilde{\boldsymbol{P}}$ as a power series of order $n \in \mathbb{N}$ allows a clean distinction between non-linear effects of different orders, which often occur separately. Each order n can be assigned a non-linear[11] optical susceptibility $\boldsymbol{\chi}^{(n)}$, which characterizes effects of order n and their scaling with the n'th power of the overall electric light field. In a more complete notation, the non-linear susceptibilities become tensors of rank $n+1$, reflecting the interaction of the light polarization vectors involved, and are functions of all contributing frequencies. For example, using the indices $ijkl$ to refer to Cartesian field components, we may characterize the third order polarization for the sum frequency $\omega_m + \omega_n + \omega_o$ response along i dependent on the electric fields $\tilde{E}_j(\omega_m)$, $\tilde{E}_k(\omega_n)$ and $\tilde{E}_l(\omega_o)$ with different frequencies and polarizations.

$$\tilde{P}_i(\omega_m + \omega_n + \omega_o) = \epsilon_0 \sum_{jkl} \sum_{(mno)} \chi^{(3)}_{ijkl}(\omega_m + \omega_n + \omega_o, \omega_m, \omega_n, \omega_o) \tilde{E}_j(\omega_m) \tilde{E}_k(\omega_n) \tilde{E}_l(\omega_o) \tag{2.34}$$

Note that various frequencies with indices n, m, and o can contribute, but in this case the sum $(\omega_m + \omega_n + \omega_o)$ is held constant. If we use three specific frequencies for ω_n, ω_m and ω_o, the sum over (nmo) may be replaced by multiplying with a degeneracy factor D, representing the number of distinct permutations of the three frequencies.

I choose the example of third order sum frequency generation here, because we observed this process in [7] between one XUV and two IR photons.

Since this description in terms of a non-linear susceptibility is quite general and phenomenological, it can be derived both from a description of matter as classical anharmonic oscillators or from a quantum mechanical density matrix formalism (naturally, with varying predictive power, depending on the sample system).

---

[11] For $n > 1$, as $\chi^{(1)}$ is the linear susceptibility.

Symmetry

General arguments can be drawn from the spatial symmetry properties of an interacting medium to show that certain tensor components of the linear and non-linear susceptibility must be zero. This is relevant in crystalline samples (see for example [51] chapter 1.5.11). While a wider discussion of these conditions is beyond the scope of this thesis, it is important to note that the second-order non-linear response of all centrosymmetric systems must be zero. This can be shown with a simple argument:
For an induced polarization $\tilde{\boldsymbol{P}}$, inversion symmetry implies that the sign of the polarization must also change if the sign of the inducing light field is flipped. Applying this condition for a second order process to equation 2.33 requires:

$$\tilde{\boldsymbol{P}} = \epsilon_0 \boldsymbol{\chi}^{(2)} \tilde{\boldsymbol{E}}^2 = \epsilon_0 \boldsymbol{\chi}^{(2)} [-\tilde{\boldsymbol{E}}]^2 = -\tilde{\boldsymbol{P}} \tag{2.35}$$

Obviously, this equation can only be true for values of zero, thus requiring $\boldsymbol{\chi}^{(2)} = 0$

This is a powerful insight, as it means that the observation of any second order non-linear process is a sign of broken inversion symmetry, which is useful to detect distortions such as crystallographic defects, excitations or simply material interfaces in normally centrosymmetric systems[12].

Parametric and Nonparametric

The processes described above in terms of real-valued susceptibilities are parametric processes, where after the interaction, the material is left in the same state as it was before. Consequently, the overall photon energy of parametric processes is always conserved.

However, photons in a non-linear process may also lose or gain energy in the material, in which case one speaks of a nonparametric process. This is, for example, the case when the transmittance of a material grows with the incident fluence because the transition responsible for the absorption becomes saturated.

In this thesis, chapter 4 deals primarily with saturation-related nonparametric non-linear processes with increasing relevance of the parametric process of (resonant) stimulated emission in chapter 5, while we observe a purely parametric wave-mixing process in chapter 6.

Momentum Conservation and Phase Matching

A parametric wave mixing process not only requires the conservation of the total photon energy but also of the total momentum of all photons involved. Consequently, if a new light wave is generated as the sum of two other waves, its wave vector corresponds to the geometric sum of the contributing waves, in addition to a possible momentum transfer into the non-linear material.

As wave-mixing is a fully coherent process, any new waves are generated with a phase that directly follows from the phases of the generating light waves. Note that the phase

---

[12] Note that 11 out of 32 crystallographic point groups are inversion symmetric. These are (in Schoenflies notation): S_2 (triclinic), C_{2h} (monoclinic), D_{2h} (orthorombic), T_h and O_h (both cubic), C_{4h} and D_{4h} (both tetragonal), S_6 and D_{3d} (both trigonal), C_{6h} and D_{6h} (both hexagonal).

velocity of light in a medium is dependent on the wavelength (dispersion). If a wave-mixing process occurs within a material over an extended volume, this means that the relative phase between the involved light waves will normally diverge due to their different phase velocities, which then prevents the constructive interference or buildup of any wave-mixing products. In the optical regime, one common solution to this problem is the use of birefringent materials in which the index of refraction differs depending on the propagation direction. By carefully controlling the propagation directions of the involved light fields, the birefringence can be used to counteract the difference between the phase velocities and thus enable constructive interference of the wave-mixing products over the entire interaction volume.

2.4 Excitation Response of the Electronic Structure

Having discussed in some detail how light interacts with atomar excitations, this section discusses some of the consequences of these excitations in a material. With the case of X-ray absorption in solids in mind, I will first discuss how X-ray induced core hole excitations decay, and then how this excitation energy ultimately leads to a modified thermal equilibrium of a material's electronic and nuclear subsystems.

2.4.1 Core Hole Decay

Most X-ray based processes involve the absorption of an X-ray photon at an electronic core level, resulting in an unoccupied core state or core hole. As a core-excited state is energetically unfavorable for the atom, these typically decay on a timescale of a few femtoseconds [136]. There are two major pathways for this decay: Fluorescence and the so called Auger or Auger-Meitner process. In the event of a fluorescent decay, an electron from an energetically higher occupied state fills the core hole and emits the energy difference in form of a photon. In the event of an Auger-Meitner decay, the hole is also filled by an electron from a higher state, but in this case, the energy difference is not radiated in form of a photon, but transferred to another, third electron, which is consequently emitted from the atom. Figure 2.6 shows both processes schematically. An Auger-process can be annotated more specifically by noting the atomic shells of the electrons involved. For example, the process illustrated in Figure 2.6 is a KLM decay, as the photo-electron originates from the K-shell, the hole is filled from the L-shell and the Auger-electron is emitted from the M-shell.

An important consideration for X-ray spectroscopy is the probability of a specific core hole to decay by the respective processes. These relative radiation yields have been tabulated for most core-excitations [135]. Generally, the total Auger-yield reduces with atomic number and photon energy in favor of the fluorescence yield. Figure 2.7 reproduces the absolute radiative versus non-radiative yields by atomic number, as reported in [135].

2.4.2 Valence Electron Distribution

The occupation probability of electronic states in the valence system in thermal equilibrium is given by the Fermi-Dirac distribution [140].

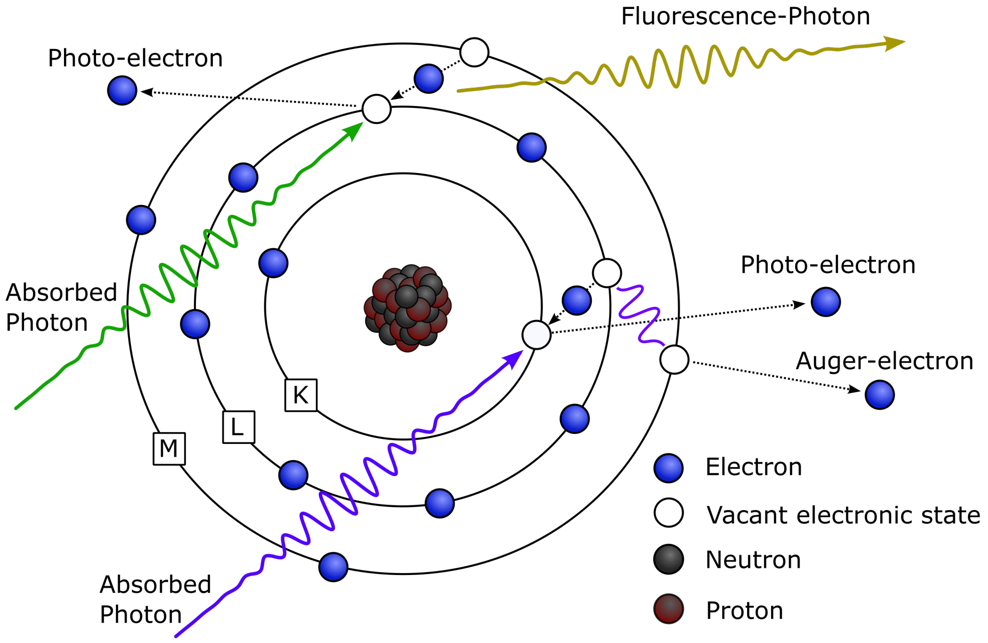

FIGURE 2.6: **Fluorescence- and Auger-Meitner-Processes.** In the upper half, a photon shown in green is absorbed in the L-shell. As a consequence, a photo-electron is emitted and the core hole decays radiatively by emitting an X-ray fluorescence photon of lower energy (shown in yellow). In the lower half, another photon (shown in purple) is absorbed by a K-shell electron, thus ejecting it as a photo-electron. This core hole decays in a KLM Auger-Meitner process: The core hole in the K-shell is replaced by an electron from the L-shell, which ejects an electron from the M-shell with the remaining energy as an Auger-electron.

$$n_E(T) = \frac{1}{e^{(E-\mu)/k_B T} + 1} \tag{2.36}$$

n_E: Occupation probability of a state with energy E
E: Electron energy
T: Temperature of the electronic system
k_B: Boltzmann constant
μ: Chemical potential

If an excitation, e.g. due to the absorption of a photon, disturbs this equilibrium by elevating one or more electrons into higher-energy states, an energy exchange between the valence electrons eventually reconstitutes a thermal equilibrium distribution[13]. This energy exchange is mediated by a multitude of collisions between valence electrons. As a complex many-body problem, the details of the re-equilibration depend strongly on the band-structure of the material [141] as well as the particular non-thermal electron energy distribution. Various approaches have been used to determine the mean free path or the lifetime between individual electron collisions [142], depending on the energy of the electrons in question relative to the chemical potential: The first developed model by

---

[13] The temperature and chemical potential will change according to the internal energy deposited and the heat capacity of the electronic system, which follows from the density of electronic states and number of electrons involved.

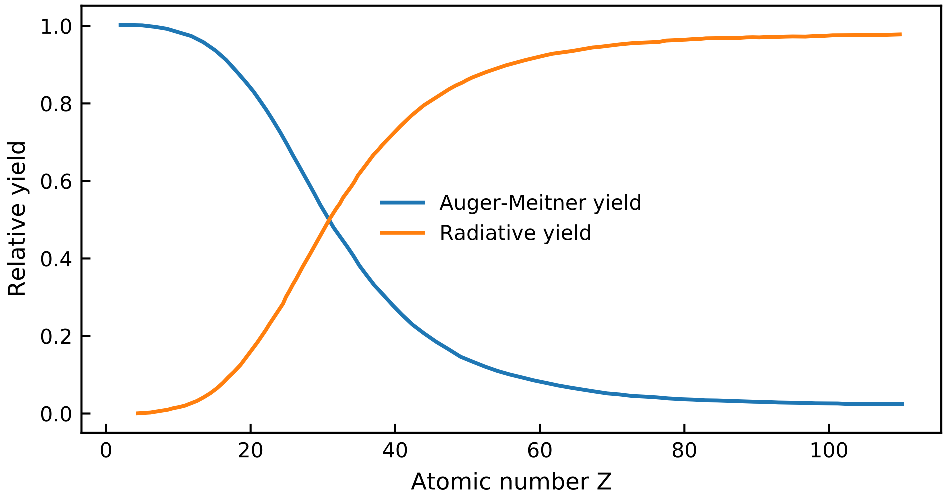

FIGURE 2.7: **Core-hole decay yields** as a fraction of K-shell excitations that decay radiatively via fluorescence and by electron-emission via the Auger-Meitner process; data from Krause [135].

Bethe (1930) can be used for fast electrons beyond 200 eV [143]. For electron energies above 50 eV, an "optical model" was developed based on the free-electron gas model [144–146]. For even lower energies, it is necessary to refer to experimental measurements or first-principles calculations (see [141, 142, 147] and the references therein).

2.4.2.1 Two-Temperature Model

When considering fast processes such as the reaction to femtosecond (X-ray) laser pulses, it becomes relevant to consider the time scale at which a solid returns to a thermal equilibrium. We find that electron-electron collisions re-establish a thermalization of the electronic system before the nuclear lattice absorbs a significant fraction of the excitation energy. This was already observed by Anisimov et al. in the 1970s, who proposed the so called *two-temperature model* [148] of two coupled temperatures T_e and T_l for the electrons and lattice respectively, which are coupled by an electron-phonon coupling parameter G. One can then describe the propagation of excitation energy into the system in form of the simple differential equations:

$$C_e(T_e)\frac{\partial T_e}{\partial t} = \frac{\partial}{\partial x}\left(\kappa \frac{\partial T_e}{\partial x}\right) - G(T_e - T_l) + H \tag{2.37}$$

$$C_l(T_l)\frac{\partial T_l}{\partial t} = G(T_e - T_l) \tag{2.38}$$

$C_e(T_e)$, $C_l(T_l)$:	Electronic and lattice heat capacity
T_e, T_l:	Electron and lattice temperature
$G(T_e - T_l)$:	Electron-phonon coupling
κ:	Thermal conductivity
H:	Source term (due to photon absorption)

While the model was not directly applied for the research presented in this thesis, it has proven extraordinarily useful for the interpretation of experiments involving ultrafast excitations [149, 150]. The general observation that the lattice temperature follows the electronic temperature usually on a timescale of 100 fs and slower motivated us to only model the electronic system in the rate model for non-linear X-ray transmission presented in [5] in chapter 4. The two-temperature model is particularly relevant in the planning and evaluation of pump-probe experiments, which are discussed in chapter 3.3.3.

2.5 Core Hole Spectroscopy

As alluded to in the introduction, X-rays have several properties that make them extremely desirable for material science. For the purposes of this thesis, however, the ability to address electronic core states is most relevant. Below, I will give a brief overview of some common techniques with varying detail based on their relevance to this thesis.

As shown in Figure 2.8, the electronic core levels of different chemical elements are generally well spaced out in binding energy. This allows to separately analyze the role of specific elements in the determination of electronic properties, even in chemically complex samples.

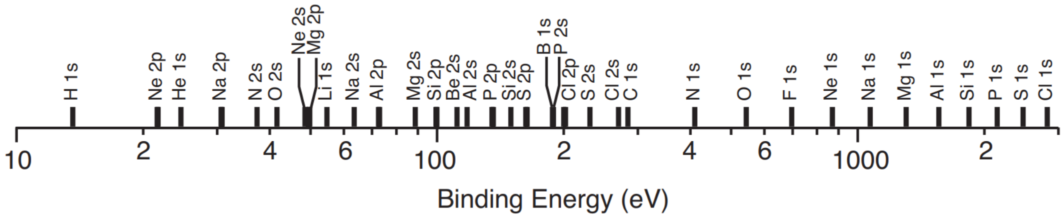

FIGURE 2.8: **Core level binding energies** of the first 17 elements of the periodic table are distributed over the soft X-ray regime; disregarding the spin-orbit splitting of *p*-levels. Note the logarithmic energy scale. Figure from [151], reproduced with permission.

Furthermore, the orbitals of core electrons are generally localized around the nucleus. Therefore, even if a technique based on core hole excitations probes properties of the valence system, it does so from the local perspective of the core orbital.[14]

These properties make core hole excitations highly informative for spectroscopic techniques.

Figure 2.9 shows an overview of the X-ray core level spectroscopy methods that feature in this thesis and are explained in more detail below. I notably omit the description of photo-electron-based techniques for brevity, but the interested reader may be referred to [152].

---

[14] With *perspective*, I refer to the symmetry-dependent projection of the core orbital through the dipole operator onto the valence orbital.

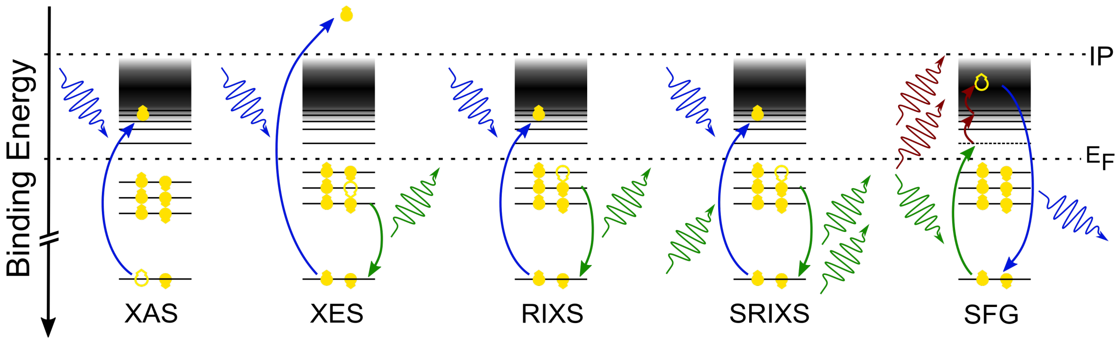

FIGURE 2.9: **Core level spectroscopy methods** in the independent electron picture. Each involves the absorption of at least one incident photon, pictured coming from the left, over the Fermi energy E_F or even exceeding the ionization potential IP. In X-ray Emission Spectroscopy (XES) and RIXS, a spontaneously emitted, lower-energy core-resonant photon is emitted and analyzed. In Stimulated Resonant Inelastic X-ray Scattering (SRIXS), a second incident photon is duplicated by stimulating a valence-core transition into the core hole left by the initial absorption. In a SFG-experiment, two (or more) incident photons mix coherently, driving the initial absorption process together. This process can be enhanced by intermediate states which are resonant to either photon. The excitation energy is then emitted in form of an outgoing photon, thus completing the parametric wave-mixing process. Energy axis not to scale.

Before addressing the individual techniques, I want to address the role of electronic screening responses, which causes a large part of the difference in results when comparing different core hole spectroscopies.

2.5.1 Screening Response and the Final State Rule

It is easy to describe electronic excitations in the independent electron picture (or one-electron picture) which describes individual electrons transitioning between otherwise rigid energy levels; but this picture is generally wrong. Instead, electronic excitations are in principle multi-electron processes, as one may notice in the dependence of the transition probability in Eq. 2.28 on the sum of all electronic momenta $\boldsymbol{p}$. In the final configuration, all other electronic states adapt to the new electronic configuration. Thankfully, it has been shown that at least for simple metals (and less generally for other systems), good predictions of X-ray spectra can be calculated based on the transition probability of only a single electron, provided that the transition matrix element is calculated considering wave functions obtained in the potential of the final state of the transition [153].

This final-state wave function is affected by the reaction of the electronic system to the excitation, which attempts to minimize its total energy in the new state. This is called the screening response and makes a decisive difference when comparing the information derived from X-ray spectroscopy methods that produce a different final state. One may, for example, derive differing values for band gaps or binding energies, depending on the X-ray spectroscopy used, as discussed for example in [154–156]. Figure 2.10 illustrates this difference by showing the same processes displayed in Figure 2.9, but in terms of the total energy instead of in terms of independent electrons. On the left, I show a non-resonant excitation into the continuum, which leaves behind a core-ionized atom. Through the XES-process, another electron, here we assume it to come from the occupied

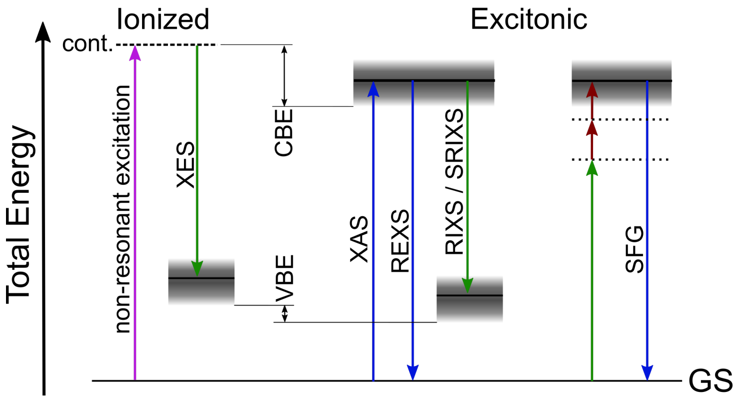

Figure 2.10: **Comparison of X-ray methods in the total energy picture**, highlighting the difference in the final state and screening response, between techniques that excite into the continuum, i.e. ionize the atom, and those that excite into localized states. The comparison reveals the core-exciton and valence-exciton binding energies in the different onset of the conduction band (labeled CBE and VBE, respectively). The unoccupied valence density of states is indicated with a shaded area, while resonant states are indicated by dashed horizontal lines. The left part is based on Figure 4 of [154]. The ground state is labeled GS. See the main text for elaboration. Energy axis not to scale.

valence states, fills the core hole and leaves the atom in a valence-ionized final state. In the middle, an electron is excited via the X-ray Absorption Spectroscopy (XAS)-process into an empty valence state, leaving the atom with a localized, i.e. excitonic core excitation. The energy difference to the ionized states is labeled the Core-exciton Binding Energy (CBE). From there, it can either decay resonantly back to the ground state (Resonant Elastic X-ray Scattering (REXS)), or the system can fill the core hole by emitting another photon of lower photon energy (either spontaneously through RIXS or due to stimulated emission through SRIXS), leaving a localized valence excitation. This excitation has a lower total energy compared to the valence-ionized state; the difference is the Valence-exciton Binding Energy (VBE) [154]. Since no electron is strongly delocalized during this process, one may call it charge-neutral. On the right, I show a SFG process involving two low-energy photons. The overall efficiency (susceptibility) of the process is enhanced if it can exploit resonances with intermediate states, as indicated by the dotted lines. While the excited state can correspond to that probed by XAS, the overall process is parametric, i.e. leaves no excitation energy in the system.

2.5.2 X-ray Absorption Spectroscopy

The initial step in all X-ray-based core hole spectroscopies is the absorption of an X-ray photon, creating a core hole excitation. In XAS, one measures the fraction of photons that are absorbed by a sample while varying the photon energy.

The energetic structure of the absorption at and shortly above a core hole resonance effectively probes the locally projected unoccupied density of states just above the Fermi level. Thus, it can provide element-specific spectroscopic information about the density of states, local atomic structure, molecular orientation as well as the nature and orientation of chemical bonds in the sample. In this regime, the method is referred to as X-ray Absorption Near-Edge Spectroscopy (XANES) or Near-Edge X-ray Absorption Fine Structure (NEXAFS). The term XANES is mostly synonymous with NEXAFS, whereas the former is more commonly used in the study of solid samples, while the latter is used in the context of molecules [139]. Since this work is primarily focused on the study of solids, I prefer the term XANES here.

At higher photon energies beyond the resonance, the X-rays excite electrons into continuum states which typically overlap less with the core states, so that the absorption gradually decreases until the next core level binding energy is reached. However, the wave functions of electrons emitted into the continuum can scatter from neighboring atoms and thus interfere with the final state of the absorption process, which modulates the signal measured for the absorption cross-section, in particular just above the XANES-region. Such measurements are referred to as Extended X-ray Absorption Fine Structure (EXAFS) and are used to derive the distances of other atoms around the resonant scattering center. Since EXAFS is not featured in this work, the interested reader may be referred to the pertinent literature, e.g. [157].

Excitations above the resonance and into the continuum at the high-energy end of XANES spectra experience additional broadening, as electrons excited to these states tend to decay back to the Fermi level as well as to the free core state. This reduced lifetime leads to the so-called final state broadening effect and should be considered when interpreting or simulating absorption spectra [139].

Circular and Linear Dichroism

As established in section 2.3.2, X-ray absorption occurs in first-order via dipole transitions. This implies on the one hand that dipole selection rules apply, and on the other hand that the absorption is dependent on the angle between the molecular orbitals involved and the polarization of the incident light.

In X-ray Magnetic Circular Dichroism (XMCD), this is used to study magnetic materials: Magnetism occurs from an imbalance in the spin-up and spin-down valence electron populations. This imbalance can be directly derived from XANES-spectra by comparing the transition intensity measured from left- and right-handed circular polarized X-rays using sum rules. See [158, 159] for details.

X-ray Magnetic Linear Dichroism (XMLD) exploits the angular dependence of dipole transitions to probe the anisotropy of unoccupied valence states around the resonant atoms via the so-called searchlight effect.[15] Such anisotropy may be caused by different chemical bonds in different directions. Unfortunately, this effect cancels out due to geometric arguments in the absence of spin order in materials with cubic (or higher) symmetry. However, charge order caused by an aligned spin system can break this symmetry sufficiently to induce a difference in the absorption cross-section (in general due to spin-orbit interaction, but in particular in the presence of multiplet splitting) depending on the angle of the absorbed light's linear polarisation with respect to the crystal axes. This way, XMLD can be used to determine the axis and strength of the

---

[15] The term is inspired by the shape of the angular dependence of dipole transitions, which in this case "searches" for overlap with valence orbitals.

spin-ordering in ferro- and antiferromagnets. See [139, 159] for details. We performed such an analysis in [3] on the nickel L_2-edge.

2.5.3 X-ray Emission Spectroscopy

Instead of observing the absorption process itself, in XES one analyzes the X-ray fluorescence after ionizing the targeted atom using non-resonant X-rays[16].

XES experiments are often performed with hard X-rays with the incident energy well above a given absorption edge while tuning a spectrometer such that certain X-ray fluorescence lines can be analyzed in detail. In the XES process, an electron from any less tightly bound occupied electronic state performs a radiative transition to fill the core hole. The electron can come from another core level, in which case one can identify the fluorescence line [132] and even preserve an indirect sensitivity to the valence electronic system. Alternatively, one may study the decay from occupied valence states, which are directly dependent on the chemical surrounding [156, 160, 161]. The mathematical description is analogous to the one described below for RIXS.

2.5.4 Resonant Inelastic X-ray Scattering

Observing the X-ray emission from core hole decays becomes particularly interesting when the core hole excitation itself is near-resonant and thus leaves the system in a localized (excitonic) core-excited state. In the RIXS process, the core hole is then filled by a valence electron, leaving behind a valence excitation.[17] In the optical regime, one would refer to this process as resonant Raman scattering.[18] By analyzing the emitted photon's properties, such as intensity, photon energy, emission angle, and polarization, and comparing them to those of the incident photon and the orientation of the sample, the nature of the excitation left behind in the sample can be determined. The scattering process is still described by second-order perturbation theory approach introduced by Kramers, Heisenberg, and Dirac [162, 163]. For the discussion in this thesis, I show the form of the inelastic scattering cross-section as presented in [6], using the dipole and rotating wave approximations:

$$
\begin{aligned}
\frac{d\sigma_{RIXS}}{d\Omega(\hbar\omega_2)} =& \frac{4\pi\hbar\omega_1\hbar\omega_2\alpha_f^2}{\lambda_2^2}\mathcal{R}^4(n_{\boldsymbol{p}\boldsymbol{k}_2}+1) \\
&\times \sum_f^{\omega_2\leq\omega_1} \left| \sum_\iota \frac{\langle f|\,\boldsymbol{r}\cdot\boldsymbol{e}_2\,|\iota\rangle\,\langle\iota|\,\boldsymbol{r}\cdot\boldsymbol{e}_1\,|g\rangle}{\hbar\omega_1-(E_\iota-E_g)+i\Gamma_\iota/2} \right|^2 \\
&\times \mathcal{L}(\hbar\omega_1-\hbar\omega_2-(E_f-E_g))
\end{aligned}
\tag{2.39}
$$

---

[16] As illustrated in section 2.4.1, a core hole relaxes either by radiating a photon or by emitting Auger electrons. One may instead analyze the electrons produced by Auger-decay of the core hole, but Auger electron spectroscopy is outside the scope of this thesis; see [81] for details.

[17] If it instead returns to the ground state, one would speak of Resonant Elastic X-ray Scattering.

[18] Older literature, e.g. [79], often used the term Resonant X-ray Raman Scattering, but the term RIXS seems to have caught on for the X-ray regime in recent years.

The energy density of the involved states is described by Lorentzian distributions, specifically:

$$\mathcal{L}(\hbar\omega_1 - \hbar\omega_2 - (E_f - E_g)) = \frac{2}{\pi\Gamma_f} \frac{\Gamma_f^2/4}{(\hbar\omega_1 - \hbar\omega_2 - (E_f - E_g))^2 + \Gamma_f^2/4} \tag{2.40}$$

$\mathcal{L}$: Final state energy density expressed as Lorentzian (corresponding to $\rho_f(E)$ in 2.29)
$|g\rangle$: Ground state
$|\iota\rangle$: Intermediate state
$|f\rangle$: Final state
E_g, E_ι, E_f: Energies of ground, intermediate and final state
Γ_ι,Γ_f: Lifetimes of intermediate and final state
ω_1,ω_2: Angular frequencies of incident and emitted waves
λ_1,λ_2: Wavelengths of incident and emitted waves
$\boldsymbol{e}_1$,$\boldsymbol{e}_2$: Polarization unit vectors of incident and emitted waves
$\boldsymbol{r}$ Sum of electron location vectors
α_f: Fine structure constant
$\mathcal{R}$: Radial matrix dipole element
$d\Omega$: Solid angle differential
$n_{p\boldsymbol{k}_2}$: Density of coherent photons in the mode volume of the emitted wave

Note that in the most commonly described case, the emitted photon carries less energy than the incident photon, so that the measured intensity of inelastic scattering informs the experimentalist about the capability of the material to accept an additional excitation with the corresponding energy difference. Thus, like XAS, RIXS can probe unoccupied electronic states. However, if the material already carries valence-excitations - be it due to a high temperature or other sources of excitation - it is also possible that the emitted photon carries a higher energy than the incident photon as it gains the energy of the corresponding excitation. This is referred to as the "anti-Stokes" process, as opposed to the "Stokes"-type energy-loss process. Thus, anti-Stokes RIXS probes excitations that are already present in the material.

As opposed to XAS, the final state in RIXS contains only a valence excitation and is thus not altered by a screening response to a core excitation (compare Figure 2.10). Furthermore, the achievable energy resolution is not determined by the core-excited state lifetime, but by the final state lifetime, which is typically longer for valence excitations and thus allows for greater energy resolution. Since the excitation is produced indirectly through two dipole transitions, RIXS is furthermore not limited to probe excitations that can be reached directly through a dipole transition from the ground state. This makes RIXS sensitive to phonons, plasmons, and magnons, as well as inter-valence and charge-transfer excitations. It can provide information about the energy, momentum, and polarization of the relevant excitation while being specific to the chemical element and even the targeted orbital, all while being bulk sensitive (in comparison to methods based on electron detection) and requiring only small sample volumes [164].

Despite these plentiful advantages, and although the process is in principle understood since the 1920s, RIXS has only risen in popularity as a spectroscopic technique in the last few decades. This is because RIXS is a very photon-hungry technique - that is, it requires a substantial incident photon flux to detect a statistically relevant number of inelastically scattered photons in reasonable time and achieve a good resolution in energy, ideally at several scattering angles in order to map out the momentum dependence of the observed excitations. Only the development of 2nd and 3rd generation synchrotrons with many orders of magnitude in brilliance increase (see chapter 2.1) has made RIXS studies feasible in practice. The photon-hunger of RIXS has two major reasons: First, especially in the soft X-ray regime, a large fraction of core holes decays via Auger-Meitner decay, thus limiting the overall cross-section of the RIXS process. Second, the inelastic scattering signal is emitted mostly isotropically, and covering a large solid angle to collect a high fraction of this radiation is technically challenging. A typical RIXS spectrometer might only cover a fraction of 10^{-4} of the total solid angle [9]. Thus, even with modern X-ray sources and equipment, integration times in the range of hours are still common for single RIXS spectra. This motivates the perspective to amplify RIXS signal level via stimulated emission, which is discussed in the next section. For a more in-depth discussion of RIXS, see [79, 81, 164].

Stimulated Resonant Inelastic X-ray Scattering

The ordinary RIXS experiment detects photons from spontaneous core hole decay. However, the transition from the intermediate to the final state can alternatively be stimulated by a suitable photon. This is expressed in equation 2.39 by the $(n_{p\boldsymbol{k}_2} + 1)$ term. Here, the +1 represents the rate of spontaneous radiative decay, which can be described as stimulated emission triggered by a photon from vacuum fluctuations. As mentioned earlier, this contribution is usually isotropic. However, in the presence of a real coherent photon density $n_{p\boldsymbol{k}_2}$, the differential cross-section in the corresponding direction can be dramatically enhanced. This is not only useful because stimulated emission can outcompete the otherwise dominant Auger-Meitner-process [165] so as to utilize a greater fraction of core-excitations, but also because the created emission is focused into a particular direction, which mitigates the problem of limited spectrometer acceptance angles [9].[19] This prospect inspired significant theoretical and experimental efforts to study RIXS-related processes exploiting stimulated emission [81–84, 98, 168–171].

2.5.5 X-ray-Optical Wave-Mixing

While stimulated X-ray emission works with two core-resonant photons, the direct mixing with low-energy photons is similarly attractive. Sum-Frequency Generation (SFG) and Difference-Frequency Generation (DFG) involving X-rays has been envisioned for X-rays as early as the 1970s [172–174]. The same advantages of wave-mixing that apply in the optical regime (see section 2.3.5) hold in the X-ray regime. Notable are the ability to probe states that are inaccessible in linear spectroscopy due to dipole selection rules and the possibility to use second-order processes that are limited to sites with broken inversion symmetry. Further, the capability to correlate how excitations couple to each other by scanning the process efficiency as a function of all involved wavelengths becomes particularly attractive to probe the localization of valence excitations (which respond to optical frequencies) around the sites of particular nuclei (which can be targeted by X-rays resonant to their respective core levels). Unlike SRIXS it is also possible to design

---

[19] Over an extended core-excited volume, such stimulated emission may even amplify itself (amplified spontaneous emission), which has not only been proposed for spectroscopic application [82], but also allowed for the creation of core-level lasing [166, 167].

SFG and DFG experiments such that the signal can be separated in photon energy and in emission angle, thus allowing a background-free detection.

A special type of DFG, the down-conversion of X-rays into one optical and one lower-energy X-ray photon [172, 173, 175] was demonstrated recently for the first time [176] as a method of probing valence charge distributions. Inversely, SFG between one optical photon and one hard X-ray photon has first been demonstrated in a solid by Glover et al. [87] in diamond, while the first SFG and DFG between two IR and one XUV photon is demonstrated later on in this thesis [7] in LiF. Gaynor et al. also demonstrated mixing between one XUV and two IR photons, albeit in a configuration where the two IR photon energies negated each other, so that no sum- or difference-frequency was generated, but the momentum conservation allowed a spatially separated background-free detection [110]. Even these tentative proof-of-principle experiments revealed information on valence charge distribution [87, 175, 176], excited state coherence times [110] and the localization of excited states which cannot be addressed with linear spectroscopy [7].

2.5.6 X-ray Coherent Raman Scattering

As an example of an advanced X-ray wave-mixing scheme that promises deep insights but has not yet been demonstrated experimentally, I present the FWM-scheme X-ray Coherent Raman Scattering (XCRS), proposed originally by S. Tanaka and S. Mukamel in 2002 [94] and illustrated in Figure 2.11. As discussed above, one attraction of X-ray-optical wave-mixing schemes is the ability to probe the localization of valence excitations. However, the individual transitions involved in X-ray-optical wave-mixing are still limited by dipole selection rules. Even more importantly, in an SFG-scheme as we present it in [7], the valence transition is probed in the presence of the core-exciton, which severely limits the use case of the derived information.

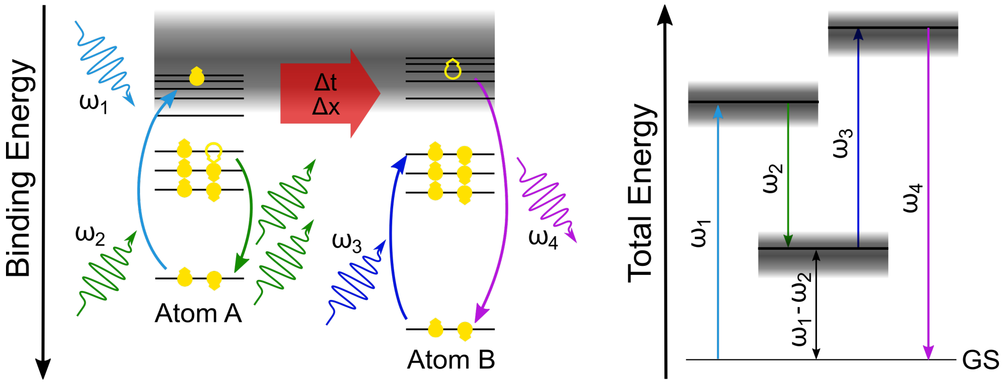

FIGURE 2.11: **The X-ray coherent Raman scattering** process proposed by Tanaka and Mukamel in 2002 [94] in both the independent electron picture (left) and the total energy picture (right). A core excitation of atom A is initiated by a first pulse of frequency ω_1 and converted into a specific localized valence excitation as the core hole is filled through a SRIXS-like process, stimulated by a wave of frequency ω_2. This excitation then evolves for a duration Δt and possibly delocalizes over a distance Δx, thus reaching atom B. The evolved valence excitation is then probed by a third irradiated pulse of frequency ω_3, which is resonant to a core level of atom B, coupling that core level to the valence excitation, which can thus contribute to the emission of the fourth wave with frequency $\omega_4 = \omega_1 - \omega_2 + \omega_3$. Energy axes not to scale.

In contrast, XCRS utilizes a SRIXS-like process to create a very specific valence excitation of interest in form of an induced polarization. Because this excitation is created by the coherent mixing of two core-resonant X-rays, one can control all its relevant parameters: its localization around the resonant element (atom A), its excitation energy $(\omega_1 - \omega_2)$, its momentum $(k_1 - k_2)$ and even its phase are determined. This excitation is then left to propagate for a variable duration before it is probed using a third incident X-ray pulse of frequency ω_3 that is resonant to a core level of atom B. Depending on how much of the excitation's coherence (the expected value of the dipole moment) reached the second atom, this can induce the coherent emission of a signal wave with frequency $\omega_4 = (\omega_1 - \omega_2) + \omega_3$. Overall, the susceptibility $|\chi_3|$ (compare eq. 2.34) measured with this process precisely characterizes the energy transfer between atoms A and B. Tanaka and Mukamel even recommend utilizing heterodyne detection in order to derive the full complex value of χ_3. Consequently, widespread availability of such a method could be revolutionary to our understanding of, e.g. the transfer of excitations from color-centers to ligands of complex bio-molecules. Nevertheless, XCRS is only one of the promising FWM-processes that have been proposed for the X-ray regime, differing in the interaction sequence and phase matching conditions of the input beams [95–97, 100–104, 108–110, 177, 178].

Chapter 3

Methods for X-ray Absorption Spectroscopy

With the conceptual aspects of X-ray absorption spectroscopy introduced above, this chapter discusses experimental schemes. I open in section 3.1 with a brief overview of how the X-ray absorption cross-section may be measured in general to contextualize why we chose transmission and reflection measurements for the studies presented in this thesis. Sequentially in section 3.2 I illustrate the need for a normalization scheme for XAS measurements with SASE-XFELs and provide a brief overview of the three variations of the split-beam normalization scheme that are relevant in this thesis in section 3.3. In sections 3.3.1 and 3.3.2, two of these schemes are treated in detail within respective technical publications contained in this chapter. Finally, section 3.3.3 discusses the application of a split-beam normalization scheme in a pump-probe experiment.

3.1 Different Methods to Measure X-ray Absorption

Experimentally, the absorption of X-rays can be measured in various ways. Each method measures an observable that is dependent on the X-ray absorption cross-section. The common observables through which X-ray absorption is measured are:

- **Electron yield:** Measures electrons emitted from the sample.
- **Drain current:** Measures electrons flowing back into the sample.
- **Fluorescence yield**: Measures the fluorescence from radiative core-hole decays.
- **Transmission:** Measures the photons transmitted through the sample.
- **Reflection:** Measures the photons reflected from the sample.

Each of these methods has unique advantages and limitations. To select a suitable method, one should consider the effective depth of the sample that is probed, the achievable signal-to-noise and signal-to-background ratios, and how reliably one may reconstruct the dependence of the selected observable on the absorption probability at the atoms of interest.

A prime consideration concerns the penetration depth of X-rays versus that of free electrons: While electrons typically penetrate solids only to a few layers of atoms or single nanometers [142], soft X-rays penetrate on the order of a hundred nanometers [132]. This makes photon-based detection more sensitive to the bulk of a sample than electron yield or drain current measurements. As discussed above, all electrons with binding energies lower than the photon energy contribute to non-resonant absorption, which constitutes a background signal for most absorption measurements. If the interesting sample sites are only present in a part of the probed volume, the background is proportionally higher. In such cases, one may consider a background-free method such as Partial Electron Yield (PEY) or Partial Fluorescence Yield (PFY). Measurements in transmission constitute the most direct measure of the absorption coefficient, which can be directly derived from the measured absorbance (see chapter 2) without additional considerations of limited bulk-sensitivity, the reflection process, self-absorption effects [74], or electron/fluorescence yields. Its main limitation is the requirement for thin films since in the soft X-ray regime, relevant attenuation lengths are typically in the range of tens to hundreds of nanometers. To achieve a good Signal-to-Noise Ratio (SNR), the sample thickness should be similar to the attenuation length of the sample. Such thin samples are not always feasible to manufacture in the first place, especially in monocrystalline form and/or in specific (crystal) orientations; unsupported films are also more susceptible to beam damage than solid samples.

Measuring the X-ray reflectivity alleviates this problem and also provides an additional degree of freedom to the experiment, as the reflection angle can be chosen to vary the reflected intensity or even the penetration depth into the sample. However, reflectivity measurements are very sensitive to surface morphology. In addition to that, the reflectivity is strongly polarization dependent and changes with both the imaginary and real part of the refractive index, as dictated by the Fresnel equations [179]. As we demonstrate in [2], at certain angles the reflection spectra can greatly resemble the X-ray absorption spectrum (measured at a synchrotron as drain current). Even so, quantitatively treating reflectivity spectra as equivalent to absorption spectra produces incorrect results, as a recent publication on this topic stresses [180]. Correctly treated, however, transmission and reflection measurements deliver in principle the same information content since the real and imaginary parts of the refractive index are rigorously linked by the Kramers-Kronig transformation (see section 2.2.2). In [3], this transformation was performed in order to relate the XMLD effect visible in the measured reflection spectra to previously published XANES spectra. The necessity of this mathematical detour can be perceived as a disadvantage from the perspective of an experimentalist who is interested in a straightforward measurement of the XANES spectrum. But, although it is beyond the scope of this thesis, it is worth acknowledging that measurements at grazing angles of the reflectivity and the fluorescence or electron yield can deliver rich additional information, especially a greatly increased sensitivity to the sample surface and the capability to analyze the depth-profile of layered materials [181–183].

Monitoring the total electron or photon yield from core-hole decay processes can be realized by positioning a photodiode (detecting electrons and/or photons) near the absorbing sample or measuring the current flowing into the sample to counterbalance electron loss from Auger-decays and the photo-electric effect (drain current measurement, which is similar to electron yield). These methods generally deliver good count rates with limited experimental complexity. However, the measured signal can be affected by reabsorption-effects [74], which are in turn a function of the angle- and photon-energy dependent penetration depths of the incident and emitted X-rays, both from the targeted chemical element and from other constituents of the sample (e.g. the solvent). Thus, the real absorption cross-section of the targeted element is not always straightforward to disentangle from the measured spectra, especially when dealing with dilute samples [184, 185].

To remedy this issue, a spectrometer may be used to limit the accepted energy range of detected electrons or photons, which can greatly reduce or eliminate the background from other emission lines at the cost of reduced overall signal intensity. Such measurements are referred to as Partial Electron Yield (PEY) or Partial Fluorescence Yield (PFY) in contrast to Total Electron Yield (TEY) and Total Fluorescence Yield (TFY), respectively. Ideally, the spectrometer constrains the observation to a specific decay channel, i.e. Auger or fluorescence line originating only from resonant absorption at the core electrons of interest[1]. However, soft X-ray spectrometers utilize mechanically ruled gratings at grazing incidences, which limits the technically achievable covered solid angle to values around 10^{-4} of the full solid angle or less [82]. In contrast, small photo-diodes can be placed close to the sample and thus cover much greater solid angles. Electron spectrometers can be used with a positive voltage relative to the sample to greatly increase the collection efficiency. However, the resulting electric fields are not always acceptable, as they may interfere with the behavior of some samples.

Electron yield and drain current measurements further require an electrically conductive sample, substrate, and sample holder to prevent the buildup of charge in the sample. This becomes even more challenging in the context of pulsed sources such as XFELs, where drain current measurements have to account for the electrical capacitance of the sample environment, while electron-yield-based methods suffer from so-called space charge effects [61, 62], where Coulomb interaction changes the energy distribution of electrons both on the sample surface and on the way between sample and detector. This effect is highly dependent on both the fluence and the temporal characteristics of the pulse and thus complicates any photoemission-based measurements at intense pulsed X-ray sources. This is the main reason why XAS at XFELs is mostly measured via fluorescence yield, in transmission, or in reflection. In the publications presented in this thesis, either of the latter two options was chosen as the higher signal levels and more straightforward interpretation were preferred over the possibility of background rejection in PFY.

---

[1] In the case of observing a specific Auger decay channel, [139] speaks of Auger Electron Yield (AEY) in contrast to PEY, where only low energy electrons are rejected.

3.2 The Necessity for Normalization

As discussed previously, a key value of X-ray absorption spectroscopy is its capability to specifically address certain chemical elements within the sample. The targeted element may be present in the sample in relatively small quantities, which reduces the achievable signal level. Further, most studies covering material dynamics require recording many spectra in quick succession in order to map out dependencies on various experimental parameters which may only manifest in minor spectral changes. All this means that despite the high brilliance of FEL-sources, an economical use of the available photons in order to minimize the statistical measurement uncertainty is imperative. This challenge is aggravated by the stochastic nature of SASE pulses that causes strong spectral intensity fluctuations (see chapter 2.1.2). As we show in [2] (see section 3.3.1.1), relying on the long-term average stability of the incident SASE-radiation leads to a greater uncertainty in the measured reflectivity or transmittance by about one order of magnitude. These circumstances make it highly advantageous to measure the incident intensity with the same priority as the transmitted intensity.

Gas Monitor Detectors (GMDs) can measure the energy of XFEL pulses and are implemented in most XFEL beamlines [186, 187]. However, these cannot resolve the SASE spectrum, so that a second GMD downstream of a monochromator is required for useful normalization in high-resolution spectroscopy. For the measurements presented in this thesis, the relevant photon energies range from around 400 eV (N K-edge) to around 875 eV (Ni L_2-edge). At FLASH, these photon energies can only be reached by the 3rd harmonic radiation of the XFEL, which is about two orders of magnitude weaker than the fundamental. This precludes the use of a GMD, even if one were installed downstream of the monochromator of the Plane Grating Monochromator (PG) beamline, as GMDs cannot disentangle the intensity of the 3rd harmonic radiation from the fundamental. It also exacerbates the requirement to make the best use of the available photons to achieve sensitive measurements.

3.3 Split-Beam Normalization for SASE-Based X-ray Absorption

This leads to the concept of split-beam normalization. All experiments discussed in this thesis except [7] fundamentally measure spectral X-ray absorption at an XFEL and make use of a split-beam normalization scheme to compensate for the fluctuating spectral intensity of SASE XFELs. The defining characteristic is splitting the XFEL beam into two parts: one *signal* beam which probes the sample, and one *reference* beam which is measured to characterize the incident spectral intensity. This approach offers the key advantage that both beams can be measured on the same area detector, usually a Charge Coupled Device (CCD). This also precludes any possible differences in the measurement of the incident and transmitted intensities due to using separate detectors.

A conventional approach to achieve a signal and reference beam is the use of Split-and-Delay-Units (SDUs), which are implemented in many XFEL beamlines around the world [188–194]. These typically split the beam into two parts by reflecting one half off a mirror's trailing edge and steering both beams back onto a similar path with several additional mirrors. While this enables the introduction of a delay or path-length difference, this aspect is unimportant when they are used for normalization. The measurements presented in [6] (see chapter 5.1) made effective use of such an SDU [188] for beam-splitting. However, the beam-splitting ratio achieved in this way is sensitive to the beam pointing and exact shape of the pulse wavefront, which in turn exhibits a pulse-to-pulse jitter. This constitutes an additional, potentially systematic source of measurement error which depends on the XFEL stability and is difficult to quantify.

An alternative solution is to split the beam wavefront into near-identical copies using a diffraction grating. As a periodic structure, the intensity ratio between the diffraction orders of a grating is not sensitive to beam pointing or wavefront instabilities, but in principle only to the grating design and the wavelength used. In fact, such a diffractive structure can be freely designed to achieve more complex modifications of the wavefront. Such specially designed diffraction structures are generally referred to as zone plates.[2] In one of the experiments presented here [4], we used a particular type of transmission zone plate design that achieves beam-splitting and focusing in a single optical element, resulting in two or three foci with a fixed intensity ratio [196]. In [4], we used the additional focusing of the transmission zone plate to achieve very small foci on the order of one μm^2, in order to enter the fluence-regime of many mJ/cm^2 required for non-linear absorption. Furthermore, the increased beam divergence introduced by the zone plate focusing spreads the signal of each beam over a larger area, i.e. a greater number of pixels on the area detector. The greater number of pixels increases the overall number of photons that can be measured in each beam without saturating the detector and therefore improves the achievable SNR [197]. Our experiment on non-linear absorption [4] was performed at the Spectroscopy and Coherent Scattering (SCS) beamline of the European X-ray Free Electron Laser (EXFEL) and constitutes the first implementation of this setup at this particular beamline (it was in fact the first user experiment of SCS), and it has since been improved to become a routine setup. Later on (but not discussed in this thesis), I took part in further successful measurements with this setup, investigating

---

[2] The Fresnel zone plate structure acts similar to a lens and is particularly well known. See, for example, [195].

the spin dynamics of nickel [11], and we published a characterization of this setup in its matured state in [8].

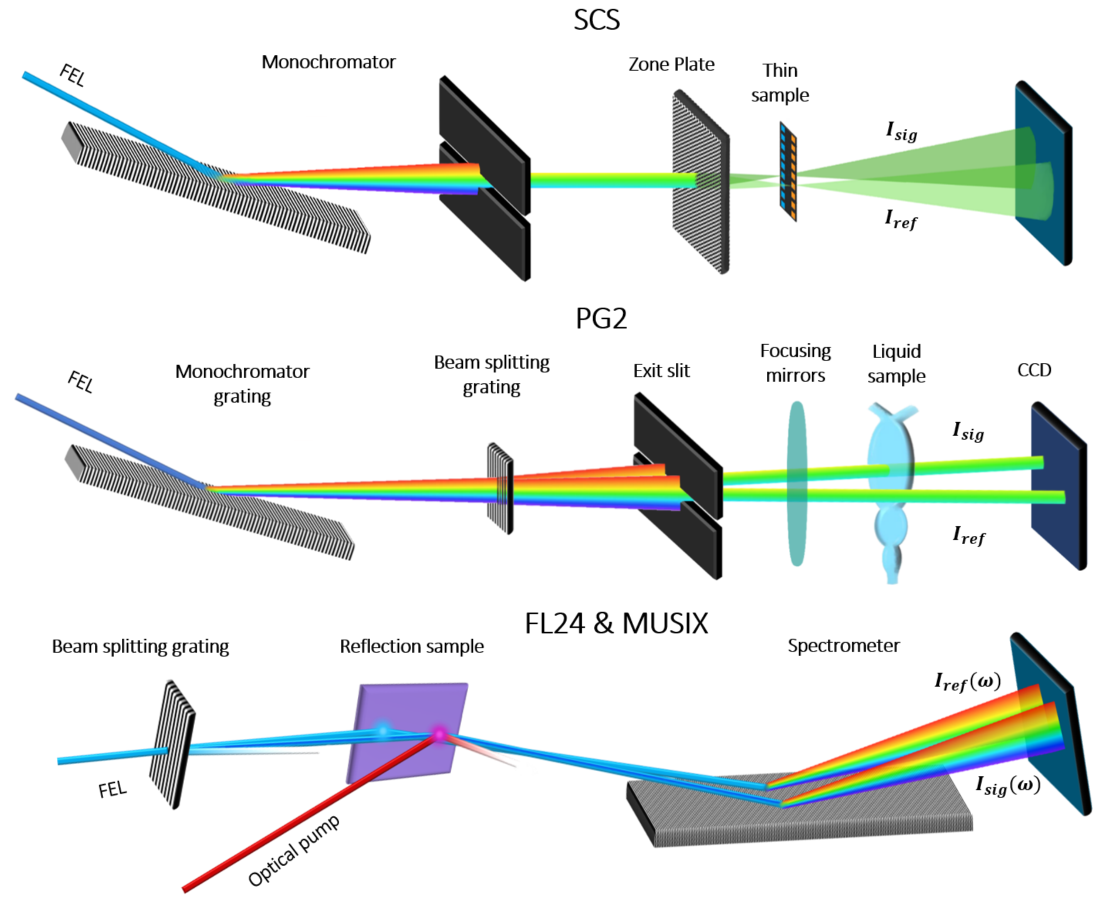

FIGURE 3.1: **Split-beam normalization setups at SCS, PG2 and FL24**. In each setup, a diffractive structure splits the XFEL beam into a reference beam and a signal beam that are measured by the same detector. While the SCS-setup and the PG2-setup both use a monochromator beamline and measure the transmission of a sample, the FL24-setup measures the reflectivity and employs the spectrometer of the MUlti-dimensional Spectroscopy and Inelastic X-ray scattering (MUSIX) endstation behind the sample.

In contrast, the setups at FLASH at the beamlines PG2 and FL24, that are discussed in this chapter, use a simple linear transmission grating. Figure 3.1 directly compares all three setups and thus enables a discussion of their relative advantages and disadvantages.

3.3.1 Monochromatic Split-Beam XANES at PG2

At PG2, the grating was inserted into the beamline between the monochromator grating and the exit slit of the monochromator, splitting the beam orthogonally to the dispersion direction of the monochromator. The two beams were then steered individually by the mirrors of an SDU [189] and directed through the monochromator exit slit and over the beamline focusing mirrors into the sample environment, which in this case contained a liquid flat-jet sample. One advantage of this configuration is that the setup makes use of the PG2 beamline monochromator [198] with minimal requirements to the sample environment. The spectral resolution can in principle reach that of the monochromator. The focusing mirrors of the beamline are configured to image the exit slit, where the dispersion of the monochromator is separated in space, onto the interaction point with the sample. Consequently, an opened exit slit illuminates the sample with a "rainbow". However, the beam divergence implies that this image of the exit slit appears blurred by about 0.53 eV at the position of the CCD, which was about 1 m behind the sample[3]. This means that the PG2 setup in principle allows for either monochromatic measurements with a narrow exit slit to reach a very good spectral resolution limited only by the monochromator, or parallel measurements with an open exit slit, where the spectral resolution is limited by the out-of-focus blurring at the CCD position[4].

In the following publication, *Shot noise limited soft x-ray absorption spectroscopy in solution at a SASE-FEL using a transmission grating beam splitter*, we demonstrate the capability to measure high-resolution XANES spectra in transmission, targeting dilute molecules in ethanol solution; we utilize a split-beam referencing scheme in combination with a liquid flat-jet sample configuration at the PG2-beamline and reach a sensitivity limited by the fundamental photon shot-noise. Although we planned to use a narrow exit slit, it ultimately needed to be opened to 200 μm (permitting a bandwidth of 0.8 eV) for reasons explained in the paper below. We also demonstrate the utility of enhancing the effective average SASE-bandwidth by chirping the central electron energy over the bunch train, which enables the acquisition of spectra in a wider energy window without tuning of the XFEL. Finally, we discuss the perspective of dramatically increasing the usable photon flux in this configuration, so as to further push the sensitivity of the setup and enable pump-probe XANES spectroscopy on even lower concentrations of solvated molecules. The publication is reproduced from [1], with the permission of AIP Publishing and in accordance with the Creative Commons Attribution 4.0 license under which the article was published.

---

[3] The blurring can be mathematically described as a convolution with a flat-top function. In the given case, I achieved the best reconstruction of the signal shape on the CCD using a Gaussian with σ=40 meV for the point-spread function of the monochromator, convolved with a flat-top function of 800 meV for the partially opened exit slit and another convolution with a flat-top of 530 meV for the out-of-focus position.

[4] This was also demonstrated in earlier work at the PG2 beamline [73]. As these measurements used a solid transmission sample (a Gd_2O_3 film) which could be inserted in the beamline directly, the detection was done via a Ce:YAG screen directly at the exit slit position, so out-of-focus blurring was no issue.

Structural Dynamics ARTICLE scitation.org/journal/sdy

Shot noise limited soft x-ray absorption spectroscopy in solution at a SASE-FEL using a transmission grating beam splitter

Cite as: Struct. Dyn. **8**, 014303 (2021); doi: 10.1063/4.0000049
Submitted: 12 November 2020 · Accepted: 11 January 2021 ·
Published Online: 29 January 2021

View Online Export Citation CrossMark

Robin Y. Engel,[1] Maria Ekimova,[2] Piter S. Miedema,[1] Carlo Kleine,[2] Jan Ludwig,[2] Miguel Ochmann,[3] Benjamin Grimm-Lebsanft,[3] Rory Ma,[3] Melissa Teubner,[3,4] Siarhei Dziarzhytski,[1] Günter Brenner,[1] Marie Kristin Czwalinna,[1] Benedikt Rösner,[5] Tae Kyu Kim,[6] Christian David,[5] Sonja Herres-Pawlis,[4] Michael Rübhausen,[3] Erik T. J. Nibbering,[2] Nils Huse,[3,a)] and Martin Beye[1,a)]

AFFILIATIONS

[1] Deutsches Elektronen Synchrotron DESY, 22607 Hamburg, Germany
[2] Max Born Institute for Nonlinear Optics and Short Pulse Spectroscopy, 12489 Berlin, Germany
[3] Institut for Nanostructure and Solid-State Physics, CFEL, University of Hamburg, 22761 Hamburg, Germany
[4] Institute of Inorganic Chemistry, RWTH Aachen University, 52074 Aachen, Germany
[5] Paul Scherrer Institute, 5232 Villigen PSI, Switzerland
[6] Department of Chemistry, Yonsei University, 03722 Seoul, South Korea

a) **Authors to whom correspondence should be addressed:** nils.huse@uni-hamburg.de and martin.beye@desy.de

ABSTRACT

X-ray absorption near-edge structure (XANES) spectroscopy provides element specificity and is a powerful experimental method to probe local unoccupied electronic structures. In the soft x-ray regime, it is especially well suited for the study of 3*d*-metals and light elements such as nitrogen. Recent developments in vacuum-compatible liquid flat jets have facilitated soft x-ray transmission spectroscopy on molecules in solution, providing information on valence charge distributions of heteroatoms and metal centers. Here, we demonstrate XANES spectroscopy of molecules in solution at the nitrogen *K*-edge, performed at FLASH, the Free-Electron Laser (FEL) in Hamburg. A split-beam referencing scheme optimally characterizes the strong shot-to-shot fluctuations intrinsic to the process of self-amplified spontaneous emission on which most FELs are based. Due to this normalization, a sensitivity of 1% relative transmission change is achieved, limited by fundamental photon shot noise. The effective FEL bandwidth is increased by streaking the electron energy over the FEL pulse train to measure a wider spectral window without changing FEL parameters. We propose modifications to the experimental setup with the potential of improving the instrument sensitivity by two orders of magnitude, thereby exploiting the high peak fluence of FELs to enable unprecedented sensitivity for femtosecond XANES spectroscopy on liquids in the soft x-ray spectral region.

I. INTRODUCTION

X-ray absorption near-edge structure (XANES) spectroscopy is one of the most common methods of x-ray spectroscopy, providing detailed information on local electronic structures: the position and magnitude of spectral features reports on oxidation states, spin configurations, and chemical bonds with element selectivity for light elements such as carbon, nitrogen, and oxygen as well as the important 3*d* transition metals.[1] For the latter elements, the absorption lines in the soft x-ray regime are typically tenfold narrower than those in the hard x-ray regime, which enhances the spectral information content.[2] Generally, the photochemistry of organic compounds and transition-metal complexes is of great interest for a variety of fields in chemistry and materials science, some examples being light harvesting in artificial photosynthesis and sensitizers for photovoltaic cells.[3–5] Many important chemical processes occur in solution, where soft XANES spectroscopy can be used to specifically investigate the state and evolution of the electronic configuration and, thus, the molecular bonds involving a targeted element (ideally a light element or 3*d* transition metal) within the liquid phase. However, the solute typically constitutes only a small fraction of the sample ($\leq 10^{-3}$) compared to the large fraction of solvent molecules. Solvent absorption in the soft x-ray range is substantial and must be addressed both experimentally and in the data analysis, which is especially challenging at sources like free-electron lasers (FELs), where the strongly fluctuating incident flux also needs to be accounted for. The very short absorption lengths (1–10 μm) severely limit the absolute amount of solute molecules that can be probed by the x-rays and require correspondingly thin samples in transmission measurements.

Early synchrotron-based static and time-resolved soft x-ray transmission studies in solution were conducted on stationary liquid targets[6–10] (with the time resolution being typically around 100 ps, at slicing sources reaching below 200 fs). The development of stable, micron-thin, free-flowing liquid sheets (flat jets) in vacuum[11] has enabled a more general application of time-resolved soft x-ray absorption spectroscopy in transmission.[12–17] Recently, split single nozzles and gas dynamic nozzles have also been used to create such flat jets.[18,19] The flow speeds of several 10 m/s (i.e., several 10 μm/μs) in these jets enable pump–probe experiments up to MHz repetition rates.

In this publication, we demonstrate the application of an advanced normalization scheme to soft x-ray spectroscopy in liquid solutions. We show transmission spectra of acetonitrile (ACN) and 4-aminoazobenzene (AAB) around the nitrogen *K*-edge, recorded from a micrometer thin free-flowing liquid sheet at the free-electron laser in Hamburg (FLASH) using a transmission grating-based beam-splitting scheme for shot-to-shot normalization. We demonstrate 95.4% confidence intervals (CIs) of ±5 mOD (about ±1% relative transmission change, see Fig. 3) within an acquisition time of 90 min. The referencing scheme reduced the noise level of our measurement setup to the fundamental limit of photon counting statistical noise. We further lay out potential improvements to the optical setup, which will increase the effective photon flux by up to four orders of magnitude, thus increasing the shot-noise limit on sensitivity by about two orders of magnitude for a similar measurement duration. With these improvements, we expect that such experiments at soft x-ray FELs with superconducting accelerators will enable unique sensitivity for ultrafast absorption studies.

II. EXPERIMENTAL

The measurements are performed at FLASH, producing x-ray bursts every 100 ms, each consisting of 400 pulses at a spacing of 1 μs. The beam path is defined through two apertures of 1 mm diameter into the second branch of the plane-grating monochromator beamline PG2.[20,21] The setup at the beam line is sketched in Fig. 1. The monochromator disperses the beam in the vertical direction and is tuned to the third-harmonic radiation with photon energies of around 400 eV, resonant to the *K*-edge absorption of nitrogen. During the measurements, the central transmitted photon energy of the monochromator is constantly scanned from 392.0 eV to 402.5 eV. The dispersed beam is directed onto a low line-density free-standing gold grating with a period of 11.3 μm, a thickness of 140 nm, a width of 300 μm, and a height of 4 mm, accepting the full height of the dispersed beam. This grating splits the FEL beam horizontally, with the zeroth diffraction order containing about 25% of the photons and two identical first orders containing about 10% of the photons each.[22] The optics of the split-and-delay unit (SDU), permanently installed at the beam line,[23] are used to separate the different orders, block the zeroth order beam, and steer the first-order beams (signal and reference) through the beam line. The photon energy is selected by the exit slit of the beam line (set to 200 μm, transmitting an energy bandwidth of about 0.8 eV), and the beams are refocused onto the liquid flat jet in the experimental chamber. The operating conditions of the jet are as previously reported.[14] One of the beams transmits centrally through the main leaf of the liquid flat jet, while the other bypasses the jet as a reference beam. Both beams are separated in the sample plane by about 1.7 mm. After transmission through a 200 nm thin aluminum filter for separating the jet chamber vacuum from the detector and blocking optical photons, both beams hit a charge-coupled device (CCD model ANDOR Ikon L936) cooled to about 210 K and installed about 1 m behind the sample. The detector is configured to read out the (13.5 μm)^2 square pixels with a binning of two by eight in the vertical

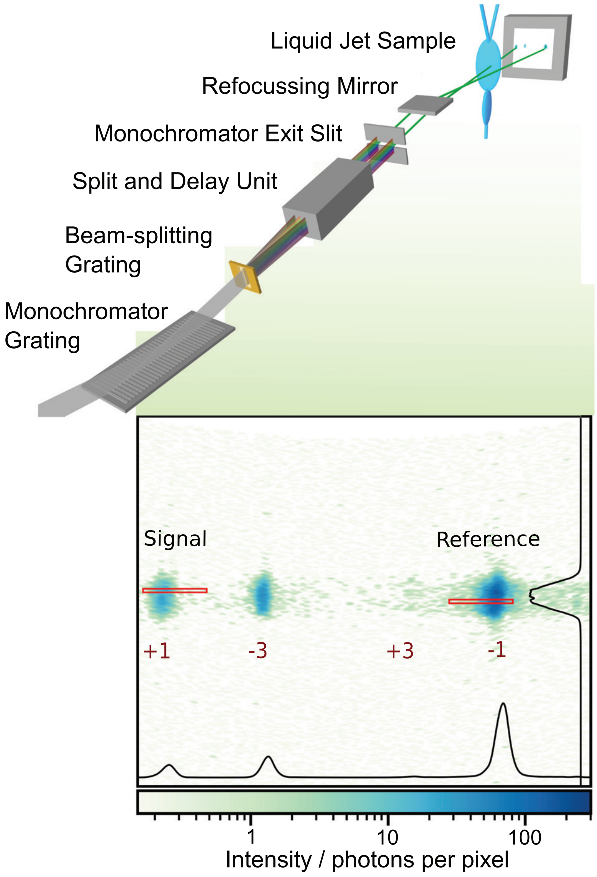

FIG. 1. Experimental setup at the plane-grating monochromator beam line at FLASH. The incident beam is vertically dispersed by a reflection grating. A low line-density transmission grating splits the beam horizontally. A split-and-delay unit steers signal and reference beams toward the CCD detector, while only the signal beam interacts with the jet. The preprocessed detector image shows the first diffraction orders of the transmission grating (which constitute signal and reference beams) as well as weak contributions from the third orders that are partially clipped by apertures in the beam line. The black projections are drawn from an average image. Red boxes display the highly correlated regions used for normalization.

and horizontal directions, respectively, generating images of 290 × 90 pixels. The pixel readout rate is set to 1 MHz, resulting in a usable frame rate of 3.3 Hz. The number of FEL bursts is accordingly reduced with a mechanical chopper.[24] Each image read from the detector is accumulated over all 400 pulses in a burst. The CCD did not exceed 12% saturation. An averaged dark image is subtracted from each raw image. To enable a finer selection of regions of interest (ROI), the number of pixels is enhanced by cubic interpolation while conserving the value of the intensity integral. Due to the CCD being positioned behind the beamline focus, the exit slit image exhibits a curved distortion, which was characterized by a second-order polynomial fit to the exit slit shadow and corrected for by shifting columns of the image along the nondispersive direction such that the exit slit appears as a straight line, as visible in the corrected CCD image in Fig. 1. The routinely usable spectral range for such measurements is given by the FEL photon energy bandwidth. FELs operated in the based on Self-Amplified Spontaneous Emission (SASE) typically produce average bandwidths on the order of 1%,[25] which are often narrower than the spectral range of interest. In order to change the central energy of FLASH1 (which uses fixed gap undulators), it is necessary to change the electron energy and, accordingly, the electron optics in the accelerator. Unfortunately, this often results in slight alterations of the photon beam path that can produce systematic deviations in the spectrum. Such artifacts are avoided by introducing a constant chirp into the electron energy across the burst, which produces a systematic shift of central photon energy evolving from the first to the last pulse in the train. This doubles the usable photon energy range for the experiment. In addition, the chirped bunch train provides a relatively flat intensity distribution across a large part of the photon energy window, as shown in Fig. 2(a). A direct measurement of the average photon energy variation across the burst is displayed in Fig. 2(b), where an acquisition from an online spectrometer[26] equipped with the MHz line-detector KALYPSO[27] is shown.

As a first assessment of this setup, XANES measurements are performed on 1 M ACN and 40 mM AAB ethanol solutions [see Figs. 3(a) and 3(b)]. Strong outliers in the intensity ratio ascribed to short-lived disturbances of the liquid jet are dropped from the analysis. The remaining images are sorted into bins corresponding to 120 meV for ACN or 240 meV intervals for the AAB solution. The recorded ACN spectrum is compared with a synchrotron spectrum, recorded from an 11.3 M solution in water as total fluorescence yield mode at the U41-PGM beam line of BESSY II with an energy resolution of 230 meV. Spectra are calibrated to the ACN resonance (1 s to 2 π^*) at 399.5 eV.

The split-beam referencing scheme works on the assumption that the signal and reference beams are identical in all aspects except for the interaction of the signal beam with the liquid jet. To properly extract correlated intensities of the two beams, the ROIs had to be carefully selected: a rotational misalignment of the fixed beam-splitting grating with respect to the dispersion direction of the monochromator resulted in different parts of the FEL spectrum reaching the CCD. To mitigate this issue, the monochromator exit slit was widened to 200 μm, transmitting a spectral window of 0.8 eV. Although this compromises the energy resolution of the acquired spectra, the dispersion preserved on the CCD retained a resolution of around 0.5 eV, dominated by the out-of-focus blurring effect. More importantly, the widened exit slit allowed for certain regions on the CCD to detect the same part of the original FEL spectrum despite the misalignment of the beam splitting grating. Thus, the energy shift between the signal and reference beams could be compensated by proper selection of adequately small ROIs on the CCD, albeit at the cost of omitting roughly 87% of detected photons. The Pearson correlation coefficient (CC) between beam intensities was chosen as a measure to judge the quality of ROI selection. Near perfect correlations between 0.97 and 0.99 are reached over the flat regions of the spectra. The height of the ROIs is kept narrow at six pixels, while positions and the common width of the ROIs are optimized for the highest CC. The ROIs are selected sufficiently wide to cover the small position variations due to the chromaticity of the beam-splitting grating. A result is shown in Fig. 1. From the optimization, we determine a rotational misalignment of the beam-splitting grating of 0.8°. This correlation analysis works best on regions of flat spectral transmission, as variations of the sample absorption reduce the correlation[29] between the signal and the reference. Therefore, the algorithm excludes images containing absorption peaks, namely, monochromator settings from 398.75 eV to 400.25 eV for ACN and from 377.3 eV to 398.7 eV for AAB. Images from outside the central range of the FEL bandwidth (393 eV–401 eV) are also excluded. A slow fluctuation in the background signal is drawn from

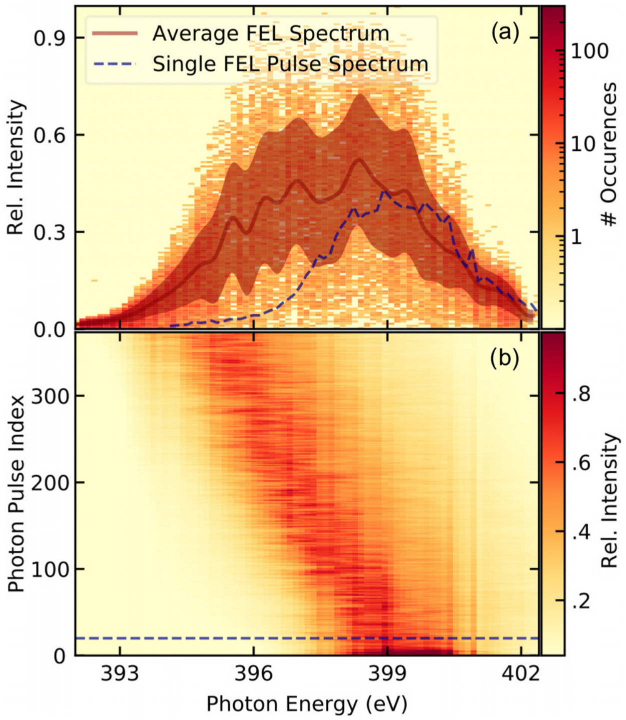

FIG. 2. (a) Intensity distribution of the reference beam during the acquisition of the spectrum of 4-aminoazobenzene shown in Fig. 3. The overall distribution is broadened in comparison to the single pulse FEL spectrum due to the energy chirp over the bunch train. The average FEL spectrum is shown as a line, and the standard deviation is shaded. (b) The photon pulse-resolved spectra of a single bunch train, measured using the KALYPSO detector, demonstrating the chirp of the central photon energy across the bunch train. The dashed line indicates where the single pulse spectrum in (a) was extracted. Systematic gain variations of the detector have been corrected for, but artifacts from inhomogeneities of the used phosphor screen are still visible.

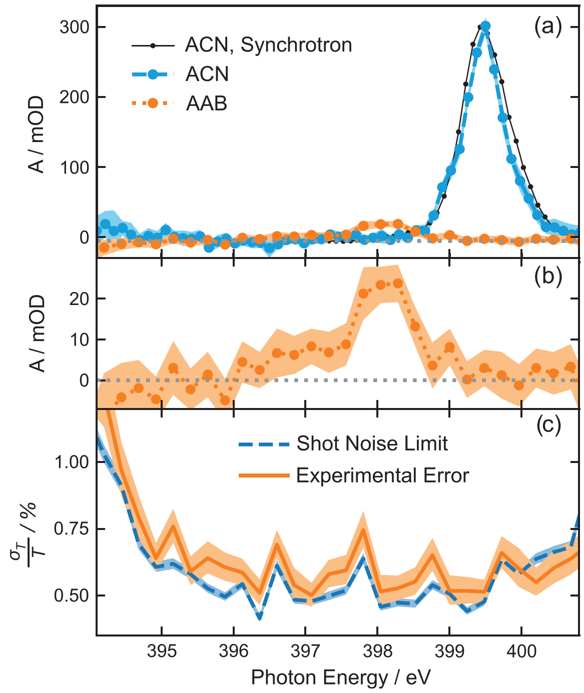

FIG. 3. (a) Nitrogen *K*-edge transmission spectra of 1 M acetonitrile (ACN) and 40 mM 4-aminoazobenzene (AAB) in ethanol solution. A rescaled reference spectrum of 11.3 M ACN in water recorded at an undulator beamline of BESSY II with a resolution of 230 meV is shown for comparison. The ACN spectrum is calculated from 7600 images recorded within 46 min, and the AAB spectrum from 17 500 images is recorded over 88 min. The colored areas around the spectra mark the boundaries of 95.4% confidence intervals (CI) of the spectral absorbance. The absorbance values of 1.79 μm and 1.71 μm of ethanol as computed based on the CXRO database[28] were subtracted from the ACN and AAB spectra, respectively. (b) Zoom in of the AAB spectrum. (c) The relative statistical uncertainty of the AAB measurement (68.3% CI of the transmittance divided by the transmittance) compared with the photon shot noise limit, i.e., the geometrically added square root of the estimated number of photons in both beams.

an equally sized ROI within the dark region of the CCD, averaged over 30 consecutive images, and subtracted from all intensities.

The transmittance in each interval of the spectrum,

$$T = \langle I_{sig}\rangle / \langle I_{ref}\rangle, \tag{1}$$

is then calculated as the ratio of averaged signal and reference intensities; absorbance A is the negative decadic logarithm of the transmittance,

$$A = -log_{10}(T). \tag{2}$$

Finally, the absorbance of the ethanol solvent is subtracted, as calculated from the Center for x-Ray Optics (CXRO) database[28] using the room temperature density of ethanol and the average jet thickness that best fits the baseline of the spectrum (1.79 μm for the ACN measurement and 1.71 μm for AAB). The ACN measurement consists of two, the AAB measurement of three combined datasets, for each of which the ROI optimization is performed individually. Error bars represent 95.4% confidence intervals (CI) for the expectation value of absorbance.

Since the intensities of the signal and the reference are strongly correlated, their statistical uncertainties (corresponding to 68.3% CI),

$$\sigma_{sig} = \sqrt{\left\langle \left(I_{sig} - \langle I_{sig}\rangle\right)^2 \right\rangle \Big/ N^2_{samples}}, \tag{3}$$

and σ_{ref} (calculated correspondingly) are propagated with consideration of the covariance $\sigma_{I_{sig}I_{ref}}$ of both intensities for each bin, following the study by Tellinghuisen[30] and the pertinent literature as

$$\sigma_T = \left|\frac{\langle I_{sig}\rangle}{\langle I_{ref}\rangle}\right| \sqrt{\left(\frac{\sigma_{sig}}{\langle I_{sig}\rangle}\right)^2 + \left(\frac{\sigma_{ref}}{\langle I_{ref}\rangle}\right)^2 - \frac{2\sigma_{I_{sig}I_{ref}}}{\langle I_{sig}\rangle\langle I_{ref}\rangle}}. \tag{4}$$

Figure 3(c) compares the measured relative statistical fluctuations σ_T/T of the transmittance with the fluctuations that should be expected theoretically from a purely shot-noise limited process. The uncertainty of the absorbance A is

$$\sigma_A = \left|\frac{\sigma_T}{Tln(10)}\right|, \tag{5}$$

which is doubled to attain the 95.4% CI.

Based on pixel-value histograms of the resulting images, the CCD reads an average of 31 (±2) analogs to digital units per 400 eV photon. Between central photon energies of 396 eV and 400 eV, we, thus, measure an effectively usable photon flux of 2.7 $\times 10^3$ photons per second in the reference beam ROI. Figure 3(c) shows that the determined experimental error is only slightly above the theoretical expectation for pure shot noise from the same number of photons. The measurements presented here are recorded within 1.5 h, mainly limited by the stability of the liquid jet conditions.

III. DISCUSSION

XANES spectra of molecules and colloidal nanoparticles in solution are accessible either directly in transmission or by observing the partial or total fluorescence yield (PFY and TFY, respectively). Transmission and TFY detection modes are experimentally much simpler to implement as they do not require a spectrally resolved detection scheme. However, transmission measurements in solution determine sample absorption on a background of relatively large nonresonant solvent absorption, requiring thin liquid sheets and a precise normalization to the incident flux. In the case of TFY, the background from solvent fluorescence often dominates the overall signal. Still, TFY detection of XANES spectra in solution has been employed although this choice of detection scheme can lead to erroneous interpretations of the resulting spectra because solvent and sample fluorescence are competing processes that cannot be spectrally discriminated in this measurement mode.[31–34] Therefore, TFY detection requires specific conditions, e.g., the solute absorption edges residing far below those of the solvent.[35] On the other hand, partial fluorescence yield is a better measure of x-ray absorption; however, it is experimentally far more challenging, as it requires spectrally resolved detection that is selective to the elemental fluorescence of interest.[36] Laser-driven high-harmonic generation (HHG) sources can provide time resolution in the femtosecond range and below,[47–50] but the relatively low spectral photon flux at short wavelengths (<4 nm) still makes such XANES studies in solution challenging, albeit these sources hold great future potential.[37] Free-electron lasers can, in principle, supply a much higher flux. However, most FELs are based on self-amplified spontaneous emission

(SASE), intrinsically displaying strong spectral intensity fluctuations. These fluctuations have so far hampered quantitative soft XANES spectroscopy at these light sources, with only a few time-resolved studies published measuring partial and total fluorescence yield.[35,36,38–40] The challenge to correctly normalize such fluctuations across a large dynamic range becomes especially severe for absorption measurements in transmission mode on dilute samples. Thus, recording solute spectra of millimolar concentrations on a background of 20–50 molar solvent density requires a high instrument sensitivity and, in turn, an excellent normalization to the incident flux. So far, no method of intensity normalization could be established as a standard in x-ray absorption measurements at FELs. Some facilities use Gas Monitor Detectors (GMDs)[41,42] to measure the intensity fluctuations behind a monochromator. However, GMDs typically have a pulse-to-pulse accuracy of around 10% and struggle with the low pulse energy after a monochromator, which precludes their use for monochromatic third-harmonic radiation at FLASH. This challenge leads to the presented normalization scheme using a transmission grating beam splitter, utilizing a single CCD detector for incident and transmitted intensities. As this method can enable very high sensitivity, versions of it have been demonstrated at SPring-8 Angstrom Compact free electron LAser (SACLA)[43,44] Linac Coherent Light Source (LCLS),[45] and FLASH,[22,46] showing considerably improved normalization of SASE fluctuations compared to previous normalization schemes. Implementing the same principle of split-beam normalization, we present the acquisition of XANES spectra from femtosecond FEL pulses with a sensitivity limited by photon counting statistics in the soft x-ray range on a liquid sample. High monochromatic x-ray flux in femtosecond pulses is currently only found at FELs and is especially beneficial in time-dependent studies of specific XANES features. We estimate an output of 7×10^9 photons/s/0.1% bandwidth in the third harmonic at 400 eV produced by FLASH during this experiment based on the specified transmission of the beamline, monochromator, beam-splitting grating, and SDU. However, the number of detected photons is still low in comparison to other FEL measurements since this experiment utilized the third-harmonic radiation and mirrors that are optimized for the extreme ultraviolet wavelength range. For future studies, the soft x-ray monochromator beamline at FLASH 2 (under construction) offers higher flux and better beamline transmission for the third-harmonic radiation. The additional mirrors of the SDU used for individual beam steering and the alignment issue discussed above further attenuated the flux by nearly three orders of magnitude. The spectral flux that we could include in our analysis in this work reaches 5.5×10^3 photons/s/eV due to the high repetition rate compared to other FEL studies. Some of these losses can be avoided in future studies as discussed below, with a potential increase by three to four orders of magnitude. Directly comparable published measurements were performed at HHG sources, which generally reach a much lower monochromatic flux: modern HHG setups can achieve tens of detected photons per second per eV, e.g., 14 photons/s/eV near the N *K*-edge in the study by Kleine *et al.*[37] The spectral flux used by Obara *et al.*[44] around the iron *K*-edge at 7.2 keV amounted to about 2.6×10^4 photons/s/eV. On solid samples, Schlotter *et al.*[45] report on average 6.4×10^6 photons/s at the O *K*-edge, well in line with our work after the proposed improvements. For lower temporal resolutions, synchrotron studies offer a viable alternative with substantially more flux. Fondell *et al.*[12] report 2.0×10^9 photons/s/eV in a train of pulses of tens of picoseconds duration at the N *K*-edge at the BESSY II storage ring.

Many studies[37,43,44,46] further exploit a dispersive acquisition scheme. Here, instead of scanning a monochromator and measuring the absorption for each step, the full spectrum of the source is dispersed onto a spatially resolving detector. Such an acquisition scheme can constitute an optimized parallel measurement utilizing the entire source bandwidth. If, as in this setup, beamline optics are used to disperse the beam and the sample is placed downstream, the sample is illuminated by a rainbow-like line focus, which necessarily couples spatial inhomogeneities into the spectrum. In the case of a liquid flat jet, the thickness often systematically varies in the vertical direction,[19] requiring appropriate corrections. On the other hand, dispersion downstream of the sample[46] allows for a small focus using the entire source bandwidth on the sample, provided that the sample can withstand the fluence of the full beam. Such a method then requires that one dimension of the detector is used for spectral resolution, so that the number of illuminated pixels per energy bin is substantially reduced. Thus, any detector inhomogeneities, nonlinearities, and digitization noise are not averaged out as well as in a monochromatic scanning scheme, where substantially larger areas of the detector can be utilized for each energy step. Building on the setup presented in Fig. 1, we propose the following adaptions for time-resolved future measurements to increase the detected flux and, thus, sensitivity:

First, we have already constructed a mount for the beam splitting grating, which allows fine-tuning the rotation angle, so that complications due to slight misalignments can be avoided in future measurements at FLASH. Furthermore, the transmission of the split-and-delay unit is optimized for longer wavelengths, but at the N *K*-edge, only 1% of the photons is transmitted. Thus, we will optimize the beam splitting grating design to directly generate the ideal beam separation in the sample plane, such that the use of the split-and-delay unit for beam steering is not required, resulting in two orders of magnitude higher effective flux. An additional step to maximize the effective photon flux can be taken by fully opening the exit slit of the monochromator and, thus, transitioning to a dispersive measurement. While this might amplify possible detector inhomogeneities and requires a normalization of varying sample thicknesses as discussed above, this imaging scheme would result in another order of magnitude increase in detected photon flux and provides a means to correct for slow drifts of the liquid jet thickness over time, which are, otherwise, likely to become the next significant source of error in long measurements with drastically reduced shot noise. Altogether, these improvements can increase the effective photon flux by up to four orders of magnitude, yielding more than 10^7 detected photons per second in the reference beam. Similar quality spectra, as shown in Fig. 3, could ideally be recorded within approximately one second instead of more than one hour. For an hour-long measurement, the shot-noise limit on the sensitivity (scaling with the square root of the flux) would improve by a factor between 30 and 100 and, thus, reach less than $\pm 100\ \mu$OD.

IV. CONCLUSION

In a setup designed for future time-resolved pump probe experiments, we measured x-ray absorption spectra of molecules in ethanol solution. We used the third-harmonic radiation of a SASE FEL and implemented a split-beam referencing scheme similar to those demonstrated at FELs in the hard x-ray regime and solid samples[22,43,45,46] to compensate for intensity fluctuations, reaching 95.4% confidence intervals of ± 5 mOD at the N *K*-edge. The sensitivity is close to the photon shot noise limit of this experiment. By introducing FELs to soft x-ray XANES spectroscopy on molecules in solution, the presented measurements are about eight times more sensitive than those previously achieved in femtosecond XANES on liquid solutions at this photon energy using an HHG source.[37] In the presented measurements, with the sensitivity down to $\sigma_T/T \simeq 0.5$, % relative transmission change (see Fig. 2) is comparable to the noise ratio of 0.26% achieved in a comparable setup in the hard x-ray regime.[43]

An alignment error and the use of the split-and-delay unit for beam steering reduced the effective photon flux. In order to better exploit the high photon flux of FLASH, we suggest an advanced configuration that fully omits both the SDU and the exit slit, thus gaining three to four orders of magnitude in intensity. As a consequence, we see the potential for acquiring spectra with mOD sensitivity within seconds, while the shot-noise limit on the 95.4% confidence intervals could be reduced to less than ± 100 μOD within one hour. This constitutes an important step to enable measurements on the photoinduced dynamics of increasingly larger, less soluble molecules on the femtosecond timescale.

AUTHORS' CONTRIBUTIONS

R.Y.E. and M.E. contributed equally to this work.

ACKNOWLEDGMENTS

We acknowledge DESY (Hamburg, Germany), a member of the Helmholtz Association HGF, for the provision of experimental facilities. The presented measurements were carried out at the PG2 monochromator beamline of FLASH. The authors are very thankful to the involved groups at DESY for the active support. We thank Simon Schreck and Philippe Wernet for recording the ACN reference spectrum. R.Y.E., P.S.M., and M.B. were funded by the Helmholtz Association through Grant No. VH-NG-1105. M.O. and N.H. gratefully acknowledge funding from the German Science Foundation (DFG) within the collaborative research center SFB 925 "Light induced dynamics and control of correlated quantum systems" (project A4). M.E., C.K., J.L., and E.T.J.N. acknowledge support from the German Science Foundation (Project No. DFG-NI 492/11–1) and the European Research Council (ERC) under the European Union's Horizon 2020 research and innovation programme (ERC Grant Agreement No. 788704; E.T.J.N.).

DATA AVAILABILITY

The data that support the findings of this study are available from the corresponding author upon reasonable request.

REFERENCES

[1] J. Stöhr, *NEXAFS Spectroscopy*, Springer Series in Surface Sciences (Springer-Verlag Belin Heidelberg GmbH, 1992), Vol. 25.
[2] F. J. Himpsel, Phys. Status Solidi B **248**, 292 (2011).
[3] I. Roger, M. A. Shipman, and M. D. Symes, Nat. Rev. Chem. **1**, 1 (2017).
[4] X. Du, X. Jiao, S. Rechberger, J. D. Perea, M. Meyer, N. Kazerouni, E. Spiecker, H. Ade, C. J. Brabec, R. H. Fink, and T. Ameri, Macromolecules **50**, 2415 (2017).
[5] C. Xie, T. Heumüller, W. Gruber, X. Tang, A. Classen, I. Schuldes, M. Bidwell, A. Späth, R. H. Fink, T. Unruh, I. McCulloch, N. Li, and C. J. Brabec, Nat. Commun. **9**, 1 (2018).
[6] B. Yang and J. Kirz, Phys. Rev. B **36**, 1361 (1987).
[7] P. Wernet, G. Gavrila, K. Godehusen, C. Weniger, E. T. Nibbering, T. Elsaesser, and W. Eberhardt, Appl. Phys. A **92**, 511 (2008).
[8] N. Huse, H. Wen, D. Nordlund, E. Szilagyi, D. Daranciang, T. A. Miller, A. Nilsson, R. W. Schoenlein, and A. M. Lindenberg, Phys. Chem. Chem. Phys. **11**, 3951 (2009).
[9] H. Wen, N. Huse, R. W. Schoenlein, and A. M. Lindenberg, J. Chem. Phys. **131**, 234505 (2009).
[10] K. Hong, H. Cho, R. W. Schoenlein, T. K. Kim, and N. Huse, Acc. Chem. Res. **48**, 2957 (2015).
[11] M. Ekimova, W. Quevedo, M. Faube, P. Wernet, and E. T. Nibbering, Struct. Dyn. **2**, 054301 (2015).
[12] M. Fondell, S. Eckert, R. M. Jay, C. Weniger, W. Quevedo, J. Niskanen, B. Kennedy, F. Sorgenfrei, D. Schick, E. Giangrisostomi, R. Ovsyannikov, K. Adamczyk, N. Huse, P. Wernet, R. Mitzner, and A. Föhlisch, Struct. Dyn. **4**, 054902 (2017).
[13] M. Ekimova, W. Quevedo, L. Szyc, M. Iannuzzi, P. Wernet, M. Odelius, and E. T. Nibbering, J. Am. Chem. Soc. **139**, 12773 (2017).
[14] M. Ekimova, M. Kubin, M. Ochmann, J. Ludwig, N. Huse, P. Wernet, M. Odelius, and E. T. Nibbering, J. Phys. Chem. B **122**, 7737 (2018).
[15] S. Eckert, J. Norell, R. M. Jay, M. Fondell, R. Mitzner, M. Odelius, and A. Föhlisch, Chemistry **25**, 1733 (2019).
[16] R. M. Jay, S. Eckert, V. Vaz da Cruz, M. Fondell, R. Mitzner, and A. Föhlisch, Angew. Chem.-Int. Ed. **58**, 10742 (2019).
[17] L. Kjellsson, K. D. Nanda, J.-E. Rubensson, G. Doumy, S. H. Southworth, P. J. Ho, A. M. March, A. Al Haddad, Y. Kumagai, M.-F. Tu, R. D. Schaller, T. Debnath, M. S. Bin Mohd Yusof, C. Arnold, W. F. Schlotter, S. Moeller, G. Coslovich, J. D. Koralek, M. P. Minitti, M. L. Vidal, M. Simon, R. Santra, Z.-H. Loh, S. Coriani, A. I. Krylov, and L. Young, Phys. Rev. Lett. **124**, 236001 (2020).
[18] G. Galinis, J. Strucka, J. C. Barnard, A. Braun, R. A. Smith, and J. P. Marangos, Rev. Sci. Instrum. **88**, 083117 (2017).
[19] J. D. Koralek, J. B. Kim, P. Bruza, C. B. Curry, Z. Chen, H. A. Bechtel, A. A. Cordones, P. Sperling, S. Toleikis, J. F. Kern, S. P. Moeller, S. H. Glenzer, and D. P. DePonte, Nat. Commun. **9**, 1 (2018).
[20] N. Gerasimova, S. Dziarzhytski, and J. Feldhaus, J. Mod. Opt. **58**, 1480 (2011).
[21] M. Wellhöfer, W. Wurth, and M. Richter, "The monochromator beamline at FLASH assembly, characterization and first experiments," Ph.D. thesis (Hamburg University, 2007).
[22] G. Brenner, S. Dziarzhytski, P. Miedema, B. Rösner, C. David, and M. Beye, Opt. Lett. **44**, 2157 (2019).
[23] F. Sorgenfrei, W. F. Schlotter, T. Beeck, M. Nagasono, S. Gieschen, H. Meyer, A. Föhlisch, M. Beye, and W. Wurth, Rev. Sci. Instrum. **81**, 043107 (2010).
[24] E. Ploenjes and K. Tiedtke, in *Optical Technologies for Extreme-Ultraviolet and Soft X-Ray Coherent Sources*, Springer Series in Optical Sciences Vol. 197, edited by F. Canova and L. Poletto (Springer, Heidelberg/Hamburg, 2015), Chap. 1, pp. 1–22.
[25] E. L. Saldin, E. A. Schneidmiller, and M. V. Yurkov, Opt. Commun. **148**, 383 (1998).
[26] G. Brenner, S. Kapitzki, M. Kuhlmann, E. Ploenjes, T. Noll, F. Siewert, R. Treusch, K. Tiedtke, R. Reininger, M. D. Roper, M. A. Bowler, F. M. Quinn, and J. Feldhaus, Nucl. Instrum. Methods Phys. Res., Sect. A **635**, 99 (2011).
[27] C. Gerth, G. Brenner, M. Caselle, S. Düsterer, D. Haack, D. Makowski, A. Mielczarek, S. Palutke, L. Rota, V. Rybnikov, C. Schmidt, B. Steffen, and K. Tiedtke, J. Synchrotron Radiat. **26**, 1514 (2019).
[28] B. Henke, E. Gullikson, and J. Davis, At. Data Nucl. Data Tables **54**, 181 (1993).
[29] S. Zohar and J. J. Turner, Opt. Lett. **44**, 243 (2019).
[30] J. Tellinghuisen, J. Phys. Chem. A **105**, 3917 (2001).
[31] F. M. De Groot, Nat. Chem. **4**, 766 (2012).
[32] T. Z. Regier, A. J. Achkar, D. Peak, J. S. Tse, and D. G. Hawthorn, Nat. Chem. **4**, 765 (2012).
[33] P. S. Miedema, P. Wernet, and A. Föhlisch, Phys. Rev. A **89**, 1 (2014).
[34] P. S. Miedema and M. Beye, J. Phys. Chem. Lett. **9**, 2579 (2018).
[35] Z. H. Loh, G. Doumy, C. Arnold, L. Kjellsson, S. H. Southworth, A. Al Haddad, Y. Kumagai, M. F. Tu, P. J. Ho, A. M. March, R. D. Schaller, M. S. Bin Mohd Yusof, T. Debnath, M. Simon, R. Welsch, L. Inhester, K. Khalili, K. Nanda, A. I. Krylov, S. Moeller, G. Coslovich, J. Koralek, M. P. Minitti, W. F. Schlotter, J. E. Rubensson, R. Santra, and L. Young, Science **367**, 179 (2020).

[36]R. Mitzner, J. Rehanek, J. Kern, S. Gul, J. Hattne, T. Taguchi, R. Alonso-Mori, R. Tran, C. Weniger, H. Schröder, W. Quevedo, H. Laksmono, R. G. Sierra, G. Han, B. Lassalle-Kaiser, S. Koroidov, K. Kubicek, S. Schreck, K. Kunnus, M. Brzhezinskaya, A. Firsov, M. P. Minitti, J. J. Turner, S. Moeller, N. K. Sauter, M. J. Bogan, D. Nordlund, W. F. Schlotter, J. Messinger, A. Borovik, S. Techert, F. M. De Groot, A. Föhlisch, A. Erko, U. Bergmann, V. K. Yachandra, P. Wernet, and J. Yano, J. Phys. Chem. Lett. **4**, 3641 (2013).

[37]C. Kleine, M. Ekimova, G. Goldsztejn, S. Raabe, C. Strüber, J. Ludwig, S. Yarlagadda, S. Eisebitt, M. J. Vrakking, T. Elsaesser, E. T. Nibbering, and A. Rouzée, J. Phys. Chem. Lett. **10**, 52 (2019).

[38]P. Wernet, K. Kunnus, I. Josefsson, I. Rajkovic, W. Quevedo, M. Beye, S. Schreck, S. Grübel, M. Scholz, D. Nordlund, W. Zhang, R. W. Hartsock, W. F. Schlotter, J. J. Turner, B. Kennedy, F. Hennies, F. M. De Groot, K. J. Gaffney, S. Techert, M. Odelius, and A. Föhlisch, Nature **520**, 78 (2015).

[39]S. Eckert, J. Norell, P. S. Miedema, M. Beye, M. Fondell, W. Quevedo, B. Kennedy, M. Hantschmann, A. Pietzsch, B. E. Van Kuiken, M. Ross, M. P. Minitti, S. P. Moeller, W. F. Schlotter, M. Khalil, M. Odelius, and A. Föhlisch, Angew. Chem.-Int. Ed. **56**, 6088 (2017).

[40]R. M. Jay, J. Norell, S. Eckert, M. Hantschmann, M. Beye, B. Kennedy, W. Quevedo, W. F. Schlotter, G. L. Dakovski, M. P. Minitti, M. C. Hoffmann, A. Mitra, S. P. Moeller, D. Nordlund, W. Zhang, H. W. Liang, K. Kunnus, K. Kubiček, S. A. Techert, M. Lundberg, P. Wernet, K. Gaffney, M. Odelius, and A. Föhlisch, J. Phys. Chem. Lett. **9**, 3538 (2018).

[41]K. Tiedtke, J. Feldhaus, U. Hahn, U. Jastrow, T. Nunez, T. Tschentscher, S. V. Bobashev, A. A. Sorokin, J. B. Hastings, S. Möller, L. Cibik, A. Gottwald, A. Hoehl, U. Kroth, M. Krumrey, H. Schöppe, G. Ulm, and M. Richter, J. Appl. Phys. **103**, 094511 (2008).

[42]A. A. Sorokin, Y. Bican, S. Bonfigt, M. Brachmanski, M. Braune, U. F. Jastrow, A. Gottwald, H. Kaser, M. Richter, and K. Tiedtke, J. Synchrotron Radiat. **26**, 1092 (2019).

[43]T. Katayama, Y. Inubushi, Y. Obara, T. Sato, T. Togashi, K. Tono, T. Hatsui, T. Kameshima, A. Bhattacharya, Y. Ogi, N. Kurahashi, K. Misawa, T. Suzuki, and M. Yabashi, Appl. Phys. Lett. **103**, 131105 (2013).

[44]Y. Obara, T. Katayama, Y. Ogi, T. Suzuki, N. Kurahashi, S. Karashima, Y. Chiba, Y. Isokawa, T. Togashi, Y. Inubushi, M. Yabashi, T. Suzuki, and K. Misawa, Opt. Express **22**, 1105 (2014).

[45]W. F. Schlotter, M. Beye, S. Zohar, G. Coslovich, G. L. Dakovski, M. F. Lin, Y. Liu, A. Reid, S. Stubbs, P. Walter, K. Nakahara, P. Hart, P. S. Miedema, L. LeGuyader, K. Hofhuis, P. T. P. Le, J. E. t Elshof, H. Hilgenkamp, G. Koster, X. H. Verbeek, S. Smit, M. S. Golden, H. A. Durr, and A. Sakdinawat, arXiv:2006.13968 (2020).

[46]R. Engel, P. Miedema, D. Turenne, I. Vaskivskyi, G. Brenner, S. Dziarzhytski, M. Kuhlmann, J. Schunck, F. Döring, A. Styervoyedov, S. Parkin, C. David, C. Schüßler-Langeheine, H. Dürr, and M. Beye, Appl. Sci. **10**, 6947 (2020).

[47]S. L. Cousin, N. Di Palo, B. Buades, S. M. Teichmann, M. Reduzzi, M. Devetta, A. Kheifets, G. Sansone, and J. Biegert, Phys. Rev. X **7**, 041030 (2017).

[48]A. S. Johnson, D. R. Austin, D. A. Wood, Christian Brahms, Andrew Gregory, K. B. Holzner, S. Jarosch, E. W. Larsen, S. Parker, C. S. Strüber, P. Ye, J. W. G. Tisch, and J. P. Marangos, Sci. Adv. **4**, eaar3761 (2018).

[49]A. D. Smith, T. Balčiūnas, Y.-P. Chang, C. Schmidt, K. Zinchenko, F. B. Nunes, E. Rossi, V. Svoboda, Z. Yin, J.-P. Wolf, and H. J. Wörner, J. Phys. Chem. Lett. **11**, 1981 (2020).

[50]L. Barreau, A. D. Ross, S. Garg, P. M. Kraus, D. M. Neumark, and Stephen R. Leone, Sci. Rep. **10**, 5773 (2020).

3.3.2 Broadband Reflection Spectroscopy at FL24

While we could demonstrate in the publication above [1] that the normalization performed ideally, which means that the measurement uncertainty was dominated by the photon shot noise, the usable flux which ultimately contributed to the measurement was relatively small with about $2.7{\times}10^3$ photons/s. In contrast to the monochromatic configuration, a parallel measurement greatly increases the effectively usable flux, as the full SASE bandwidth can contribute to the measurement at once. This was implemented in the setup at FL24, which is described in the second publication in this chapter [2] and implemented for pump-probe measurements in the third [3].

The first significant difference of this setup to the ones at PG2 and SCS is that the sample sees the entire SASE-spectrum at once. Instead of extracting a small part of the spectrum upstream of the sample, the full spectrum is analyzed downstream of the sample using the spectrometer of the MUSIX endstation [9]. This allows for a parallel acquisition and makes the use of a monochromator beamline unnecessary. The lack of a monochromator also implies a greater, broadband flux on the sample, which for the case of linear spectroscopy mostly affects considerations of the damage threshold, but becomes highly relevant in non-linear spectroscopy, as is discussed at length in the next chapter.

The other significant difference is the reflection configuration: Instead of transmitting one of the beams through a sample film, both beams were reflected from a sample film on a thick substrate. While in principle, the MUSIX endstation would also enable measurements in transmission, the reflection geometry was chosen for two major reasons (compare discussion above): First, a sample on a thick substrate is significantly more robust than a transmission film, as a locally deposited heat load can be transported away through more material, and a thin film carries the additional risk of tearing. Second, the direct XFEL beam being directed into the spectrometer necessitates careful control of the beam divergence and fluence, as beam damage to either the spectrometer grating or the CCD must be avoided under any circumstances. Adjusting the angle of reflection from the sample offers a straightforward method to tune the intensity impinging on the grating and CCD.

In a transmission setup, the reference beam can pass by the sample or be transmitted through an equivalent substrate, so that it provides a direct measure of the incident intensity. A consequence of combining a split-beam referencing scheme with a reflectivity geometry is that the reference beam must also be reflected somehow, and thus necessarily is also subjected to some reflection spectrum. For this reason, we initially attempted in [2] to use a second piece of material[5] next to the sample to reflect the reference beam from. However, a separate piece proved very challenging to install sufficiently co-planar with the sample to align both beams through the spectrometer. This led us to the configuration where both beams were reflected from the same sample, which was much easier to align reliably. As a downside, such a normalization cannot be used to normalize the absolute value of the absorbance, but only the difference between the signal and reference beams, which is the difference between the ground-state spectrum and the optically pumped spectrum. This turns out unproblematic for pump-probe measurements, where the difference between the ground-state and photo-excited spectra is precisely the quantity of interest. The ground-state spectrum can then either be

---

[5] Specifically MgO, which we selected because it also formed the sample substrate and has a relatively featureless spectrum near the Ni *L*-edges that we aimed to investigate.

measured at a synchrotron or in a longer FEL-measurement without normalization by relying on a constant long-term average of the SASE intensity. We demonstrate both below [2].

However, not being able to normalize in terms of absolute absorbance also affects the description of the measurement uncertainty, which both publications ([1, 2]) therefore discuss in different terms. To facilitate the comparison, I want to illustrate this difference in the following.

3.3.2.1 Comparing Measures of Uncertainty

Since the reference beam in the PG2-setup is a direct measure of the incident intensity, I was able to specify the relative error of the transmission measurement directly in the bottom panel of Figure 3.2, which reproduces Figure 3 of the publication [1]. In the FL24-setup, the discussion of measurement uncertainty is instead done in terms of the Fraction of Variance Unexplained (FVU), which is simply

$$FVU = 1 - \rho_{cc}, \tag{3.1}$$

where ρ_{cc} is the Pearson correlation coefficient, plotted in the top panel of Figure 3.2. In this case, ρ_{cc} describes how well the reflectivity measured by both beams is correlated over repeated measurements (details in the publication itself [2]). To provide further context and relate both the error discussions, in Figure 3.2 I show a breakdown of the error analysis of both publications, using the spectrum of 4-AminoAzoBenzene (AAB) recorded with the PG2-setup as example data.

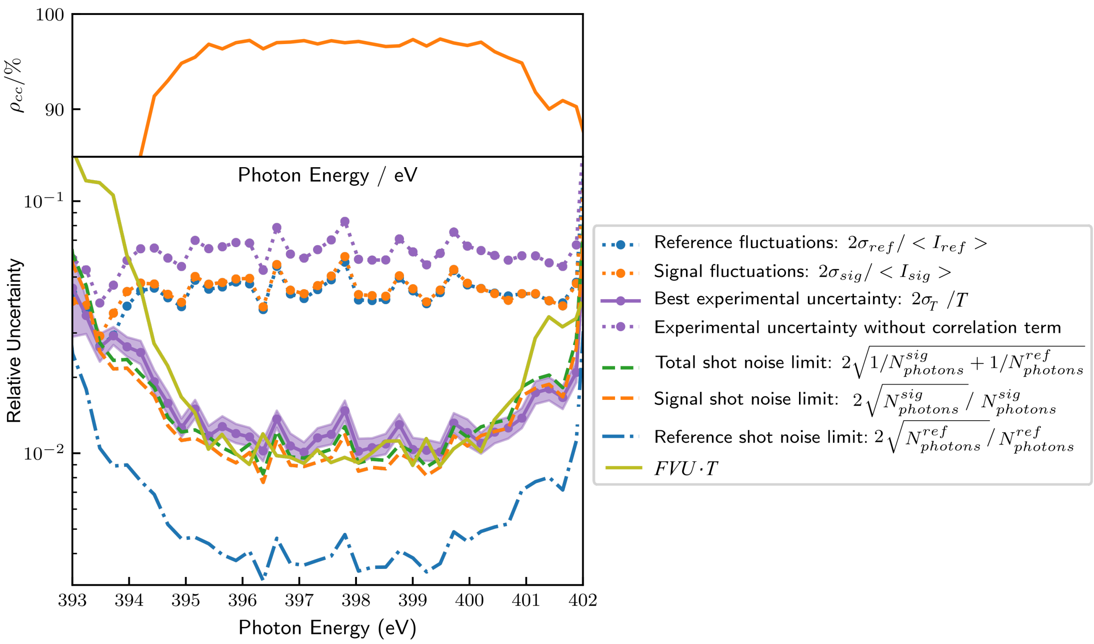

FIGURE 3.2: **Comparing different measures of uncertainty** using the example of the AAB spectrum shown in Figure 3 from [1].

The various measures of relative uncertainty shown in the main panel of Figure 3.2 are discussed below in the order shown in the legend, top to bottom. First, I show the relative fluctuations in the measured intensity of signal and reference (blue and orange dotted). This fluctuation constitutes the measurement uncertainty when a spectrum is measured by a single beam without normalization, but instead relying on the stability of the incident intensity in the long-term average.

At this point, it is worth briefly discussing that there are two obvious ways that one may compute the absorption spectrum when given a number of signal and reference intensity measurements for each photon energy. One may either compute the transmission (signal/reference ratio) for each shot and then compute the average transmittance, or one may first average all signal and reference intensities respectively, and then compute the ratio from these two averages. Both procedures deliver similar, but different results. I found in the analysis for [1] that the latter procedure delivers more reliable results; the comparison of the two procedures is also discussed in [8] with the same conclusion.

Under this procedure, the measurement uncertainty in terms of relative transmission is calculated according to Eq. 4 in [1], which I repeat here for the reader's convenience (brackets $\langle\rangle$ denote the mean over the ensemble):

$$\sigma_T = \left|\frac{\langle I_{sig}\rangle}{\langle I_{ref}\rangle}\right| \sqrt{\left(\frac{\sigma_{sig}}{\langle I_{sig}\rangle}\right)^2 + \left(\frac{\sigma_{ref}}{\langle I_{ref}\rangle}\right)^2 - \frac{2\sigma_{I_{sig}I_{ref}}}{\langle I_{sig}\rangle\,\langle I_{ref}\rangle}} \tag{3.2}$$

Its values are shown in Figure 3 of [1] and here in Figure 3.2, relative to the absolute transmission (purple line with dots and shaded region representing 95.4 % Confidence Interval (CI)). This calculation accounts for the fluctuations of the two measured intensities. Here, the fact that they fluctuate together greatly reduces the uncertainty of the measurement, which is described by the covariance term in Eq. 3.2. Note that the covariance $\sigma_{I_{ref}I_{sig}}$ is the un-normalized form of the correlation coefficient:

$$\rho_{cc} = \frac{\sigma_{I_{ref}I_{sig}}}{\sigma_{I_{ref}}\sigma_{I_{sig}}} \tag{3.3}$$

I also show the same estimate of uncertainty of the transmission calculated without the covariance term (purple dotted line) to emphasize the importance of considering the correlation between both intensity measurements. The correlation must be evaluated for every bin in the spectrum and is also shown in the top panel of Figure 3.2. Finally, I show the product of the FVU and the transmission T (yellow line), which behaves very similarly to the measurement uncertainty of T. While this does not demonstrate a rigorous relationship between the two quantities, it makes intuitive sense that the unexplained fraction of the measurement variation multiplied with the transmission is closely related to the relative uncertainty with which the transmission can be determined.

In the following publication, *Parallel Broadband Femtosecond Reflection Spectroscopy at a Soft X-Ray Free-Electron Laser*, we demonstrate the capability to record high-resolution X-ray reflectivity spectra utilizing the entire SASE-bandwidth of the XFEL using a split-beam normalization setup. We show that the split-beam normalization setup reduced the measurement uncertainty by about one order of magnitude and discuss how the reflectivity spectra can be utilized as a more practicable alternative to transmission spectra. Finally, we discuss the development of measurement uncertainty with acquisition times in the context of pump-probe studies with this setup. The publication is reproduced from [2], in accordance with the Creative Commons Attribution 4.0 license under which the article was published.

applied sciences

MDPI

Article

Parallel Broadband Femtosecond Reflection Spectroscopy at a Soft X-Ray Free-Electron Laser

Robin Y. Engel [1,2], Piter S. Miedema [1], Diego Turenne [3], Igor Vaskivskyi [3,4], Günter Brenner [1], Siarhei Dziarzhytski [1], Marion Kuhlmann [1], Jan O. Schunck [1,2], Florian Döring [5], Andriy Styervoyedov [6], Stuart S.P. Parkin [6], Christian David [5], Christian Schüßler-Langeheine [7], Hermann A. Dürr [3] and Martin Beye [1,2,*]

[1] Deutsches Elektronen Synchrotron, 22607 Hamburg, Germany; robin.engel@desy.de (R.Y.E.); piter.miedema@desy.de (P.S.M.); guenter.brenner@desy.de (G.B.); siarhei.dziarzhytski@desy.de (S.D.); marion.kuhlmann@desy.de (M.K.); jan.schunck@desy.de (J.O.S.)
[2] Department of Physics, University of Hamburg, 20355 Hamburg, Germany
[3] Department of Physics and Astronomy, Uppsala University, S-75120 Uppsala, Sweden; diego.turenne@physics.uu.se (D.T.); igor.vaskivskyi@physics.uu.se (I.V.); hermann.durr@physics.uu.se (H.A.D.)
[4] Center for Memory and Recording Research, University of California San Diego, 9500 Gilman Drive, La Jolla, CA 92093-0401, USA
[5] Paul Scherrer Institut, 5232 Villigen-PSI, Switzerland; florian.doering@psi.ch (F.D.); christian.david@psi.ch (C.D.)
[6] Max-Planck Institut für Mikrostrukturphysik, Weinberg 2, 06108-06132 Halle, Germany; andriy.styervoyedov@mpi-halle.mpg.de (A.S.); stuart.parkin@mpi-halle.mpg.de (S.S.P.P.)
[7] Helmholtz-Zentrum Berlin für Materialien und Energie GmbH, 12489 Berlin, Germany; christian.schuessler@helmholtz-berlin.de
* Correspondence: martin.beye@desy.de

Received: 15 September 2020; Accepted: 2 October 2020; Published: 4 October 2020

check for updates

Featured Application: Exploiting the full flux and temporal resolution of SASE-FELs for highly sensitive X-ray absorption measurements.

Abstract: X-ray absorption spectroscopy (XAS) and the directly linked X-ray reflectivity near absorption edges yield a wealth of specific information on the electronic structure around the resonantly addressed element. Observing the dynamic response of complex materials to optical excitations in pump–probe experiments requires high sensitivity to small changes in the spectra which in turn necessitates the brilliance of free electron laser (FEL) pulses. However, due to the fluctuating spectral content of pulses generated by self-amplified spontaneous emission (SASE), FEL experiments often struggle to reach the full sensitivity and time-resolution that FELs can in principle enable. Here, we implement a setup which solves two common challenges in this type of spectroscopy using FELs: First, we achieve a high spectral resolution by using a spectrometer downstream of the sample instead of a monochromator upstream of the sample. Thus, the full FEL bandwidth contributes to the measurement at the same time, and the FEL pulse duration is not elongated by a monochromator. Second, the FEL beam is divided into identical copies by a transmission grating beam splitter so that two spectra from separate spots on the sample (or from the sample and known reference) can be recorded in-parallel with the same spectrometer, enabling a spectrally resolved intensity normalization of pulse fluctuations in pump–probe scenarios. We analyze the capabilities of this setup around the oxygen *K*- and nickel *L*-edges recorded with third harmonic radiation of the free electron laser in Hamburg (FLASH), demonstrating the capability for pump–probe measurements with sensitivity to reflectivity changes on the per mill level.

Keywords: X-ray absorption spectroscopy; free electron laser; intensity normalization; transmission grating; X-ray reflectivity

---

1. Introduction

X-ray absorption spectroscopy (XAS) is a common method for characterizing materials in a variety of fields due to its fundamental simplicity, flexibility and element-specificity. Tuning to absorption edges allows probing the unoccupied electronic states localized around specific elements. Although experimentally more challenging, this information content is especially high at the absorption edges in the soft X-ray regime [1], since core hole lifetimes are longer and spectral features sharper than at higher photon energies. In a pump–probe experiment with sufficiently short pulses, e.g., in free electron lasers (FELs), transient XAS can be used to track changes of the electronic structure during chemical reactions and phase transitions on the femtosecond (fs) to picosecond (ps) scale [2–4].

XAS measures the spectral absorption coefficient, i.e., the imaginary part of the index of refraction. Measurements in specular reflectivity additionally measure the real part of the refractive index, which is rigorously connected with the imaginary part, through the Kramers–Kronig transform [5]. Thus, the same spectroscopic information is transported [6]. The most straightforward method of measuring XAS is in transmission by monitoring the intensity of an incident and the transmitted monochromatic beam as a function of photon energy. However, short absorption lengths in the soft X-ray regime necessitate sub-μm thin samples, which can be a prohibitive limitation in terms of properties and manufacturability of the sample. Therefore, XAS is often performed indirectly, by observing either electron yield or drain current resulting from the photoelectric effect or the fluorescence yield. Each of these methods has advantages and disadvantages. Broadly speaking, electron-based methods constitute a powerful approach but limit the obtained information to the surface region and suffer from space-charge and capacitance effects when implemented with intense pulsed sources. Fluorescence based methods are free of such charge effects but struggle from low signal levels in the soft X-ray regime, as the Auger process is dominant and suppresses radiative decay. Furthermore, additional selection rules constraining fluorescent decay as well as competing fluorescence channels can lead to deviations in the spectra that can only be fully interpreted and disentangled [7–9] after spectral analysis of the isotropically emitted fluorescence from the sample, using a spectrometer. As in the soft X-ray regime, spectrometers operate with gratings at grazing incidence angles, such spectrometers exhibit small solid acceptance angles, strongly reducing the overall detected signal. Therefore, although a multitude of these methods are applied with great success at synchrotron sources, performing XAS studies at FEL facilities [2,10,11] remains challenging. Another challenge particular to FELs, is the stochastic nature of radiation from the self-amplified spontaneous emission (SASE) process on which most FELs rely (except those that implement seeding). The X-ray pulses produced by the SASE process exhibit a number of Fourier-limited modes of random intensity, which are randomly distributed within overall pulse durations typically on the order of 50 fs and a spectral bandwidth of typically 0.5–1% [12]. Using a monochromator to gain higher spectral resolution enhances the strong intensity fluctuations of the resulting beam and discards a significant part of the incoming flux. For XAS measurements, this means that the incident flux cannot be approximated as constant, but must be measured with the same fidelity, sensitivity and dynamic range as the signal. Furthermore, monochromators can significantly elongate the FEL pulse duration due to grating induced pulse-front tilting, which scales with the number of illuminated grating lines and is thus especially severe (up to a picosecond) at very high spectral resolutions.

Here, we demonstrate the use of a transmission grating beam-splitter to split the FEL into practically identical signal and reference beams, both of which are analyzed in-parallel with the same spectrometer after interaction with the sample. Thus, both FEL fluctuations, as well as possible nonlinearities in the detector are exactly reproduced in both signals and can thus be renormalized.

Unlike comparable schemes with monochromatic beams [13–16], our method places the grating for spectral analysis after the sample interaction, so that the full SASE bandwidth contributes to the measurement. For a given FEL fluence on the sample, measuring the collimated specular reflection as opposed to isotropic fluorescence provides much stronger signals. The signal intensity can even be tuned by adjusting the angle of incidence to optimally exploit the detector dynamic range, since varying the angle will generally alter the spectral shape but not change the spectroscopic information. Here, we analyze the sensitivity of this experimental scheme for spectral (e.g., pump-induced) changes by evaluating pairs of simultaneously recorded reflectivity spectra of NiO at the oxygen *K*- and nickel $L_{2,3}$-edges, respectively.

2. Experimental Design

A simplified schematic of the setup is shown in Figure 1. Measurements were performed with the MUSIX experimental end station [17] at the FL24 beam line of the free-electron laser in Hamburg (FLASH). The FEL was tuned to generate third harmonic radiation around the oxygen *K*- and nickel $L_{2,3}$-edges (from 506 eV to 566 eV and 842 eV to 887 eV, respectively), producing bursts of 40 pulses with 10 µs spacing within the burst and 10 bursts per second. Before the beam line, the beam is defined by two apertures: 5 mm apertures are used at the O *K*-edge and 2 mm apertures at the Ni *L*-edges. Then, the average FEL pulse energy was monitored using the signal from an X-ray gas monitor detector (XGMD) [18], after which the fundamental radiation was suppressed by a 13 meter long gas attenuator unit containing 9.7×10^{-2} mbar of neon (O *K*-edge) or 1.7×10^{-2} mbar of krypton (Ni *L*-edges) in addition to two Si membrane filters of 401 nm and 200 nm thickness.

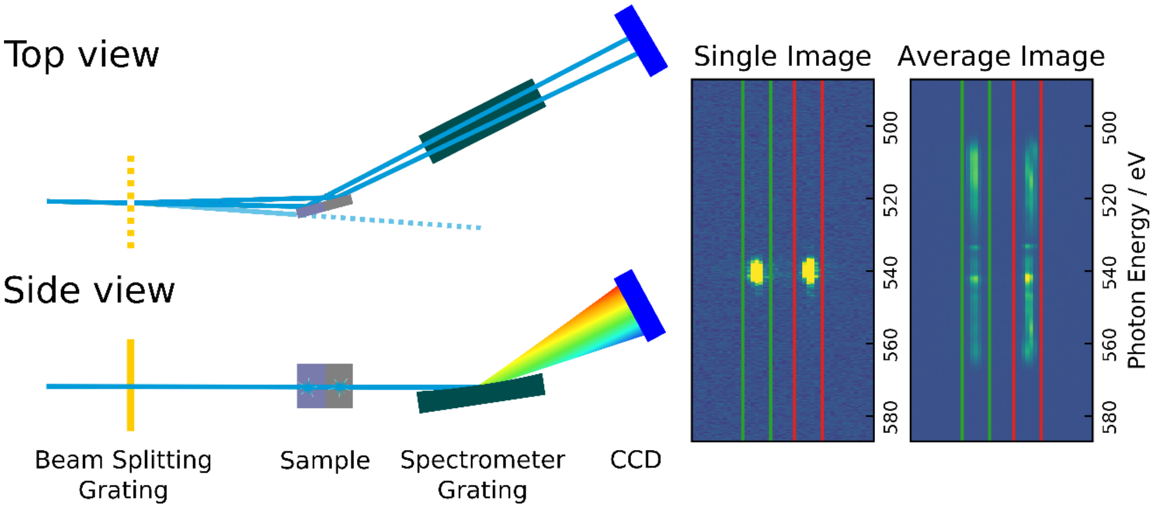

Figure 1. Schematic setup Experimental setup at the FL24 beam line of the free electron laser in Hamburg (FLASH) (left) and exemplary detector images (right). The free electron laser (FEL) beam is initially transmitted through a beam splitting grating, optimized for high intensity in the first diffraction orders. The zeroth and one of the first diffraction orders are then focused onto the sample with a vertical focal size of about 35 µm at a grazing incidence of 11.5 °. The specular reflection of both beams is directed onto the variable line spacing diffraction grating of the spectrometer and dispersed onto a charge-coupled device (CCD). Since the spectrometer disperses both beams orthogonally to the beam separation, the two beams yield separate spectra on the detector. The green and red lines mark the regions of interest in which spectral intensity is integrated and correspond to the spectra in Figure 2a. 1208 single images are averaged while the undulators are scanned across the O *K*-edge with both beams on the NiO sample. The average image shows the spectral structure within the scanned spectral interval.

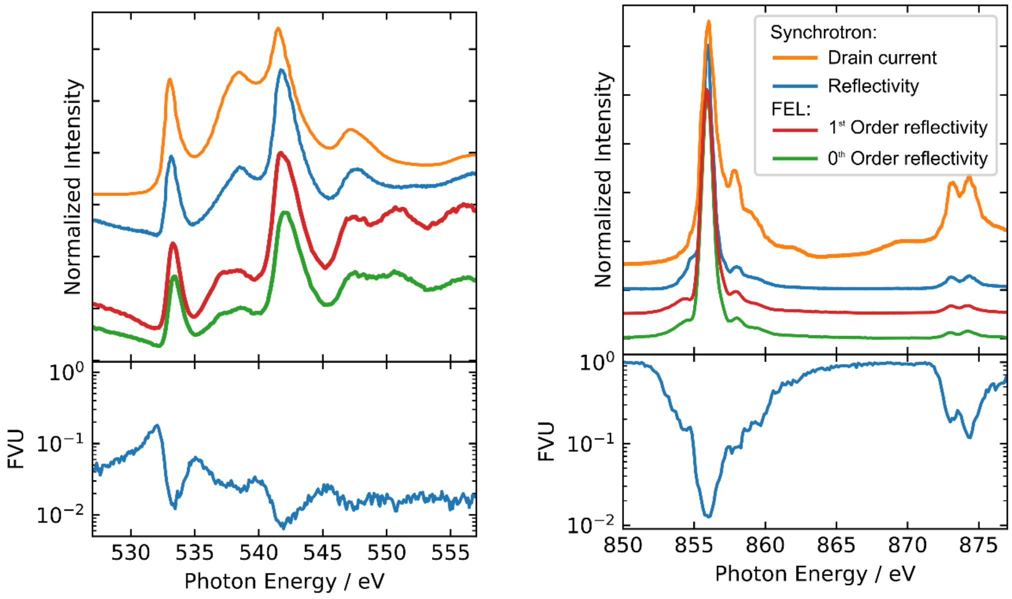

(**a**) (**b**)

Figure 2. Reflectivity spectra pairs (red and green) recorded in-parallel at FLASH including the spectrally resolved fraction of variance unexplained (FVU) between the FEL spectra. Reflectivity (blue) and drain current (orange) spectra recorded at a synchrotron are given for comparison. The FEL spectra, each pair acquired within 4 minutes, are normalized so that their relative intensity is conserved. A constant shift in photon energy is applied to match the calibration of the synchrotron spectra. Reference spectra are recorded from the same samples at the beam line PM3 of BESSY II. (**a**) Oxygen *K*-edge. Additional structure from water residue on the surface contributes additional intensity, mostly to the high energy side (>545 eV) of the spectra since the samples were exposed to air before both FEL and synchrotron measurements. (**b**) Ni L_3-and L_2-edges.

The beam is then split horizontally by a transmission grating of 3.8 mm height and 0.9 mm width, optimized to produce similar intensity in the zeroth and first diffraction orders: It is made from a Si-membrane of 1.1 µm thickness with rectangular grooves of 960 nm depth and 7.9 µm period at 50% aspect ratio. The zeroth and first diffraction orders are each directed onto the sample, focused by bendable mirrors to a spot of about 35 µm height and 80 µm width, at a grazing angle θ of 11.5°. The specular reflections of both beams are analyzed by the spectrometer of the MUSIX endstation [17], consisting of a variable line spacing grating and an in-vacuum charge-coupled device (CCD) (GreatEyes Model GE-VAC 2048 2048). The 13.5 µm square pixels of the CCD were read out with an ADC clocked with 3 MHz in high gain mode and 16 pixel binning orthogonal to the spectral axis to increase the frame rate and decrease noise while preserving the spectral resolution. This resulted in a framerate of 5 Hz. The FEL, producing bursts of 10 Hz, was chopped accordingly, so that each detector image represented an average over one burst of 40 pulses. The photon energy dispersion on the CCD was measured as 10.73 pixel/eV at the O *K*-edge and 7.8 pixel/eV at the Ni *L*-edges.

Samples consisted of epitaxial NiO films of 40 nm thickness, grown on MgO(001) substrates. A 2 nm thick MgO underlayer was deposited by radio frequency magnetron sputtering in 3 mTorr argon at a temperature below 100 °C followed by a NiO layer that was deposited at 700 °C in an Ar (90%)/O_2 (10%) gas mixture at a pressure of 3 mTorr and was then annealed in-situ at the same temperature (700 °C) for 15 min in the same Ar-O_2 gas mixture.

To acquire spectra within a wider window than the 0.5–1% natural bandwidth of the FEL, the photon energy is scanned in steps of 0.75 eV by varying the undulator gap. As datasets include multiple scans over the desired range, data taken at the same undulator settings are averaged in the data analysis. Two spectra are extracted from each image by integration along the non-dispersive direction of the CCD within manually selected regions of interest such as indicated in Figure 1. Before computing the average spectrum, each single-image spectrum was cropped to the range deviating less than 1 % from the FEL photon energy set-point, as no significant intensity is found outside this window.

3. Results and Discussion

To understand the benefits of acquiring two spectra in-parallel, we consider the measured spectral intensity on the detector $S(\omega)$, which depends on the photon frequency ω for each beam, to be proportional to the spectral reflectivity $R(\omega)$ of the sample, the diffraction efficiency O of the beam-splitting grating in the zeroth or first order and the spectral intensity $I(\omega)$ of the FEL:

$$S_1(\omega) \propto R_1(\omega) O_1 I(\omega) S_2(\omega) \propto R_2(\omega) O_0 I(\omega) \tag{1}$$

It is apparent that the measured spectrum $S(\omega)$ of a single beam can be used to measure the reflected spectrum $R(\omega)$, if the FEL intensity $I(\omega)$ is either known or constant. If many pulses are averaged, SASE fluctuations average out, but potential slow drifts of the average pulse energy remain. Since the third harmonic radiation intensity scales roughly with the square of the fundamental [17], slow fluctuations are mitigated by normalizing each spectrum with the square intensity measured by the XGMD which monitors the fundamental radiation of the FEL further upstream. This leads to the FEL spectra shown in Figure 2a,b, each pair was measured in-parallel using 10^5 SASE pulses within four minutes. Synchrotron spectra of reflectivity and drain current recorded on the same sample with a similar angle of incidence ($\theta = 11°$ for the O K-edge, $\theta = 12°$ for the Ni $L_{2,3}$-edges) are shown for comparison and demonstrate a good agreement to the FEL spectra. The FEL-reflectivity spectra recorded at these angles reproduce the relevant structures of the drain current absorption spectra. We ascribe the minor differences to sample inhomogeneity and the difference of the incident angle. Especially the O K-edge spectra also show signs of surface contamination with water (especially the structure above 545 eV), as the sample was exposed to air both before and between FEL and synchrotron measurements. In the following, we analyze how accurate changes in one spectrum due to FEL fluctuations can be used to measure the changes in the other spectrum. Our main motivation for recording two spectra in-parallel is to exploit one of them as a spectrally resolved intensity reference in a pump–probe scenario. In this case, a crucial parameter is the precision with which (pump-induced) changes in one spectrum may be determined from the other. The fraction of fluctuation that cannot be explained from the variations in the reference spectrum is quantified by the so-called fraction of variance unexplained (FVU). The FVU for a set of N pairs of spectra equal unity minus the coefficient of determination r^2 between both spectra, which is in this case, the square of the Pearson correlation coefficient r:

$$r(\omega) = \frac{\sum_{i=1}^{N}\left(S_1^i(\omega) - \overline{S}_1(\omega)\right)\left(S_2^i(\omega) - \overline{S}_2(\omega)\right)}{\sqrt{\sum_{i=1}^{N}\left(S_1^i(\omega) - \overline{S_1}(\omega)\right)^2}\sqrt{\sum_{i=1}^{N}\left(S_2^i(\omega) - \overline{S_2}(\omega)\right)^2}} \tag{2}$$

$$FVU = 1 - r^2 \tag{3}$$

Here, $\overline{S}$ denotes the average spectrum over the set. We find that minor alignment imperfections and pointing drifts can lead to a small offset along the dispersive direction of the detector between two simultaneously recorded spectra. Similar to previous work [15], this offset is determined by shifting the reference spectrum along the dispersive axis (see Appendix A for details) such that the logarithmic FVU, integrated over the entire spectrum, is minimized. The offset is determined in this way for every measurement (each in the order of several minutes) separately, yielding a shift between one and three pixels, i.e., some tens of µm on the CCD detector. The optimized spectrally resolved FVU is shown in Figure 2 and reproduces the structure of the spectrum as it scales inversely with the reflected intensity. The scaling of the FVU with intensity is shown in Figure 3a and is compared to a simulation of the FVU which may be expected from of a Poisson-distributed noise process, scaling with the square root of the intensity like a photon shot noise (orange), and an additional normally-distributed noise process with constant variance like readout noise (green). Since the fast readout of the CCD prevented a calibration of the sensitivity from single-photon incidences, the number of photons per detector count was estimated based on the assumption that the noise level at high intensities is dominated by photon shot noise, as was found in a similar setup before [15]. This assumption is supported by the scaling behavior shown in Figure 3a and is in rough agreement with the manufacturer specifications of the CCD.

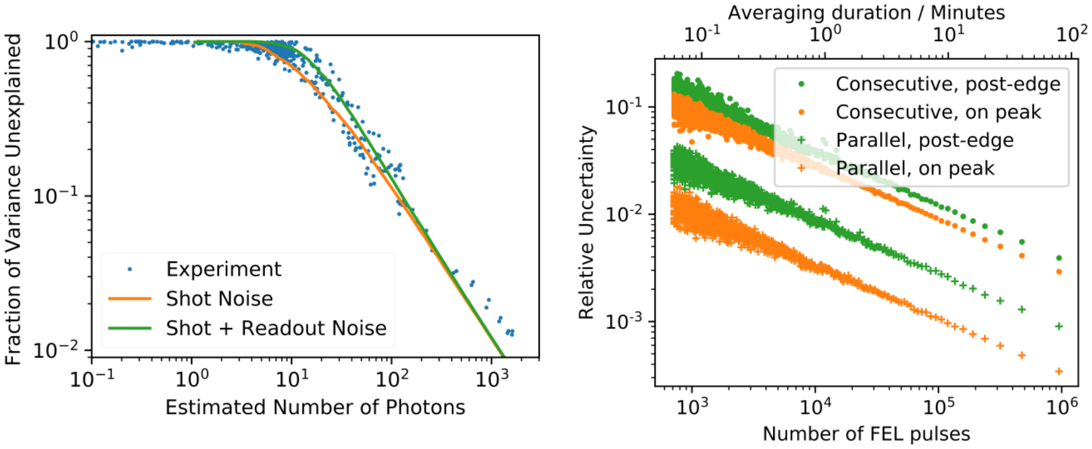

(**a**) (**b**)

Figure 3. Evaluations of the setup sensitivity: (**a**) The fraction of variance unexplained, (FVU, see Equation 3) between the two FEL-spectra shown in Figure 2b plotted against intensity, given as an estimated number of detected photons within a given spectral interval. We show experimental data points (blue) along with a simulation that accounts for photon shot noise only (orange), as well as additionally including a Gaussian readout noise contribution (green). (**b**) Uncertainty to spectral changes, such as pump–probe effects, considering two methods of acquisition. The plot shows the uncertainty of the average ratio between intensities at the Ni L_3-edge (orange) and 1 eV beyond the edge (green, each within a 245 meV window), measured with the FEL photon energy at the L_3-edge. The uncertainty for parallel acquisition (crosses) considers the correlation between the two intensities and thus, yields an order of magnitude lower uncertainties for this measurement mode. The consecutive acquisition uncertainty (circles) is calculated from the same data, assuming no correlation between the intensity fluctuations.

Figure 3b further illustrates the uncertainty with which the ratio between the reflectivity probed by both beams may be determined with increasing acquisition time. This uncertainty is the precision with which pump–probe changes in one spectrum could be detected. To this purpose, the undulators are tuned to the Ni L_3-edge. Without scanning the undulators, the ratio between the intensities in both spectra was evaluated. Two exemplary regions in the spectra were analyzed: First, a 245 meV region around the L_3-edge peak at 857 eV (corresponding to two rows on the detector). Second, an equally sized window from the same dataset was evaluated 1 eV above the peak, where the detected intensity was lower by about a factor of nine on average, due to both the lower reflectivity and the FEL being tuned to the L_3-edge. The plot shows the relative uncertainty with which the ratio may be determined for increasingly larger subsets of CCD images, randomly drawn (without replacing) from an 80-min measurement. Two different measures for the uncertainty are shown: First, the uncertainty regarding the parallel acquisition, which considers that the correlation between the two intensities reduces the uncertainty for the estimator of the mean. This error propagation was discussed previously [15] and is reiterated in Appendix B. Second, the error is calculated under the assumption that the fluctuations of both intensities are uncorrelated, which would be the case if the spectra had been recorded consecutively instead of in-parallel.

4. Conclusions

As demonstrated in Figure 3b, the acquisition of two spectra in-parallel merits about one order of magnitude of sensitivity compared to consecutive acquisition. Spectral changes can be monitored within the entire FEL bandwidth at the same time. The sensitivity in the middle of the FEL spectrum reaches a 10^{-3} relative reflectivity change within about 10 min of acquisition for a 245 meV window. The reflectivity spectra acquired in this way reproduce the features of conventional X-ray absorption spectra, so that equivalent information may be gained by pump–probe experiments in reflectivity. As the spectrometer grating analyzes the full reflected beams after sample interaction, the temporal resolution is not diminished by monochromatization. This makes the presented setup ideally suited for time resolved XAS and reflectivity studies in FELs.

Author Contributions: Conceptualization, P.S.M., C.S.-L., H.A.D. and M.B.; Data curation, R.Y.E., D.T. and I.V.; Formal analysis, R.Y.E.; Funding acquisition, H.A.D. and M.B.; Investigation, R.Y.E., P.S.M., D.T., I.V., G.B., S.D., M.K., H.A.D. and M.B.; Methodology, R.Y.E., F.D., C.D., C.S., H.A.D. and M.B.; Project administration, M.B.; Resources, F.D., Stuart S.P. Parkin, C.D., C.S.-L., H.A.D. and M.B.; Software, R.Y.E. and A.S.; Supervision, M.B.; Validation, M.B.; Visualization, R.Y.E.; Writing—original draft, R.Y.E.; Writing—review and editing, R.Y.E., J.O.S., C.S.-L., H.A.D. and M.B. All authors have read and agreed to the published version of the manuscript.

Funding: M.B., P.S.M., J.O.S. and R.Y.E. received funding from the Helmholtz Association through grant VH-NG-1105. IV acknowledges support by the U.S. Department of Energy, Office of Science, Office of Basic Energy Sciences under the X-Ray Scattering Program Award Number DE-SC0017643. Work at UU was supported by the Swedish Research Council (VR) grants 2017-06711 and 2018-04918. F.D. received funding from the EU-H2020 Research and Innovation Programme under the Marie Skłodowska-Curie grant agreement No. 701647.

Acknowledgments: We acknowledge DESY (Hamburg, Germany) and the Helmholtz-Zentrum Berlin, both members of the Helmholtz Association HGF, for the provision of experimental facilities. FEL measurements were carried out at the FL24 beam line of FLASH. Synchrotron measurements were carried out at the PM3 beam line of BESSY II, operated by HZB. The samples were prepared at the MPI-Halle by A.S. and S.S.P.P.

Conflicts of Interest: The authors declare no conflict of interest. The funders had no role in the design of the study; in the collection, analyses, or interpretation of data; in the writing of the manuscript, or in the decision to publish the results.

Appendix A

Shifting spectra with sub-pixel accuracy was achieved by resampling the spectrum with a 100-fold frequency using the resample function of the python library scipy [19]. A Gaussian window function with a width of half the number of points in the original spectrum was applied to suppress high-frequency components arising in the oversampling process. The oversampled spectra were then shifted by an integer number of points, such that the logarithmic FVU is minimized. Finally, the spectrum is resampled back to the original spectral axis using the same resample function.

Appendix B

The uncertainty of the expectation value of the ratio between two spectral intensities which were measured in-parallel, i.e., not independent of each other, can be propagated as follows.

$$\sigma_T = \left|\frac{\langle I_2\rangle}{\langle I_1\rangle}\right| \sqrt{\left(\frac{\sigma_2}{\langle I_2\rangle}\right)^2 + \left(\frac{\sigma_1}{\langle I_1\rangle}\right)^2 - \frac{2\,\sigma_{I_2 I_1}}{\langle I_2\rangle\langle I_1\rangle}}$$

Here, σ_1 and σ_2 represent the uncertainty of the expectation value (i.e., the standard deviation divided by the square root of the number of measurements) for the intensities I_1 and I_2 and $\sigma_{I_2 I_1}$ is the covariance between both. Brackets $\langle\ \rangle$ denote the ensemble mean value.

References

1. Himpsel, F.J. Photon-in photon-out soft X-ray spectroscopy for materials science. *Phys. Status Solidi Basic Res.* **2011**, *248*, 292–298. [CrossRef]

2. Wernet, P.; Kunnus, K.; Josefsson, I.; Rajkovic, I.; Quevedo, W.; Beye, M.; Schreck, S.; Grübel, S.; Scholz, M.; Nordlund, D.; et al. Orbital-specific mapping of the ligand exchange dynamics of Fe(CO)$_5$ in solution. *Nature* **2015**, *520*, 78–81. [CrossRef] [PubMed]
3. Bressler, C.; Milne, C.; Pham, V.T.; Elnahhas, A.; Van Der Veen, R.M.; Gawelda, W.; Johnson, S.; Beaud, P.; Grolimund, D.; Kaiser, M.; et al. Femtosecond XANES study of the light-induced spin crossover dynamics in an iron(II) complex. *Science* **2009**, *323*, 489–492. [CrossRef] [PubMed]
4. Cavalleri, A.; Rini, M.; Chong, H.H.W.; Fourmaux, S.; Glover, T.E.; Heimann, P.A.; Kieffer, J.C.; Schoenlein, R.W. Band-selective measurements of electron dynamics in VO2 using femtosecond near-edge X-ray absorption. *Phys. Rev. Lett.* **2005**, *95*, 067405. [CrossRef] [PubMed]
5. Watts, B. Calculation of the Kramers-Kronig transform of X-ray spectra by a piecewise Laurent polynomial method. *Opt. Express* **2014**, *22*, 23628. [CrossRef] [PubMed]
6. Alders, D.; Hibma, T.; Sawatzky, G.A.; Cheung, K.C.; van Dorssen, G.E.; Roper, M.D.; Padmore, H.A.; van der Laan, G.; Vogel, J.; Sacchi, M. Grazing incidence reflectivity and total electron yield effects in soft x-ray absorption spectroscopy. *J. Eng. Appl. Sci.* **1997**, *82*, 3120–3124. [CrossRef]
7. Miedema, P.S.; Beye, M. Total 3s Emission Yield as Bulk-Sensitive Probe for a True Soft X-ray Absorption Spectrum? *J. Phys. Chem. Lett.* **2018**, *9*, 2579–2583. [CrossRef] [PubMed]
8. Miedema, P.S.; Wernet, P.; Föhlisch, A. State-dependent fluorescence yields through the core-valence Coulomb exchange parameter. *Phys. Rev. A At. Mol. Opt. Phys.* **2014**, *89*, 052507. [CrossRef]
9. de Groot, F.M.F.; Arrio, M.A.; Sainctavit, P.; Cartier, C.; Chen, C.T. Fluorescence yield detection: Why it does not measure the X-ray absorption cross section. *Solid State Commun.* **1994**, *92*, 991–995. [CrossRef]
10. Mitzner, R.; Rehanek, J.; Kern, J.; Gul, S.; Hattne, J.; Taguchi, T.; Alonso-Mori, R.; Tran, R.; Weniger, C.; Schröder, H.; et al. L-edge x-ray absorption spectroscopy of dilute systems relevant to metalloproteins using an x-ray free-electron laser. *J. Phys. Chem. Lett.* **2013**, *4*, 3641–3647. [CrossRef] [PubMed]
11. Loh, Z.H.; Doumy, G.; Arnold, C.; Kjellsson, L.; Southworth, S.H.; Al Haddad, A.; Kumagai, Y.; Tu, M.F.; Ho, P.J.; March, A.M.; et al. Observation of the fastest chemical processes in the radiolysis of water. *Science* **2020**, *367*, 179–182. [CrossRef] [PubMed]
12. Saldin, E.L.; Schneidmiller, E.A.; Yurkov, M.V. Statistical properties of the radiation from VUV FEL at DESY operating at 30 nm wavelength in the femtosecond regime. *Nucl. Instruments Methods Phys. Res. Sect. A Accel. Spectrometers Detect. Assoc. Equip.* **2006**, *562*, 472–486. [CrossRef]
13. Schlotter, W.F.; Beye, M.; Zohar, S.; Coslovich, G.; Dakovski, G.L.; Lin, M.-F.; Liu, Y.; Reid, A.; Stubbs, S.; Walter, P.; et al. Balanced Detection in Femtosecond X-ray Absorption Spectroscopy to Reach the Ultimate Sensitivity Limit. *arxiv* **2020**, arXiv:2006.13968.
14. Katayama, T.; Inubushi, Y.; Obara, Y.; Sato, T.; Togashi, T.; Tono, K.; Hatsui, T.; Kameshima, T.; Bhattacharya, A.; Ogi, Y.; et al. Femtosecond x-ray absorption spectroscopy with hard x-ray free electron laser. *Appl. Phys. Lett.* **2013**, *103*, 131105. [CrossRef]
15. Engel, R.Y.; Ekimova, M.; Miedema, P.S.; Kleine, C.; Ludwig, J.; Ochmann, M.; Grimm-lebsanft, B.; Ma, R.; Teubner, M.; Dziarzhytski, S.; et al. Shot noise limited soft X-ray absorption spectroscopy in solution at a SASE-FEL using a transmission grating beam splitter. *Struct. Dyn.* **2020**. (submitted).
16. Brenner, G.; Dziarzhytski, S.; Miedema, P.S.; Rösner, B.; David, C.; Beye, M. Normalized single-shot X-ray absorption spectroscopy at a free-electron laser. *Opt. Lett.* **2019**, *44*, 2157. [CrossRef] [PubMed]
17. Beye, M.; Engel, R.Y.; Schunck, J.O.; Dziarzhytski, S.; Brenner, G.; Miedema, P.S. Non-linear soft x-ray methods on solids with MUSIX-The multi-dimensional spectroscopy and inelastic x-ray scattering endstation. *J. Phys. Condens. Matter* **2019**, *31*. [CrossRef] [PubMed]
18. Sorokin, A.A.; Bican, Y.; Bonfigt, S.; Brachmanski, M.; Braune, M.; Jastrow, U.F.; Gottwald, A.; Kaser, H.; Richter, M.; Tiedtke, K. An X-ray gas monitor for free-electron lasers. *J. Synchrotron Radiat.* **2019**, *26*, 1092–1100. [CrossRef] [PubMed]
19. Virtanen, P.; Gommers, R.; Oliphant, T.E.; Haberland, M.; Reddy, T.; Cournapeau, D.; Burovski, E.; Peterson, P.; Weckesser, W.; Bright, J.; et al. SciPy 1.0: Fundamental algorithms for scientific computing in Python. *Nat. Methods* **2020**, *17*, 261–272. [CrossRef] [PubMed]

3.3.3 The Pump-Probe Scheme

Pump-probe-schemes are very common and fruitfully employed at XFELs to study dynamics of samples on a femto- to picosecond time scale [20, 21, 36–47, 199]. A first electromagnetic pulse (which can have photon energies anywhere from terahertz radiation to X-rays) is used to excite the sample, and a second XFEL pulse is used to probe its momentary state at a fixed time-delay after the excitation occurred. The fluence of the probe pulse should be limited to avoid non-parametric non-linear absorption, so that the measured effects can be fully attributed to the influence of the pump. Further, the total absorbed fluence of pump and probe together must be weighed against the repetition rate of the experiment to ensure that the system fully returns to the ground state between pulse pairs. The time resolution of such an experiment is determined by the convolution of the two temporal pulse profiles in addition to the pulse-to-pulse fluctuations in the relative arrival time of the pulses (temporal jitter).[6] Given a sufficiently high temporal resolution, such studies make it possible to disentangle electronic excitations from those that involve nuclear motion by analyzing the time scale on which the excitation appears after the initial absorption.

3.3.3.1 Broadband Split-Beam Normalization in a Pump-Probe Experiment

The third and final publication in this chapter is a study exploiting the above-described setup at FL24 using MUSIX for a pump-probe experiment. In contrast to the previous two technical publications, the subject of the following study, *Ultrafast manipulation of the NiO antiferromagnetic order via sub-gap optical excitation*, is the response of NiO to excitation by an infrared pulse. We observed optically induced changes in the X-ray reflectivity spectrum at the nickel $L_{2,3}$- and oxygen K-edges. As discussed in the publication below, we found evidence that the optical excitation couples strongly to the antiferromagnetic spin system and likely occurs via transient mid-gap states. Subsequently, we observe a temperature rise of the spin system, which reaches a thermalized state after about 400 fs; at this point the XMLD lineshape at the L_2-edge matched (via the aforementioned transformation using Fresnel and Kramers-Kronig relations) spectra from published literature that were recorded at $65 \pm 5\,\mathrm{K}$ above room temperature. We further observed an oscillation of the upper band edge in the O K-edge spectra with a frequency of about 1 THz, corresponding to an out-of-plane magnon mode in NiO; the appearance of the magnon in the O K-edge spectrum is interpreted with the help of first-principles calculations, relating the magnonic spin precession to an oscillating shift in the O $2p$ states which define the upper band edge.

Given the topic of this chapter, I want to highlight a technical aspect that is only briefly discussed in the paper below: In the online analysis during the pump-probe measurements for this study, we made the observation that the two spectra acquired in parallel over time were in fact not perfectly matched, and - even worse - changed slightly over time. We connected the reason for this drift tentatively to sample inhomogeneity in connection with beam-pointing drifts as well as the possibility of a slow buildup of sample damage from the optical laser. Either way, a time-dependence of one or both reflection spectra makes the normalization methods described above ineffective or at the very least, imprecise.

---

[6] More precisely, the uncertainty with which the relative arrival times are known or measured is what contributes to the temporal resolution.

This leads us to extend the normalization scheme to account for slow changes in the reflectivity of both beams. This requires a comparison of the reflectivity seen by both beams when both are undisturbed by the optical laser. Thus, we blocked every fourth shot of the pump laser using a mechanical shutter. The resulting data set contains four measured intensities for each photon energy and each relative delay between optical and X-ray laser: The intensities of signal- and reference-beams from events where the pump laser was off, $I_{\text{sig}}^{\text{pump off}}$ and $I_{\text{ref}}^{\text{pump off}}$ as well as from those events when the pump laser was on, $I_{\text{sig}}^{\text{pump on}}$ and $I_{\text{ref}}^{\text{pump on}}$. The ratio of the "laser off"-intensities can be used to disentangle the reflectivity ratio of the "laser on"-intensities between changes caused by optical pumping and changes caused by sample inhomogeneity. Ultimately, we evaluated both the reflectivity ratio (in Figure 3 of the paper)

$$R_R = \frac{I_{\text{sig}}^{\text{pump on}}}{I_{\text{ref}}^{\text{pump on}}} \frac{I_{\text{ref}}^{\text{pump off}}}{I_{\text{sig}}^{\text{pump off}}}, \tag{3.4}$$

as well as the reflectivity difference (in Figures 2, 5, 6, and 8 of the paper)

$$\Delta R = I_{\text{sig}}^{\text{pump on}} - I_{\text{ref}}^{\text{pump on}} \frac{I_{\text{sig}}^{\text{pump off}}}{I_{\text{ref}}^{\text{pump off}}}. \tag{3.5}$$

The following publication is reproduced from [3] in accordance with the Creative Commons Attribution 3.0 Unported license under which the article was published originally.

Faraday Discussions

Cite this: DOI: 10.1039/d2fd00005a

PAPER

View Article Online
View Journal

Ultrafast manipulation of the NiO antiferromagnetic order *via* sub-gap optical excitation

Xiaocui Wang,[a] Robin Y. Engel,[bc] Igor Vaskivskyi,[d] Diego Turenne,[a] Vishal Shokeen,[a] Alexander Yaroslavtsev,[a] Oscar Grånäs,[a] Ronny Knut,[a] Jan O. Schunck,[bc] Siarhei Dziarzhytski,[b] Günter Brenner,[b] Ru-Pan Wang,[c] Marion Kuhlmann,[b] Frederik Kuschewski,[b] Wibke Bronsch,[e] Christian Schüßler-Langeheine,[f] Andriy Styervoyedov,[g] Stuart S. P. Parkin,[g] Fulvio Parmigiani,[e] Olle Eriksson,[a] Martin Beye[bc] and Hermann A. Dürr*[a]

Received 10th January 2022, Accepted 15th February 2022

DOI: 10.1039/d2fd00005a

Wide-band-gap insulators such as NiO offer the exciting prospect of coherently manipulating electronic correlations with strong optical fields. Contrary to metals where rapid dephasing of optical excitation *via* electronic processes occurs, the sub-gap excitation in charge-transfer insulators has been shown to couple to low-energy bosonic excitations. However, it is currently unknown if the bosonic dressing field is composed of phonons or magnons. Here we use the prototypical charge-transfer insulator NiO to demonstrate that 1.5 eV sub-gap optical excitation leads to a renormalised NiO band-gap in combination with a significant reduction of the antiferromagnetic order. We employ element-specific X-ray reflectivity at the FLASH free-electron laser to demonstrate the reduction of the upper band-edge at the O 1s–2p core–valence resonance (K-edge) whereas the antiferromagnetic order is probed *via* X-ray magnetic linear dichroism (XMLD) at the Ni 2p–3d resonance (L_2-edge). Comparing the transient XMLD spectral line shape to ground-state measurements allows us to extract a spin temperature rise of 65 ± 5 K for time delays longer than 400 fs while at earlier times a non-equilibrium spin state is formed. We identify transient mid-gap states being formed during the first 200 fs accompanied by a band-gap

---

[a] *Department of Physics and Astronomy, Uppsala University, 75120 Uppsala, Sweden. E-mail: hermann.durr@physics.uu.se*

[b] *Deutsches Elektronen-Synchrotron DESY, Notkestr. 85, 22607 Hamburg, Germany*

[c] *Department of Physics, Universität Hamburg, Luruper Chaussee 149, 22761 Hamburg, Germany*

[d] *Department for Complex Matter, Jozef Stefan Institute, Jamova cesta 39, 1000 Ljubljana, Slovenia*

[e] *Elettra-Sincrotrone Trieste S.C.p.A., 34149 Basovizza, Italy*

[f] *Helmholtz-Zentrum Berlin für Materialien und Energie, Albert-Einstein-Str. 15, 12489 Berlin, Germany*

[g] *Max-Planck Institut für Mikrostrukturphysik, Weinberg 2, 06120 Halle, Germany*

reduction lasting at least up to the maximum measured time delay of 2.4 ps. Electronic structure calculations indicate that magnon excitations significantly contribute to the reduction of the NiO band gap.

1 Introduction

Antiferromagnets (AFMs) have gained increasing interest and attention in both fundamental research and technological development. Since AFMs have zero net magnetization in their ground state, they are robust against external magnetic fields and have the promising potential to facilitate spintronic devices with ultrahigh speeds in the THz range.[1,2] Despite intense experimental studies and theoretical modelling efforts that have been dedicated to the coupling mechanisms between charge, spin and lattice degrees of freedom, the important interaction pathways remain elusive.

Owing to the development of ultrafast optical laser and free-electron laser (FEL) radiation sources that improve the temporal resolution even towards the few-femtosecond regime and the development of computing algorithms, scholars in this field have been able to unambiguously detect and model the complex dynamics in strongly correlated materials. With scattering techniques, using electrons,[3] X-ray photons[4] or neutrons,[5] one can investigate the ordering of the lattice or the AFM order. The diffraction signal of multiple-integer Bragg peaks is assigned to the structural re-arrangement, while the multiples of half-integer peaks are assigned to the magnetic ordering.[6] With spectroscopic techniques, one can study the electronic configurations with element specificity[7–9] and spin excitations in magnetic systems.[10]

Nickel oxide (NiO), as a prototype AFM, is a good candidate for studies in strongly correlated materials due to its well separated intra-gap states,[11] large spin density[5,12,13] and a high Néel temperature ($T_N \sim 523$ K).[7,14,15] Above T_N, NiO has a rock-salt structure (point group $Fm\bar{3}m$) with a lattice constant of 4.176 Å. Below T_N, the Ni^{2+} spins are ferromagnetically aligned along $\langle 11{-}2 \rangle$ directions within the (111) plane, and adjacent (111) planes are coupled antiferromagnetically, which composes two sublattice AFM systems. Due to exchange striction, the AFM ordering of the spins induces a small contraction along the $\langle 111 \rangle$ direction, resulting in a rhombohedral distortion of the crystalline structure. This distortion induces a reduction of the crystallographic symmetry from point group $Fm\bar{3}m$ of the cubic structure to point group $C2/m$ of the rhombohedral structure. Since there are four energetically degenerate $\langle 111 \rangle$ directions, the distortion can occur along any of the four equivalent directions. This results in four types of twin-domains (T-domain). For each T-domain, there are three possible spin orientations (S-domain). In total, there can be 12 orientational domains in NiO crystals.

In various static measurements, the typical X-ray magnetic linear dichroic (XMLD) line shape, which is directly linked to the long-range ordering in AFMs, has been observed in NiO by varying the temperature,[7] the experimental geometry[7,16] or measuring XMLD from different AFM domains in microscopy.[17,18] There have also been a large number of time-resolved measurements carried out in NiO in order to disentangle the coupling between different degrees of freedom. With time-resolved optical measurements, oscillations with THz frequencies have been observed and assigned to magnon excitation.[14,19,20] In a recent experiment, researchers have investigated the lattice dynamics of NiO using femtosecond electron diffraction,[3] and the origin of the rhombohedral lattice distortion was assigned to the weakening of the AFM order. However, there is so far no direct evidence of a laser-induced change in the AFM order driven by femtosecond laser pulses in time-resolved magnetic diffraction measurements.[6]

In this article, we report the investigation of the ultrafast manipulation of the AFM order in NiO films *via* sub-gap optical excitation. Using time-resolved resonant X-ray reflectivity, we observe XMLD line shape changes at the nickel L_2-edge, *i.e.*, for $2p_{1/2}$–3d transitions, and band gap renormalisation at the oxygen K-edge (1s–2p transitions). By comparing with static XMLD measurements at different temperatures,[7] we determine the laser-induced temperature change of the spin system to be 65 ± 5 K. In order to explain the band gap renormalisation observed at the oxygen K-edge, we use first principles calculations to investigate the influence of magnetic excitations on the band structure with the density-functional theory + Hubbard U formalism.

2 Methods

2.1 Sample preparation and characterization

NiO(001) crystalline films were used as our samples. The NiO films were epitaxially grown with surface normal along the [001] direction on a single crystal MgO(001) substrate. The MgO substrate was polished on both sides. A 2 nm thick MgO underlayer was first deposited by radio frequency magnetron sputtering in 3 mTorr argon at a temperature below 100 °C. The NiO layer was then deposited at 700 °C in a gas mixture of Ar(90%)/O_2(10%) at a pressure of 3 mTorr and was annealed *in situ* for 15 min with the same temperature and gas mixture condition. The thickness of the NiO film was 40 nm.

The ground-state electronic and magnetic structure of NiO crystalline films was characterised by performing X-ray absorption spectroscopy (XAS) measurements in drain current mode at the PM3 beamline at the BESSY II electron storage ring operated by Helmholtz-Zentrum Berlin.[21] Static XAS spectra were acquired for various incidence angles at room temperature.

The previous optical measurements of NiO,[22,23] show a variation in the optical absorption coefficient. Therefore, optical spectroscopy measurements were carried out prior to the time-resolved X-ray reflectivity experiment in order to evaluate the optical absorption properties of the NiO film during the optical pump–X-ray probe experiments, as shown in Fig. 1. The symbols in Fig. 1 represent the measured optical absorption between 450 nm and 1450 nm, and the dashed lines represent the calculated absorption for a 40 nm NiO film using the tabulated absorption coefficient.[22,23] The sharp drop at 860 nm in the experimental data is due to the change of photodetector in the optical measurements. From experimental data one can see two absorption bands that are centred at 720 nm and 1150 nm. The peak position of these two absorption bands is close to the values reported in previous work.[22–24] The origin of these two absorption bands has been assigned to the crystal-field d–d transitions.[25,26] We note that the dashed red line is truncated at 500 nm because the short wavelength limit reported in ref. 23 is 500 nm. Overall, the absorption bands shown in the experimental data indicate the good quality of our sample.

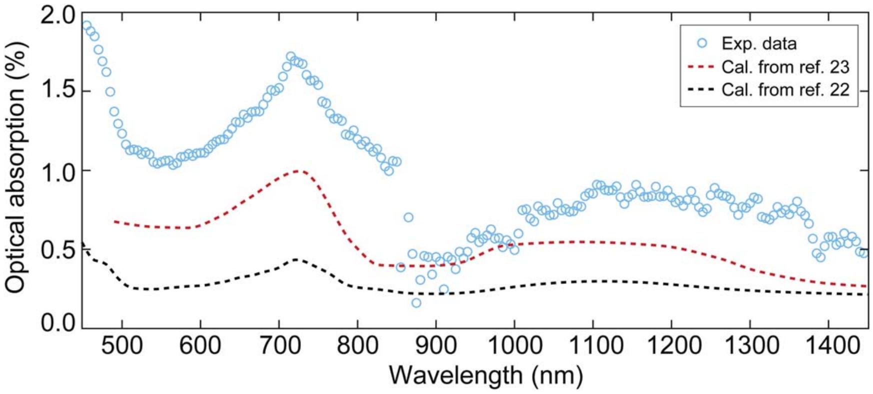

Fig. 1 The optical absorption of the NiO film with a thickness of 40 nm at wavelengths between 450 nm and 1450 nm. The circles represent the experimental data obtained from visible-infrared spectroscopy measurements. The sharp drop at 860 nm is due to the change of photodetector in the measurement. The dashed black and red lines denote the calculated optical absorption using the reported absorption coefficient in ref. 22 and 23, respectively.

2.2 Time-resolved X-ray reflectivity measurements at grazing angles

The time-resolved X-ray reflectivity experiments were carried out using the MUSIX end-station at beamline FL24 at the free-electron laser, FLASH, in Hamburg.[27,28] Experiments were carried out in reflection geometry as illustrated in Fig. 2(a). The NiO film was excited by a femtosecond laser pulse with a central wavelength around 800 nm and a pulse duration of 50 fs. The temporal evolution of the X-ray reflectivity following laser excitation was probed at both the oxygen K-edge and the nickel $L_{2,3}$-edges. The angle between the incident pump and the probe beams was 0.75°, *i.e.* nearly collinear.

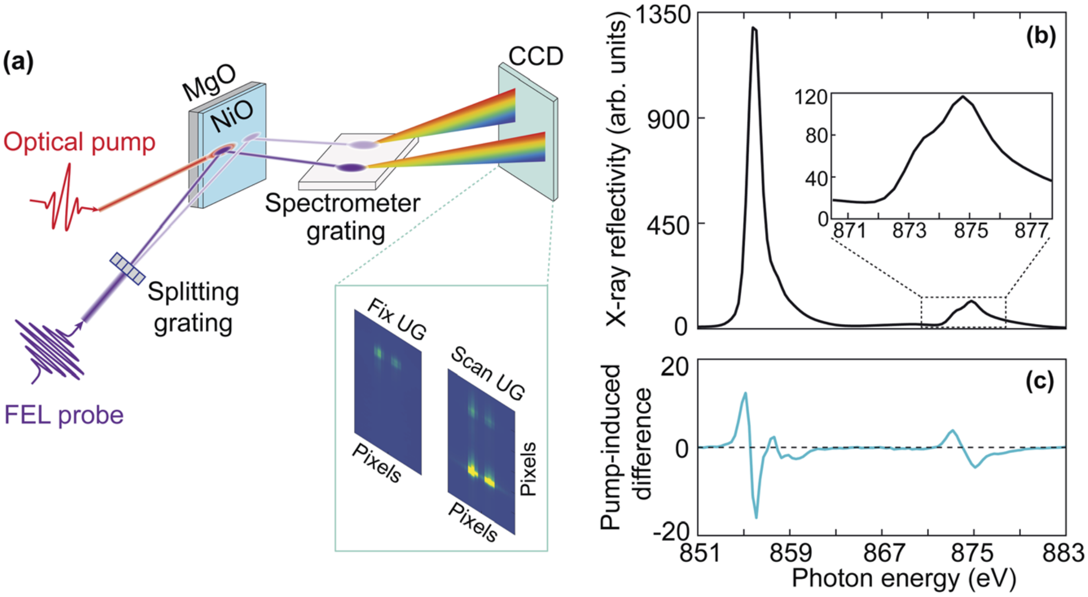

Fig. 2 (a) Schematic of experimental set-up for time-resolved X-ray reflectivity measurements. The inset shows two representative CCD images for measurements with fixed undulator gap (UG) and scanning UG. (b) Static X-ray reflectivity spectrum of NiO at the nickel $L_{2,3}$-edges. The inset shows the enlarged spectrum at the nickel L_2-edge. (c) Pump-induced difference in the X-ray reflectivity spectrum for time delays longer than 400 fs.

FLASH was operated in a 10 Hz burst mode with each burst consisting of 40 X-ray pulses. The FEL was tuned for the third harmonic radiation to reach the oxygen K-edge and the nickel $L_{2,3}$-edges. Reflectivity spectra were recorded utilizing a split-beam normalisation scheme.[28] As illustrated in Fig. 2(a), the FEL probe beam propagated through a beam splitting grating and was horizontally split such that the zeroth and first diffraction orders hit the sample. The zeroth order beam overlapped both spatially and temporally with the optical pump beam to record the transient X-ray reflectivity. The zeroth and first diffraction orders were separated by 3 mm on the sample, ensuring that the first diffraction order of the FEL beam had no overlap with the optical laser beam and could be used to normalise fluctuations of the FEL spectral intensity stemming from the self-amplified spontaneous emission (SASE) process. X-ray energy resolution was obtained by directing both the zeroth and first diffraction orders onto a downstream spectrometer grating and consecutively, a CCD camera. The dispersion of the spectrometer was calibrated and found to be 0.33 eV per pixel. To measure reflectivity spectra around the absorption edges, the photon energy was scanned in steps of 0.5 eV at the fundamental wavelength by varying the undulator gap, which corresponds to 1.5 eV at the third harmonic in the time-resolved X-ray reflectivity measurement. As each FEL spectrum covers a bandwidth of about 1% of the total photon energy, this ensures a seamless spectrum of the scanned range. In reflection geometry, by varying the angle of incidence, one can access different parts of the Brillouin zone. The size of the X-ray beam was 50 μm × 75 μm. The X-ray angle of incidence was set to 7.23° at the nickel $L_{2,3}$-edges and 9.00° at the oxygen K-edge in order to access a similar q-range in reciprocal space and match the X-ray penetration depth with the sample thickness. The X-ray penetration depth is 50 nm at the oxygen K-edge and 60 nm at the nickel $L_{2,3}$-edges.[29] The transferred wave-vector q was 0.85 nm^{-1} at oxygen K-edge and 1.09 nm^{-1} at the nickel $L_{2,3}$-edges, which corresponds to 0.06 and 0.07 reciprocal lattice units, respectively. Therefore, the q-range lies close to the Γ point of the Brillouin zone. Fig. 2(b) shows a static X-ray reflectivity spectrum of NiO at the nickel $L_{2,3}$-edges, and the enlarged nickel L_2-edge is displayed in the inset.

The size of the optical pump beam was characterised both by imaging a virtual focus on an equivalent plane and by a knife-edge measurement. The size of the pump beam was (270 ± 10) μm × (257 ± 2) μm. The incident pump fluence was 60 mJ cm^{-2} and 75 mJ cm^{-2} due to the different angles of incidence at the nickel $L_{2,3}$-edges and the oxygen K-edge, respectively. Fig. 2(c) shows the pump-induced change of the X-ray reflectivity spectrum at the nickel L_3- and L_2-edges averaged over time delays between 400 fs and 2.4 ps. We will describe in the following Section 2.3 the data analysis procedure and involved uncertainties. The temporal resolution and pump–probe temporal overlap were characterised at regular intervals during the measurements by probing the transient optical reflectivity change of a GaAs single crystal induced by the FEL pulse.[30] The temporal resolution was found to be 300 ± 100 fs full-width half-maximum (FWHM), which mainly arises from the jitter between the pump and probe pulses. The temporal resolution evaluated from the GaAs single crystal is overestimated because the measurements at the oxygen K-edge reveal dynamics faster than 300 fs. Therefore, the GaAs single crystal was mainly used to monitor the temporal overlap, *i.e.*, time zero. During the experiments, the delay between the optical laser and the FEL was varied by a delay stage in the optical path. The delay was scanned across a 3 ps time window in steps of 100 fs.

2.3 Data analysis for the normalisation of the SASE FEL fluctuations and slow drifts

In order to quantitatively extract the laser-induced reflectivity changes from spectra acquired at SASE FELs in an unambiguous manner, one needs to account for the shot-to-shot fluctuations in spectral intensity caused by the SASE process. Since the measured reflectivity spectrum is proportional to the product of the FEL spectrum, the spectral reflectivity of the sample, and the efficiency of the diffraction grating, the direct measure of the laser-induced reflectivity change is the ratio of the measured spectra without and with laser excitation. To compensate for the slow drifts between the spectra acquired with and without laser excitation, spectral changes observed from the signal sample spot, which is illuminated by both the optical laser beam and the FEL beam, are normalised by the changes observed from the reference sample spot illuminated only by the FEL beam. The normalised ratio eventually gives the real pump–probe effect.

Fig. 3(a) and (b) show the X-ray reflectivity spectra at the nickel $L_{2,3}$-edges, respectively. The dashed black and the solid red lines represent the spectra acquired without and with laser excitation, respectively. From the comparison in Fig. 3(a) and (b), one can directly see that the change at the nickel L_3-edge is significantly smaller than at the nickel L_2-edge. To quantify the relative change induced by the optical laser, we calculated the ratio of the spectra with and without laser excitation. Fig. 3(c) and (d) show the ratio plots as a function of delay and photon energy at the nickel $L_{2,3}$-edges, respectively. In Fig. 3(c) and (d), it can be seen that the laser-induced change at the nickel L_2-edge is less noisy than that at the nickel L_3-edge. Therefore, in the results and discussion about the nickel L-edge measurements, we will focus mainly on the nickel L_2-edge.

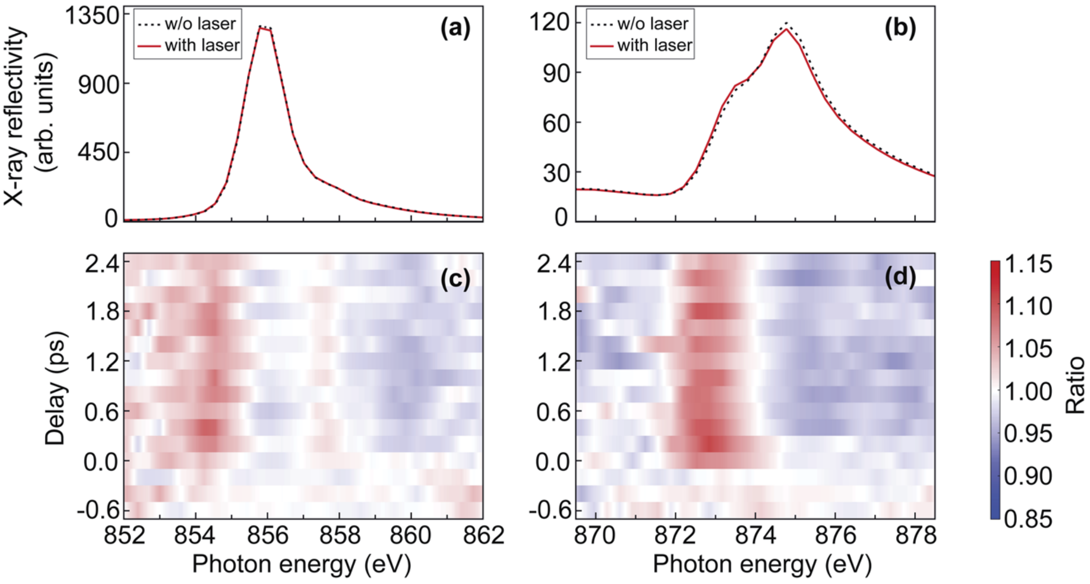

Fig. 3 (a and b) X-ray reflectivity spectra of NiO at the nickel $L_{2,3}$-edges. The dashed black and solid red lines represent the spectra acquired at time delays longer than 400 fs without and with laser excitation, respectively. (c and d) The ratio map as a function of delay and photon energy at the nickel $L_{2,3}$-edges.

3 Results and discussion

In this section we present time-resolved measurements at the O K-edge and Ni $L_{2,3}$-edges that probe O 1s–2p and Ni 2p–3d core–valence excitations, respectively. These orbitally resolved measurements enable us to extract information about the temporal evolution of the band-gap renormalisation and the modification of the AFM order, respectively. We will finally present a model that relates the changes of the upper band-edge, composed of O 2p and Ni 4s orbitals, to canted AFM moments that typically occur during magnon excitation. We start the section by describing the measured X-ray reflectivity spectra and relating them to XAS measurements *via* Kramers–Kronig analysis.

3.1 Comparison of X-ray reflectivity and XAS spectral line shape

Fig. 2(b) shows a Ni L-edge reflectivity spectrum obtained without laser excitation. The spectral line shape compares well with literature measurements on similar NiO/MgO(001) samples.[7,28,31] The dominant feature is a sharp peak at the Ni L_3-edge and a double-peak structure at the Ni L_2-edge. We note that the width of the sharp L_3-edge peak is limited by the energy resolution of the down-stream spectrometer grating. As mentioned above, the energy resolution of the spectrometer grating was 0.33 eV per pixel and the corresponding energy step size can be seen from the flat top of the L_3-peak. In the following we focus mainly on the L_2-edge since (i) the spectral features are broader and, therefore, contain a sufficient amount of energy steps, and (ii) XMLD measurements have mainly been done using the double-peak structure that gives rise to a characteristic derivative-like XMLD line shape.[7] Since XMLD measurements are typically performed in absorption, we performed ground-state reference XAS measurements monitoring the sample drain current for various grazing incidence angles between 7–26°, as shown in Fig. 4(a). In all the XAS spectra, one can see the crystal field induced peak splitting at the nickel L_2-edge whose energy positions compare well with the shoulder at 873.3 eV and the main peak at 874.5 eV observed in the reflectivity spectra. However, the respective peak intensities differ for XAS and reflectivity. While the XAS spectra correspond to the imaginary part of the X-ray dielectric constant, both imaginary and real parts of the X-ray dielectric constant contribute to the reflectivity. In principle, the real part of the dielectric constant can be computed from the imaginary part using Kramers–Kronig transformation, and consequently, the X-ray reflectivity spectra can be calculated using Fresnel's equation for a specific polarization.[31]

The XAS spectra in Fig. 4(a) show the typical line shape variations that are expected for L_2-edge XMLD of NiO/MgO(001).[7] As the incidence angle increases, the intensity of the second peak decreases gradually. The dip between the two peaks slightly shifts towards higher photon energy as the incident angle increases. There is also a red shift of the slope on the right side of the second peak along with increasing incident angles. To calculate the X-ray reflectivity spectrum, we chose the XAS spectrum at a grazing angle of 7° in Fig. 4(a), as it is the closest angle to the one in our time-resolved reflectivity measurement at FLASH. We follow ref. 31 to calculate the reflectivity spectrum. Briefly, (i) use the XAS spectrum as the input to calculate the extinction coefficient k, which is the imaginary part of the complex refractive index; (ii) compute the real part n of the complex

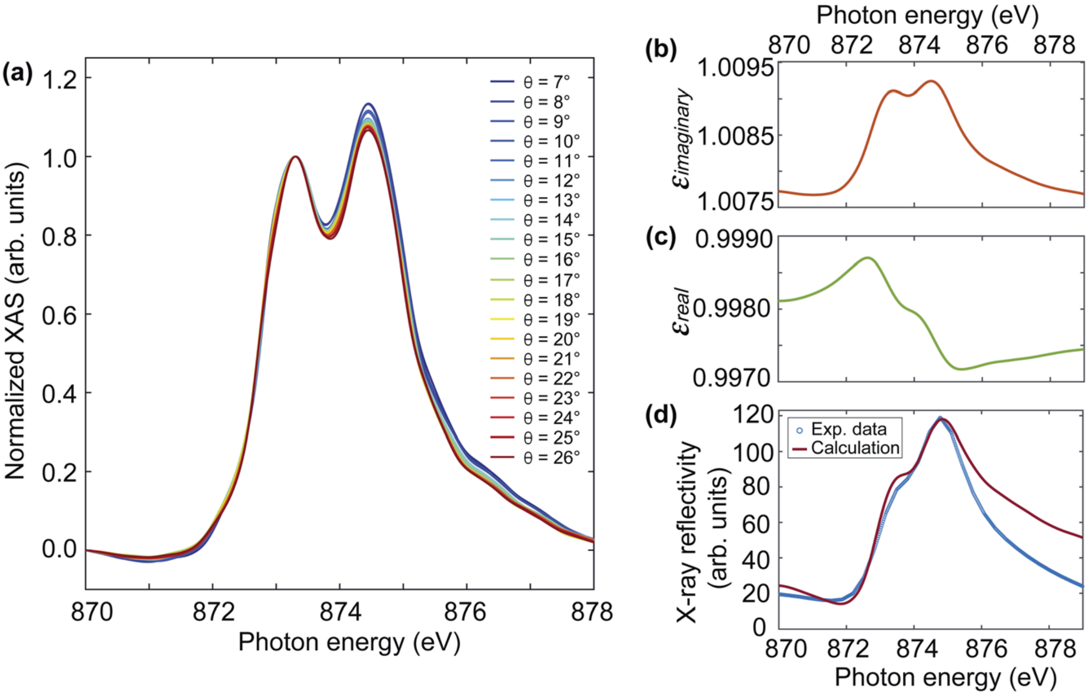

Fig. 4 (a) Static XAS spectra measured at the nickel L_2-edge at different grazing angles. Each XAS spectrum was normalised to the first peak at 873.3 eV. (b) The imaginary part of the dielectric constant, which was calculated using the XAS spectrum at a grazing angle of 7°. (c) The real part of the dielectric constant, which was calculated from the imaginary part in (b) using Kramers–Kronig transformation. (d) Comparison of the experimental X-ray reflectivity spectrum measured at FLASH (blue symbols) and the calculated reflectivity (red line).

refractive index from the imaginary part k using Kramers–Kronig transformation; (iii) calculate the reflectivity R using the Fresnel equation for p-polarized light, which is the polarisation in our reflectivity experiment. The Kramers–Kronig transformation is performed using Maclaurin's formula.[32,33] This results in similar line shapes of the X-ray dielectric constant compared to the reported values in ref. 31. However, their magnitude was rescaled to the literature values to take the different detection efficiency into account. Fig. 4(b) and (c) show the imaginary and real parts of the X-ray dielectric constant, respectively. From the comparison in Fig. 4(d), one can see reasonable agreement between the measured (blue symbols) and the calculated (red line) X-ray reflectivity spectra. The lower intensity in the measured reflectivity around 878 eV can occur due to lower flux from the FEL since this energy is close to the end of the scan range.

3.2 Temporal evolution of AFM order visualised at the nickel L_2-edge

The double-peak multiplet structure of the nickel L_2-edge has been used extensively to probe the NiO AFM order in thermal equilibrium. The interplay between AFM order, crystalline field effects and spin–orbit coupling gives rise to a characteristic XMLD line shape depending on the alignment of the X-ray polarisation and the AFM moment orientation.[7,16,17] In static measurements, the sign of the XMLD line shape can be reversed due to the angle between the X-ray polarisation and the crystal orientation[16] or the subtraction of the X-ray signal between different AFM domains.[17] Here we describe the first NiO XMLD measurement in the time-domain caused by pump-induced changes to the AFM order.

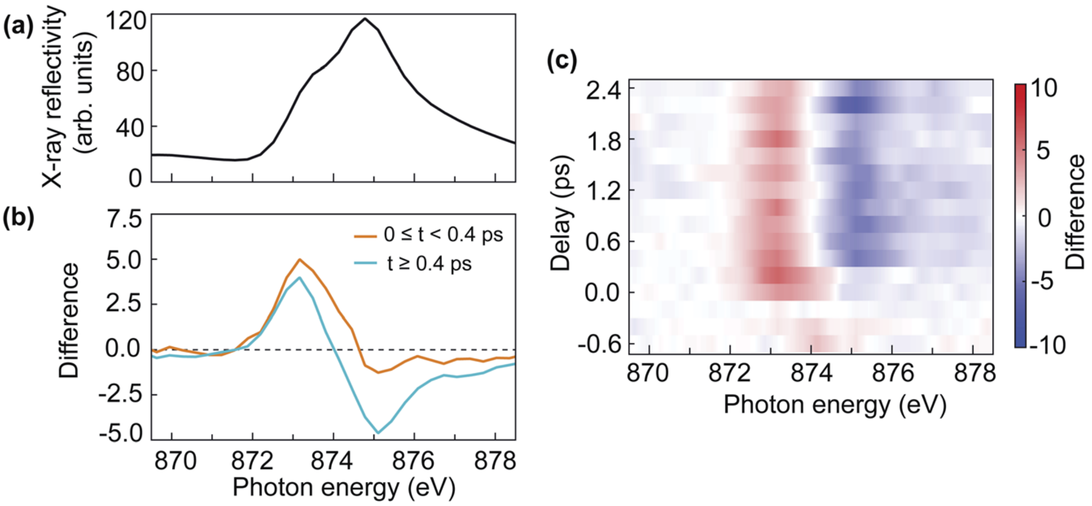

Fig. 5 (a) The static X-ray reflectivity spectrum at the nickel L_2-edge. (b) The difference spectra of the X-ray reflectivity with laser and without laser at transient time ($0 \leq t < 400$ fs, orange line) and at longer delays ($t \geq 400$ fs, cyan line). (c) The map of the difference spectra as a function of delay and photon energy.

Fig. 5(a) shows the static Ni L_2-edge X-ray reflectivity of NiO. The difference in reflectivity between laser on and laser off is shown in Fig. 5(b) for two time-delay regions, averaged for the first 400 fs (orange line) and between 400 fs and 2.4 ps (cyan line). The difference reflectivity spectra as a function of time delay and photon energy are shown as a colour map in Fig. 5(c). From Fig. 5(b), one can see that the spectral difference line shape evolves with time delay. After 400 fs the displayed difference spectra in Fig. 5(b) are essentially indistinguishable from what is expected for XMLD in thermal equilibrium.[7,16,17] Moreover, the observed positive–negative spectral difference line shape with increasing photon energy demonstrates that a reduction of AFM order takes place.[7] Interestingly, the spectral difference line shape is very different for the first 400 fs. It is characterised by a positive peak at lower photon energy and a negligible negative tail for the high photon-energy multiplet peak. This is an indication of a non-thermal state of the laser-excited spin system, which means the spin system has not reached a local thermal equilibrium. Around 400 fs the difference spectrum changes its line shape which remains unaltered afterwards, as can be clearly seen in the difference map of Fig. 5(c). This implies that the system reaches a local metastable equilibrium after 400 fs. It is conceivable that the XMLD line shape during the first 400 fs is also influenced by electronic excitations that could alter the effective local crystalline field experienced by the nickel ions. Crystalline field changes in monolayer thin NiO films have been reported to lead to changes in the L_2 multiplet peaks different from XMLD.[34]

Since the spin system reaches a local equilibrium after 400 fs, it is of interest to evaluate the temperature change of the spin system. It has been observed that the temperature dependence of the ratio between the two multiplets peaks at the nickel L_2-edge follows a Brillouin–Langevin function.[7] We observe a 7% change in the cyan XMLD spectrum of Fig. 5(b). This implies that we can use a linear approximation to evaluate the spin-temperature-change of the system. We convert the L_2 multiplet peak ratio measured in reflectivity to absorption as outlined in Section 3.1 and use the measured temperature dependence in ref. 7 to obtain an effective spin temperature increase of 65 ± 5 K, relative to the room temperature starting condition before optical excitation. The uncertainty is estimated from the photon statistics.

This observation of a significant reduction of the AFM order in NiO thin films is surprising especially since a negligible change was reported in a bulk sensitive magnetic scattering experiment performed under very similar excitation conditions.[6] In the following we discuss if optical excitation can indeed deposit enough energy to drive a comparable temperature increase. We evaluated the absorption coefficient of our NiO film at 800 nm to be around 1860 cm^{-1}. The refractive index of NiO at the excitation wavelength is 2.35 and the reflection of the sample is about 20% for p-polarized light.[35] Using the Beer–Lambert law and the magnetic specific heat of NiO,[36] we estimated the maximum temperature rise of the spin system to be ~150 K. This represents an upper limit since the magnetic specific heat increases rapidly as the temperature approaches T_N.[36] We alternatively estimated the lattice temperature rise base on a previous ultrafast electron diffraction measurement.[3] Assuming that at the slightly higher pump photon energy used in ref. 3 the optical absorption is of at least similar strength, we can extrapolate the measured lattice temperature in ref. 3 to ~85 K given our pump fluence. We note that in ref. 3 no optical absorption data for the measured sample was available and the available literature data provided an insufficient heat deposition leading the authors in ref. 3 to conclude that two-photon above-gap excitation was the actual driving force. However, our lower photon energy would require three-photon events for above-gap absorption. We can conclude that the enhanced optical absorption in thin NiO films is sufficient to explain our observed level of AFM order reduction.

3.3 Band gap renormalisation visualised at the oxygen K-edge

Fig. 6 displays the results of transient reflectivity spectra measured at the oxygen K-edge. We focus on the lowest photon energy feature as this is the one that defined the upper gap-edge. However, we corroborated in static measurements that our samples display the typical three-peak structure between 525 eV and 545 eV expected for NiO.[37–39] Fig. 6(a) shows the static X-ray reflectivity as a reference for the map of the difference spectra between laser on and laser off in Fig. 6(b). The pre-edge dip at 531.5 eV in Fig. 6(a) is related to the reflection geometry, which can also be seen from the calculated spectrum in Fig. 4(d). The evolution of the difference spectra shown in Fig. 6(b) is plotted using a temporal binning of 200 fs to improve the signal-to-noise ratio (SNR). The positive signal region centred around 532 eV in Fig. 6(b) is an indication of a red-shift (≈60 meV) of the oxygen K-edge. The amount of the red-shift will be discussed in detail in the next section in combination with first-principles modelling.

The most prominent feature visible in the difference map of Fig. 6(b) is clearly the red-shifted absorption edge, indicated by the red intensity increase near 532 eV photon energy and a broader blue decrease above the edge (533–534 eV). A gap reduction following sub-gap optical excitation has been observed in the charge-transfer insulator, La_2CuO_4,[40] and it is tempting to relate our observation to the same effect. However, strictly speaking we observe in the present experiment only the red-shifted upper gap-edge while a lower gap-edge shift would have to be assessed *e.g.* in complementary time-resolved photoemission experiments. The

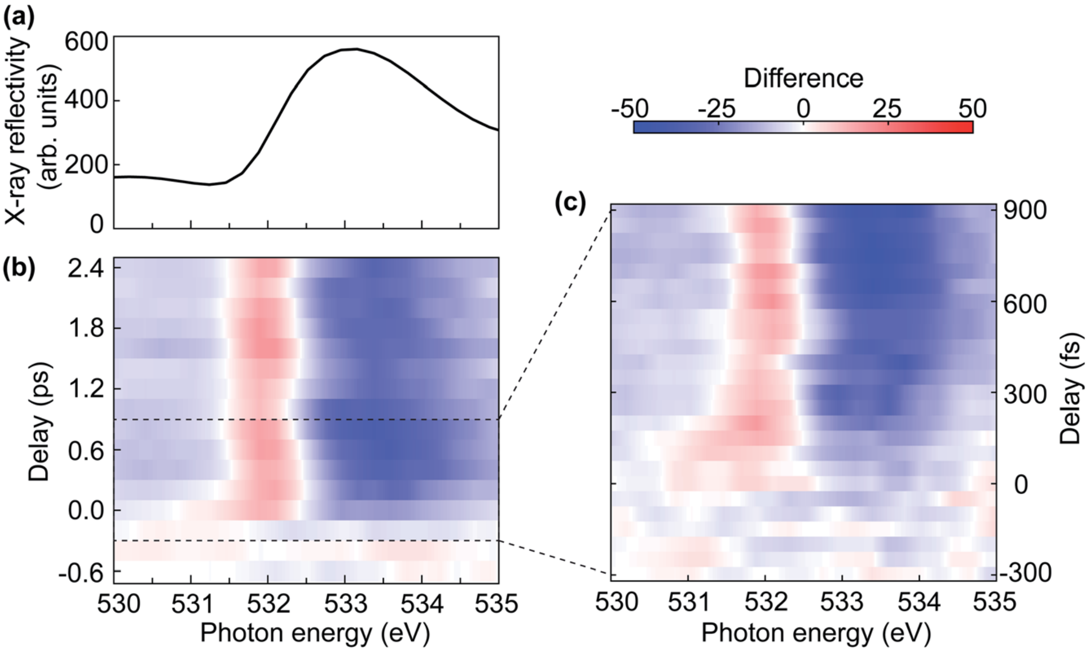

Fig. 6 (a) The static X-ray reflectivity spectrum at the oxygen K-edge. (b) The map of the difference spectra of the X-ray reflectivity with laser and without laser as a function of delay and photon energy. (c) The map of laser-induced difference in X-ray reflectivity as a function of delay and photon energy at a fixed undulator gap. The delay step size is 50 fs.

gap renormalisation in ref. 40 was assigned to the coupling of optical excitation to a bosonic field, although it remained unclear if this is composed of phonons or magnons. A possible magnetic origin of the red-shifted NiO upper gap-edge becomes apparent when we analyse the observed oscillations visible in Fig. 6(b).

The oscillation of the positive difference signal centred around 532 eV is compatible with a period of ~1 ps, which corresponds to a frequency of ~1 THz. This frequency is close to the eigenfrequency of the out-of-plane magnon mode, which has been extensively studied in both optical and THz spectroscopy measurements.[14,19,41–49] There are two magnon eigenmodes: in-plane and out-of-plane modes. For the in-plane mode, the AFM vector between two adjacent ferromagnetic planes is modulated along the $[1\bar{1}0]$ direction, which lies in the (111) plane. For the out-of-plane mode, the modulation of the AFM vector is along the [111] direction, which is perpendicular to the ferromagnetic plane.[20] Due to the large magnetic anisotropy along the easy axis (*i.e.* [111] direction), the out-of-plane mode has a much higher eigenfrequency than the in-plane mode. Both of these two magnon modes are excitable by ultrashort optical laser pulses and have been detected at around 0.14 THz (ref. 20 and 46) and 1.07 THz (ref. 20, 42, 45–47 and 49) for the in-plane mode and the out-of-plane mode, respectively. The mode also displays a temperature dependence with a frequency reduction as the Néel temperature is approached.[14,42,49] We note that also the observed phase of the oscillation in Fig. 6(b) matches that reported for the out-of-plane magnon mode.[20]

Fig. 6(c) shows the oxygen K-edge difference reflectivity signal up to 900 fs with 50 fs step size. The measurements were performed at a fixed undulator gap corresponding to a nominal photon energy of 533 eV. The displayed photon energy region therefore represents the full bandwidth of the undulator emission. The line shape of the X-ray reflectivity (not shown) is similar to the one displayed in Fig. 6(a), however, the best SNR is obtained for the undulator maximum (533 eV).

Fig. 6(c) shows, with a much better time resolution than Fig. 6(b), that the red-shift of the upper gap-edge is preceded by the appearance of transient states much further into the band-gap. The temporal duration of such transient mid-gap states seems to essentially be determined our temporal resolution, *i.e.* the optical and FEL pulse durations and the jitter between them. This reflects to some degree earlier measurements at pump photon energies off-resonant to any d–d transitions in the NiO band-gap.[9] It is conceivable that the appearance of transient mid-gap states are a consequence of the strong optical driving field. However, with off-resonance excitation no significant lasting band-gap renormalisation was observed.[9] The red-shift of the upper gap-edge is therefore likely a consequence of the energetic proximity of our excitation frequency to d–d transitions that may facilitate the coupling to spin excitations.[50]

3.4 A simple model for the band gap renormalisation in NiO

With the evidence of the laser-induced XMLD line shape changes at the nickel L_2-edge (Section 3.2) and the observation of the 1 THz magnon oscillation in the NiO upper gap-edge red-shift (Section 3.3), it is of interest to investigate how changes in the spin orientation influence the band gap in NiO. Therefore, we performed first-principles calculations of the NiO band structure with different canting angles of the Ni^{2+} spins, to mimic various spin temperatures. The super-exchange and correlation in the calculations were taken into account using local density approximation together with an on-site Hubbard U term in the Hamiltonian. Although dynamical correlations have been pointed out to be important for NiO, we adopt for simplicity here the LDA+U formalism, that is based on single determinant states. A detailed description of the theoretical modelling can be found in ref. 9. The canting angles at different temperatures were derived from the reduction of the magnetic moment of the Ni^{2+} spins.[15]

Fig. 7(a) shows the band structure calculated with Ni^{2+} spins oriented along the $[11\bar{2}]$ directions. The conduction band is composed of essentially dispersionless bands of Ni 3d character and dispersive bands consisting of hybridised O 2p and Ni 4s states. The upper gap-edge is composed of the latter and is marked by the light blue shaded rectangular in Fig. 7(a). The green and orange dots in Fig. 7(a) represent the experimental q values probed in our time-resolved X-ray reflectivity measurements. Fig. 7(b) shows the influence of canted magnetic moments on adjacent Ni atoms along the [111] direction on the dispersive band near the upper gap-edge. The chosen spin canting pattern is that of the 1 THz magnon mode[20] (see Fig. 7(c)). Initially degenerate bands are split in energy once the spins are canted. This splitting increases as the canting angle becomes larger. The band shifting downwards in energy at the Γ point [000] of the Brillouin zone reduces the NiO band gap as probed by the oxygen K-edge. Although the band structure in Fig. 7 was calculated for frozen magnetic moments, it is straightforward to see that for oscillating spins the upper gap-edge position would also be modulated by the magnon frequency.

In the following we quantify the redshift of the upper gap-edge and separate the coherent oscillatory part from an incoherent redshift. Fig. 8(a) compares the measured ground-state X-ray reflectivity spectrum (solid line) to the redshifted experimental spectra for 60 (blue dashed line) and 80 meV (red dashed line) shifts. In addition to the redshift, we also observe experimentally a 5% reduction

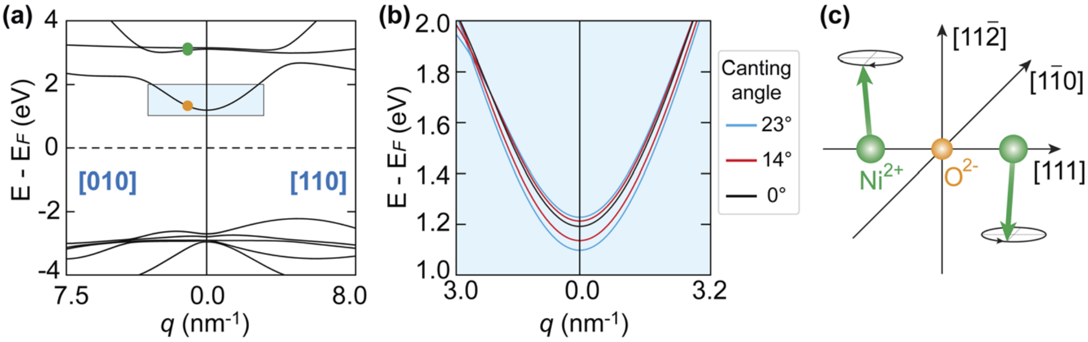

Fig. 7 (a) First-principles calculations of the NiO band structure along two high symmetry lines:[9] [010] and [110]. The green and orange dots along the [010] direction denote the experimental wavevectors that were probed in the time-resolved X-ray reflectivity measurement. (b) Zoom-in view of the band structure marked within the light blue shaded rectangle in (a). The band structure was calculated for different canting angles of the Ni^{2+} spins. (c) Illustration of the canting angle of the Ni^{2+} spins in the NiO unit cell that was employed in the calculations. The canting angle is defined as the angle between the Ni^{2+} spins and the plane that is spanned by [11$\bar{2}$] and [111] directions. The spin canting pattern is the same as the out-of-plane mode in ref. 20. The Ni^{2+} and the O^{2-} ions are shown with green and orange spheres, respectively.

to the spectral peak intensity likely related to the blueshift of some initially degenerate bands as seen in Fig. 7(b). This results in good agreement with the experiment for a redshift of 80 ± 10 meV at 0.6 ps time delay (see Fig. 8(b)) and 60 ± 10 meV at 1.0 ps time delay (see Fig. 8(c)). We note that for increasing photon energy the agreement becomes less good, possibly due to the influence of the additional O K-edge spectral peaks neglected here. From Fig. 6(b) one can see that the positive signal around 532 eV is composed of an overall intensity increase and

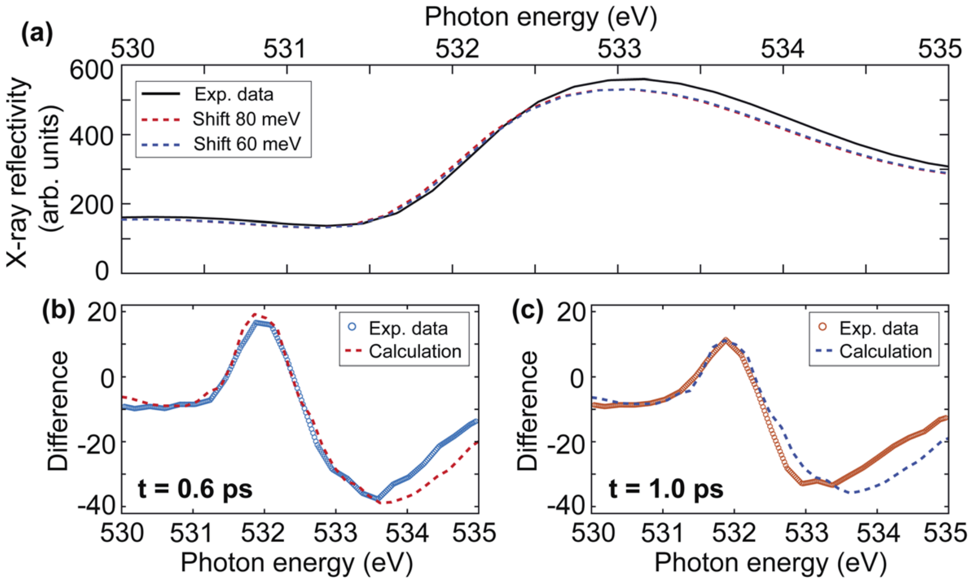

Fig. 8 (a) The black line represents the static X-ray reflectivity spectrum acquired at FLASH. The dashed red and blue lines represent the shifted spectra by 80 meV and 60 meV, respectively. (b) Comparison of the experimental difference spectrum at 0.6 ps after laser excitation and the calculated spectrum that is obtained by subtracting the black line from the dashed red line in (a). (c) Comparison between the experimental data at 1.0 ps after laser excitation and calculated difference spectrum; that is the subtraction of the black line and the dashed blue line in (a).

an oscillatory intensity variation. The overall intensity increase corresponds to an incoherent redshift of 70 meV. The amplitude of the coherent oscillatory redshift related to the 1 THz magnon mode is approximately 10 meV. Using the calculations in Fig. 7(b) we can estimate the corresponding magnon precession angle to ∼2.5°. We note that the reduction of AFM due to such large spin precession amplitude would amount to about 28% of the spin temperature increase we observed in Section 3.2.

4 Conclusions

In conclusion, we performed time-resolved resonant X-ray reflectivity measurements in NiO following femtosecond 1.5 eV sub-gap excitation. The temporal evolution of the X-ray reflectivity spectra was monitored at the Ni L_2-edge and the O K-edge to probe the dynamics of the AFM order and the band gap renormalisation, respectively.

At the Ni L_2-edge, we observed laser-induced XMLD spectral line shape for time delays longer than ∼400 fs after laser excitation. By comparing the transient XMLD spectra with temperature-dependent ground-state measurements, we extracted a spin temperature rise of 65 ± 5 K. The transient XMLD line shape demonstrates a significant reduction of the AFM order in NiO. The change of the spin temperature is consistent with what is expected from optical absorption measurements. At the O K-edge, we observed the red-shift of the upper band gap edge across the measured time delay range up to 2.4 ps. This upper gap-edge renormalisation is accompanied by a coherent oscillation with ∼1 THz frequency. During the optical driving field we find evidence for the formation of transient mid-gap states that were also observed previously for optical frequencies off-resonant to d–d excitations.[9]

We finally discuss a ground-state model of coupling Ni spin precession to the electronic band-structure. Using first-principles calculations, we find that the O 2p dispersive states forming the upper gap-edge shift in energy as the Ni magnetic moments precess as given by the 1 THz magnon mode. This even allows us to model the observed O K-edge measurements.

The high-quality X-ray spectroscopy measurements presented here have become possible due to the implementation of a multiple X-ray beams experimental setup that enables us to significantly reduce the intensity and photon-energy fluctuations inherent to SASE FELs. This opens up new possibilities to investigate the ultrafast dynamics of electronic structure and the magnetic ordering phenomena across a wide range of materials.

Author contributions

M. B. and H. A. D. designed the experiments. X. W., R. Y. E., I. V., D. T., J. O. S., S. D., G. B., R.-P. W., M. K., F. K., W. B., M. B. and H. A. D. performed the time-resolved X-ray reflectivity experiment and on-site data analysis. R. K. and I. V. performed the optical spectroscopy experiment. C. S.-L. performed the static XAS experiment. X. W. conducted the post data analysis. O. G. conducted the theoretical calculations. X. W., R. Y. E., I. V., D. T., V. S., A. Y., O. G., F. P., O. E., M. B., and H. A. D. discussed the results. X. W. wrote the first draft of the manuscript. X. W. and H. A. D. revised the manuscript with inputs from all other authors.

Conflicts of interest

There are no conflicts to declare.

Acknowledgements

The authors acknowledge FLASH in Hamburg, Germany, for the provision of X-ray free-electron laser beamtime at beamline FL24 and thank the machine group and facility staff for their assistance during the beamtime. The beamtime was allocated for proposal F-20191553 EC. The research work at FLASH has been supported by the project CALIPSOplus under the Grant Agreement 730872 from the EU Framework Programme for Research and Innovation HORIZON 2020. X. W., D. T., V. S., and H. A. D. acknowledge support from the Swedish Research Council (VR), Grants 2017-06711 and 2018-04918. A. Y. acknowledges support from the Carl Trygger Foundation. O. G. acknowledges support from the Strategic Research Council (SSF) grant ICA16-0037 and the Swedish Research Council (VR) grant 2019-03901. The computations were enabled by resources provided by the Swedish National Infrastructure for Computing (SNIC), partially funded by the Swedish Research Council through grant agreement no. 2018-05973. R. Y. E., J. O. S., and M. B. were supported by the Helmholtz Association through grant VH-NG-1105. I. V. acknowledges support from the Slovene Ministry of Science (Raziskovalci-2.1-IJS-952005). R.-P. W. acknowledges support from the German Ministry of Education and Research, grant number 05K19GU2. We thank Prof. Arne Roos for his help with the optical spectroscopy measurements.

References

1 T. Jungwirth, X. Marti, P. Wadley and J. Wunderlich, *Nat. Nanotechnol.*, 2016, **11**, 231–241.

2 V. Baltz, A. Manchon, M. Tsoi, T. Moriyama, T. Ono and Y. Tserkovnyak, *Rev. Mod. Phys.*, 2018, **90**, 015005.

3 Y. W. Windsor, D. Zahn, R. Kamrla, J. Feldl, H. Seiler, C.-T. Chiang, M. Ramsteiner, W. Widdra, R. Ernstorfer and L. Rettig, *Phys. Rev. Lett.*, 2021, **126**, 147202.

4 M. A. Peck and M. A. Langell, *Chem. Mater.*, 2012, **24**, 4483–4490.

5 A. M. Balagurov, I. A. Bobrikov, S. V. Sumnikov, V. Y. Yushankhai, J. Grabis, A. Kuzmin, N. Mironova-Ulmane and I. Sildos, *Phys. Status Solidi B*, 2016, **253**, 1529–1536.

6 L. Huber, A. Ferrer, T. Kubacka, T. Huber, C. Dornes, T. Sato, K. Ogawa, K. Tono, T. Katayama, Y. Inubushi, M. Yabashi, Y. Tanaka, P. Beaud, M. Fiebig, V. Scagnoli, U. Staub and S. L. Johnson, *Phys. Rev. B*, 2015, **92**, 094304.

7 D. Alders, L. H. Tjeng, F. C. Voogt, T. Hibma, G. A. Sawatzky, C. T. Chen, J. Vogel, M. Sacchi and S. Iacobucci, *Phys. Rev. B*, 1998, **57**, 11623.

8 L.-C. Duda, T. Schmitt, M. Magnuson, J. Forsberg, A. Olsson, J. Nordgren, K. Okada and A. Kotani, *Phys. Rev. Lett.*, 2006, **96**, 067402.

9 O. Grånäs, I. Vaskivskyi, X. Wang, P. Thunström, S. Ghimire, R. Knut, J. Söderström, L. Kjellsson, D. Turenne, R. Y. Engel, M. Beye, J. Lu, A. H. Reid, W. Schlotter, G. Coslovich, M. Hoffmann, G. Kolesov,

C. Schüßler-Langeheine, A. Styervoyedov, N. Tancogne-Dejean, M. A. Sentef, D. A. Reis, A. Rubio, S. S. P. Parkin, O. Karis, J. Nordgren, J.-E. Rubensson, O. Eriksson and H. A. Dürr, 2020, arXiv:2008.11115.

10 D. Betto, Y. Y. Peng, S. B. Porter, G. Berti, A. Calloni, G. Ghiringhelli and N. B. Brookes, *Phys. Rev. B*, 2017, **96**, 020409(R).

11 G. Lefkidis and W. Hübner, *Phys. Rev. Lett.*, 2005, **95**, 077401.

12 A. K. Cheetham and D. A. O. Hope, *Phys. Rev. B*, 1983, **27**, 6964.

13 Y. Gao, Q. Sun, J. M. Yu, M. Motta, J. McClain, A. F. White, A. J. Minnich and G. K.-L. Chan, *Phys. Rev. B*, 2020, **101**, 165138.

14 J. Nishitani, K. Kozuki, T. Nagashima and M. Hangyo, *Appl. Phys. Lett.*, 2010, **96**, 221906.

15 N. Rinaldi-Montes, P. Gorria, D. Martínez-Blanco, A. B. Fuertes, I. Puente-Orench, L. Olivi and J. A. Blanco, *AIP Adv.*, 2016, **6**, 056104.

16 E. Arenholz, G. van der Laan, R. V. Chopdekar and Y. Suzuki, *Phys. Rev. Lett.*, 2007, **98**, 197201.

17 H. Ohldag, G. van der Laan and E. Arenholz, *Phys. Rev. B*, 2009, **79**, 052403.

18 J. Xu, C. Zhou, M. Jia, D. Shi, C. Liu, H. Chen, G. Chen, G. Zhang, Y. Liang, J. Li, W. Zhang and Y. Wu, *Phys. Rev. B*, 2019, **100**, 134413.

19 T. Satoh, S.-J. Cho, R. Iida, T. Shimura, K. Kuroda, H. Ueda, Y. Ueda, B. A. Ivanov, F. Nori and M. Fiebig, *Phys. Rev. Lett.*, 2010, **105**, 077402.

20 C. Tzschaschel, K. Otani, R. Iida, T. Shimura, H. Ueda, S. Günther, M. Fiebig and T. Satoh, *Phys. Rev. B*, 2017, **95**, 174407.

21 T. Kachel, F. Eggenstein and R. Follath, *J. Synchrotron Radiat.*, 2015, **22**, 1301–1305.

22 R. Newman and R. M. Chrenko, *Phys. Rev.*, 1959, **114**, 1507.

23 I. G. Austin, B. D. Clay and C. E. Turner, *J. Phys. C: Solid State Phys.*, 1968, **1**, 1418.

24 G. R. Rossman, R. D. Shannon and R. K. Waring, *J. Solid State Chem.*, 1981, **39**, 277–287.

25 T. Tsuboi and W. Kleemann, *J. Phys.: Condens. Matter*, 1994, **6**, 8625.

26 V. I. Sokolov, V. A. Pustovarov, V. N. Churmanov, V. Y. Ivanov, N. B. Gruzdev, P. S. Sokolov, A. N. Baranov and A. S. Moskvin, *Phys. Rev. B*, 2012, **86**, 115128.

27 M. Beye, R. Y. Engel, J. O. Schunck, S. Dziarzhytski, G. Brenner and P. S. Miedema, *J. Phys.: Condens. Matter*, 2018, **31**, 014003.

28 R. Y. Engel, P. S. Miedema, D. Turenne, I. Vaskivskyi, G. Brenner, S. Dziarzhytski, M. Kuhlmann, J. O. Schunck, F. Döring, A. Styervoyedov, S. S. P. Parkin, C. David, C. Schüßler-Langeheine, H. A. Dürr and M. Beye, *Appl. Sci.*, 2020, **10**, 6947.

29 B. L. Henke, E. M. Gullikson and J. C. Davis, *At. Data Nucl. Data Tables*, 1993, **54**, 181–342.

30 C. Gahl, A. Azima, M. Beye, M. Deppe, K. Döbrich, U. Hasslinger, F. Hennies, A. Melnikov, M. Nagasono, A. Pietzsch, M. Wolf, W. Wurth and A. Föhlisch, *Nat. Photonics*, 2008, **2**, 165–169.

31 D. Alders, T. Hibma, G. A. Sawatzky, K. C. Cheung, G. E. van Dorssen, M. D. Roper, H. A. Padmore, G. van der Laan, J. Vogel and M. Sacchi, *J. Appl. Phys.*, 1997, **82**, 3120–3124.

32 K. Ohta and H. Ishida, *Appl. Spectrosc.*, 1988, **42**, 952–957.

33 T. G. Mayerhöfer and J. Popp, *Spectrochim. Acta, Part A*, 2019, **213**, 391–396.

34 M. W. Haverkort, S. I. Csiszar, Z. Hu, S. Altieri, A. Tanaka, H. H. Hsieh, H.-J. Lin, C. T. Chen, T. Hibma and L. H. Tjeng, *Phys. Rev. B*, 2004, **69**, 020408(R).

35 M. M. El-Nahass, M. Emam-Ismail and M. El-Hagary, *J. Alloys Compd.*, 2015, **646**, 937–945.

36 R. J. Radwanski and Z. Ropka, *Acta Phys. Pol., A*, 2008, **114**, 213–218.

37 H. Y. Peng, Y. F. Li, W. N. Lin, Y. Z. Wang, X. Y. Gao and T. Wu, *Sci. Rep.*, 2012, **2**, 442.

38 R. J. O. Mossanek, G. Domínguez-Cañizares, A. Gutiérrez, M. Abbate, D. Díaz-Fernández and L. Soriano, *J. Phys.: Condens. Matter*, 2013, **25**, 495506.

39 J. Y. Zhang, W. W. Li, R. L. Z. Hoye, J. L. MacManus-Driscoll, M. Budde, O. Bierwagen, L. Wang, Y. Du, M. J. Wahila, L. F. J. Piper, T.-L. Lee, H. J. Edwards, V. R. Dhanak and K. H. L. Zhang, *J. Mater. Chem. C*, 2018, **6**, 2275–2282.

40 F. Novelli, G. De Filippis, V. Cataudella, M. Esposito, I. Vergara, F. Cilento, E. Sindici, A. Amaricci, C. Giannetti, D. Prabhakaran, S. Wall, A. Perucchi, S. Dal Conte, G. Cerullo, M. Capone, A. Mishchenko, M. Grüninger, N. Nagaosa, F. Parmigiani and D. Fausti, *Nat. Commun.*, 2014, **5**, 5112.

41 S. Kovalev, Z. Wang, J.-C. Deinert, N. Awari, M. Chen, B. Green, S. Germanskiy, T. V. A. G. de Oliveira, J. S. Lee, A. Deac, D. Turchinovich, N. Stojanovic, S. Eisebitt, I. Radu, S. Bonetti, T. Kampfrath and M. Gensch, *J. Phys. D: Appl. Phys.*, 2018, **51**, 114007.

42 T. Moriyama, K. Hayashi, K. Yamada, M. Shima, Y. Ohya and T. Ono, *Phys. Rev. Mater.*, 2020, **4**, 074402.

43 T. Kampfrath, A. Sell, G. Klatt, A. Pashkin, S. Mährlein, T. Dekorsy, M. Wolf, M. Fiebig, A. Leitenstorfer and R. Huber, *Nat. Photonics*, 2011, **5**, 31–34.

44 J. Nishitani, T. Nagashima and M. Hangyo, *Phys. Rev. B*, 2012, **85**, 174439.

45 S. Baierl, J. H. Mentink, M. Hohenleutner, L. Braun, T.-M. Do, C. Lange, A. Sell, M. Fiebig, G. Woltersdorf, T. Kampfrath and R. Huber, *Phys. Rev. Lett.*, 2016, **117**, 197201.

46 T. Kohmoto, T. Moriyasu, S. Wakabayashi, H. Jinn, M. Takahara and K. Kakita, *J. Infrared, Millimeter, Terahertz Waves*, 2018, **39**, 77–92.

47 Z. Wang, S. Kovalev, N. Awari, M. Chen, S. Germanskiy, B. Green, J.-C. Deinert, T. Kampfrath, J. Milano and M. Gensch, *Appl. Phys. Lett.*, 2018, **112**, 252404.

48 O. V. Chefonov, A. V. Ovchinnikov, C. P. Hauri and M. B. Agranat, *Opt. Express*, 2019, **27**, 27273–27281.

49 T. Moriyama, K. Hayashi, K. Yamada, M. Shima, Y. Ohya, Y. Tserkovnyak and T. Ono, *Phys. Rev. B*, 2020, **101**, 060402(R).

50 R. Gómez-Abal, O. Ney, K. Satitkovitchai and W. Hübner, *Phys. Rev. Lett.*, 2004, **92**, 227402.

Chapter 4

Non-Linear X-ray Absorption Spectroscopy

By definition, non-linear light-matter interaction scales with the higher powers (≥ 2) of the applied light field, and thus requires significant intensities to become relevant next to the leading linear term of Eq. 2.33. Consequently, it is fundamental to the development of non-linear X-ray spectroscopy to understand the interaction of high X-ray fluences with relevant materials in detail.

Due to the high pulse energy and short overall pulse duration (tens of fs), the absorption of focused XFEL-pulses leads to extreme excitations of the electronic system. Such excitations of matter by XFEL radiation into highly ionized plasma-states has been studied for various material systems from atoms [53, 54] over molecules [55–57] to atomic clusters [58–60] and solids [22–25, 28–35] by analyzing the X-ray emission and ion-time-of-flight spectra of the plasma.

This chapter is in particular concerned with the transmission of high-fluence X-rays through solids, where the non-linearities are primarily caused by non-parametric effects: The fluence-dependence of the overall pulse absorption emerges because, over the entire duration of the pulse, the X-rays act simultaneously as a pump that excites the material, and as a probe that is sensitive to the electronic system. In addition, the electronic system reacts with its own dynamics to the X-ray excitation on the same femtosecond time scale, which also affects the further interaction with the X-ray pulse.

Earlier studies of X-ray transmission through metals found that the core-valence transition saturates, leading to induced transparency of the material, also referred to as *saturable absorption* [26, 27, 63, 64, 66–70]. While these studies were mostly limited to transmission measurements either at specific photon energies or spectra at one or two fluences, in the publication below, we recorded a set of XANES spectra of the Ni L_3-edge from a range over more than three orders of magnitude in fluence. We observed not only a fluence-dependent increase of transmission (saturation) on and beyond the resonance, but also a decrease of transmission before the resonance onset, as well as a red-shift of the absorption peak of 0.9 ± 0.1 eV.

Due to the sensitivity of XANES to the unoccupied distribution of electronic valence states, this gives us insights into the distribution of the valence electrons. Based on the information gained through the fluence-dependence of the spectra, we model the history of the material's electronic system dynamics within the time window of interaction with the XFEL pulse.

To this purpose we constructed a rate model, which we describe in detail in the second publication enclosed in this chapter, *A Rate Model of Electron Populations for Non-linear High-Fluence X-ray Absorption Near-Edge Spectra*. The term rate model, in this context, implies a finite-element simulation implementing differential equations that quantify rates with which the relevant physical processes occur, in order to iteratively reconstruct the temporal development of the electronic state and X-ray photon density in time and space, tracked for each volume-element (voxel) of the sample. This type of phenomenological model operates in terms of volume-averaged, non-quantized properties and rates, which is fundamentally different to e.g. Monte-Carlo simulations, where a large set of individual particle interactions is computed and finally averaged to derive macroscopic results.

Simpler implementations of rate models that involve only three states[1] have been successfully utilized to characterize saturated absorption at specific photon-energies [66, 75]. In order to extend such a model to resolve the transmission behavior around an absorption edge, it proved necessary to fully resolve the non-thermal energy distribution of valence electrons for each simulated voxel, which implies tracking a much larger number of electronic states [76]. We further constructed the equation system such that all state differentials are assembled as a sum of rates of the relevant physical processes.

In contrast to, e.g. time-dependent density functional theory, this allows a rather straightforward interpretation of how various parameters of the experiment or the material manifest in the predicted spectra, which we demonstrate in form of a brief parameter study. We find that, despite utilizing multiple approximations in the interest of simplicity and computational tractability, our model reproduces the majority of the observed fluence-dependent changes in the measured non-linear XANES spectra. Thus, our model provides a relatively simple, largely quantitative understanding of the temporal evolution of the system and the processes responsible for spectral changes, making it a valuable tool in the planning and interpretation of future high-fluence and non-linear X-ray studies.

At the danger of repeating some contents of chapter 2 and the upcoming papers, I will for the reader's convenience briefly list the relevant processes considered in the rate model in advance:

- **Resonant absorption and stimulated emission** refer to radiative transitions between the resonant core level (in case of the presented measurements, the $2p_{3/2}$ electrons) and the valence system. Since both processes use the same interaction cross-section with photons, they can be described with the same rate equation which changes sign depending on the difference in relative population between core level and resonant valence state.
- **Non-resonant absorption** refers to absorption at electrons other than the resonant core level. Such an absorption event creates high-energy photo-electrons which later scatter with the valence electron system.

---

[1] (These usually represent a ground state, a core-excited state and an intermediate/valence-excited state.

- **Core-hole decay** in the soft X-ray regime occurs predominantly via Auger-Meitner decay (see section 2.6), which also leads to the emission of high-energy electrons. The radiative decay channel (fluorescence) is neglected in our model due to its small yield compared to the Auger process, which is further reduced when stimulated emission becomes relevant as an additional competing decay channel.
- **Scattering** of photo- and Auger-electrons with other electrons ultimately leads to many low-energy valence excitations, as each high-energy electron triggers a cascade of secondary electron scattering events. This complex many-body problem is represented in our model by a much-simplified description of electron energy redistribution.
- **Thermalization** describes the tendency of the system to return to an equilibrium state in accordance with its current internal energy. This process is mediated by a multitude of low-energy scattering processes. Since coupling to the nuclear lattice typically occurs on a time-scale that is slower than the typical XFEL pulse duration (see section 2.4.2.1), we limit our description to the isolated electronic system.

With this introduction, I present the following two publications back-to-back, including the supplemental material to [4], which covers the extensive data analysis effort that was required to compile the non-linear spectra and associate reliable fluence-values with each XFEL-shot.

The following publications are reproduced from [4] and [5] in accordance with the Creative Commons Attribution-ShareAlike 4.0 International license under which the articles are published.

Electron Dynamics at High-Energy Densities in Nickel from Non-linear Resonant X-ray Absorption Spectra

Robin Y. Engel,[1, 2] Oliver Alexander,[3] Kaan Atak,[1] Uwe Bovensiepen,[4, 5] Jens Buck,[1, 6] Robert Carley,[7] Michele Cascella,[8] Valentin Chardonnet,[9] Gheorghe Sorin Chiuzbaian,[9] Christian David,[10] Florian Döring,[10] Andrea Eschenlohr,[4] Natalia Gerasimova,[7] Frank de Groot,[11] Loïc Le Guyader,[7] Oliver S. Humphries,[7] Manuel Izquierdo,[7] Emmanuelle Jal,[9] Adam Kubec,[10] Tim Laarmann,[1, 12] Charles-Henri Lambert,[13] Jan Lüning,[14] Jonathan P. Marangos,[3] Laurent Mercadier,[7] Giuseppe Mercurio,[7] Piter S. Miedema,[1] Katharina Ollefs,[4] Bastian Pfau,[15] Benedikt Rösner,[10] Kai Rossnagel,[1, 6] Nico Rothenbach,[4] Andreas Scherz,[7] Justine Schlappa,[7] Markus Scholz,[1, 7] Jan O. Schunck,[1, 2] Kiana Setoodehnia,[7] Christian Stamm,[13, 16] Simone Techert,[1, 17] Sam M. Vinko,[18, 19] Heiko Wende,[4] Alexander A. Yaroslavtsev,[20] Zhong Yin,[21, 22] and Martin Beye[1, 2]

[1] *Deutsches Elektronen-Synchrotron DESY, Notkestr. 85, 22607 Hamburg, Germany*
[2] *Department of Physics, Universität Hamburg, Luruper Chaussee 149, 22761 Hamburg, Germany*
[3] *Imperial College London, Department of Physics,*
Exhibition Rd, London SW7 2BX, United Kingdom
[4] *Faculty of Physics and Center for Nanointegration Duisburg-Essen (CENIDE),*
University of Duisburg-Essen, Lotharstr. 1, 47057 Duisburg, Germany
[5] *Institute for Solid State Physics, University of Tokyo, Kashiwa, Chiba, 277-8581, Japan*
[6] *Christian-Albrechts-Universität zu Kiel, Institut für Experimentelle*
und Angewandte Physik, Leibnizstraße 11-19, 24118 Kiel, Germany
[7] *European XFEL, Holzkoppel 4, 22869 Schenefeld, Germany*
[8] *MAX IV Laboratory, Lund University, PO Box 118, SE-221 00 Lund, Sweden*
[9] *Sorbonne Université, CNRS, Laboratoire de Chimie Physique-Matière et Rayonnement,*
4 Pl. Jussieu Barre 43-44, 75005 Paris, France
[10] *Paul Scherrer Institut, Forschungsstrasse 111, 5232 Villigen, Switzerland*
[11] *Utrecht University, Debye Institute for Nanomaterials Science,*
Inorganic Chemistry and Catalysis, Princetonplein 1,
Universiteitsweg 99, 3584 CC Utrecht, Netherlands
[12] *The Hamburg Centre for Ultrafast Imaging CUI,*
Luruper Chaussee 149, 22761 Hamburg, Germany
[13] *Department of Materials, ETH Zurich, 8093 Zurich, Switzerland*
[14] *Helmholtz-Zentrum Berlin für Materialien und Energie GmbH, Hahn-Meitner-Platz 1, 14109 Berlin, Germany*
[15] *Max Born Institute for Nonlinear Optics and Short Pulse Spectroscopy, Max-Born-Str. 2A, 12489 Berlin, Germany*
[16] *Institute for Electric Power Systems, University of Applied Sciences*
and Arts Northwestern Switzerland, 5210 Windisch, Switzerland
[17] *Institute for X-ray Physics, Goettingen University,*
Friedrich Hund Platz 1, 37077 Goettingen, Germany
[18] *Department of Physics, Clarendon Laboratory, University of Oxford,*
Parks Road, Oxford OX1 3PU, United Kingdom
[19] *Central Laser Facility, STFC Rutherford Appleton Laboratory, Didcot OX11 0QX, United Kingdom*
[20] *Uppsala University, Department of Physics and Astronomy, Regementsvägen 1 Uppsala, Sweden*
[21] *International Center for Synchrotron Radiation Innovation Smart,*
Tohoku University, 2-1-1 Katahira, Aoba-ku, Sendai, Miyagi 980-8577, Japan
[22] *ETH Zürich, Laboratorium für Physikalische Chemie,*
Vladimir-Prelog-Weg 1-5, 8093 Zürich, Switzerland

(Dated: November 30, 2022)

The pulse intensity from X-ray free-electron lasers (FELs) can create extreme excitation densities in solids, entering the regime of non-linear X-ray-matter interactions. We show L_3-edge absorption spectra of metallic nickel thin films with fluences entering a regime where several X-ray photons are incident per absorption cross-section. Main features of the observed non-linear spectral changes are described with a predictive rate model for electron population dynamics during the pulse, utilizing a fixed density of states and tabulated ground-state properties.

The modern understanding of complex solid materials relies on appropriate approximations to the unabridged quantum mechanical description of the full, correlated many-body problem. To assess the predictive power of theoretical models and the selected approximations, detailed experimental studies far away from known territory are especially insightful. Absorbing the high power densities available from an X-ray free-electron laser (FEL) in a solid metal generates a very unusual state of warm dense matter far from equilibrium: Individual electronic excitations reach up to hundreds of eV and excitation levels average out to many eV per atom [1–9]. As the absorption of an intense X-ray pulse depends on the changes it drives in the electronic system [10–16], a single-pulse non-linear absorption measurement can be used to investigate its evolution on the timescale of the pulse duration.

We present fluence-dependent X-ray absorption spectra recorded with monochromatic X-rays on metallic nickel thin films around the nickel $2p_{3/2}$ (L_3) edge, revealing a changing valence electron system around the Fermi level as a consequence of the high excitation densities from fluences up to 60 J/cm^2 (corresponding to $2{\times}10^{15}$ W/cm^2).

The electronic processes that ensue after the absorption of photons at core levels trigger a complex dynamical process that is challenging to treat in purely *ab-initio* simulations [17–21]. Here, we take an alternative approach and develop a simple rate equation model that provides an intuitive understanding of the relevant processes [22]. The resulting picture of the evolution of electronic populations within a fixed ground-state density of states successfully describes the largest part of the non-linear changes in the spectra. This corroborates the dominant impact of electron redistribution from the strong non-equilibrium state towards a thermalized electronic system. Some of the observed changes, especially in the close vicinity of the resonance, deviate from the predictions of the rate model and call for more evolved theories. Here, our work provides a benchmark to identify observations of advanced physical processes and effects. While this letter discusses the experiment and resulting insights, we lay out the framework of the model in detail in a separate publication [22].

Additionally, our straightforward picture of intense core-resonant X-ray pulse interaction with the valence system of a $3d$ metal lays a solid knowledge-based foundation for the planning and interpretation of non-linear X-ray spectroscopy experiments at FELs; in particular, the relevance of electronic scattering processes observed here is expected to affect methods relying on stimulated emission from core excitations and X-ray or X-ray/optical wave-mixing [23–38].

X-ray absorption spectra of the nickel $2p_{3/2}$ (L_3) edge were recorded at the Spectroscopy and Coherent Scattering Instrument (SCS) of the European XFEL [40].

The XAS spectra were measured by continuously scanning the SASE3 monochromator [41] (synchronized with the undulator gap) back-and-forth many times in the range 846-856 eV. The photon bandwidth was about 420 meV and the FEL pulse duration on the sample was about 30 fs FWHM. The overall beam intensity was controlled using a gas attenuator filled with nitrogen and monitored using an X-ray gas-monitor (XGM) downstream of the monochromator [42, 43].

For X-ray absorption measurements at FELs based on Self-Amplified Spontaneous Emission (SASE), beam-splitting schemes can deliver optimal normalization of SASE-fluctuations [44–46]. Here, a focusing and beam-splitting zone plate also creates the required tight focusing to achieve extreme fluences. Figure 1 shows the schematic experimental layout.

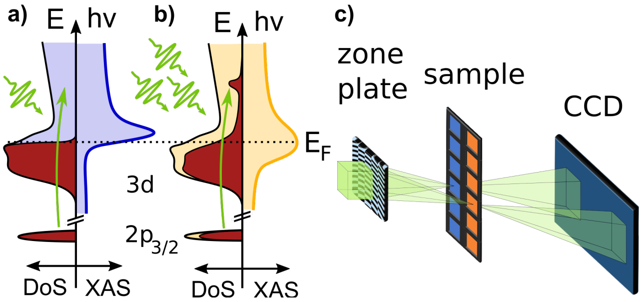

FIG. 1. **(a&b) Sketch of absorption at different fluences.** The unoccupied states determine the XAS spectrum as they are probed by core-resonant photons. **(a)** In the low-fluence case (blue unoccupied states and resulting spectrum), the electronic system mostly remains in the ground state. **(b)** In the high-fluence case (yellow unoccupied states and spectrum), later parts of the X-ray pulse probe a hot electronic system and experience spectral bleaching at the probed photon energy.
Setup for non-linear XAS (c) The split-beam-normalization scheme uses a special zone plate [39], which generates two adjacent beam foci for transmission through the sample and a reference membrane before the beams impinge on the detector.

The zone plate combines an off-axis Fresnel structure for focusing and a line grating for beam-splitting in a single optical element [39]. It thus produces two μm-sized, identical foci in the sample plane, 1.9 mm apart, originating from the first-order diffraction of the zone plate, as well as the positive and negative first orders of the line grating.

The sample has a square support of 25 mm size, containing Si_3N_4 membrane windows (orange in Figure 1) of 0.5 mm size and 200 nm thickness with a distance of 2 mm between adjacent windows. Every second pair of rows (blue in Figure 1) was additionally coated with a 20 nm sample layer of polycrystalline metallic Ni by sputter deposition, on top of a 2 nm bonding layer of Ta; a 2 nm Pt capping layer prevents oxidation during sample-handling.

The sample frame was positioned such that one zone plate focus impinged on a nickel-coated membrane, while the other hit a bare silicon-nitride membrane. Thus, the difference in transmission of both beams can be attributed solely to the nickel film.

The detector was a fast readout-speed charge-coupled device (FastCCD) with high dynamic range, enabling 10 Hz read-out and increasing the fluence range available to the experiment [47–49]. Due to the unstable detector temperature, significant retroactive calibration of the detector was necessary (see supplement). To prevent detector saturation, an additional aluminum filter of about 13 μm thickness was used between sample and detector for measurements with the unattenuated beam.

During these high-intensity measurements, sample and

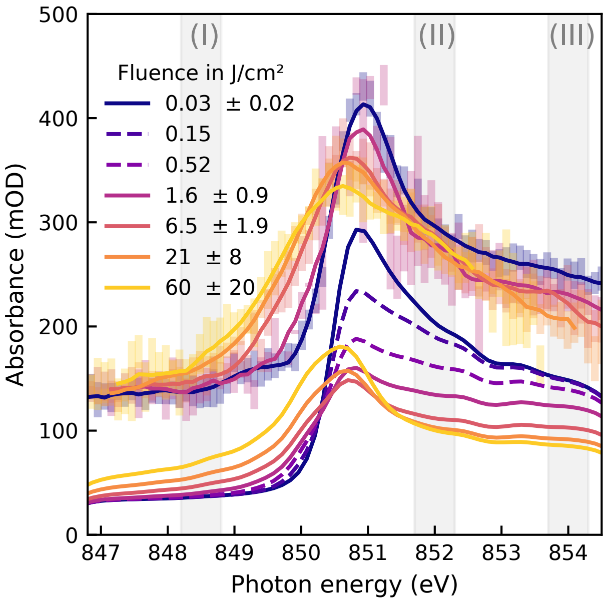

FIG. 2. **Fluence-dependent Ni L_3-edge spectra, measured (top) and simulated (bottom).** The fluence of events contributing to each spectrum is given in the legend in terms of mean and standard deviation. Dashed simulated spectra do not have a corresponding measurement. The regions of interest from which absorbance changes shown in panels b), d), and e) of Figure 3 were quantified are shaded and labeled (I), (II), and (III), respectively. The error bars are shown for the measured spectra and represent the 95% confidence intervals for each bin of 102 meV width; solid lines of the measured spectra are smoothed using a Savitzky-Golay filter using windows of 21 bins and 4th-order polynomials. The experimental spectra are vertically offset by 100 mOD.

reference films were locally damaged by intense individual FEL shots. Thus, the FEL was operated in single-shot mode at 10 Hz repetition rate, and the sample was scanned through the beam continuously at $0.5\,\mathrm{mm}\cdot\mathrm{s}^{-1}$, resulting in 10 shots per membrane window.

The shot craters in the reference membranes were later analyzed with scanning electron microscopy (SEM) to determine the effective focal size at specific photon energies. The resulting spot sizes were used to calibrate ray-tracing calculations which delivered the photon-energy-dependent spot size, ranging from $0.4\,\mu\mathrm{m}^2$ to about $3\,\mu\mathrm{m}^2$ (see supplement for details on the spot size determination).

Figure 2 shows the spectra for the nickel L_3-edge next to simulated spectra for increasing X-ray fluence over more than 3 orders or magnitude, from 0.03 to 60 $\mathrm{J/cm}^2$. Each measured point represents an average of several FEL shots, sorted by X-ray fluence and photon energy. The varying statistical uncertainty is a result of the pulse intensity fluctuations of monochromatized SASE radiation [50] in combination with photon energy-dependent spot sizes (see supplement for details on the shot sorting).

We observe four main fluence-dependent effects, which we quantify and compare to the simulated results in Figure 3: a) a red-shift of the absorption peak of up to 0.9 ± 0.1 eV in the rising flank; b) an increase of the pre-edge absorbance, as the rising edge of the absorption peak shifts and broadens; c) a reduced peak absorbance and d), e) a reduced post-edge absorbance. The integration regions from which the effects b), d) and e) are derived, are highlighted in Figure 2 as (I), (II) and (III), respectively. The shift of the absorption edge is quantified by the photon energy at which the absorbance reaches half of the peak value; its uncertainty is propagated from the statistical uncertainty of the absorption peak measurement.

Before we analyze these observations in detail, let us quickly paraphrase our modeling approach [22]: In contrast to earlier rate models [12, 51], we describe the evolution of the electronic system with an energy-resolved population of the valence band. Tracking the full non-thermal population history proved crucial to describe the non-linear absorption changes near and around the Fermi level. As coupling between electrons and phonons in metals is typically not yet important on the timescale of 30 fs [52–54] and we do not account for collective electron correlation effects, we test the approximation that the Density of States (DoS) remains unchanged within the pulse duration.

Transition rates between electronic states are determined by scaling ground state rates with the populations of initial and final states. The relevant process rates are compiled into differentials of electronic populations and photon density in space and time and implemented in a finite-element simulation to derive the electron population history and ultimately the X-ray transmission of a three-dimensional sample.

The model implements the processes of resonant absorption from the $2p_{3/2}$ core level and non-resonant absorption from other (mostly valence) electrons. Stimulated emission is described as a time-inverted resonant absorption process. Electronic thermalization is modeled with a bulk timescale τ_{th} (essentially quantifying electron-electron scattering) that moves the non-thermal valence electron distribution towards a target Fermi-Dirac distribution that corresponds to the momentary internal energy and population of the valence band. Finally, scattering cascades initiated by fast Auger-electrons and photo-electrons from non-resonant absorption are parameterized by another scattering time τ_{scatt}.

With this simple description of the underlying processes, we provide a microscopic picture of the electronic system and its interaction with resonant X-rays as a complementary approach to more complex calculations [20, 21].

Solely considering the population dynamics of the electronic system, the simulation already achieves good agreement with the experimental data across more than three orders of magnitude in fluence. This is particularly remarkable since nearly all input parameters are experi-

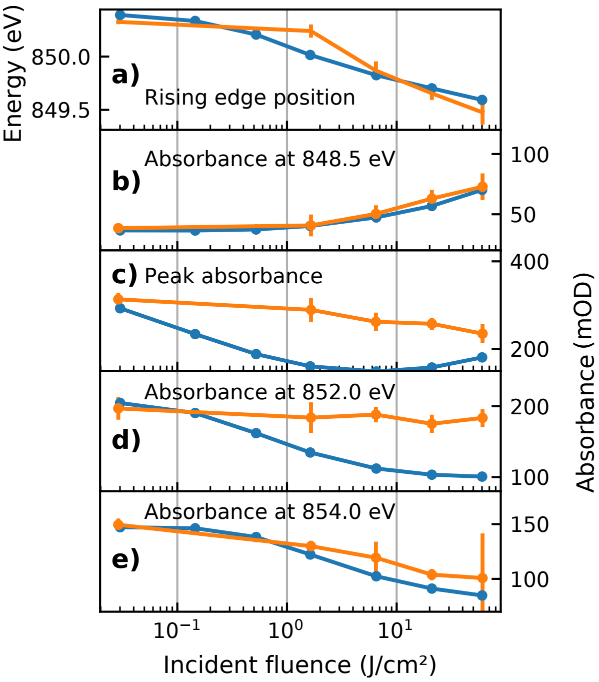

FIG. 3. **Comparison of spectral effects** between simulation (blue lines) and experiment (orange lines with error bars). The shift of absorption edge in panel a) represents the photon energy at which the half-maximum of the absorption peak is reached. The absorbance changes in panels b), d) and e) are integrated from the gray shaded regions in Figure 2, while panel c) shows the global maximum of the spectrum.

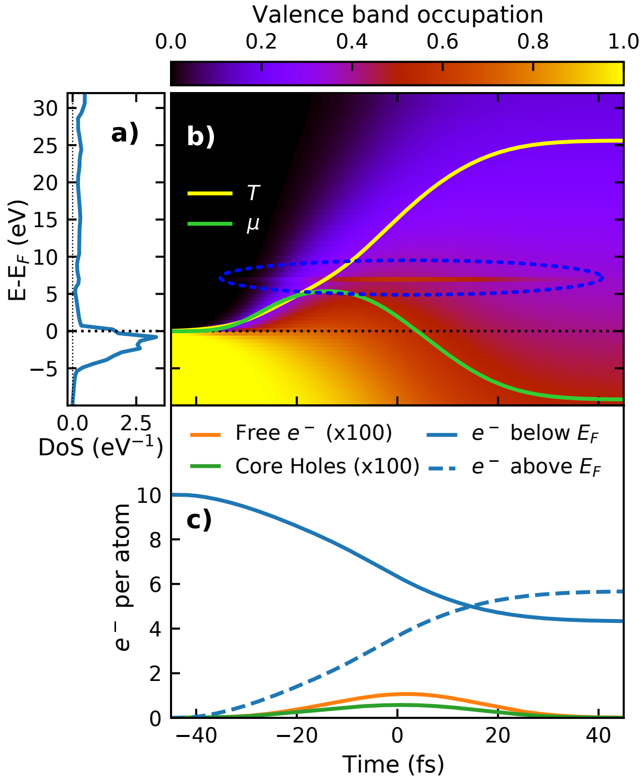

FIG. 4. **Evolution of electronic populations (simulation)** in a single voxel at the sample surface for a pulse of 858.3 eV, with a pulse energy of 30 J/cm^2. Panel a) shows the total DoS used as an input for the simulation. Panel b) shows the energy-resolved (relative to the Fermi energy) occupation of the valence band over time. The population (in electrons/atom/eV) is the product of the DoS and the occupation. The thermalized valence occupation lags a few femtoseconds behind the current chemical potential μ; the temperature T of the valence system rises rapidly, ultimately reaching up to 25 eV. The bleaching of valence states (highlighted with a blue dotted ellipse) is visible as a high non-thermal population at the resonant photon energy around 7 eV above the Fermi level. Panel c) shows the number of core holes and free electrons over time, as well as the number of electrons in the valence system below and above the Fermi energy.

mental parameters or well-known ground-state properties of the material, such as density, electronic configuration, and ground-state spectrum. Only the valence thermalization time τ_{th} and electron scattering time τ_{scatt} were varied to achieve the best match to the experimental results. The found value $\tau_{\text{th}} = 6$ fs compares well to recent estimates for excitations on this energy scale [33, 38, 55, 56].

The time constant $\tau_{\text{scatt}} = 1.5$ fs characterizes the secondary electron scattering cascade which transfers energy (and population) from fast electrons to (unoccupied) valence states. The constant summarizes many individual electron scattering events and compares to the tabulated time between individual collisions in ground-state nickel of roughly 100 attoseconds [57].

Figure 4 shows an example of a simulated valence band population history, specifically from the uppermost 4 Å thick layer of the sample, excited with a Gaussian pulse profile centered around $t = 0$ with 30 fs FWHM duration and 30 J/cm^2 fluence. While panel a) shows the calculated DoS as used by the simulation and published in [58, 59], the colormap in b) shows the occupation of these states over time. Panel c) shows the number of electrons per atom in the valence band below and above the Fermi level (blue solid and dashed curves, respectively) as well as the average number of core holes and the number of free electrons over time. Even though the direct interaction with the photons creates core holes via resonant absorption and free electrons via non-resonant absorption, the excitation energy of both processes is so quickly transferred to the valence electrons that only the valence electron distribution ever deviates strongly from the ground state. By the end of the pulse in this example, more than half of the 3d valence electrons are excited to valence states above the Fermi level, while the highest instantaneous number of core holes was only about one per 100 atoms, as shown in Figure 4 c). Due to the small-bandwidth excitation, the core- and resonant valence states operate like a two-level system. Since the number of resonant valence states is small in comparison to the number of core electrons, the resonant absorption process saturates due to occupied valence states long before the core level is depleted. A heated Fermi-Dirac distribution further contributes to the occupation of states above the Fermi level.

Since in our experiment, the same monochromatic pulse excites and probes the sample, the situation is different for energies below the edge: absorption only rises after non-resonant absorption has led to sufficient electronic heating until the tail of the hot hole distribution reaches the probed energy. Only then, additional resonant absorption begins to occur and accelerates further electronic heating and in turn additional pre-edge absorption. Since this process occurs exponentially faster near the absorption edge, it contributes significantly to the observed spectral red-shift (see Figure 3 a) and b)).

Another cause of the observed edge shift is the shift of the chemical potential μ, which strongly depends on the exact shape of the DoS and is shown in Figure 4 b) as a green line. Initially, μ increases with absorbed fluence, as thermally excited electrons from the $3d$ states must spread out in energy to the lower DoS above the Fermi level. With rising electronic temperature, the high DoS of the $3d$ states becomes less relevant and the chemical potential drops again as expected in regular metals. A similar evolution of the chemical potential and electronic temperature was predicted for optically excited nickel by previous experiments and calculations [4, 60–62].

A significant deviation between model and experiment can be observed at the resonance peak itself, where the simulated electron dynamics lead us to expect a much stronger saturation effect than observed experimentally (Figure 3 c)). This underestimation may be related to a fluence-dependent decrease of the excited state lifetime and consequent energetic broadening of the resonant core-valence transition, which is not considered in our model. While it is unsurprising to find additional resonant effects in the resonance peak itself, the lack of any significant saturation around 852 eV (Figure 3 d)) is even more surprising. Both disagreements point to additional physical effects and call for more sophisticated models.

We speculatively propose mechanisms which could contribute to these disagreements: The transition matrix elements could get modified at higher excitation densities, especially around the resonance, while we model the absorption only based on the ground-state spectrum. An energy dependence of the electron-electron scattering cross-section could allow for particularly fast scattering of electrons with certain energies, counteracting the saturation. Furthermore, a collective, correlated response of the electronic system could modify the DoS or the transitions even on the fast time scale of the FEL pulse duration [63]. Despite these remaining discrepancies, the main aspects of the spectral changes are covered in our very simple population dynamics model.

We want to point out that substantially smaller spectral red-shifts were observed before in nickel after excitation with optical lasers, albeit at three orders of magnitude lower excitation fluence. These required qualitatively different interpretations [56, 63–65], where the explanation for time-dependent changes included a variable DoS, calculated using (Time-Dependent) Density Functional Theory (TD)DFT; this dependency is overshadowed in our high-fluence study by the effects of electron population dynamics.

To summarize, we interpret the fluence-dependent near-edge X-ray absorption spectra of the nickel $2p_{3/2}$ core level at X-ray fluences of up to $60\,\mathrm{J/cm^2}$. We propose a rate-equation model, describing the various excitation and decay processes that connect core- and valence electronic states using differential equations based on scaling of known ground-state properties with the evolving electron populations. For the measured spectra of metallic nickel, the model successfully predicts the increase of absorption before and its decrease beyond the resonance, as well as the observed shift of the absorption peak over more than three orders of magnitude in fluence.

It therefore allows us to identify the most important processes responsible for spectral changes: Heating of valence electrons due to secondary electron cascades from Auger electrons, as well as electrons emitted from the valence band due to non-resonant absorption, appeared particularly relevant. Furthermore, saturation appears dominated to by the heated valence states rather than the core holes.

This study provides the fingerprints of how strong X-ray fluences may alter the electronic system and thus the spectra in studies, where the X-ray pulses were originally assumed to be non-disturbing. It becomes clear that a complete modeling of high-fluence spectra needs to build upon dominant population dynamics and requires special treatment around resonances. This provides an excellent benchmark for sophisticated theories. Our results also apply to the resonant regime which is particularly interesting for pioneering non-linear X-ray studies.

ACKNOWLEDGMENTS

We acknowledge European XFEL in Schenefeld, Germany, for provision of X-ray free-electron laser beamtime at the SCS instrument and would like to thank the staff for their assistance. Funding by the Deutsche Forschungsgemeinschaft (DFG, German Research Foundation) - Project-ID 278162697 - SFB 1242 and the Helmholtz Association (grant VH-NG-1105) is gratefully acknowledged. Access to Synchrotron SOLEIL through proposal ID 20160880 for characterization of static properties of the Ni films is acknowledged. Parts of this work were funded by the Swiss National Science Foundation (Grants No. PZ00P2-179944)

AUTHOR CONTRIBUTIONS

M.B., C.D., F.D., L.L.G., J.L., J.P.M., B.R. and S.T. conceptualized and planned the experiment; M.C., C.D., F.D., N.G., L.L.G., M.I., E.J., A.K., C.-H.L., L.M., B.P., B.R., A.S., K.S., C.S., H.W. and A.Y. prepared the measurement apparatus and samples; O.A., K.A., M.B., J.B., R.C., M.C., V.C., G.S.C., C.D., F.D., R.Y.E., A.E., N.G., L.L.G., O.S.H., M.I., L.M., G.M., P.S.M., B.R., N.R., A.S., J.S., S.T. A.Y. and Z.Y. performed the experiment; O.A., R.Y.E, L.L.G., O.S.H., B.R. and N.R. analyzed and visualized the results; M.B. and R.Y.E. wrote the manuscript; M.B., U.B., C.D., R.Y.E., A.E., L.L.G., O.S.H., M.I., E.J., T.L., P.S.M., K.O., K.R., M.S., J.O.S., S.M.V., H.W. and Z.Y. reviewed and edited the manuscript; M.B. and J.P.M. supervised or administered the project.

---

[1] U. Zastrau, C. Fortmann, R. R. Fäustlin, L. F. Cao, T. Döppner, S. Düsterer, S. H. Glenzer, G. Gregori, T. Laarmann, H. J. Lee, A. Przystawik, P. Radcliffe, H. Reinholz, G. Röpke, R. Thiele, J. Tiggesbäumker, N. X. Truong, S. Toleikis, I. Uschmann, A. Wierling, T. Tschentscher, E. Förster, and R. Redmer, Bremsstrahlung and line spectroscopy of warm dense aluminum plasma heated by xuv free-electron-laser radiation, Phys. Rev. E **78**, 066406 (2008).

[2] S. M. Vinko, O. Ciricosta, B. I. Cho, K. Engelhorn, H.-K. Chung, C. R. D. Brown, T. Burian, J. Chalupský, R. W. Falcone, C. Graves, V. Hájková, A. Higginbotham, L. Juha, J. Krzywinski, H. J. Lee, M. Messerschmidt, C. D. Murphy, Y. Ping, A. Scherz, W. Schlotter, S. Toleikis, J. J. Turner, L. Vysin, T. Wang, B. Wu, U. Zastrau, D. Zhu, R. W. Lee, P. A. Heimann, B. Nagler, and J. S. Wark, Creation and diagnosis of a solid-density plasma with an X-ray free-electron laser, Nature **482**, 59 (2012).

[3] B. I. Cho, K. Engelhorn, S. M. Vinko, H.-K. Chung, O. Ciricosta, D. S. Rackstraw, R. W. Falcone, C. R. D. Brown, T. Burian, J. Chalupský, C. Graves, V. Hájková, A. Higginbotham, L. Juha, J. Krzywinski, H. J. Lee, M. Messersmidt, C. Murphy, Y. Ping, N. Rohringer, A. Scherz, W. Schlotter, S. Toleikis, J. J. Turner, L. Vysin, T. Wang, B. Wu, U. Zastrau, D. Zhu, R. W. Lee, B. Nagler, J. S. Wark, and P. A. Heimann, Resonant Kα Spectroscopy of Solid-Density Aluminum Plasmas, Physical Review Letters **109**, 245003 (2012).

[4] O. S. Humphries, R. S. Marjoribanks, Q. Y. van den Berg, E. C. Galtier, M. F. Kasim, H. J. Lee, A. J. F. Miscampbell, B. Nagler, R. Royle, J. S. Wark, and S. M. Vinko, Probing the electronic structure of warm dense nickel via resonant inelastic x-ray scattering, Phys. Rev. Lett. **125**, 195001 (2020).

[5] E. García Saiz, G. Gregori, D. O. Gericke, J. Vorberger, B. Barbrel, R. J. Clarke, R. R. Freeman, S. H. Glenzer, F. Y. Khattak, M. Koenig, O. L. Landen, D. Neely, P. Neumayer, M. M. Notley, A. Pelka, D. Price, M. Roth, M. Schollmeier, C. Spindloe, R. L. Weber, L. Van Woerkom, K. Wünsch, and D. Riley, Probing warm dense lithium by inelastic X-ray scattering, Nature Physics **4**, 940 (2008).

[6] S. M. Vinko, X-ray free-electron laser studies of dense plasmas, Journal of Plasma Physics **81**, 365810501 (2015).

[7] J. E. Bailey, T. Nagayama, G. P. Loisel, G. A. Rochau, C. Blancard, J. Colgan, P. Cosse, G. Faussurier, C. J. Fontes, F. Gilleron, I. Golovkin, S. B. Hansen, C. A. Iglesias, D. P. Kilcrease, J. J. MacFarlane, R. C. Mancini, S. N. Nahar, C. Orban, J. C. Pain, A. K. Pradhan, M. Sherrill, and B. G. Wilson, A higher-than-predicted measurement of iron opacity at solar interior temperatures, Nature **517**, 56 (2015).

[8] P. Hollebon, O. Ciricosta, M. P. Desjarlais, C. Cacho, C. Spindloe, E. Springate, I. C. E. Turcu, J. S. Wark, and S. M. Vinko, Ab initio simulations and measurements of the free-free opacity in aluminum, Physical Review E **100**, 043207 (2019), arXiv:1806.02726.

[9] T. R. Preston, S. M. Vinko, O. Ciricosta, P. Hollebon, H.-K. Chung, G. L. Dakovski, J. Krzywinski, M. Minitti, T. Burian, J. Chalupský, V. Hájková, L. Juha, V. Vozda, U. Zastrau, R. W. Lee, and J. S. Wark, Measurements of the K-Shell Opacity of a Solid-Density Magnesium Plasma Heated by an X-Ray Free-Electron Laser, Physical Review Letters **119**, 085001 (2017).

[10] B. Nagler, U. Zastrau, R. R. Fäustlin, S. M. Vinko, T. Whitcher, A. J. Nelson, R. Sobierajski, J. Krzywinski, J. Chalupsky, E. Abreu, S. Bajt, T. Bornath, T. Burian, H. Chapman, J. Cihelka, T. Döppner, S. Düsterer, T. Dzelzainis, M. Fajardo, E. Förster, C. Fortmann, E. Galtier, S. H. Glenzer, S. Göde, G. Gregori, V. Hajkova, P. Heimann, L. Juha, M. Jurek, F. Y. Khattak, A. R. Khorsand, D. Klinger, M. Kozlova, T. Laarmann, H. J. Lee, R. W. Lee, K.-H. Meiwes-Broer, P. Mercere, W. J. Murphy, A. Przystawik, R. Redmer, H. Reinholz, D. Riley, G. Röpke, F. Rosmej, K. Saksl, R. Schott, R. Thiele, J. Tiggesbäumker, S. Toleikis, T. Tschentscher, I. Uschmann, H. J. Vollmer, and J. S. Wark, Turning solid aluminium transparent by intense soft x-ray photoionization, Nature Physics **5**, 693 (2009).

[11] V. Recoules and S. Mazevet, Temperature and density dependence of XANES spectra in warm dense aluminum plasmas, Physical Review B **80**, 064110 (2009).

[12] A. Di Cicco, K. Hatada, E. Giangrisostomi, R. Gunnella, F. Bencivenga, E. Principi, C. Masciovecchio, and A. Filipponi, Interplay of electron heating and saturable absorption in ultrafast extreme ultraviolet transmission of condensed matter, Phys. Rev. B **90**, 220303(R) (2014).

[13] D. S. Rackstraw, O. Ciricosta, S. M. Vinko, B. Barbrel, T. Burian, J. Chalupský, B. I. Cho, H.-K. Chung, G. L. Dakovski, K. Engelhorn, V. Hájková, P. Heimann, M. Holmes, L. Juha, J. Krzywinski, R. W. Lee, S. Toleikis, J. J. Turner, U. Zastrau, and J. S. Wark, Saturable absorption of an x-ray free-electron-laser heated solid-density aluminum plasma, Phys. Rev. Lett. **114**, 015003 (2015).

[14] E. Principi, E. Giangrisostomi, R. Cucini, F. Bencivenga,

A. Battistoni, A. Gessini, R. Mincigrucci, M. Saito, S. Di Fonzo, F. D'Amico, A. Di Cicco, R. Gunnella, A. Filipponi, A. Giglia, S. Nannarone, and C. Masciovecchio, Free electron laser-driven ultrafast rearrangement of the electronic structure in Ti, Structural Dynamics **3**, 023604 (2016).

[15] Z. Chen, D. J. Higley, M. Beye, M. Hantschmann, V. Mehta, O. Hellwig, A. Mitra, S. Bonetti, M. Bucher, S. Carron, T. Chase, E. Jal, R. Kukreja, T. Liu, A. H. Reid, G. L. Dakovski, A. Föhlisch, W. F. Schlotter, H. A. Dürr, and J. Stöhr, Ultrafast Self-Induced X-Ray Transparency and Loss of Magnetic Diffraction, Physical Review Letters **121**, 137403 (2018).

[16] H. Yoneda, Y. Inubushi, M. Yabashi, T. Katayama, T. Ishikawa, H. Ohashi, H. Yumoto, K. Yamauchi, H. Mimura, and H. Kitamura, Saturable absorption of intense hard x-rays in iron, Nature communications **5**, 5080 (2014).

[17] M. Chen and K. Lopata, First-Principles Simulations of X-ray Transient Absorption for Probing Attosecond Electron Dynamics, Journal of Chemical Theory and Computation **16**, 4470 (2020).

[18] C. Mo, Z.-G. Fu, P. Zhang, W. Kang, W. Zhang, and X. T. He, First-principles method for x-ray Thomson scattering including both elastic and inelastic features in warm dense matter, Physical Review B **102**, 195127 (2020).

[19] G. O. Williams and M. Fajardo, Collisional ionization and recombination in degenerate plasmas beyond the free-electron-gas approximation, Phys. Rev. E **102**, 063204 (2020).

[20] N. Medvedev, V. Tkachenko, V. Lipp, Z. Li, and B. Ziaja, Various damage mechanisms in carbon and silicon materials under femtosecond x-ray irradiation, 4open **1**, 3 (2018).

[21] V. Lipp, V. Tkachenko, M. Stransky, B. Aradi, T. Frauenheim, and B. Ziaja, Density functional tight binding approach utilized to study x-ray-induced transitions in solid materials, Scientific reports **12**, 1551 (2022).

[22] R. Y. Engel, M. Scholz, J. O. Schunck, and M. Beye, A rate-model for nonlinear x-ray near edge absorption spectra, Jointly submitted to Phys. Rev. B (2022).

[23] S. Mukamel, Multiple core-hole coherence in x-ray four-wave-mixing spectroscopies, Phys. Rev. B **72**, 235110 (2005).

[24] T. E. Glover, D. M. Fritz, M. Cammarata, T. K. Allison, S. Coh, J. M. Feldkamp, H. Lemke, D. Zhu, Y. Feng, R. N. Coffee, M. Fuchs, S. Ghimire, J. Chen, S. Shwartz, D. A. Reis, S. E. Harris, and J. B. Hastings, X-ray and optical wave mixing, Nature **488**, 603 (2012).

[25] M. Beye, S. Schreck, F. Sorgenfrei, C. Trabant, N. Pontius, C. Schüßler-Langeheine, W. Wurth, and A. Föhlisch, Stimulated x-ray emission for materials science, Nature **501**, 191 (2013).

[26] C. Weninger, M. Purvis, D. Ryan, R. A. London, J. D. Bozek, C. Bostedt, A. Graf, G. Brown, J. J. Rocca, and N. Rohringer, Stimulated electronic x-ray raman scattering, Phys. Rev. Lett. **111**, 233902 (2013).

[27] S. Shwartz, M. Fuchs, J. B. Hastings, Y. Inubushi, T. Ishikawa, T. Katayama, D. A. Reis, T. Sato, K. Tono, M. Yabashi, S. Yudovich, and S. E. Harris, X-ray second harmonic generation, Physical Review Letters **112**, 163901 (2014).

[28] K. Tamasaku, E. Shigemasa, Y. Inubushi, T. Katayama, K. Sawada, H. Yumoto, H. Ohashi, H. Mimura, M. Yabashi, K. Yamauchi, and T. Ishikawa, X-ray two-photon absorption competing against single and sequential multiphoton processes, Nature Photonics **8**, 313 (2014).

[29] F. Bencivenga, R. Cucini, F. Capotondi, A. Battistoni, R. Mincigrucci, E. Giangrisostomi, A. Gessini, M. Manfredda, I. P. Nikolov, E. Pedersoli, E. Principi, C. Svetina, P. Parisse, F. Casolari, M. B. Danailov, M. Kiskinova, and C. Masciovecchio, Four-wave mixing experiments with extreme ultraviolet transient gratings, Nature **520**, 205 (2015).

[30] S. Schreck, M. Beye, and A. Föhlisch, Implications of stimulated resonant x-ray scattering for spectroscopy, imaging, and diffraction in the regime from soft to hard x-rays, Journal of Modern Optics **62**, S34 (2015).

[31] R. K. Lam, S. L. Raj, T. A. Pascal, C. D. Pemmaraju, L. Foglia, A. Simoncig, N. Fabris, P. Miotti, C. J. Hull, A. M. Rizzuto, J. W. Smith, R. Mincigrucci, C. Masciovecchio, A. Gessini, E. Allaria, G. De Ninno, B. Diviacco, E. Roussel, S. Spampinati, G. Penco, S. Di Mitri, M. Trovò, M. Danailov, S. T. Christensen, D. Sokaras, T. C. Weng, M. Coreno, L. Poletto, W. S. Drisdell, D. Prendergast, L. Giannessi, E. Principi, D. Nordlund, R. J. Saykally, and C. P. Schwartz, Soft x-ray second harmonic generation as an interfacial probe, Physical Review Letters **120**, 023901 (2018).

[32] K. Tamasaku, E. Shigemasa, Y. Inubushi, I. Inoue, T. Osaka, T. Katayama, M. Yabashi, A. Koide, T. Yokoyama, and T. Ishikawa, Nonlinear spectroscopy with x-ray two-photon absorption in metallic copper, Physical Review Letters **121**, 083901 (2018).

[33] D. J. Higley, A. H. Reid, Z. Chen, A. A. L. Loïc Le Guyader and, T. Liu, T. Chase, G. L. Dakovski, A. Mitra, E. Yuan, H. A. Dürr, W. F. Schlotter, and J. Stöhr, Femtosecond x-ray induced changes of the electronic and magnetic response of solids from electron redistribution, Nature communications **10**, 5289 (2019).

[34] H. Rottke, R. Y. Engel, D. Schick, J. O. Schunck, P. S. Miedema, M. C. Borchert, M. Kuhlmann, N. Ekanayake, S. Dziarzhytski, G. Brenner, U. Eichmann, C. von Korff Schmising, M. Beye, and S. Eisebitt, Probing electron and hole colocalization by resonant four-wave mixing spectroscopy in the extreme ultraviolet, Science Advances **8**, eabn5127 (2022).

[35] J. R. Rouxel, D. Fainozzi, R. Mankowsky, B. Rösner, G. Seniutinas, R. Mincigrucci, S. Catalini, L. Foglia, R. Cucini, F. Döring, A. Kubec, F. Koch, F. Bencivenga, A. A. Haddad, A. Gessini, A. A. Maznev, C. Cirelli, S. Gerber, B. Pedrini, G. F. Mancini, E. Razzoli, M. Burian, H. Ueda, G. Pamfilidis, E. Ferrari, Y. Deng, A. Mozzanica, P. J. M. Johnson, D. Ozerov, M. G. Izzo, C. Bottari, C. Arrell, E. J. Divall, S. Zerdane, M. Sander, G. Knopp, P. Beaud, H. T. Lemke, C. J. Milne, C. David, R. Torre, M. Chergui, K. A. Nelson, C. Masciovecchio, U. Staub, L. Patthey, and C. Svetina, Hard X-ray transient grating spectroscopy on bismuth germanate, Nature Photonics **15**, 499 (2021).

[36] F. Bencivenga, R. Mincigrucci, F. Capotondi, A. Calvi, R. Cucini, L. Foglia, E. Pedersoli, E. Principi, A. Simoncig, P. Cinquegrana, M. B. Danailov, G. De Ninno, S. Di Mitri, G. Gaio, A. Gessini, L. Giannessi, N. Mahne, M. Manfredda, I. P. Nikolov, G. M. Penco, L. Raimondi, P. R. Ribic, C. Svetina, M. Trovo, M. Zangrando, and

C. Masciovecchio, An approach for realizing four-wave-mixing experiments stimulated by two-color extreme ultraviolet pulses, in *International Conference on X-Ray Lasers 2020*, July 2021, edited by D. Bleiner (SPIE, 2021) p. 28.

[37] S. Wirok-Stoletow, R. Jin, D. Kolbasova, S.-K. Son, A. Aquila, and R. Santra, Nonsequential two-photon absorption in solid Ge irradiated by an intense x-ray free-electron-laser pulse, Physical Review A **106**, 023118 (2022).

[38] D. J. Higley, Z. Chen, M. Beye, M. Hantschmann, A. H. Reid, V. Mehta, O. Hellwig, G. L. Dakovski, A. Mitra, R. Y. Engel, T. Maxwell, Y. Ding, S. Bonetti, M. Bucher, S. Carron, T. Chase, E. Jal, R. Kukreja, T. Liu, A. Föhlisch, H. A. Dürr, W. F. Schlotter, and J. Stöhr, Stimulated resonant inelastic x-ray scattering in a solid, Communications Physics **5**, 1 (2022).

[39] F. Döring, B. Rösner, M. Langer, A. Kubec, A. Kleibert, J. Raabe, C. A. F. Vaz, M. Lebugle, and C. David, Multifocus off-axis zone plates for x-ray free-electron laser experiments, Optica **7**, 1007 (2020).

[40] T. Tschentscher, C. Bressler, J. Grünert, A. Madsen, A. Mancuso, M. Meyer, A. Scherz, H. Sinn, and U. Zastrau, Photon Beam Transport and Scientific Instruments at the European XFEL, Applied Sciences **7**, 592 (2017).

[41] N. Gerasimova, D. La Civita, L. Samoylova, M. Vannoni, R. Villanueva, D. Hickin, R. Carley, R. Gort, B. E. Van Kuiken, P. Miedema, L. Le Guyarder, L. Mercadier, G. Mercurio, J. Schlappa, M. Teichman, A. Yaroslavtsev, H. Sinn, and A. Scherz, The soft X-ray monochromator at the SASE3 beamline of the European XFEL: from design to operation, Journal of Synchrotron Radiation **29**, 1299 (2022).

[42] J. Grünert, M. P. Carbonell, F. Dietrich, T. Falk, W. Freund, A. Koch, N. Kujala, J. Laksman, J. Liu, T. Maltezopoulos, K. Tiedtke, U. F. Jastrow, A. Sorokin, E. Syresin, A. Grebentsov, and O. Brovko, X-ray photon diagnostics at the European XFEL, Journal of Synchrotron Radiation **26**, 1422 (2019).

[43] T. Maltezopoulos, F. Dietrich, W. Freund, U. F. Jastrow, A. Koch, J. Laksman, J. Liu, M. Planas, A. A. Sorokin, K. Tiedtke, and J. Grünert, Operation of X-ray gas monitors at the European XFEL, Journal of Synchrotron Radiation **26**, 1045 (2019).

[44] R. Y. Engel, M. Ekimova, P. S. Miedema, C. Kleine, J. Ludwig, M. Ochmann, B. Grimm-Lebsanft, R. Ma, M. Teubner, S. Dziarzhytski, G. Brenner, M. K. Czwalinna, B. Rösner, T. K. Kim, C. David, S. Herres-Pawlis, M. Rübhausen, E. T. J. Nibbering, N. Huse, and M. Beye, Shot noise limited soft x-ray absorption spectroscopy in solution at a SASE-FEL using a transmission grating beam splitter, Structural Dynamics **8**, 014303 (2021).

[45] W. F. Schlotter, M. Beye, S. Zohar, G. Coslovich, G. L. Dakovski, M. F. Lin, Y. Liu, A. Reid, S. Stubbs, P. Walter, K. Nakahara, P. Hart, P. S. Miedema, L. Le Guyader, K. Hofhuis, P. T. P. Le, J. E. T. Elshof, H. Hilgenkamp, G. Koster, X. H. Verbeek, S. Smit, M. S. Golden, H. A. Durr, and A. Sakdinawat, Balanced detection in femtosecond x-ray absorption spectroscopy to reach the ultimate sensitivity limit (2020), arXiv:2006.13968.

[46] L. L. Guyader, A. Eschenlohr, M. Beye, W. Schlotter, F. Döring, C. Carinan, D. Hickin, N. Agarwal, C. Boeglin, U. Bovensiepen, J. Buck, R. Carley, A. Castoldi, A. D'Elia, J.-T. Delitz, W. Ehsan, R. Engel, F. Erdinger, H. Fangohr, P. Fischer, C. Fiorini, A. Föhlisch, L. Gelisio, M. Gensch, N. Gerasimova, R. Gort, K. Hansen, S. Hauf, M. Izquierdo, E. Jal, E. Kamil, S. Karabekyan, T. Kluyver, T. Laarmann, T. Lojewski, D. Lomidze, S. Maffessanti, T. Mamyrbayev, A. Marcelli, L. Mercadier, G. Mercurio, P. S. Miedema, K. Ollefs, K. Rossnagel, B. Rösner, N. Rothenbach, A. Samartsev, J. Schlappa, K. Setoodehnia, G. S. Chiuzbaian, L. Spieker, C. Stamm, F. Stellato, S. Techert, M. Teichmann, M. Turcato, B. Van Kuiken, H. Wende, A. Yaroslavtsev, J. Zhu, S. Molodtsov, C. David, M. Porro, and A. Scherz, Photon shot-noise limited transient absorption soft x-ray spectroscopy at the european xfel (2022), arXiv:2211.0426.

[47] P. Denes, D. Doering, H. A. Padmore, J.-P. Walder, and J. Weizeorick, A fast, direct x-ray detection charge-coupled device, Review of Scientific Instruments **80**, 083302 (2009).

[48] F. Januschek, I. Klačkova, N. Andresen, P. Denes, S. Hauf, J. Joseph, M. Kuster, and C. Tindall, Performance of the LBNL FastCCD for the European XFEL, in *2016 IEEE Nuclear Science Symposium, Medical Imaging Conference and Room-Temperature Semiconductor Detector Workshop (NSS/MIC/RTSD)* (2016) pp. 1–3.

[49] I. Klačková, G. Blaj, P. Denes, A. Dragone, S. Göde, S. Hauf, F. Januschek, J. Joseph, and M. Kuster, Characterization of the ePix100a and the FastCCD semiconductor detectors for the european XFEL, Journal of Instrumentation **14** (01), C01008.

[50] E. Saldin, E. Schneidmiller, and M. Yurkov, Statistical properties of the radiation from VUV FEL at DESY operating at 30 nm wavelength in the femtosecond regime, Nuclear Instruments and Methods in Physics Research Section A: Accelerators, Spectrometers, Detectors and Associated Equipment **562**, 472 (2006).

[51] K. Hatada and A. Di Cicco, Modeling saturable absorption for ultra short x-ray pulses, Journal of Electron Spectroscopy and Related Phenomena **196**, 177 (2014).

[52] S. Anisimov, B. L. Kapeliovich, and T. L. Perel'man, Electron emission from metal surfaces exposed to ultrashort laser pulses, Sov. Phys. JETP **39**, 375 (1973).

[53] J. Chen, D. Tzou, and J. Beraun, A semiclassical two-temperature model for ultrafast laser heating, International Journal of Heat and Mass Transfer **49**, 307 (2006).

[54] N. Hartley, J. Grenzer, W. Lu, L. Huang, Y. Inubushi, N. Kamimura, K. Katagiri, R. Kodama, A. Kon, V. Lipp, M. Makita, T. Matsuoka, N. Medvedev, S. Nakajima, N. Ozaki, T. Pikuz, A. Rode, K. Rohatsch, D. Sagae, A. Schuster, K. Tono, J. Vorberger, T. Yabuuchi, and D. Kraus, Ultrafast anisotropic disordering in graphite driven by intense hard X-ray pulses, High Energy Density Physics **32**, 63 (2019).

[55] B. Y. Mueller and B. Rethfeld, Relaxation dynamics in laser-excited metals under nonequilibrium conditions, Phys. Rev. B **87**, 035139 (2013).

[56] H.-T. Chang, A. Guggenmos, S. K. Cushing, Y. Cui, N. U. Din, S. R. Acharya, I. J. Porter, U. Kleineberg, V. Turkowski, T. S. Rahman, D. M. Neumark, and S. R. Leone, Electron thermalization and relaxation in laser-heated nickel by few-femtosecond core-level transient absorption spectroscopy, Phys. Rev. B **103**, 064305 (2021).

[57] C. Powell and A. Jablonski, NIST electron inelastic-mean-free-path database 71, version 1.1 (2000).

[58] A. Jain, S. P. Ong, G. Hautier, W. Chen, W. D. Richards, S. Dacek, S. Cholia, D. Gunter, D. Skinner, G. Ceder, and K. a. Persson, The Materials Project: A materials genome approach to accelerating materials innovation, APL Materials **1**, 011002 (2013).

[59] K. Persson, Materials data on Ni (sg:225) by materials project (2016).

[60] E. Bévillon, J. P. Colombier, V. Recoules, and R. Stoian, Free-electron properties of metals under ultrafast laser-induced electron-phonon nonequilibrium: A first-principles study, Phys. Rev. B **89**, 115117 (2014).

[61] Z. Lin, L. V. Zhigilei, and V. Celli, Electron-phonon coupling and electron heat capacity of metals under conditions of strong electron-phonon nonequilibrium, Phys. Rev. B **77**, 075133 (2008).

[62] Z. Lin and L. V. Zhigilei, Temperature dependences of the electron–phonon coupling, electron heat capacity and thermal conductivity in Ni under femtosecond laser irradiation, Applied Surface Science **253**, 6295 (2007).

[63] T. Lojewski, M. F. Elhanoty, L. L. Guyader, O. Grånäs, N. Agarwal, C. Boeglin, R. Carley, A. Castoldi, C. David, C. Deiter, F. Döring, R. Y. Engel, F. Erdinger, H. Fangohr, C. Fiorini, P. Fischer, N. Gerasimova, R. Gort, F. de Groot, K. Hansen, S. Hauf, D. Hickin, M. Izquierdo, B. E. Van Kuiken, Y. Kvashnin, C.-H. Lambert, D. Lomidze, S. Maffessanti, L. Mercadier, G. Mercurio, P. S. Miedema, K. Ollefs, M. Pace, M. Porro, J. Rezvani, B. Rösner, N. Rothenbach, A. Samartsev, A. Scherz, J. Schlappa, C. Stamm, M. Teichmann, P. Thunstrom, M. Turcato, A. Yaroslavtsev, J. Zhu, M. Beye, H. Wende, U. Bovensiepen, O. Eriksson, and A. Eschenlohr, The interplay of local electron correlations and ultrafast spin dynamics in fcc Ni (2022), arXiv:2210.13162.

[64] C. Stamm, T. Kachel, N. Pontius, R. Mitzner, T. Quast, K. Holldack, S. Khan, C. Lupulescu, E. F. Aziz, M. Wietstruk, H. A. Dürr, and W. Eberhardt, Femtosecond modification of electron localization and transfer of angular momentum in nickel, Nature materials **6**, 740 (2007).

[65] H. A. Dürr, C. Stamm, T. Kachel, N. Pontius, R. Mitzner, T. Quast, K. Holldack, S. Khan, C. Lupulescu, E. F. Aziz, M. Wietstruk, and W. Eberhardt, Ultrafast electron and spin dynamics in nickel probed with femtosecond x-ray pulses, IEEE Transactions on Magnetics **44**, 1957 (2008).

Supplementary Information for: Electron Population Dynamics Dominate Non-linearities in X-ray Absorption Near-Edge Spectra from Focused FEL Pulses

DATA ACQUISITION

The experimental X-ray absorption spectra presented here were collected in the scope of a community proposal as the first user-beamtime at the SCS instrument. The intensities of the two beams generated by the beam-splitting zone plate were recorded using a FastCCD detector [1] with 1920×960 pixels of $30\times30\,\mu\mathrm{m}^2$. The intensities of both beams were integrated over a Region Of Interest (ROI) corresponding to 350×350 pixels each to retrieve the signal and reference intensities for each FEL shot. The high beam divergence due to the zone plate focusing distributed the signal on a 4 mm wide square on the detector 1 m downstream of the sample, thus greatly decreasing the fluence incident per detector area in order to avoid detector saturation. The gas-attenuator was filled with varying low pressure of nitrogen gas to regulate the transmission through the beamline to the required fluence. We refer to low-intensity spectra if the fluence was consistently below the sample damage threshold and the full measurement could be recorded on a single spot, without scanning the sample.

For measuring high-intensity spectra, the fluence often exceeded the material damage threshold, creating shot craters and sometimes causing larger fractures in the support membrane. For measurements at these fluences, the sample holder was scanned at a speed of $0.5\,\mathrm{mm\,s^{-1}}$. Therefore, only about 50 % of all FEL shots were transmitted through the windows; in the other cases, one or both beams were blocked or clipped by the frame. The membranes were arranged on the frame in a periodic pattern of two rows of sample and two rows of reference membranes with a distance of 1 mm between rows. This ensured that the two FEL foci always impinged on one row of sample and one reference membranes; a third row was unused in between. Therefore, every time the currently scanned rows were incremented, the upper beam would switch from probing reference membranes to probing sample membranes or vice versa, while the opposite holds for the lower beam. To prevent detector saturation, an additional aluminum filter of about $13\,\mu m$ thickness was installed in front of the detector during these measurements.

DETECTOR CALIBRATION

The temperature of the FastCCD rose consistently during operation and required cool-down periods in between measurements, leading to the temperature varying between -27 °C and -5 °C not only over time during the measurement, but also spatially over the detector area. The detector dark signal, as well as the gain coefficients for the three gain settings between which the detector pixels switch automatically, depend on the detector temperature. This made it necessary to reconstruct a temperature-dependent gain calibration. The three temperature-dependent background levels were drawn from dark images collected at various temperatures for each gain setting; the gain coefficients for each setting were drawn from a statistical analysis of the observed gain switching thresholds, such that the calibrated histogram of pixel intensities becomes continuous over all three gain levels. While the calibration accounts for the temperature measured using a temperature sensor on the detector, spatial variations over the detector area remain. The primary effect of this temperature variation was a varying background signal, following a spatial exponential distribution between the detector center and rim, with a higher baseline near the detector center. To account for this, an estimated background signal was derived from the measurements themselves: For a running average of 100 images, the illuminated area was cut out and interpolated using fits to the background level in the non-illuminated area. This additional background variation was then integrated into the gain calibration described above. Furthermore, a mask of hot and dark pixels with irregular behavior was generated from separate measurements and the respective pixels were excluded from the analysis. Despite these corrections, the detector inhomogeneities constitute a significant part of measurement uncertainty in the presented spectra. In particular, the uneven warming of the two detector halves on which the upper and lower beam respectively impinged has the potential of introducing systematic uncertainties. Thus, the shot-sorting algorithm described below was applied separately for all rows where the sample was in the upper beam and the reference in the lower and then to all rows where the orientation was reversed. Fortunately, differences between the temperature of both detector hemispheres affect the two equally sized groups of data (sample up and sample down) with equal and opposite magnitude. Therefore, possible systematic deviations are eliminated in the average over both groups and instead contribute to the statistical uncertainty which is represented in the error shown in Figure 2 of the manuscript.

EVENT CLASSIFICATION

Furthermore, whenever the sample or reference membrane was torn due to a particularly intense shot, subsequent shots sometimes impinged on the torn rim of the sample, possibly at an angle to the membrane surface, or did not hit any sample material at all. Shots affected in this way were not always trivial to identify from any single measurement parameter, which lead to the following procedure to identify and exclude faulty FEL shots: First, the detector image in the ROI around one beam was compared to an extended ROI around the other beam using a normalized two-dimensional cross-correlation algorithm. For this, the images were first smoothed by convolution with a Gaussian kernel to remove the influence of the rough surface structure of the aluminum filter before applying the cross-correlation function, both algorithms implemented in the scikit-image [2] package. This procedure yields a correlation coefficient and a displacement vector. The correlation coefficient was used as an indicator that both beams were transmitted through a window without significant differences in the wavefront.

Since data-acquisition of the motor encoder for the position transverse to the scanning direction was dysfunctional, the real path of the beam over the sample frame was reconstructed by combining knowledge of the beam position along the scanning direction and the manual notes in the laboratory book with the correlation coefficients between both beams on the detector. In the later analysis of the damaged samples, this allowed associating specific shot craters scrutinized with SEM-microscopy to specific FEL shots.

From the FEL shots which hit sample windows according to this reconstruction, outliers were dropped if either the correlation coefficient dropped below 85 % or the displacement vector deviated by a significant margin (manually calibrated for each measurement setting) from the expected beam-splitting. Likewise, extreme outliers in the ratio of reference to sample intensity were also dropped at this stage. These criteria proved to be largely redundant as they mostly agree with each other on which events to exclude. Using all of these criteria, events where either or both beams are blocked or clipped can be excluded reliably. In Figure 1, the thus excluded points are shown in gray. Each dot represents one FEL shot; its y-position is the logarithmic ratio between sample and reference intensity; the x-position is the photon energy setting of the monochromator, while the gray-scale encodes the Pearson correlation coefficient $\mathrm{C}_{\mathrm{corr}}$ of the two regions of interest.

From the distribution of the remaining events, shown in color, it is obvious that further classification is needed. This is because shots onto a damaged or missing membrane can produce spots with good correlation and the expected displacement vector. These can only be distinguished by the fact that the apparent optical density deviates unreasonably from the expected value at the given photon energy. However, this transmission ratio is also the quantity of interest for the final spectrum. To disentangle events affected by prior sample damage from true measurements, an iterative approach using a Bayesian Gaussian mixture model was utilized: To start, an initial guess for a spectrum is computed using the events that passed filter conditions described above and shown as a green line in Figure 1. Then, for each FEL shot, the deviation of the logarithmic ratio between sample and reference intensity from the initially guessed spectrum is computed. This allows for generating a histogram of these absorbance deviations from the initial guess. Assuming a good guess of the initial spectrum, one may expect that the "good" FEL shots are normally distributed around zero deviation, while shots affected by various sources of uncertainty are distributed with some other distribution, dependent on the type of uncertainty. Thus, the histogram is fitted with four Gaussian distributions which are used as prior probability distributions, the first of which corresponds to "good" FEL shots. Then, the posterior probability of belonging to the category of "good" shots is computed for each FEL shot. These posterior probabilities are used as statistical weights to compute an improved guess of the measured spectrum. This improved guess was convoluted with a Gaussian kernel to prevent over-fitting before using it as a new initial guess for the Gaussian mixture model. The spectrum is considered converged when the average change per iteration anywhere in the spectrum is less than 5μOD. This procedure converges (if at all) within a few (between 3 and 20) iterations to a solution that is robust even against a strong variation of the initial guess. In Figure 1, the thus analyzed shots are shown in colors encoding the final posterior probability P_{ok}, indicating the estimate of the model about the validity of each shot. The final guess of the average spectrum is shown as an orange line.

This final procedure rejects outliers purely based on their deviation from the expected value, which requires further justification: In this case, the procedure should return valid results under the condition that all valid FEL shots at a certain photon energy measure a transmission value within a single continuous range. The width of the distribution is resulting from a combination of non-linear changes and measurement noise. This condition must be fulfilled in the present case as long as the fluence-dependent transmission curve of the sample is continuous and a continuous range of pulse energies is contained in the data set (which is the case for SASE fluctuations). Apart from this logic, the rejected outliers do not appear systematic, further supporting the applicability of the algorithm.

DETERMINATION OF THE EFFECTIVE SPOT SIZE

The zone plate has a size of $(1\,\mathrm{mm})^2$ and combines a focusing Fresnel zone plate, off-axis by 0.55 mm with

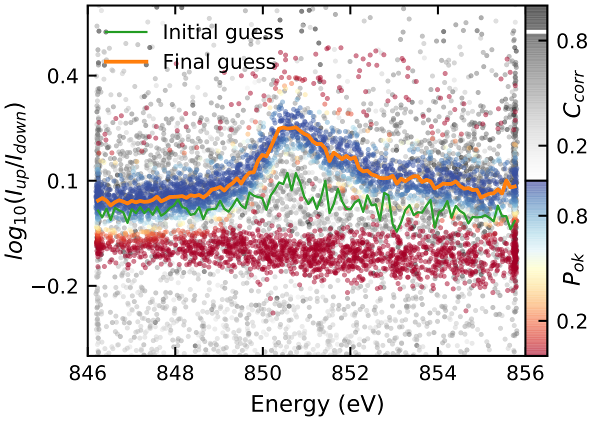

FIG. 1. **Sorting of FEL-shots**. Gray points represent events which were excluded based on rigid criteria, mainly their correlation coefficient C_{corr}. Colored points were analyzed using the iterative GMM optimization. The colorbar shows the estimated posterior probability P_{ok} that a given shot cleanly probed an unperturbed sample. The green and orange solid lines represent the initial and final average spectrum estimated by the GMM, respectively.

250 mm focal length (at 860 eV) with a line grating with 379.4 nm pitch in a single optical element. Details on the zone plate can be found in [3]. While the monochromator was scanned between 846 eV and 856 eV, the effective size of the foci on the sample changed due to the wavelength dependency of the zone plate diffraction. The photon energy-dependent focal size of the zone plate foci was calculated by ray optics calculations based on the beamline settings [4]. Uncertainties in the exact beam path parameters along the beamline were accounted for by matching the ray optics calculations to effective spot size estimates derived from analyzing the shot craters on the used samples using a simplified form of the procedure laid out in [5, 6]. Since a full intensity profile could not be measured from the shot craters, the concept of the effective area of the focal size is used. This area connects the peak fluence F_0 with the overall pulse energy E_{pulse}, i.e.

$$A_{eff} = \frac{E_{\mathrm{pulse}}}{F_0}, \tag{1}$$

and it can be defined for an arbitrary spot profile.

To characterize the effective focal size, the reference membranes were analyzed using scanning electron microscopy (SEM). Figure 2 shows two SEM images: one overview image of an entire membrane one example of a high-resolution image of a single imprint. Such high-resolution images were taken of 85 selected spots which were associated with the corresponding FEL photon diagnostics data by matching the reconstructed movement of the sample stage to the pattern of imprints on the sample. The reference membranes were chosen for the imprint analysis since their X-ray absorbance can be considered constant for the scanned photon energies.

Since the zone plate is a diffractive element, its properties such as focal length are energy-dependent. Furthermore, the fluence-dependent spectra presented in this paper are combined from measurements at two distinct object distances of 250.84 mm and 252.14 mm.

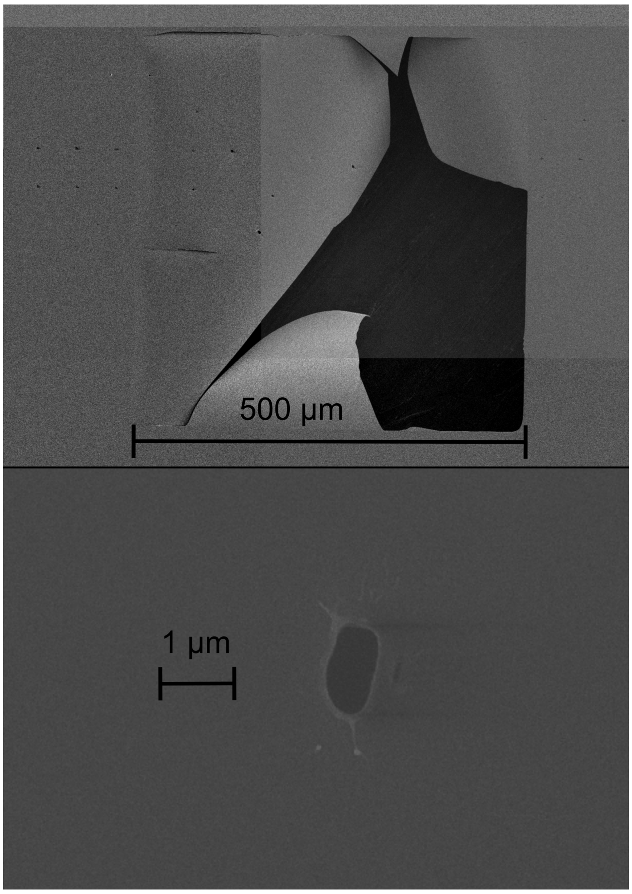

FIG. 2. **SEM images of the used samples** The top image shows a stitched overview image of a nickel film window. One can see rows of FEL imprints as well as the tearing of the membrane. The bottom image shows a single FEL imprint in a SiN reference membrane.

Thus, the SEM images were grouped into six groups (see table I) by focal length and photon energy of the associated shot, and the total damaged or ablated surface area was determined for each shot. For each group, the minimum FEL pulse energy at which damage is observed on the reference membranes was determined by a Liu's plot [7] as shown in Figure 3: The ablated area was plotted over the logarithm of the shot energy and a linear fit was applied to the shots with less than 1 μm^2 ablated area to determine the pulse energy damage threshold.
Following the concept outlined in [5], the pulse energy of all shots was then normalized using this damage threshold to derive the normalized fluence level $f(S)$ as a func-

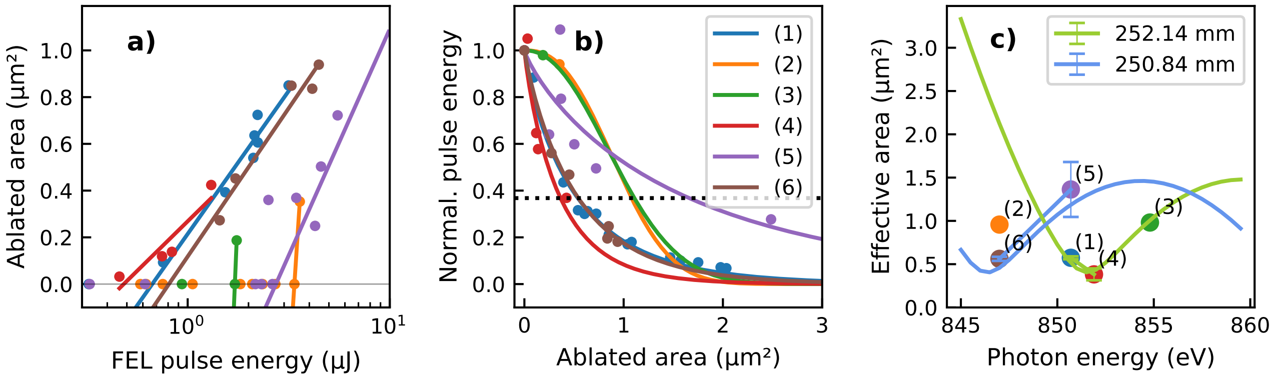

FIG. 3. **Spot size characterization**. a) Liu's plot to determine the pulse energy damage thresholds. b) Normalized pulse energy plot to determine the effective area. The legend differentiates the spot groups corresponding to table I with colors valid for all three panels. c) Area of FEL foci, comparing the effective area measurements (dots and error bars) to the ray tracing results (line plots) for two focal distances. For groups (2) and (3) no error estimate could be calculated (see text).

Group	Object distance (mm)	Photon energy (eV)	Pulse energy threshold (μJ)	Effective area (μm^2)
1	252.14	850.7	0.308	0.584
2	252.14	847.0	3.374	0.957
3	252.14	854.8	1.712	0.981
4	252.14	851.9	0.482	0.383
5	250.84	850.7	2.733	1.618
6	250.84	847.0	0.807	0.567

TABLE I. **Results of the spot size characterization**. The object distance refers to the distance between sample and zone plate. Pulse energies are shown as measured at the XGM without accounting for the efficiency of the zone plate (about 9 %) and the transmission of the beamline KB-mirrors (about 80 %). The effective area of groups 2 and 3 is under-determined (see text).

tion of the ablated area S. If the spot size were Gaussian, the function $f(S)$ should be a simple negative exponential, and the effective area would correspond to the value of S where $f(S)$ equals $1/e$, which is indicated in Figure 3 b) as a horizontal dotted line. For the given non-Gaussian case, the function $f(S)$ was fitted with a modified exponential $f(S) = e^{(-aS^b)}$, yielding for each group of shots fit parameters a and b and their unceratinties σ_a and σ_b. The effective area is then calculated as the integral of $f(S)$. For the estimate of the uncertainty shown as error bars of Figure 3 c), the integral was also evaluated for $a + \sigma_a$ and $b + \sigma_b$ as well as $a - \sigma_a$ and $b - \sigma_b$. Groups (2) and (3) each contained only a single FEL shot with visible damage. While this does allow for an estimate of the damage threshold (compare Figure 3 a)), the function $f(S)$ shown in b) is barely determined by fitting only to the normalization point and a single further point. Thus, no mathematical uncertainty estimate can be given and resulting points (2) and (3) shown without error bars in Figure 3 c) should be considered as tentative estimates.

The ray optics calculation tracks the beams in the vertical and horizontal planes. The focus area was calculated from the ray optics calculations assuming an elliptical beam shape. It revealed a slightly astigmatic focus on the sample, due to the beamline optics using separate horizontal and vertical focusing, thus illuminating the zone plate with slightly non-uniform beam divergence. The separate location of horizontal and vertical foci leads to the two minima visible in Figure 3. Based on the measurements, a minimal beam-waist radius of 80 nm was imposed on the ray tracing calculations, accounting for imperfections in beam quality and optics.

The fluences for the high-fluence spectra shown in this paper are calculated based on the pulse energy measured by the XGM behind the monochromator, multiplied with the efficiency of the focusing optics (80 %) [8] and zone plate (9 %) and divided by the effective area derived with the presented ray optics calculations. Since the XGM was calibrated for high pulse energies, the fluences for the low-fluence spectra are based on the reference intensities measured on the CCD and calibrated to be consistent with the reference intensities measured for the high-fluence data, accounting for the calculated transmission of the aluminum filter.

---

[1] F. Januschek, I. Klačkova, N. Andresen, P. Denes, S. Hauf, J. Joseph, M. Kuster, and C. Tindall, Performance of the LBNL FastCCD for the European XFEL, in *2016*

IEEE Nuclear Science Symposium, Medical Imaging Conference and Room-Temperature Semiconductor Detector Workshop (NSS/MIC/RTSD) (2016) pp. 1–3.

[2] S. Van der Walt, J. L. Schönberger, J. Nunez-Iglesias, F. Boulogne, J. D. Warner, N. Yager, E. Gouillart, and T. Yu, scikit-image: image processing in python, PeerJ **2**, e453 (2014).

[3] F. Döring, B. Rösner, M. Langer, A. Kubec, A. Kleibert, J. Raabe, C. A. F. Vaz, M. Lebugle, and C. David, Multifocus off-axis zone plates for x-ray free-electron laser experiments, Optica **7**, 1007 (2020).

[4] L. L. Guyader, Boz calculator, `https://rtd.xfel.eu/docs/bozcalc/en/latest/` (2022).

[5] J. Chalupský, J. Krzywinski, L. Juha, V. Hájková, J. Cihelka, T. Burian, L. Vyšín, J. Gaudin, A. Gleeson, M. Jurek, A. R. Khorsand, D. Klinger, H. Wabnitz, R. Sobierajski, M. Störmer, K. Tiedtke, and S. Toleikis, Spot size characterization of focused non-gaussian x-ray laser beams, Opt. Express **18**, 27836 (2010).

[6] R. Sobierajski, M. Jurek, J. Chalupský, J. Krzywinski, T. Burian, S. D. Farahani, V. Hájková, M. Harmand, L. Juha, D. Klinger, R. A. Loch, C. Ozkan, J. B. Pełka, K. Sokolowski-Tinten, H. Sinn, S. Toleikis, K. Tiedtke, T. Tschentscher, H. Wabnitz, and J. Gaudin, Experimental set-up and procedures for the investigation of XUV free electron laser interactions with solids, Journal of Instrumentation **8** (02), P02010.

[7] J. M. Liu, Simple technique for measurements of pulsed gaussian-beam spot sizes, Optics letters **7**, 196 (1982).

[8] G. Mercurio, J. Chalupský, I.-T. Nistea, M. Schneider, V. Hájková, N. Gerasimova, R. Carley, M. Cascella, L. L. Guyader, L. Mercadier, J. Schlappa, K. Setoodehnia, M. Teichmann, A. Yaroslavtsev, T. Burian, V. Vozda, L. Vyšín, J. Wild, D. Hickin, A. Silenzi, M. Stupar, J. T. Delitz, C. Broers, A. Reich, B. Pfau, S. Eisebitt, D. L. Civita, H. Sinn, M. Vannoni, S. G. Alcock, L. Juha, and A. Scherz, Real-time spatial characterization of micrometer-sized x-ray free-electron laser beams focused by bendable mirrors, Opt. Express **30**, 20980 (2022).

A Rate Model of Electron Populations for Non-linear High-Fluence X-ray Absorption Near-Edge Spectra

Robin Y. Engel,[1, 2] Markus Scholz,[1, 3] Jan O. Schunck,[1, 2] and Martin Beye[1, 2]
[1]*Deutsches Elektronen-Synchrotron DESY, Notkestr. 85, 22607 Hamburg, Germany*
[2]*Physics Department, Universität Hamburg, Luruper Chaussee 149, 22761 Hamburg, Germany*
[3]*European XFEL, Holzkoppel 4, 22869 Schenefeld, Germany*

Absorbing a focused, femtosecond X-ray pulse from a Free-Electron Laser (FEL) can lead to extreme electronic excitations in solids. This excitation drives changes of the electronic system over the course of the pulse duration and the overall absorption of the pulse becomes fluence-dependent. Thus, fluence-dependent non-linear X-ray Absorption Near Edge Spectroscopy (XANES) is sensitive to the valence excitation dynamics around the Fermi level on the few-femtosecond timescale. Here we present a simplified rate model based on well-established physical mechanisms to describe the evolution of the electronic system.

We construct temporal and spatial differentials for the processes of resonant absorption, stimulated emission, non-resonant absorption, Auger decay, valence band thermalization and scattering cascades of free electrons.

The phenomenological rate model approach provides a direct understanding how each physical process contributes to the fluence-dependent changes observed in XANES measurements. Without accounting for fluence-dependent changes to the density of states, the model shows good agreement with experimental results on metallic nickel over more than three orders of magnitude in fluence, establishing electron redistribution as the main driver of non-linear absorption changes at high fluences. Although in the closest vicinity of the resonance, more complex approaches are necessary to describe remaining discrepancies of the fluence-dependence changes, the demonstrated capability to describe spectral changes up to extreme fluences yields fundamental insights into the complex dynamics after intense core excitation and provides an important tool for the design and evaluation of future FEL experiments, in particular for the development of non-linear X-ray spectroscopy.

I. INTRODUCTION

Translating non-linear spectroscopy methods that are well established in the longer wavelength ranges [1–3] to the X-ray regime is particularly attractive, since the strong localization of transitions involving core electrons as well as element-specific absorption edges promise additional selectivity to these already potent analytical tools [4–22]. A prerequisite for non-linear X-ray spectroscopy is a high density of X-ray photons, such as those found in the tightly focused X-ray radiation from a Free-Electron Laser (FEL). The absorption of such pulses drastically modifies the electronic structure of any investigated material, even on the timescale of femtosecond-short pulses. Absorption around material resonances directly probes transitions between the core-levels and states around the Fermi level and is thus sensitive to the electron dynamics in the valence band of materials. Electronic structure changes in this region affect the degree of absorption experienced by later parts of the same pulse and the fluence-dependent absorption can be used to derive information on the excited state and its evolution [15, 23–30].

Several models have been put forward to describe aspects of this interplay between photon absorption and electronic system [15, 25, 29–31]. Away from material resonances, fluence-dependent X-ray absorption has been successfully modeled using rate models in three-level systems [25, 31] modeling a ground, core-excited and intermediate valence excited state. When probing the valence bands around material resonances however, three population parameters representing the state of the material at a given point in time become insufficient to represent the non-thermal electron energy distribution around the Fermi level in an extended solid that is relevant for the rates of excitation and relaxation. This makes rate models using only three levels unsuitable to model non-linear absorption near resonances.

In this work, we present an expanded rate model to describe the evolution of the electronic system in terms of an energy-resolved population of the valence band within a constant Density of States (DoS). The valence electrons are heated through energy transfer from the scattering of free electrons from Auger decays and non-resonant absorption. The model uses material parameters known or calculated for the ground-state and scales these parameters in accordance with changes in electronic populations. Only the time constants for the valence band thermalization and the scattering cascades of free electrons are treated as free parameters. We present calculations matching measurements of X-ray absorption spectra recorded with monochromatic X-rays in transmission through metallic nickel foils around the nickel $2p_{3/2}$ (L_3) edge [32]; our model reproduces the main fluence-dependent changes in the measured spectra over more than three orders of magnitude. While the measurements are discussed in detail in a separate publication [32], this paper illustrates the framework of the rate model and strives to provide an intuitive understanding of the mechanisms that drive non-linear changes.

The following text is structured as follows. In section

(II), we give a qualitative overview of the rate model: Section II A describes the algorithm and approximations made in the interest of computational viability, Section II B outlines the mathematical formulation for the rates of all relevant processes, which are then assembled into differentials of the photon and electron populations in section II C. Section II D elaborates on relevant input parameters. Finally, we discuss the use and implications of our model in section III.

II. THE RATE MODEL

We describe the propagation of X-ray photons through the sample as well as the dynamics of electron populations within the sample using a set of ordinary differential equations. These rate equations describe the evolution of photon and electron densities and are assembled from terms that each describe a specific physical process. The rate of each process is based on ground-state rates, scaled with the appropriate fractional occupation (the number of electrons divided by the number of states). Each process rate is described in detail in section II B. Such scaling inherently prevents any state from exceeding its physically meaningful population (between zero and the number of available states) and also enforces that the number of electrons in the sample is conserved over the simulated time.

The model allows for an arbitrary number of incident resonant photon energies E_i, for each of which a Gaussian temporal profile of incident intensity is assumed. For the presented calculations, only a single resonant photon energy was used, representing measurements with monochromatic X-rays. Incident photons are the only source of energy flow into the system, and all energy eventually contributes to the thermal energy of the valence system.

Figure 1 schematically summarizes the modeling of the electronic system: The electron populations R_C and R_V describe the total number of electrons bound in the core and valence system, respectively, for a single atom in the sample. Their values are limited by the number of available states, M_C and M_V. In the presented example on the nickel L$_3$-edge spectra, the ground-state populations are $R_C = 4$, representing the 2p$_{3/2}$-electrons and $R_V = 10$, representing electrons from the 3*d* and 4*s* states. Electrons in intermediate shells (in the given example the 3*p* and 3*s* electrons) contribute to the non-resonant absorption but are not explicitly simulated. We describe the electronic population of the valence system in an energy-resolved manner, splitting it up into a discrete number of densities ρ_j, where j represents the index along the valence energy axis. The number of available states m_j for each energy bin in the valence system is derived from the calculated ground-state DoS [33, 34] up to 30 eV above the Fermi level E_F. Beyond this value, the free electron gas model is used to calculate the density of states [35]. We set the energy cutoff of the energy-resolved valence band at 800 eV above the Fermi level. All electrons with even higher energies, such as photoelectrons created via non-resonant absorption and Auger-electrons from the decay of core-holes, are described in a separate pool of electrons R_{free} without energy resolution, although the total energy in this pool is tracked by the parameter E_{free}.

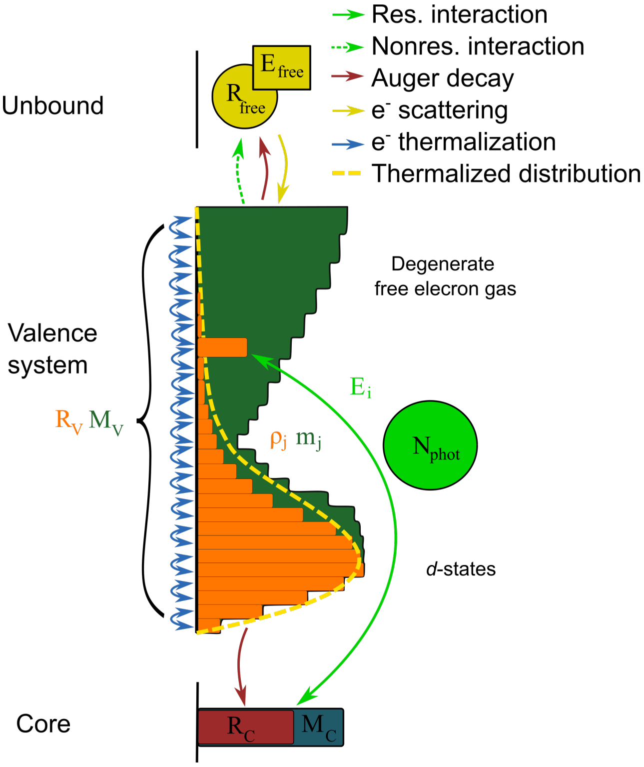

FIG. 1. **Photon-, electron- and energy-densities and their interactions.** A photon density N_{phot} drives resonant interactions between the core electrons R_C and specific valence electrons ρ_j. It also drives non-resonant excitations from the entire valence electron system $R_V = \sum_j \rho_j$ to free electrons R_{free}, which have a total energy of E_{free}. Auger decays transfer electrons from the valence system to both core states and free electrons; scattering cascades transfer electrons and energy from the free states to the valence system; thermalization drives the valence system towards a thermalized Fermi-Dirac distribution. M_C, M_V and m_j represent the number of available states and are pictured as bars to represent the energy bins of the numerical calculation.

Within our model, the DoS does not change over time since the DoS is dominated by the atomic lattice potentials and thus mainly affected by nuclear motion [36]. Since the coupling of electronic excitations to nuclear motion is much slower than the purely electronic dynamics, observations that are temporally confined to the duration of a single FEL pulse (on the order of tens of femtoseconds) are usually dominated by electronic processes.

A. Algorithm

In contrast to a Monte-Carlo approach, where interaction pathways of many individual particles are computed and averaged, our rate model describes processes in terms of non-quantized, average quantities (densities) in a finite-element analysis.

The problem is formulated as an idealized X-ray pulse, Gaussian in time and space, traveling at the speed of light through a three-dimensional sample. The photon density interacts non-linearly with the sample. Each voxel of the sample is characterized by a complex electronic state as described above and in Figure 1, which itself evolves in time after excitation. To make this problem tractable, we apply additional key approximations that allow for a drastic reduction of the computational effort that would come with a naive implementation of this problem in a four-dimensional (three spatial dimensions and time) finite elements algorithm: First, we describe electronic excitations as strictly localized and neglect their propagation; instead, only photons propagate through the sample, and only in forward direction[1]. Considering that a sample of 20 nm thickness is traversed by light in less than 100 as, the propagation of photons is calculated as if it happened instantaneous in between the time-steps performed to depict the evolution of the electronic system. This de-coupling of dimensional dependence effectively simplifies the problem into two sets of separately solvable, one-dimensional initial value problems: the photon propagation in space and the electronic evolution in time.

To solve these, we formulate the time-differential of all electronic states (see section II C), depending on the photon density incident at a certain time. The temporal evolution is solved using the fourth-order Runge-Kutta method with adaptive time-stepping based on a fifth-order local approximation [38]. In the meantime, whenever a time-differential is computed, the current incident photon density is first propagated through the sample using the explicit fourth-order Runge-Kutta method (in space) to retrieve the photon density at each depth of the sample.

This way, the time-dependent transmission for a Gaussian temporal pulse profile is calculated for a range of different overall pulse energies incident per sample area. This treatment yet neglects the transversal profile of the beam. Because the absorption is non-linearly dependent on the incident fluence, the transmission of a transversally inhomogeneous beam must be integrated over a specific spot profile with spatially varying transmission. Here, a two-dimensional Gaussian profile of the FEL spot is then accounted for by integrating the transmitted intensity based on previously calculated fluence-dependent transmission. The Figures 2, 3, 4 and 5 in the following section show intermediate results from simulations calculated for a specific fluence, as opposed to integrating over the transmission in a Gaussian spot-profile. With these simplifications, the overall computational complexity is drastically reduced.

B. Processes

The following describes the rates at which the physical processes occur for each atom. For a better overview, we introduce the processes as individual terms and assemble them into differential equations in the next section. In principle, each process is described using an absorption length or lifetime which is known from ground-state measurements and then scaled linearly with the changing electron populations with respect to the ground state. The normalization is such that the ground-state rate is reproduced for an undisturbed electron system and the rate vanishes when the corresponding transition cannot happen due to a lack of electrons or holes. We use the indices j and i to refer to specific energies, where the index i is used for photon energies of X-rays and the index j for the energy of electronic states in the valence band.

1. Resonant interaction

The resonant interaction describes both resonant absorption (core-valence transitions) and stimulated emission (valence-core transitions) as a single process. It is calculated for each energy E_j in the valence system that is resonant with a given photon energy E_i.

$$P_j^{res} = \left(\frac{R_C}{M_C} - \frac{\rho_j}{m_j}\right) \frac{N_i}{\lambda_i^{res}} \delta_{ij}$$

λ_i^{res}: Resonant absorption length
R_C: Number of core electrons
M_C: Number of core states
ρ_j: Valence electrons at E_j
m_j: Valence states at E_j
N_i: Number of photons per nm^2 at E_i
δ_{ij}: Kronecker-delta

The first terms (in brackets) represent the difference in the occupation of core states R_C/M_C and resonant valence states ρ_j/m_j. The dominance of absorption over stimulated emission or vice-versa is determined solely by this difference, as they represent an optically driven two-level system in the incoherent limit. If the core level population is smaller than the valence population, the resonant interaction process becomes negative, representing the dominance of stimulated emission. The second term on the right is the number of irradiated photons divided by the penetration length. The Kronecker delta ensures that only photons and electrons in corresponding energy bins interact.

---

[1] We neglect spontaneous X-ray emission, which would constitute up to 0.9 % of nickel L_3 core-hole decays [37].

2. Non-Resonant absorption

The non-resonant absorption summarizes photon absorption from other electronic states than the resonant core-level, especially from the valence electrons. Photon densities N_i at all incident energies reduce each population ρ_j.

$$P_{i,j}^{\text{non-res}} = \frac{\rho_j}{R_V^0} \frac{N_i}{\lambda^{non-res}}$$

$\lambda^{non-res}$: Non-resonant absorption length
R_V^0: Total number of valence electrons in the ground state

The interaction is normalized by the total valence band population in the ground state R_V^0, so that the sum of the first term over all j becomes unity if all $\rho_j = \rho_j^0$ (since $R_V^0 \equiv \sum_j \rho_j^0$). The second term represents the non-resonant absorption in the ground state as can be experimentally determined sufficiently before the resonance in the spectrum.

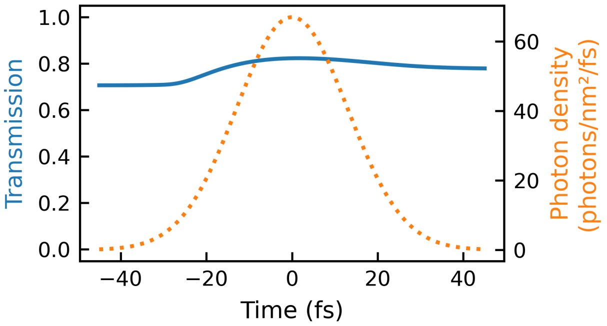

FIG. 2. **Instantaneous transmission** (including resonant and non-resonant absorption) over time for a pulse at 857.5 eV with a pulse energy of 30 J/cm^2 (blue line, left axis), as well as the temporal profile of the incident photon density (orange dots, right axis).

This treatment does not explicitly differentiate the non-resonant absorption from core energy levels other than the one treated by R_C. In the given example with photons resonant to the nickel $2p$-absorption, the $3s$ and $3p$ core electrons only contribute to a minority of the non-resonant absorption events. In this model, we choose for simplicity to scale this contribution together with the non-resonant scattering from the valence electrons.

An exemplary incidence profile and the resulting transmission over time are shown in Figure 2.

3. Auger decay

The model explicitly treats Auger decays that involve one core-hole and two electrons from the valence band. The rate at which an electron in density ρ_j would decay via an Auger process is calculated as:

$$P_j^{\text{Auger}} = (M_C - R_C) \frac{\rho_j}{R_V^0} \frac{R_V}{R_V^0} \frac{1}{\tau_C}$$

τ^C: Core-hole lifetime
R_V: Total number of valence electrons

The first factor (in brackets) is the number of unoccupied core states, i.e. core-holes. The second factor describes the relative population of electrons at the energy E_j and the third term is the relative population of the entire valence band to which the electron could transfer its energy. The latter two are normalized by the respective ground state population. The last term is the decay rate in the ground state, where τ_C represents the ground-state lifetime of a single core-hole. Altogether, this describes Auger decays as interactions between two valence electrons, one emitted and one filling the $2p_{3/2}$ core-hole. In reality, some fraction of Auger decays will emit electrons from the $3s$ or $3p$ core levels instead, followed by further Auger processes which emit electrons with the remaining energy of the original core-hole. These are not treated separately in our description, since the indirect decay is, on the one hand, a minority contribution and on the other hand, ultimately results in the same energy transfer to the valence band, albeit with a slightly longer time delay due to the intermediate steps.

4. Free-electron scattering

Inspired by earlier approaches to a simplified solution of the Boltzmann equation [39], we approximate the scattering rates of electrons in terms of characteristic time constants τ_{scatt} and τ_{th} for the free electrons and valence electrons, respectively.

The lifetime of free electrons τ_{scatt} represents the inverse rate at which free electrons R_{Free} scatter and decay to the valence system. While this parameter is ultimately empirical, it depicts a cascade of individual scattering events between electrons. In such a cascade, each free electron eventually transfers all its kinetic energy to the valence system.

$$P^{\text{scatt}} = R_{Free} \frac{1}{\tau_{scatt}}$$

τ_{scatt}: Free electron scattering time constant
R_{Free}: Number of free electrons

5. Electron thermalization

Similarly, τ_{th} characterizes the time with which the valence system approaches an internal thermal equilibrium.

$$P_j^{\text{therm}} = [r_j(T,\mu) - \rho_j] \frac{1}{\tau_{th}}$$

τ_{th}: Valence thermalization time constant
T: Equivalent electronic temperature
μ: Chemical potential

To this end, the chemical potential and equivalent electronic temperature are calculated in each time-step based on the current internal energy U and number of valence electrons R_V. The Fermi distribution for the calculated chemical potential and temperature then yields a momentary target electron distribution $r_j(T,\mu)$, which is approached with the electron thermalization constant τ_{th}.

$$r_j(T,\mu) = m_j \frac{1}{e^{(E_j-\mu)/k_B T}+1}$$
$$U = \sum_j \rho_j E_j / \sum_j \rho_j$$
$$R_V = \sum_j \rho_j$$

U: Total energy of the valence system
R_V: Current total population of the valence system
$r_j(T,\mu)$: Electron density expected for a fully thermalized valence system
k_B: Boltzmann constant

While the calculation of r_j from T and μ is straightforward, determining T and μ from U and R_V is an inverse problem. This is solved by iterative optimization using the Levenberg-Marquardt method[2].

Note that, because by definition both electron densities: the momentary ρ_j and the thermalized goal distribution r_j hold the same amount of electrons and internal energy, the sum over the valence band of all electron-distributing thermalization rates is always zero and the change in overall energy is also zero, i.e. $\sum_j P_j^{\text{therm}} = 0$ and $\sum_j E_j P_j^{\text{therm}} = 0$.

Figure 3 shows how the temperature (given as an energy $k_B T$ in units of eV) and the chemical potential develop over time for a high fluence of $30\,\mathrm{J/cm^2}$. Although reaching higher temperatures, these results are in agreement with studies treating the nickel valence system heated with optical lasers [40, 41].

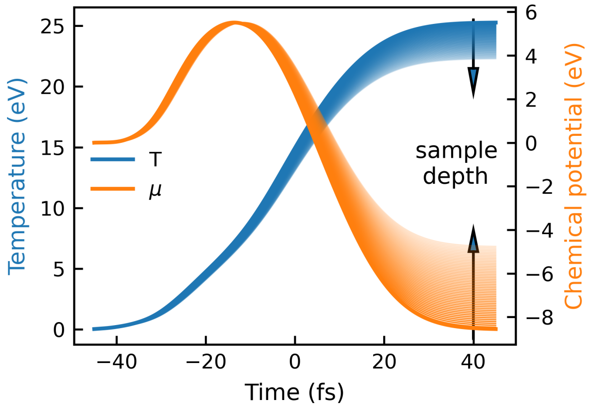

FIG. 3. **Temperature and chemical potential** over time for a pulse at 857.5 eV with a pulse energy of $30\,\mathrm{J/cm^2}$. The solid line represents the properties at the sample surface and the thin lines represent the deeper layers that are exposed to less X-ray fluence, as indicated by arrows and increasing transparency.

C. Differentials

From these process terms, we can assemble the time-differential of the various pools of electrons, photons, and energy. Because the simulation conserves the number of electrons in the sample, in the sum over all j, every process term describing electronic transitions appears equally often with positive and negative sign, representing a transition of electrons from one state to another. For example, the term for Auger decay appears twice with a negative sign in the valence electron differential, and each once with a positive sign in the differential for core- and free electrons.

1. *Valence electrons*

$$\begin{aligned}\frac{d\rho_j}{dt} &= P_{i=j}^{res} \\ &- \sum_i P_{i,j}^{\text{non-res}} \\ &- P_j^{\text{Auger}} - \frac{\sum_j \rho_j P_j^{\text{Auger}}}{R_V} \\ &+ P_j^{\text{therm}} \\ &+ \frac{h_j}{H_V} P^{\text{scatt}} + P_{red}\left(\frac{-\rho_j}{R_V} + \frac{h_j}{H_V}\right)\end{aligned}$$

h_j: Number of valence holes, $h_j = m_j - \rho_j$
H_V: Total number of valence holes, $H_V = \sum_j h_j$
P_{red}: Electron re-distribution rate due to scattering cascades from free electrons

The valence system interacts via all modeled processes, therefore we comment on the equation above line by line. The resonant absorption rate P_j^{res} changes the valence electron densities ρ_j at all incident photon energies E_i

---

[2] First, the Levenberg-Marquardt root-finding algorithm is applied with a maximum of 400 iterations. If the required residual is still exceeded, the algorithm switches to least-squares optimization to refine the root-finding result. This combination proved a good compromise between computation speed and stability in regions with small gradients in the loss function.

where $i = j$. Via non-resonant absorption, incident photon energies E_i can remove electrons from ρ_j. The third line shows the primary and secondary Auger electrons. Note that in the sum over all energies E_j, terms 3 and 4 each remove one electron from the valence band for each Auger process occurring. The thermalization term in line four drives electrons towards the thermal distribution based on the current internal energy and population of the valence band, without changing the total valence occupation, as discussed in section II B 5. The last line describes the effect of electron scattering. The first term represents electrons from the free electron pool that are re-joining the valence system into a random unoccupied state h_j.

The second term describes the electron redistribution inside the valence system in order to take up the energy released by the re-joining electron. This redistribution is calculated as a function of the rate of electronic scattering P^{scatt} and represents the effect of electronic scattering cascades. In such a cascade, a number of electrons is moved from occupied states ρ_j to unoccupied states h_j. The total rate of electrons redistributed in this time step through scattering P_{red} is given by the ratio of the energy that needs to be taken up by the valence system to the energy that the valence system can additionally accommodate.

$$P_{red} = \frac{S_{scatt} - S_{joining}}{U_h - U_e}$$

The denominator of P_{red} represents the energy that can maximally be redistributed to the valence system as the difference between the energy that could be contained in the unoccupied states

$$U_h = \frac{\sum_j h_j E_j}{H_V}$$

and the one already contained in the occupied states

$$U_e = \frac{\sum_j \rho_j E_j}{R_V}.$$

The numerator is given by the difference between the rates at which energy is released from the free electron energy pool

$$S_{scatt} = P^{\text{scatt}} \frac{E_{free}}{R_{free}}$$

and the rate at which energy is gained in the valence system due to the formerly free electrons occupying random unoccupied valence states:

$$S_{joining} = \sum_j \frac{h_j}{H_V} P^{\text{scatt}} E_j$$

Figure 4 shows an example for the development of the valence system within a single voxel at the sample surface, exposed to a pulse of 30 J/cm^2 fluence, resonant to states 7 eV above E_F.

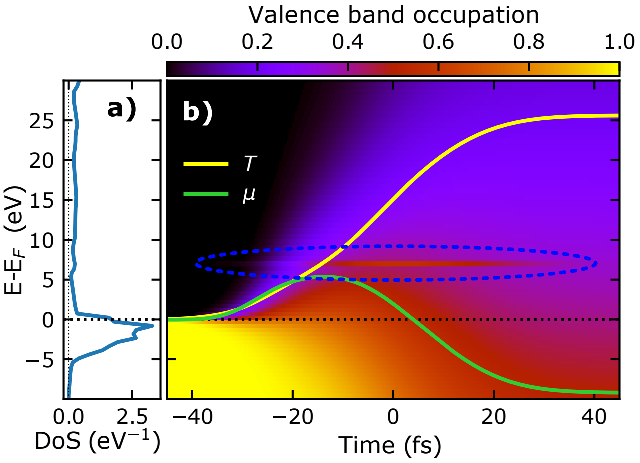

FIG. 4. **Density of states**. Panel a) shows the total DoS as used by the algorithm. Panel b) shows the relative population of the valence band over time at the sample surface for a pulse of 857.5 eV with a pulse energy of 30 J/cm^2. The non-thermal saturation of the valence states (sometimes called spectral bleaching or hole burning) is clearly visible at the resonant energy 7 eV above E_F and highlighted with a blue ellipse. Apart from that, the shifting and broadening of the thermalizing valence distribution is apparent, together with the rising electronic temperature T and shifting chemical potential μ. The valence thermalization time is evident here in the visible lag of the thermalizing valence occupation behind the chemical potential.

2. Core electrons

$$\frac{dR_C}{dt} = -\sum_{i,j} P^{res}_{i,j} + \sum_j P^{\text{Auger}}_j$$

The population of core electrons is reduced (or increased, depending on the sign of $P^{res}_{i,j}$) by resonant transitions of all incident photon energies E_i to states at all energies ρ_j (although this contribution is only non-zero at $i = j$), and is increased by Auger decay from electrons of all energies j in the valence system. Note that the spontaneous emission channel is neglected in our model as it is designed for soft X-ray energies where Auger emission accounts for most core-hole decays (here specifically, 99.1% of the nickel L$_3$ core-hole decays [37, 42]). In another concession to the specific experiment simulated here, we further neglect fast electrons leaving the sample, since the electron mean free path is much shorter than the sample thickness (about 1.3 nm [43] compared to a 20 nm thick sample). While a loss process for free electrons would be trivial to implement, the total number of electrons in the system being strictly constant over time is a valuable indicator for the self-consistency of the calculation.

3. *Free electrons*

$$\frac{dR_{Free}}{dt} = \sum_{i,j} P_{i,j}^{\text{non}-\text{res}} + \sum_{j} P_{j}^{\text{Auger}} - P^{\text{scatt}}$$

Unbound or free electrons are generated by non-resonant absorption from all incident photon energies E_i as well as Auger-decays from all energies in the valence band. The population is reduced by the free electron scattering rate P^{scatt}.

4. *Photon absorption and emission*

$$\frac{dN_i}{dz} = -P_{i=j}^{res} - \sum_{j} P_{i,j}^{\text{non}-\text{res}}$$

The number of photons is reduced or increased by resonant interaction and reduced by non-resonant absorption. Note that this is a purely spatial differential that depicts the instantaneous transmission of a certain number of photons through the entire sample in each time-step.

5. *Energy of free electrons*

$$\begin{aligned}\frac{dE_{Free}}{dt} &= \sum_{i,j} P_{i,j}^{\text{non}-\text{res}}(E_F + E_i - E_j) \\ &+ \left(\frac{\sum_j E_j(\rho_j - P_j^{\text{Auger}})}{\sum_j(\rho_j - P_j^{\text{Auger}})} + E_F\right)\sum_j P_j^{\text{Auger}} \\ &- P^{\text{scatt}}\frac{E_{Free}}{R_{Free}}\end{aligned}$$

E_F: Energy of the Fermi level

Because photons can "kick out" electrons from arbitrary states in the valence system, it becomes necessary to track the total kinetic energy of the free electrons, even though the distribution of energy among these electrons is not tracked. The rate of energy transfer to the free electron bath is described as the sum of non-resonant absorption and Auger decays, each multiplied by their respective energies (first and second line, respectively). The energy of the secondary Auger electrons is calculated as the average energy of all electrons other than the primary Auger electrons, as those drop to the core level. Finally, each electron that leaves R_{Free} reduces the energy of the bath by the average energy, which is $\frac{E_{Free}}{R_{Free}}$.

Explicitly tracking this energy also enables us to demonstrate the conservation of energy within the simulation; since there is no channel that allows energy to leave the sample, the energy held in the electronic subsystems matches that of the absorbed photons at all times. Figure 5 shows the internal energy of the electronic subsystems over time, integrated over an area of 1 nm^2 and the full 20 nm thickness of the sample. The comparison of the energy in various sub-systems demonstrates how quickly the energy of the photon pulse is transferred to valence excitations. Furthermore, observing the energy conservation has proven to be an invaluable tool to select sufficiently fine binning in time, space and energy, as it is particularly sensitive to the accumulation of numerical errors. For example, the calculation for the homogeneous illumination with 30 J/cm^2 shows a cumulative error in energy of 0.35%. This is in contrast to the electron conservation, which is strictly kept to machine precision level due to the symmetric way the process terms are arranged to form the time differentials.

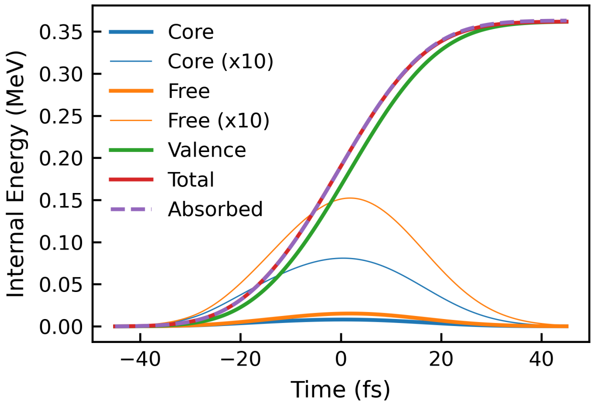

FIG. 5. **Energy in the sample system** over time for a pulse at 857.5 eV, integrated over the full 20 nm thickness of the sample and a 1 nm^2 area illuminated with a fluence of 30 J/cm^2. The absorbed energy is calculated from the difference between incident and transmitted photons, while the total energy is a sum of the energy held in the electronic sub-systems of core-holes, free electrons, and valence excitation. Due to the fast process rates in comparison to the pulse duration, the energy held in core excitations and free electrons remains small, which is why a 10 times scaled curve is also shown.

D. Parameters

There are four categories of parameters: First, resolution parameters for the number of steps in time, space, and energy are chosen as a compromise between calculation time and numerical error; second, experimental parameters such as the pulse duration, peak fluence, and bandwidth of the interacting photons reflect experimental conditions; third, ground-state properties such as the atomic density and number of states and electrons, as well as Auger-decay limited core-hole lifetime are drawn from published literature, while the resonant and non-resonant absorption lengths are derived from the ground-state spectrum as described below. Fourth, the model-inherent phenomenological parameters are the valence thermalization time τ_{th} and electron scattering time τ_{scatt}, which are varied to achieve the best match to the experimental results. A list of the relevant parameters and the chosen values for the present calculations, selected to match the experiment presented in [32], is shown in the appendix Table I.

The parameterization of several ground-state properties deserves further comment. Firstly, the DoS (motivated at the start of this section) was subdivided into bins m_j of varying size, favoring a fine resolution for the bound states. The size of the energy bin that is resonantly coupled to the core level by the incident photons is chosen such that it represents the interaction bandwidth of the photons. The interaction bandwidth is calculated as the convolution of the bandwidth of incident photons (i.e. the resolution of the experiment) and the natural line width of the core excitation. We further account for the final state broadening of excitations into less tightly bound states by enlarging the interaction bandwidth by 0.1 eV per eV above the Fermi level. Furthermore, the resonant and non-resonant absorption lengths are derived from the ground-state spectrum. We treat the non-resonant absorption length as constant, i.e. independent of photon energy, and derive it from the pre-edge absorption level. The transition matrix element of a core-valence transition exhibits a resonant enhancement close to the absorption edge, which translates into an energy dependence of the resonant absorption length. Above the Fermi level, where the DoS is unoccupied in the ground state, the resonant absorption length is encoded in the ground-state absorption spectrum. As the transition matrix element from the core level to states below the Fermi level is experimentally not straightforward to access, we use the approximation that the energy-dependence of the transition matrix element is symmetric around the Fermi energy. To derive the resonant absorption length, the non-resonant absorption level is subtracted from the spectrum and line broadening is accounted for by deconvolution with a pseudo-Voigt-profile of 50% Gaussian and Lorentzian share and a width of 640 meV Full-Width Half-Maximum (FWHM), representing 420 meV broadening from the experimental resolution and 480 meV from the core-hole lifetime [42]. The deconvolved resonant absorption spectrum above the Fermi level is then mirrored around the Fermi energy and the discontinuity within 320 meV around it is reconstructed with cubic interpolation. This results in the mirrored resonant absorption spectrum shown in Figure 6, which is used as the resonant absorption length parameter λ_i^{res}. Note that the results of simulated spectra were finally re-convolved with the same pseudo-Voigt-profile to simulate the same experiment.

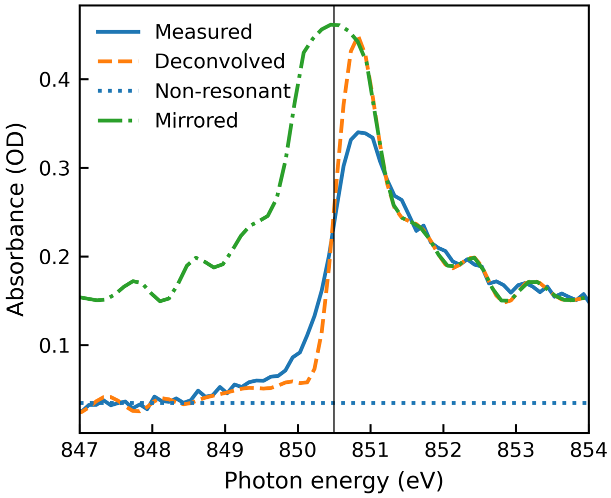

FIG. 6. **Derivation of absorption lengths as input parameters**, reconstructed from a measured ground-state spectrum (blue line). The non-resonant absorption level (blue dots) was determined from the pre-edge region. The measured resonant absorption length was deconvolved with the experimental resolution (orange dashes) and mirrored around the rising edge to retrieve a symmetric resonant absorption length around the resonance (green dot-dashed line). See main text for details.

III. DISCUSSION

A. Parameter Study

In Figure 7 we show the measured non-linear X-ray absorption spectra labeled (I) presented and discussed in [32] together with sets of simulated spectra computed for different sets of parameters.

The first set of simulated spectra (also presented in [32]) represents the best match with the experimental conditions and the parameters shown in table I and is labeled (II), while the consecutive sets, labeled (III) to (VI), demonstrate how the results change when individual parameters are modified. We present this set of simulations to showcase how our model may be used to understand the relation between the non-linear changes and various parameters. To fit the experimental results, however, only the parameters τ_{th} and τ_{scatt} are treated as unknowns, while all other parameters are known experimental or ground-state parameters.

In the best matching simulation (II), the experimental observations of a red-shifted rising edge, increased pre-edge absorption, as well as reduced absorption at and beyond the absorption peak, are reproduced. However, the saturation effect at the resonance is over-estimated and the lack of measured saturation around 852 eV cannot be explained by our model. See [32] for a more detailed discussion of these deviations.

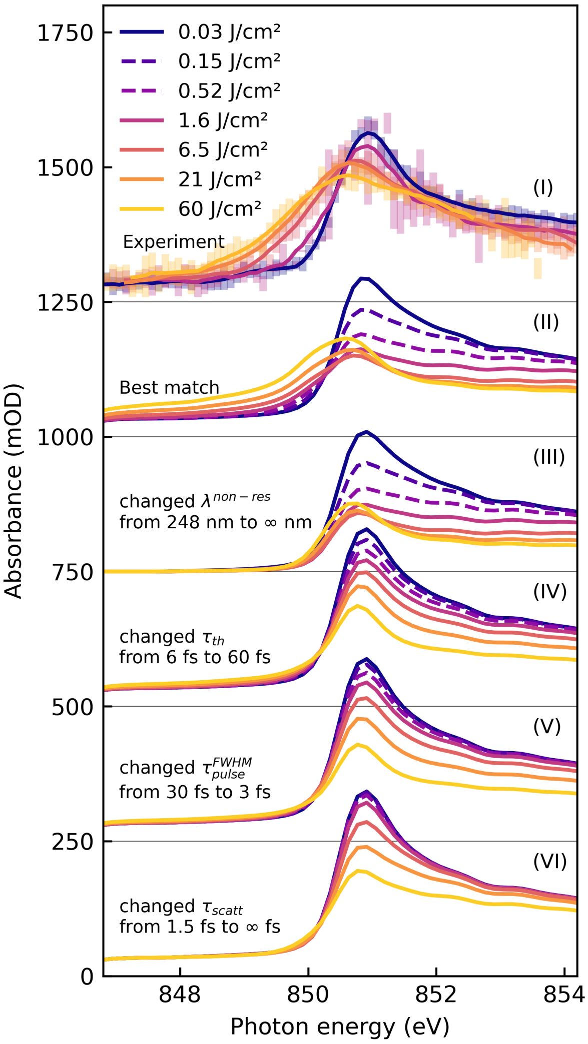

FIG. 7. **Fluence-dependent Ni L_3-edge spectra, simulated with different parameters and compared to the measurements presented in [32]** For the spectra (III) to (VI), one parameter was varied with respect to the best batch (II). Each set of spectra is offset by another 250 mOD as indicated by the horizontal lines. The error bars of the experimental data represent the 95% confidence intervals for each bin of 102 meV width; the solid lines represent smoothed spectra using a Savitzky-Golay filter using windows of 21 bins and 4th-order polynomials. The average fluence of events contributing to each spectrum is given in the legend. Dashed simulated spectra do not have a corresponding measurement.

The next simulation (III) was performed without non-resonant absorption. While this eliminates the pre-edge absorption rise, some shift of the absorption onset is still predicted within the original peak, while the spectra above the resonance onset behave similarly to the best-matching simulation.

With simulations (IV) and (V), we demonstrate the effect of prolonging the thermalization time or shortening the pulse duration by a factor of ten, respectively. Both have the similar effect of strongly reducing the peak shift and a moderate decrease of saturation beyond the resonance.

Finally, we show non-linear spectra (VI) where the free electron scattering process was eliminated ($\tau_{scatt} = \infty$). This prevents the majority of the excitation energy from entering the valence system and thus drastically reduces valence heating. This causes the pre-edge absorption rise and rising edge shift to vanish nearly entirely, and absorption-decrease due to saturation at and above the resonance is also strongly reduced. These differences underscore the importance of electronic scattering cascades to these phenomena.

While an extensive study of the correlations between the various model parameters and the observed effects is beyond the scope of this work, this brief parameter study allows an interpretation of how red-shift and pre-edge absorption rise occur: Let us consider a case where the incident photon energy is slightly below the absorption edge. Initially, only non-resonant absorption transfers energy to the sample, specifically by creating free electrons in form of photo-electrons. This energy is then transferred to the valence band due to electronic scattering cascades, where it causes many small, non-thermal excitations. These are homogeneously distributed over all valence energies and thus only lead to a small increase in pre-edge absorption (see the simulation with slow thermalization). However, this distribution of excitations develops towards the shape of a Fermi distribution over time, specifically with the thermalization time constant. If the pulses are long in comparison to the thermalization time, a significant number of states below the Fermi level becomes available for core-valence transitions during the pulse duration. This causes the observed increase in pre-edge absorption. Once the first empty valence states become available at the current photon energy, resonant absorption begins to occur in addition to the non-resonant absorption. The additional resonant absorption leads to more free electrons from Auger-decay, which in the same way as the photo-electrons further contribute to secondary electron scattering and thermalization. Because thermalization mostly creates free states just below the Fermi level, this process of self-enhancing rise of overall absorption manifests in a fluence-dependent shift of the rising edge to lower energies.

B. Limitations and Potential

As demonstrated in the parameter study above, this kind of analysis can provide a straightforward interpretation of how non-linear changes to the absorption spectrum emerge, and what each change says about the development of the electronic populations.

While the model already demonstrates good agreement with experimental results [32], below we discuss the limitations of our approach and possibilities for expanding or refining it.

In the model as described here, the DoS is not only assumed constant but also does not differentiate between spin-up and spin-down states, although we are treating a magnetic material. Splitting up the DoS in spin-up and spin-down states would allow for the inclusion of angular momentum conservation and transfer in the various scattering rates.

For thin samples where the electron mean free path becomes similar to the layer thickness, a loss process for free electrons should be introduced to account for electrons leaving the sample.

Fluorescent decay should be accounted for when moving to harder X-rays [37]. While introducing the decay channel itself would be simple, accurately accounting for reabsorption may be less straightforward, since the model only propagates light in one direction.

Furthermore, the thermalization time τ_{th} is used in this work as a global fitting parameter, although electron thermalization times have been suggested to depend on electronic temperature [44]. Since the electronic temperature and target distribution are calculated every timestep, an arbitrary dependence could be easily introduced, albeit with the necessity of additional fitting parameters.

The DoS is dominated by the crystal lattice, which is typically stable on the sub-100 fs timescale. However, recent Time-Dependent Density Functional Theory (TDDFT) calculations show that electronic processes (i.e. sub 100 fs) can also lead to modifications of the DoS via spin-orbit coupling modeled by introducing an onsite Hubbard correlation U to the mean-field Hamiltonian [45]. Since the rate model approach is generally not suited to calculate the DoS, incorporating modifications to the DoS would require a close interplay of the rate model with (TD)DFT calculations, leading to an ultimately much more complex approach reminiscent of models developed for the study of radiation-induced damage mechanisms [46, 47].

Furthermore, we derive the interaction bandwidth (the valence energy range to which core states can be resonantly coupled by incident photons) as a convolution of instrumental resolution and the lifetime of the core excitation, i.e. the Auger lifetime. The final state lifetime broadening of excitations into continuum states is described as a continuous broadening of 0.1 eV per eV above the Fermi energy [48]. It is however reasonable to expect that the final state lifetime is further shortened at higher fluences, due to increased rates of both electronic scattering and stimulated emission; the latter would be particularly relevant at the resonance peak. Such further broadening would cause more valence states to be available for resonant interaction and reduce the observed saturation effect while increasing the number of core-holes that may be created by high fluences[3]. Accounting for a fluence-dependent broadening of the interaction bandwidth in a refined rate model might help to remedy the overestimation of the saturation effect at the absorption peak in the presented calculations.

Another candidate for further refinement is an energy dependence of the electronic scattering rates. The presented model uses fixed rates for thermalization and scattering cascades, which both act on all valence states indiscriminately. This description would be especially inadequate when applied without modifications to a bandgap material. An advanced model could describe both the thermalization rate of the valence band and the energy of excitations from scattering cascades in an energy-resolved manner[4].

While such refinements may seem attractive, a core strength of the rate model approach is its relative simplicity and computational tractability, as well as the use of known ground-state parameters, which supports a straightforward physical interpretation. It is ultimately a mostly classical, phenomenological model which offers a complementary approach to ab-initio calculations. Every added complexity should therefore be weighed against its relevance, as a simpler model facilitates a meaningful interpretation and avoids introducing ambiguity in the results due to correlations between redundant input parameters.

Since the model operates on widely applicable principles, we expect that it may be applied to a wide range of materials with some predictive power, while the limitations described above apply. The results will especially deviate from observations wherever multi-particle effects, such as electron correlations or quasiparticles become relevant.

As presented, the model enables an understanding of the electronic population history under strong X-ray fluences and characterization of the resulting non-linear absorption near a core resonance. Non-linear absorption studies like the one analyzed here [32] allow one to characterize the excitation dynamics of the electronic system under study. Furthermore, consideration of these dynamics is, due to the extreme fluences required, particularly relevant for methods in the emerging field of non-linear X-ray spectroscopy [4–21].

IV. CONCLUSION

In this work, we propose a model of differential rate equations describing the various excitation and decay

---

[3] When considering only resonant absorption, the core level, and resonant valence states constitute a classic two-level system. In the extreme fluence limit, the relative populations of such a system are given by the state degeneracy ratio, i.e. the ratio between the number of involved core and valence states.

[4] It might be non-trivial to normalize this energy dependence such that the electronic scattering processes do not violate the conservation of energy.

processes that connect core- and valence electronic states to quantitatively describe the non-linear changes to X-ray absorption around a core resonance that occur when employing increasingly high FEL pulse energies. We present the framework of the model in detail, applying it to the case of recently measured non-linear absorption spectra of nickel films at the L_3 edge, recorded with monochromatic X-rays [32].

We demonstrate how the rate model reaches good agreement with the experimental results while disentangling the contributions of the relevant physical processes: resonant and non-resonant absorption, Auger decay, electron thermalization, and electronic scattering cascades. Our rate model contains numerous simplifications in order to approximate the result of complex interactions between many particles in terms of average transition rates. Nevertheless, the resulting description enables a quantitative understanding of the evolution of the system and the processes responsible for spectral changes. In the presented calculations, the most relevant effect is valence system heating due to secondary electron cascades from free electrons. Our results allow quantifying the absorbance changes caused by fundamental electron population dynamics, which are crucial to disentangle from collective quantum effects studied with currently evolving non-linear X-ray spectroscopy techniques.

ACKNOWLEDGMENTS

Funding by the Helmholtz Association (grant VH-NG-1105) is gratefully acknowledged. This research was supported in part through the Maxwell computational resources operated at Deutsches Elektronen-Synchrotron DESY, Hamburg, Germany
Author Contributions: R.Y.E. and M.B. developed the model. R.Y.E. wrote the manuscript with contributions from all authors.

Appendix A: Run-Time and Code Availability

Using adequate multiprocessing on a single node of a computing cluster allows computation of non-linear spectra such as presented here within many minutes to several hours, depending on the required number of steps in space, time, and energy. The simulation code is publicly available [49].

Appendix B: Parameter table

Symbol	Code	Description	Unit	Value
N_z	`Nsteps_z`	Steps in sample depth	-	50
N_{E_j}	`N_j`	Steps in energies considered in valence system	-	90
N_{E_i}	`N_points_E`	Number of photon energies / points in the spectrum	-	69
-	`N_local_fluences _to_calculate`	Number of fixed fluences that are directly simulated	-	30
-	`N_pulse_energies`	Number of final pulse energies with a Gaussian spot profile	-	20
-	`Nsteps_r`	Number of steps in the radial integration of the Gaussian spot	-	100
dt_{min}	`timestep_min`	Minimum allowed time-step	fs	0.15
-	`Energy_axis_max`	Maximum energy in the valence system	eV	800
-	`Energy_axis_fine_until`	Finer sampling for energies lower than this	eV	30
-	`Energy_axis_min`	Valence band origin	eV	-10
-	`DoS_band_origin`	Energy minimum from where to use the loaded DOS	eV	-10
-	`DoS_band_dd_end`	Energy maximum from where to use the loaded DOS	eV	30
σ_{tj}	`tdur_sig`	Rms pulse duration of photons	fs	13
E_i	`E_i`	Photon energy of incident photons	eV	848-856
I_0	`I_0`	Number of photons irradiated	photons nm^{-2}	$0 - 1.4$e4
N_{E_i}	`N_photens`	Number of different photon energies irradiated	-	1
T_0	`temperature`	Initial sample temperature	K	300
σ_{BW}	`interaction_bandwidth`	Bandwidth of resonant interaction at E_j	eV	0.638
τ_{scatt}	`tau_scattering`	Scattering time of free electrons	fs	1.5
τ_{th}	`tau_th`	Thermalization time of non-thermal valence states	fs	6
-	`DoS_shapefile`	Filename of the total DOS from DFT-calculation	-	from [33]
Z	`Z`	Total sample thickness	nm	20
ρ	`atomic_density`	Atomic density	atoms nm^{-3}	91.4
R_V^0	`valence_GS_occupation`	Valence electrons per atom in the ground state	states atom^{-1}	10
M_C	`core_states`	Core electrons/states per atom in the L$_3$ core level	states atom^{-1}	4
E_f	`E_f`	Fermi level; used as zero for energy axes of E_j and E_i	eV	850.5
τ_C	`tau_core_hole`	core-hole lifetime, from [42]	fs	1.4
$\lambda^{non-res}$	`lambd_nonres`	Absorption length due to non-resonant absorption	nm	248
λ_{Ej}^{res}	`lambd_res_Ej`	Absorption length due to resonant absorption	nm	20-83

TABLE I: Parameters for the presented simulation results. The first block lists parameters that define the resolution of the simulation, the second block shows experimental conditions, the third phenomenological fitting parameters and the last block contains physical ground-state properties of the sample.

---

[1] R. W. Boyd, *Nonlinear optics*, 3rd ed. (Academic press, 2008).

[2] W. Demtröder, *Laser Spectroscopy 2: Experimental Techniques, Fifth Edition* (Springer Berlin Heidelberg, Berlin, Heidelberg, 2015) pp. 1–757.

[3] M. D. Levenson and S. S. Kano, *Introduction to nonlinear laser spectroscopy* (Academic Press, Inc. (London) LTD., 1987).

[4] M. Beye, R. Y. Engel, J. O. Schunck, S. Dziarzhytski, G. Brenner, and P. S. Miedema, Non-linear soft x-ray methods on solids with MUSIX—the multi-dimensional spectroscopy and inelastic x-ray scattering endstation, Journal of Physics: Condensed Matter **31**, 014003 (2019).

[5] S. Mukamel, Multiple core-hole coherence in x-ray four-wave-mixing spectroscopies, Phys. Rev. B **72**, 235110 (2005).

[6] T. E. Glover, D. M. Fritz, M. Cammarata, T. K. Allison, S. Coh, J. M. Feldkamp, H. Lemke, D. Zhu, Y. Feng, R. N. Coffee, M. Fuchs, S. Ghimire, J. Chen, S. Shwartz, D. A. Reis, S. E. Harris, and J. B. Hastings, X-ray and optical wave mixing, Nature **488**, 603 (2012).

[7] M. Beye, S. Schreck, F. Sorgenfrei, C. Trabant, N. Pontius, C. Schüßler-Langeheine, W. Wurth, and A. Föhlisch, Stimulated x-ray emission for materials science, Nature **501**, 191 (2013).

[8] C. Weninger, M. Purvis, D. Ryan, R. A. London, J. D. Bozek, C. Bostedt, A. Graf, G. Brown, J. J. Rocca, and N. Rohringer, Stimulated electronic x-ray raman scattering, Phys. Rev. Lett. **111**, 233902 (2013).

[9] S. Shwartz, M. Fuchs, J. B. Hastings, Y. Inubushi, T. Ishikawa, T. Katayama, D. A. Reis, T. Sato, K. Tono, M. Yabashi, S. Yudovich, and S. E. Harris, X-ray second harmonic generation, Physical Review Letters **112**, 163901 (2014).

[10] K. Tamasaku, E. Shigemasa, Y. Inubushi, T. Katayama, K. Sawada, H. Yumoto, H. Ohashi, H. Mimura, M. Yabashi, K. Yamauchi, and T. Ishikawa, X-ray two-photon absorption competing against single and sequential multiphoton processes, Nature Photonics **8**, 313 (2014).

[11] F. Bencivenga, R. Cucini, F. Capotondi, A. Battistoni, R. Mincigrucci, E. Giangrisostomi, A. Gessini, M. Manfredda, I. P. Nikolov, E. Pedersoli, E. Principi, C. Svetina, P. Parisse, F. Casolari, M. B. Danailov, M. Kiskinova, and C. Masciovecchio, Four-wave mixing experiments with extreme ultraviolet transient gratings, Nature **520**, 205 (2015).

[12] S. Schreck, M. Beye, and A. Föhlisch, Implications of stimulated resonant x-ray scattering for spectroscopy, imaging, and diffraction in the regime from soft to hard x-rays, Journal of Modern Optics **62**, S34 (2015).

[13] R. K. Lam, S. L. Raj, T. A. Pascal, C. D. Pemmaraju, L. Foglia, A. Simoncig, N. Fabris, P. Miotti, C. J. Hull, A. M. Rizzuto, J. W. Smith, R. Mincigrucci, C. Masciovecchio, A. Gessini, E. Allaria, G. De Ninno, B. Diviacco, E. Roussel, S. Spampinati, G. Penco, S. Di Mitri, M. Trovò, M. Danailov, S. T. Christensen, D. Sokaras, T. C. Weng, M. Coreno, L. Poletto, W. S. Drisdell, D. Prendergast, L. Giannessi, E. Principi, D. Nordlund, R. J. Saykally, and C. P. Schwartz, Soft x-ray second harmonic generation as an interfacial probe, Physical Review Letters **120**, 023901 (2018).

[14] K. Tamasaku, E. Shigemasa, Y. Inubushi, I. Inoue, T. Osaka, T. Katayama, M. Yabashi, A. Koide, T. Yokoyama, and T. Ishikawa, Nonlinear spectroscopy with x-ray two-photon absorption in metallic copper, Physical Review Letters **121**, 083901 (2018).

[15] D. J. Higley, A. H. Reid, Z. Chen, A. A. L. Loïc Le Guyader and, T. Liu, T. Chase, G. L. Dakovski, A. Mitra, E. Yuan, H. A. Dürr, W. F. Schlotter, and J. Stöhr, Femtosecond x-ray induced changes of the electronic and magnetic response of solids from electron redistribution, Nature communications **10**, 5289 (2019).

[16] H. Rottke, R. Y. Engel, D. Schick, J. O. Schunck, P. S. Miedema, M. C. Borchert, M. Kuhlmann, N. Ekanayake, S. Dziarzhytski, G. Brenner, U. Eichmann, C. von Korff Schmising, M. Beye, and S. Eisebitt, Probing electron and hole colocalization by resonant four-wave mixing spectroscopy in the extreme ultraviolet, Science Advances **8**, eabn5127 (2022).

[17] J. R. Rouxel, D. Fainozzi, R. Mankowsky, B. Rösner, G. Seniutinas, R. Mincigrucci, S. Catalini, L. Foglia, R. Cucini, F. Döring, A. Kubec, F. Koch, F. Bencivenga, A. A. Haddad, A. Gessini, A. A. Maznev, C. Cirelli, S. Gerber, B. Pedrini, G. F. Mancini, E. Razzoli, M. Burian, H. Ueda, G. Pamfilidis, E. Ferrari, Y. Deng, A. Mozzanica, P. J. M. Johnson, D. Ozerov, M. G. Izzo, C. Bottari, C. Arrell, E. J. Divall, S. Zerdane, M. Sander, G. Knopp, P. Beaud, H. T. Lemke, C. J. Milne, C. David, R. Torre, M. Chergui, K. A. Nelson, C. Masciovecchio, U. Staub, L. Patthey, and C. Svetina, Hard X-ray transient grating spectroscopy on bismuth germanate, Nature Photonics **15**, 499 (2021).

[18] F. Bencivenga, R. Mincigrucci, F. Capotondi, A. Calvi, R. Cucini, L. Foglia, E. Pedersoli, E. Principi, A. Simoncig, P. Cinquegrana, M. B. Danailov, G. De Ninno, S. Di Mitri, G. Gaio, A. Gessini, L. Giannessi, N. Mahne, M. Manfredda, I. P. Nikolov, G. M. Penco, L. Raimondi, P. R. Ribic, C. Svetina, M. Trovo, M. Zangrando, and C. Masciovecchio, An approach for realizing four-wave-mixing experiments stimulated by two-color extreme ultraviolet pulses, in *International Conference on X-Ray Lasers 2020*, July 2021, edited by D. Bleiner (SPIE, 2021) p. 28.

[19] S. Wirok-Stoletow, R. Jin, D. Kolbasova, S.-K. Son, A. Aquila, and R. Santra, Nonsequential two-photon absorption in solid Ge irradiated by an intense x-ray free-electron-laser pulse, Physical Review A **106**, 023118 (2022).

[20] C. Boemer, D. Krebs, A. Benediktovitch, E. Rossi, S. Huotari, and N. Rohringer, Towards novel probes for valence charges via X-ray optical wave mixing, Faraday Discussions **228**, 451 (2021), arXiv:2103.14710.

[21] C. Serrat, Localized core four-wave mixing buildup in the x-ray spectrum of chemical species, The Journal of Physical Chemistry Letters **12**, 1093 (2021).

[22] D. Schwickert, M. Ruberti, P. Kolorenč, S. Usenko, A. Przystawik, K. Baev, I. Baev, M. Braune, L. Bocklage, M. K. Czwalinna, S. Deinert, S. Düsterer, A. Hans, G. Hartmann, C. Haunhorst, M. Kuhlmann, S. Palutke, R. Röhlsberger, J. Rönsch-Schulenburg, P. Schmidt, S. Toleikis, J. Viefhaus, M. Martins, A. Knie, D. Kip, V. Averbukh, J. P. Marangos, and T. Laarmann, Electronic quantum coherence in glycine molecules probed with ultrashort x-ray pulses in real time, Science Advances **8**, 1 (2022).

[23] B. Nagler, U. Zastrau, R. R. Fäustlin, S. M. Vinko, T. Whitcher, A. J. Nelson, R. Sobierajski, J. Krzywinski, J. Chalupsky, E. Abreu, S. Bajt, T. Bornath, T. Burian, H. Chapman, J. Cihelka, T. Döppner, S. Düsterer, T. Dzelzainis, M. Fajardo, E. Förster, C. Fortmann, E. Galtier, S. H. Glenzer, S. Göde, G. Gregori, V. Hajkova, P. Heimann, L. Juha, M. Jurek, F. Y. Khattak, A. R. Khorsand, D. Klinger, M. Kozlova, T. Laarmann, H. J. Lee, R. W. Lee, K.-H. Meiwes-Broer, P. Mercere, W. J. Murphy, A. Przystawik, R. Redmer, H. Reinholz, D. Riley, G. Röpke, F. Rosmej, K. Saksl, R. Schott, R. Thiele, J. Tiggesbäumker, S. Toleikis, T. Tschentscher, I. Uschmann, H. J. Vollmer, and J. S. Wark, Turning solid aluminium transparent by intense soft x-ray photoionization, Nature Physics **5**, 693 (2009).

[24] S. M. Vinko, U. Zastrau, S. Mazevet, J. Andreasson, S. Bajt, T. Burian, J. Chalupsky, H. N. Chapman, J. Cihelka, D. Doria, T. Döppner, S. Düsterer, T. Dzelzainis, R. R. Fäustlin, C. Fortmann, E. Förster, E. Galtier, S. H. Glenzer, S. Göde, G. Gregori, J. Hajdu, V. Hajkova, P. A. Heimann, R. Irsig, L. Juha, M. Jurek, J. Krzywinski, T. Laarmann, H. J. Lee, R. W. Lee, B. Li, K.-H. Meiwes-Broer, J. P. Mithen, B. Nagler, A. J. Nelson, A. Przystawik, R. Redmer, D. Riley, F. Rosmej, R. Sobierajski, F. Tavella, R. Thiele, J. Tiggesbäumker, S. Toleikis, T. Tschentscher, L. Vysin, T. J. Whitcher, S. White, and J. S. Wark, Electronic structure of an XUV pho-

togenerated solid-density aluminum plasma, Phys. Rev. Lett. **104**, 225001 (2010).

[25] A. Di Cicco, K. Hatada, E. Giangrisostomi, R. Gunnella, F. Bencivenga, E. Principi, C. Masciovecchio, and A. Filipponi, Interplay of electron heating and saturable absorption in ultrafast extreme ultraviolet transmission of condensed matter, Phys. Rev. B **90**, 220303(R) (2014).

[26] H. Yoneda, Y. Inubushi, M. Yabashi, T. Katayama, T. Ishikawa, H. Ohashi, H. Yumoto, K. Yamauchi, H. Mimura, and H. Kitamura, Saturable absorption of intense hard x-rays in iron, Nature communications **5**, 5080 (2014).

[27] D. S. Rackstraw, O. Ciricosta, S. M. Vinko, B. Barbrel, T. Burian, J. Chalupský, B. I. Cho, H.-K. Chung, G. L. Dakovski, K. Engelhorn, V. Hájková, P. Heimann, M. Holmes, L. Juha, J. Krzywinski, R. W. Lee, S. Toleikis, J. J. Turner, U. Zastrau, and J. S. Wark, Saturable absorption of an x-ray free-electron-laser heated solid-density aluminum plasma, Phys. Rev. Lett. **114**, 015003 (2015).

[28] E. Principi, E. Giangrisostomi, R. Cucini, F. Bencivenga, A. Battistoni, A. Gessini, R. Mincigrucci, M. Saito, S. Di Fonzo, F. D'Amico, A. Di Cicco, R. Gunnella, A. Filipponi, A. Giglia, S. Nannarone, and C. Masciovecchio, Free electron laser-driven ultrafast rearrangement of the electronic structure in Ti, Structural Dynamics **3**, 023604 (2016).

[29] M. Hantschmann and A. Föhlisch, A rate model approach for FEL pulse induced transmissions changes, saturable absorption, x-ray transparency and stimulated emission, Journal of Electron Spectroscopy and Related Phenomena **256**, 147139 (2022).

[30] D. J. Higley, Z. Chen, M. Beye, M. Hantschmann, A. H. Reid, V. Mehta, O. Hellwig, G. L. Dakovski, A. Mitra, R. Y. Engel, T. Maxwell, Y. Ding, S. Bonetti, M. Bucher, S. Carron, T. Chase, E. Jal, R. Kukreja, T. Liu, A. Föhlisch, H. A. Dürr, W. F. Schlotter, and J. Stöhr, Stimulated resonant inelastic x-ray scattering in a solid, Communications Physics **5**, 1 (2022).

[31] K. Hatada and A. Di Cicco, Modeling saturable absorption for ultra short x-ray pulses, Journal of Electron Spectroscopy and Related Phenomena **196**, 177 (2014).

[32] R. Y. Engel and et al, High-fluence changes to resonant nonlinear x-ray absorption spectra are dominated by electron dynamics, Jointly submitted to Phys. Rev. Lett. (2022).

[33] K. Persson, Materials data on Ni (sg:225) by materials project (2016).

[34] A. Jain, S. P. Ong, G. Hautier, W. Chen, W. D. Richards, S. Dacek, S. Cholia, D. Gunter, D. Skinner, G. Ceder, and K. a. Persson, The Materials Project: A materials genome approach to accelerating materials innovation, APL Materials **1**, 011002 (2013).

[35] G. O. Williams and M. Fajardo, Collisional ionization and recombination in degenerate plasmas beyond the free-electron-gas approximation, Phys. Rev. E **102**, 063204 (2020).

[36] J. Chen, D. Tzou, and J. Beraun, A semiclassical two-temperature model for ultrafast laser heating, International Journal of Heat and Mass Transfer **49**, 307 (2006).

[37] M. O. Krause, Atomic radiative and radiationless yields for k and l shells, Journal of Physical and Chemical Reference Data **8**, 307 (1979).

[38] P. Virtanen, R. Gommers, T. E. Oliphant, M. Haberland, T. Reddy, D. Cournapeau, E. Burovski, P. Peterson, W. Weckesser, J. Bright, S. J. van der Walt, M. Brett, J. Wilson, K. J. Millman, N. Mayorov, A. R. J. Nelson, E. Jones, R. Kern, E. Larson, C. J. Carey, İ. Polat, Y. Feng, E. W. Moore, J. VanderPlas, D. Laxalde, J. Perktold, R. Cimrman, I. Henriksen, E. A. Quintero, C. R. Harris, A. M. Archibald, A. H. Ribeiro, F. Pedregosa, P. van Mulbregt, and SciPy 1.0 Contributors, SciPy 1.0: Fundamental algorithms for scientific computing in python, Nature Methods **17**, 261 (2020).

[39] P. L. Bhatnagar, E. P. Gross, and M. Krook, A Model for Collision Processes in Gases. I. Small Amplitude Processes in Charged and Neutral One-Component Systems, Physical Review **94**, 511 (1954).

[40] E. Bévillon, J. P. Colombier, V. Recoules, and R. Stoian, Free-electron properties of metals under ultrafast laser-induced electron-phonon nonequilibrium: A first-principles study, Phys. Rev. B **89**, 115117 (2014).

[41] Z. Lin, L. V. Zhigilei, and V. Celli, Electron-phonon coupling and electron heat capacity of metals under conditions of strong electron-phonon nonequilibrium, Phys. Rev. B **77**, 075133 (2008).

[42] M. O. Krause and J. H. Oliver, Natural widths of atomic K and L levels, Kα x-ray lines and several KLL auger lines, Journal of Physical and Chemical Reference Data **8**, 329 (1979).

[43] C. Powell and A. Jablonski, NIST electron inelastic-mean-free-path database 71, version 1.1 (2000).

[44] B. Y. Mueller and B. Rethfeld, Relaxation dynamics in laser-excited metals under nonequilibrium conditions, Phys. Rev. B **87**, 035139 (2013).

[45] T. Lojewski, M. F. Elhanoty, L. L. Guyader, O. Grånäs, N. Agarwal, C. Boeglin, R. Carley, A. Castoldi, C. David, C. Deiter, F. Döring, R. Y. Engel, F. Erdinger, H. Fangohr, C. Fiorini, P. Fischer, N. Gerasimova, R. Gort, F. de Groot, K. Hansen, S. Hauf, D. Hickin, M. Izquierdo, B. E. Van Kuiken, Y. Kvashnin, C.-H. Lambert, D. Lomidze, S. Maffessanti, L. Mercadier, G. Mercurio, P. S. Miedema, K. Ollefs, M. Pace, M. Porro, J. Rezvani, B. Rösner, N. Rothenbach, A. Samartsev, A. Scherz, J. Schlappa, C. Stamm, M. Teichmann, P. Thunstrom, M. Turcato, A. Yaroslavtsev, J. Zhu, M. Beye, H. Wende, U. Bovensiepen, O. Eriksson, and A. Eschenlohr, The interplay of local electron correlations and ultrafast spin dynamics in fcc Ni (2022), arXiv:2210.13162.

[46] N. Medvedev, V. Tkachenko, V. Lipp, Z. Li, and B. Ziaja, Various damage mechanisms in carbon and silicon materials under femtosecond x-ray irradiation, 4open **1**, 3 (2018).

[47] V. Lipp, V. Tkachenko, M. Stransky, B. Aradi, T. Frauenheim, and B. Ziaja, Density functional tight binding approach utilized to study x-ray-induced transitions in solid materials, Scientific reports **12**, 1551 (2022).

[48] J. Stöhr, *NEXAFS spectroscopy*, Vol. 25 (Springer Science & Business Media, 1992).

[49] R. Engel, x-ray non-linear dynamics simulation code [yet private], `https://github.com/F00lWise/XNLdyn` (2022).

Chapter 5

Stimulated Resonant Inelastic X-ray Scattering

Experimentally, the following work is very similar to the measurements performed at SCS presented above, as it is also based on a non-linear absorption measurement at the L_3-edge of a $3d$-metal[1]. The most relevant distinction between the two experiments is the incident photon bandwith: While the study above used monochromatic radiation, the experiment described in the following uses the full SASE-bandwidth and a broadband normalization scheme similar to that presented in chapter 3.3.2.2.

This difference is much more impactful in non-linear measurements than in linear XANES: In linear XANES one would measure the exact same spectrum, regardless if it was measured with a parallel acquisition as in the FL24&MUSIX-setup [2] or using a monochromator as in the PG2 or SCS setups [1, 8]. In non-linear XANES, the wider bandwidth of the pulse not only makes a higher overall fluence available, but the electrons excited through resonant absorption are also distributed over a broader range of the valence density of states. The greater number of resonant valence states also changes the state degeneracy ratio between core- and valence-states (compare chapter 2.3.1), which proportionally increases the number of core holes in the transparent limit of full saturation. The term *saturation* evokes the mental image that absorption events cannot occur because the upper states are equally occupied as lower states. However, the more accurate description (which yields the same predictions for a macroscopic sample) is that a number of absorption events is balanced out by an equal number of stimulated emission events at the same energy (compare Eq. 2.22). Compared to the linear absorption spectrum, we refer to the non-linear excess in transmission due to elastic stimulated emission as stimulated REXS.

A broad incident spectrum additionally enables the analog inelastic process (SRIXS) to occur, where a core electron is excited into one valence state and an electron from a different valence state is stimulated to repopulate the core hole.[2]

---

[1] The sample was a multilayer structure of cobalt (the sample) and palladium (as a buffer material) in 25 layer pairs of 1 nm and 0.7 nm, respectively.

[2] Higley et al. only label the inelastic scattering with energy loss as stimulated RIXS. In my opinion, there is no reason to assume that the corresponding process with energy gain does not occur, albeit as a minority channel and difficult to disentangle from the observed stimulated REXS signal.

In the following study, the stimulated gain in transmission due to the RIXS and REXS processes is disentangled. In addition, as in our study on nickel, redistribution of hot electrons caused by scattering cascades from Auger- and photo-electrons was identified as a major non-linear feature.

The results were interpreted using two models: On the one hand, a three-level Maxwell-Bloch model is used to estimate the overall stimulated inelastic scattering efficiency. This model is conceptually similar to earlier three-level rate models [75] in that it describes propagation through a sample that is described as a one-dimensional "slab" of atoms that are in turn characterized by a ground, core-excited, and valence-excited state. In contrast to the rate models, which work strictly in the incoherent limit and are solved through iterative integration of the differential equations, the Maxwell-Bloch model operates in a semi-classical picture of time-dependent material polarization in connection with a time-evolution matrix describing the temporal evolution of the sample (see [200] for details). On the other hand, the Kramers-Heisenberg-Dirac description of the stimulated elastic and inelastic scattering cross-section is formulated, as I have introduced it in chapter 2.5.4 to quantify the observed signal in dependence of the coherent fraction of the SASE pulses.

The study found that the achieved SRIXS signal was six orders of magnitude larger than the (conventional) spontaneous RIXS signal. The largest part of this enhancement, about four to five orders of magnitude, is due to the angular enhancement, i.e. the fact that the SRIXS signal is focused forward as opposed to the isotropically emitted spontaneous RIXS signal. Despite this promising result, the effect of electron redistribution, which was also modeled in the previous chapter, is found to be deleterious to the measurement of SRIXS, as the features of both effects overlap in the spectra and must be disentangled in the analysis.

The following publication is reproduced from [6], in accordance with the Creative Commons Attribution 4.0 International license under which the article is published.

I include this study due to its high relevance in the context of this thesis, although my own contribution was limited to performing a pulse-duration analysis of the spectra, using algorithms presented in my earlier work [130, 131].

communications
physics

ARTICLE

https://doi.org/10.1038/s42005-022-00857-8 OPEN

Stimulated resonant inelastic X-ray scattering in a solid

Daniel J. Higley[1,2✉], Zhao Chen[1,3], Martin Beye[4], Markus Hantschmann[5,6], Alex H. Reid[1], Virat Mehta[7], Olav Hellwig[7,8,9], Georgi L. Dakovski[1], Ankush Mitra[1,10], Robin Y. Engel[4], Tim Maxwell[1], Yuantao Ding[1], Stefano Bonetti[1,11], Maximilian Bucher[1], Sebastian Carron[1], Tyler Chase[1,2], Emmanuelle Jal[1,12], Roopali Kukreja[1,13], Tianmin Liu[1,3], Alexander Föhlisch[5,6], Hermann A. Dürr[1,14], William F. Schlotter[1] & Joachim Stöhr[1✉]

When materials are exposed to X-ray pulses with sufficiently high intensity, various nonlinear effects can occur. The most fundamental one consists of stimulated electronic decays after resonant absorption of X-rays. Such stimulated decays enhance the number of emitted photons and the emission direction is confined to that of the stimulating incident photons which clone themselves in the process. Here we report the observation of stimulated resonant elastic (REXS) and inelastic (RIXS) X-ray scattering near the cobalt L_3 edge in solid Co/Pd multilayer samples. We observe an enhancement of order 10^6 of the stimulated over the conventional spontaneous RIXS signal into the small acceptance angle of the RIXS spectrometer. We also find that in solids both stimulated REXS and RIXS spectra contain contributions from inelastic electron scattering processes, even for ultrashort 5 fs pulses. Our results reveal the potential and caveats of the development of stimulated RIXS in condensed matter.

---

[1] SLAC National Accelerator Laboratory, 2575 Sand Hill Road, Menlo Park, CA 94025, USA. [2] Department of Applied Physics, Stanford University, Stanford, CA 94305, USA. [3] Department of Physics, Stanford University, Stanford, CA 94305, USA. [4] Deutsches Elektronen-Synchrotron DESY, Notkestr. 85, 22607 Hamburg, Germany. [5] Institute of Physics and Astronomy, University of Potsdam, Karl-Liebnecht-Straße 24/25, 14476 Potsdam, Germany. [6] Institute of Methods and Instrumentation for Synchrotron Radiation Research, Helmholtz-Zentrum Berlin für Materialien und Energie GmbH, Albert-Einstein-Straße 15, 12489 Berlin, Germany. [7] San Jose Research Center, HGST a Western Digital Company, 3403 Yerba Buena Rd., San Jose, CA 95135, USA. [8] Institute of Physics, Chemnitz University of Technology, 09107 Chemnitz, Germany. [9] Institute of Ion Beam Physics and Materials Research, Helmholtz-Zentrum Dresden-Rossendorf, 01328 Dresden, Germany. [10] Department of Physics, University of Warwick, Coventry CV4 7AL, UK. [11] Department of Physics, Stockholm University, S-10691 Stockholm, Sweden. [12] Sorbonne Université, CNRS, Laboratoire de Chemie Physique—Matière et Rayonnement, LCPMR, 75005 Paris, France. [13] Department of Materials Science and Engineering, University of California Davis, Davis, CA 95616, USA. [14] Department of Physics and Astronomy, Uppsala University, 75120 Uppsala, Sweden. ✉email: dhigley@alumni.stanford.edu; stohr@slac.stanford.edu

Elastic and inelastic X-ray scattering have long provided detailed information on the static atomic arrangement in solids and the associated fundamental electronic, magnetic and lattice excitations. In recent years, conventional X-ray Thomson scattering has been increasingly supplemented by resonant elastic (REXS) and inelastic (RIXS) X-ray scattering which offer enhanced cross sections as well as atomic and bonding specificity. RIXS has been used to study the low-energy excitations in atoms and molecules[1], in chemisorption systems[2] and the momentum-dependent charge and spin excitations in solids[3,4]. REXS has been mostly utilized for diffractive imaging of the nanoscale charge[5] and spin[6] distributions in solids.

REXS and RIXS processes involve excitations of atomic core electrons into unfilled localized electronic valence states. The resonant x-ray absorption (XAS) step is followed by so-called spontaneous electronic decays resulting in the creation of photons or Auger electrons. The radiative (photon) and non-radiative (Auger) spontaneous decay probabilities are linked through the fluorescence yield which to a good approximation is an atomic core shell specific tabulated quantity[7]. Resonant X-ray scattering in the form of REXS and RIXS consists of two consecutive and linked absorption and emission processes. In the widely used Kramers-Heisenberg-Dirac (KHD) perturbation description of X-ray/matter interactions, absorption and emission, alone, are first order processes, while the link of the two processes in REXS and RIXS requires a second order perturbation treatment[1,4]. All first and spontaneous second order processes scale linearly with the incident intensity.

Of all X-ray processes, resonant absorption has the largest cross section. The spontaneous emission probability of a photon in the decay step is typically considerably smaller than that of an Auger electron in the soft X-ray range. This together with the random spontaneous emission direction of the photons causes a great reduction in the number of photons detected within the small solid angle of a spectrometer. For example, in L-edge RIXS measurements of the important $3d$ transition metal atoms, the photon emission probability given by the fluorescence yield, is of order $Y_\mathrm{f} = 10^{-3}$–10^{-2} of the Auger decay probability[7] and the solid angle of acceptance of state-of-the-art RIXS spectrometers is of order 10^{-5} of 4π steradians[8]. Thus the measured spontaneous RIXS signal is typically of order of a single photon for about 10^7 photons absorbed by a sample[9].

The development of RIXS, which has the advantage over optical techniques of atomic specificity, has greatly benefitted from the increased brightness of modern synchrotron radiation sources which offer an incident photon flux within a bandwidth of 100 meV of order 10^{13} photons. Remarkably, however, even at such intensities, the photon degeneracy parameter, defined as the number of photons $n_{p\mathbf{k}}$ in the same polarization mode p and wavevector (direction) mode $\mathbf{k}$, is still less than 1[10]. This means that when an absorption event is triggered by an incident photon, there is no second photon available to influence, i.e. stimulate, the decay. This dilemma has only been overcome by the advent of X-ray Free Electron Lasers (XFELs) where individual pulses may contain coherent spikes (modes) of large degeneracy parameters[10,11].

The benefit of X-ray stimulation may be seen by writing the RIXS emission cross section per atom, σ_RIXS, in KHD perturbation theory in a simplified "two-step" or "direct" RIXS form[1,4] (see Methods) as,

$$\frac{d\sigma_\mathrm{RIXS}}{d\Omega} = \frac{1}{4\pi}\underbrace{\frac{\Gamma_\mathrm{X}}{\Gamma_\mathrm{X}+\Gamma_\mathrm{A}}}_{Y_\mathrm{f}}\left(1+n_{p\mathbf{k}}\right)\sigma_\mathrm{XAS} \tag{1}$$

Here $d\Omega$ is the solid acceptance angle of the spectrometer, $\Gamma_\mathrm{X}/\hbar$ the dipolar X-ray emission rate, $\Gamma_\mathrm{A}/\hbar$ the Auger electron emission rate, Y_f the fluorescence yield per atom[7], and σ_XAS the spontaneous resonant absorption cross section per atom. The well-known factor $1+n_{p\mathbf{k}}$, introduced by Dirac[12], distinguishes the spontaneous decay probability induced by 1 virtual photon in the zero-point quantum vacuum and the stimulated decay probability driven by $n_{p\mathbf{k}}$ real photons in the polarization mode p and wavevector mode $\mathbf{k}$ contained in the mode volume $V_{p\mathbf{k}} = \lambda^3\hbar\omega/\Delta_{p\mathbf{k}}$, where $\Delta_{p\mathbf{k}}$ is the incident energy bandwidth. In the time-independent KHD theory, the stimulation rate depends on the incident bandwidth $\Delta_{p\mathbf{k}}$.

In the stimulation process, incident photons in a mode $p\mathbf{k}$ drive atomic decays and the emitted photons preserve the energy, polarization and direction of the driving photons, first pointed out by Einstein in 1917[13] in the derivation of Planck's formula for the black body spectrum. Stimulation has two beneficial effects. If $\mathbf{k}$ is aligned with the acceptance cone $d\Omega$ of the spectrometer, the spontaneous RIXS cross section is directionally enhanced by $4\pi/d\Omega \simeq 10^5$. In addition, the small spontaneous fluorescent yield $Y_\mathrm{f} \le 10^{-2}$ is increased by the driving action of the stimulating photons.

The KHD perturbation formula (1) ignores changes in occupation of the electronic states during absorption and emission and its linear scaling with photon number breaks down for large $n_{p\mathbf{k}}$[14,15]. Proper treatment by use of the time-dependent optical Bloch equations or the related Maxwell-Bloch theory[16], shows that at large values of $n_{p\mathbf{k}} > 10^3$ the stimulated fluorescence yield saturates at $Y_\mathrm{f}\, n_{p\mathbf{k}} \to 1/2$. The stimulated RIXS cross section therefore saturates at about half of the spontaneous absorption cross section, $\sigma_\mathrm{RIXS} \to \sigma_\mathrm{XAS}/2$. The maximum enhancement of stimulated over spontaneous RIXS consist of a dominant solid angle contribution of $4\pi/d\Omega \simeq 10^5$ and a smaller "photon number" increase given by $1/(2Y_\mathrm{f})$ which in practice is of order 50–500.

Pioneering studies with XFELs have utilized the large photon degeneracy parameter to create a large number of core holes, and the spontaneously emitted photons may then amplify by stimulation as they propagate in the sample, a process called amplified spontaneous emission (ASE)[17–21]. The direct or "impulsive" stimulation of the elastic REXS channel by a strong incident beam has also been observed in a thin film sample[22,23]. A stimulated inelastic RIXS signal has so far been detected only for atomic gas samples[24] while similar studies for molecules remained inconclusive[25]. In related studies molecular products resulting from stimulated RIXS have been observed instead of the scattered X-rays themselves[26,27].

In condensed matter, stimulated RIXS processes have not yet been demonstrated. This is mainly due to the increased complexity of electronic processes in solids, in particular the effect of inelastic cascading of photoelectrons and Auger electrons[18,28,29]. By use of XFEL-generated X-ray pulses centered around a strong XAS resonance of a solid sample, we here specifically address the interplay between pure photon driven, i.e. stimulated, valence to core transitions and intra-valence electron reshuffling effects due to inelastic scattering of photoelectrons and Auger electrons. This is accomplished by use of a transmission geometry through a thin film Co/Pd multilayer sample where the transmitted spectrum near the Co L_3 XAS resonance is measured as a function of the incident intensity and energy distributions of 5 fs and 25 fs Full-Width-at-Half-Maximum (FWHM) pulses. A split pulse scheme is used for accurate pulse structure normalization. We observe the interplay between three different non-linear effects. The expected stimulated photon scattering enhancements in REXS and RIXS are accompanied by spectral changes due to inelastic scattering of the primary photo- and Auger-electrons. The latter effect leads to an electron redistribution near the Fermi energy that modifies the pure photon based stimulated REXS and RIXS spectra. The relative size of the three effects is quantified by use of a simple

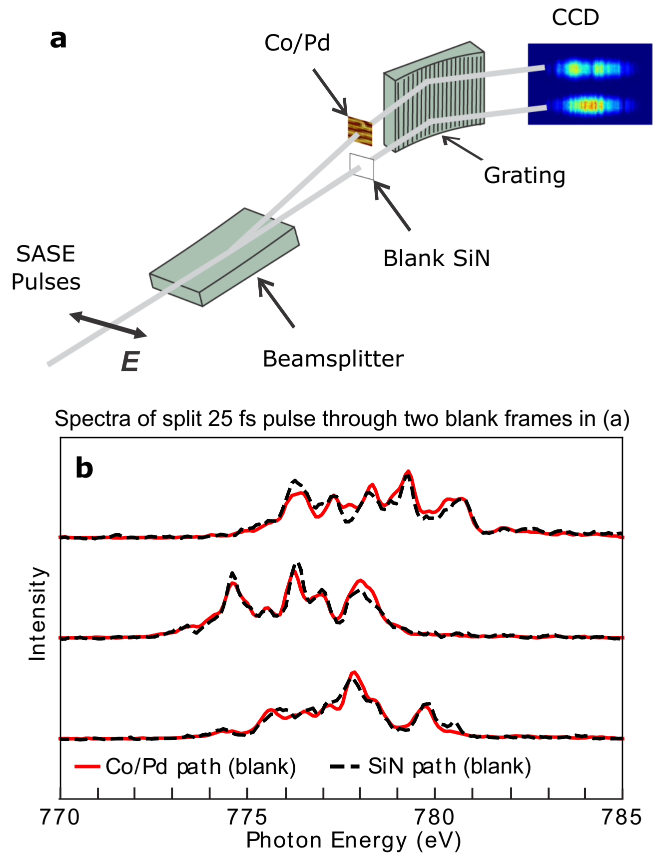

Fig. 1 Experimental setup. **a** Simplified schematic of the experimental setup, which was also used in Chen et al.[23]. Linearly polarized Self-Amplified Spontaneous Emission (SASE) X-ray pulses are produced by an X-ray free electron laser. The X-ray pulses are split into two components with an X-ray beam splitter. One of the resultant X-ray beams passes through a blank SiN membrane while the other passes through a membrane with a Co/Pd magnetic multilayer. The beams emerging from the membranes in the forward direction are measured with a grating-based spectrometer which uses a Charge-Coupled Device (CCD) for photon detection. **b** Examples of single-shot spectra for a 25 fs pulse, recorded when the membranes and Co/Pd multilayers were removed from the X-ray paths. The spectra recorded from each beam align very well, demonstrating our ability to normalize the Co/Pd multilayer spectra by the bare membrane reference spectra.

rigid density of states model for the studied Co/Pd sample which is in agreement with experiment. At our highest incident intensities of ≃300 mJ per cm^2 per fs, the spontaneous RIXS signal is found to be enhanced by a factor of ≃10^6 for both 5 fs and 25 fs (FWHM) pulse lengths, close to the theoretical limit. Both stimulated gains are accompanied, however, by inelastic electron scattering which distorts the stimulated REXS and RIXS spectra due to changes in the valence band occupation near the Fermi energy. Their onset has previously been observed at lower intensities by detailed fluence-dependent XAS studies[29]. These secondary electron scattering effects are observed even for X-ray pulse lengths of 5 fs, indicating that their timescale is comparable to the "atomic clock" timescale set by the lifetime of the Co $2p$ core hole (1.5 fs).

Results and discussion

Experimental details. In order to reduce complexity, we study RIXS in a transmission geometry through a thin Co/Pd multilayer film, and detect the transmitted intensity in the forward scattering direction (momentum transfer $\mathbf{q} \simeq 0$) with an energy resolving grating spectrometer, as illustrated in Fig. 1a.

We used 5 fs and 25 fs (FWHM) linearly polarized X-ray pulses (see methods) produced through self-amplified spontaneous emission (SASE) at the Linac Coherent Light Source (LCLS)[11]. The pulses were directed to the Atomic Molecular and Optical station[30] where they were split into two similar intensity pulses by a mirror with a sharp edge[31]. Both split pulses came to a focus near a Si chip containing 100 nm thick silicon nitride membrane windows. Half of the membranes had Co/Pd magnetic multilayers deposited on top of the SiN.

The multilayers were sputter deposited[32] and had the metal layer sequence Ta(1.5)/Pd(3)/[Co(1)Pd(0.7)]x25/Pd(2), where the thicknesses in parentheses are in nm. One of the X-ray pulses passed through a membrane with the multilayer on top, while the other passed through a bare SiN membrane, acting as a reference as shown in Fig. 1a. The relative transmitted intensity through the sample had an energy-independent constant background, mostly due to Pd, which reduced the sample transmission to 55% of that through the bare SiN reference samples. The X-rays emerging from the membranes in the forward direction were detected at separate positions of a spectrometer with ≈1000 resolving power (see Methods). As shown in Fig. 1b, the photon energy content of the two X-ray beams was very similar, which enabled accurate normalization of our nonlinear X-ray transmission spectra, overcoming difficulties of earlier studies[25].

The individual pulses contained coherent spikes as shown in Fig. 1b and their central X-ray photon energy was nominally set to 778 eV corresponding to the Co L$_3$ resonance energy. As shown in the figure, the central pulse energy and spike structure varied pulse-to-pulse. The X-ray fluence onto the Co/Pd multilayers ranged from 0.1 through 9500 mJ per cm^2 (see Methods). When the X-ray fluence exceeded about 50 mJ per cm^2, the sample was damaged after the pulse through aftereffects of atomic diffusion or even explosion. Samples were therefore replaced every few X-ray shots and only the transmission spectrum of the first shot on each sample was analyzed. At low fluence (<10 mJ per cm^2), spectra were recorded at the full 120 Hz repetition rate of LCLS for about five minutes and the samples were then replaced.

As shown in Fig. 1b, the incident pulses always contained photons at the resonant Co L$_3$ absorption energy of $E_0 \simeq 778$ eV to produce Co $2p_{3/2}$ core holes. At low incident fluence, the transmitted spectrum is completely dominated by the dominant XAS intensity loss near E_0, corresponding to the well-known strong XAS resonance[29]. Since in XAS, electrons are excited from Co $2p_{3/2}$ core electrons to empty $3d$ valence states above the Fermi level E_F, this energy corresponds to the inflection point onset of the XAS resonance and serves as a natural demarcation line of the RIXS intensity below E_F and the XAS and REXS intensities above E_F.

The conventional spontaneous RIXS intensity from the sample is emitted into a 4π solid angle and is weak due to the Co fluorescence yield of only $Y_f = 8 \times 10^{-3}$ [7]. At low incident fluence, RIXS emission at energies below E_0 into the forward direction of our spectrometer is therefore completely negligible relative to the large XAS response. At high incident fluence, absorption above E_0 will decrease due to stimulated REXS in the forward direction[15,23], resulting in transmission increase at the resonant XAS energy. If the strong incident pulse also contains photons at energies below E_0, the small spontaneous RIXS emission probability of $Y_f = 8 \times 10^{-3}$ into 4π will be replaced by stimulated RIXS emission into the forward direction $d\Omega/(4\pi)$ (see Eq. 1), i.e. directly into the spectrometer. Then the stimulated RIXS increase into the spectrometer acceptance cone

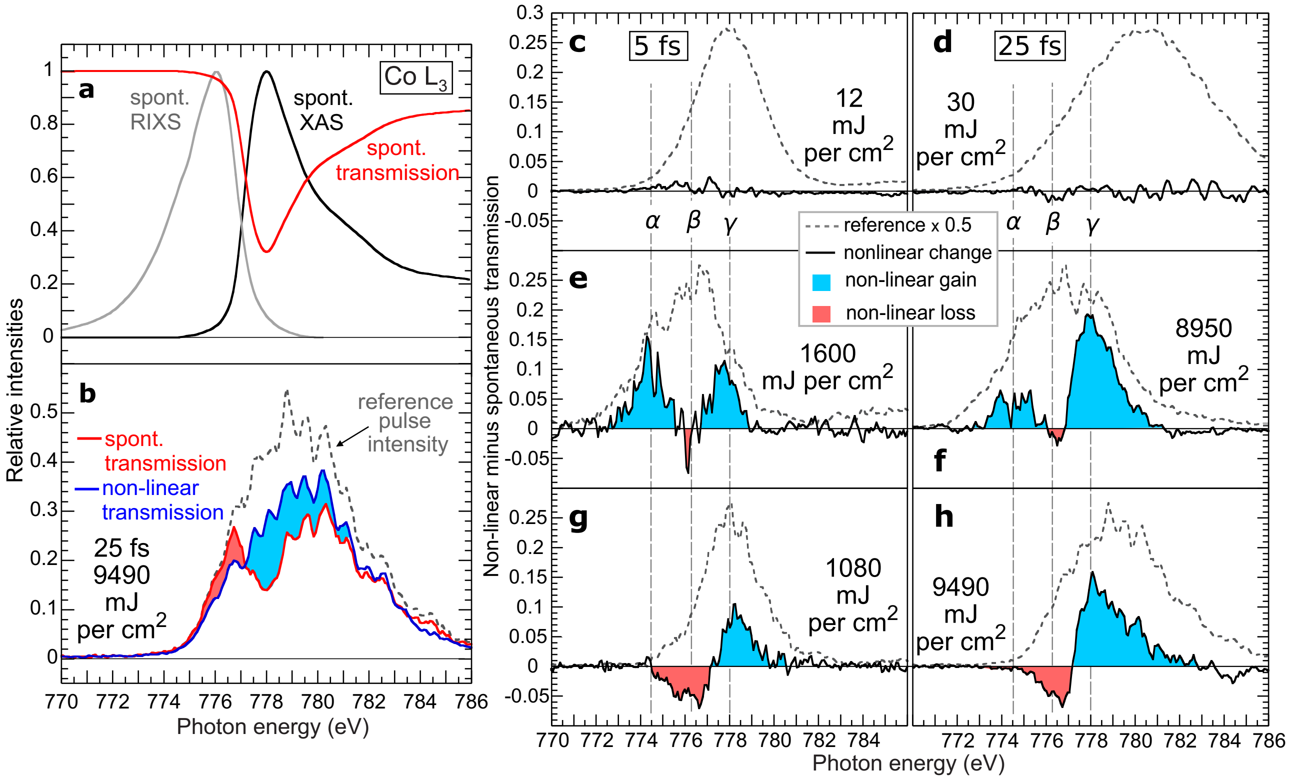

Fig. 2 Summary of experimental results. a Comparison of the scaled spontaneous Co L$_3$ Resonant Inelastic X-ray Scattering spectrum (RIXS, gray) for Co metal[33] and the Co/Pd X-Ray Absorption Spectrum (XAS, black), both recorded at synchrotron light sources (low fluence limit). The red spectrum is the transmission version of the XAS spectrum. **b** Example of data extraction and normalization. The dashed gray line is the reference spectrum of a 25 fs pulse of 9490 mJ per cm^2 fluence transmitted through the SiN window, multiplied by 0.55 to account for the constant non-resonant absorption of the Co/Pd sample. The blue curve is the measured transmission spectrum through the Co/Pd sample at the stated high fluence. The red curve is the spontaneous (low fluence) transmission spectrum, obtained by multiplying the red spectrum in (**a**) by the dashed-gray reference spectrum. Light blue shaded areas indicate non-linear gain and red areas non-linear loss. (**c**–**h**) show as dashed lines the reference spectra transmitted through the SiN for 5 fs and 25 fs pulses for different pulse shapes and fluences. The associated transmission difference spectra are shown as solid black lines. They were obtained by subtraction of the spontaneous low-fluence spectra from the non-linear high-fluence spectra for the respective transmission curves. The shading of areas corresponds to the procedure (blue minus red curves) illustrated in (**b**). Each spectrum is an average of many shots. The centers of three regions with non-linear response are denoted by dashed vertical lines and labeled α, β and γ.

may be of order 10^6–10^7 so that it may become directly visible below E_0 on the same intensity scale as the reduced XAS intensity above E_0. This is the key to observing non-linear effects across the entire spectral energy range, containing both the XAS (REXS) and RIXS signatures in our experimental arrangement.

Experimental results. Figure 2 summarizes our experimental results. Of interest is the change in transmission through Co/Pd as a function of different incident pulse lengths, fluences and photon energy distributions. In practice, the incident intensity distributions have to overlap with the Co XAS resonance since any resonant non-linear response originates from the created Co $2p_{3/2}$ core holes.

Figure 2 (a) shows low fluence spontaneous RIXS (gray curve) and XAS (black) spectra recorded with synchrotron radiation. The RIXS spectrum is that of Co metal, taken from Nilsson et al.[33] and black curve is the polarization averaged XAS spectrum of our Co/Pd sample. It was recorded in the conventional synchrotron transmission geometry with the monochromator spectral resolution matched to our spectrometer in Fig. 1a. Any background below the Co absorption edge corresponding to 55% non-resonant absorption has been subtracted. We will refer to the shown spectra, scaled to the same unit peak value, as the spontaneous Co L$_3$ XAS and RIXS spectra. Also shown as a red curve is the corresponding spontaneous resonant transmission spectrum given by

$$I_{\text{trans}}(\hbar\omega) = I_0 e^{-\sigma_{\text{XAS}}\rho_a d} \tag{2}$$

where $\rho_a = 91$ atoms per nm^3 is the atomic number density of Co and $d = 25$ nm the total Co thickness. In our case, the transmission at the Co L$_3$ resonance is 32%.

Figure 2b illustrates the extraction of the transmission difference spectra to obtain the nonlinear relative to the spontaneous response. The dashed gray line is the reference transmission spectrum of a 25 fs pulse of 9490 mJ per cm^2 fluence, which after beam splitting was transmitted through the SiN window. Its intensity was adjusted by a factor of 0.55, accounting for the non-resonant constant absorption of the Co/Pd sample. The red curve is the calculated spontaneous (low fluence) transmission spectrum through the Co/Pd sample for the reference pulse intensity and distribution, obtained by multiplying the red curve in (a) by the reference pulse transmission spectrum. The blue curve is the transmission spectrum measured for the indicated pulse length and high fluence. The shaded areas highlight the nonlinear changes in transmission, with light-blue areas indicating nonlinear transmission gain and red areas nonlinear transmission loss.

The experimental transmission difference spectra obtained with the procedure of Fig. 2b are shown in c–h for 5 fs and 25 fs

X-ray pulses for different incident fluences and associated energy distributions of the pulses. The shown data for both 5 fs and 25 fs pulses correspond to multiple shots that were binned by the XFEL electron beam energy which is strongly correlated with the central photon energy of the X-ray pulses[34]. For each case, the dashed gray curves are the reference pulse spectra, scaled by 0.5 to emphasize the difference spectra shown as a solid black line. They represent the difference in transmission of Co/Pd for the respective pulse shapes and fluences and the low-fluence spontaneous transmission.

Figure 2c, d show the quality of our normalization procedure. At low fluences the calculated spontaneous transmission curves, obtained by multiplying the red curve in (a) with the pulse transmission function, are identical within noise with the measured transmission curves. In all high fluence cases, shown in Fig. 2e, f, g and h, the nonlinear response is negligible outside the Co L_3 resonance region and exists only in the three regions indicated by vertical dashed lines, labeled in the figure. The central and bottom rows, respectively, show incident intensity distributions for 5 fs and 25 fs pulses, centered at similar central energy positions.

In the high-fluence spectra in Fig. 2e, f, g and h, the feature γ around the XAS peak position at 778 eV appears prominently as a transmission gain (blue) in all difference spectra. In contrast, the nonlinear features α and β show different behavior when the incident fluence distribution is shifted. As shown in Fig. 2g, h, the α feature disappears and the β feature becomes stronger when the incident distribution shifts to higher energy.

Assignment of non-linear features. We assign the lowest energy feature α, which is about 3.5 eV below the XAS peak, to stimulated RIXS. The feature is present only when there is sufficient incident intensity at its position, as shown in Fig. 2e and f. Since feature γ occurs at the XAS resonance position, we assign it partially to stimulated REXS, as suggested previously[22,23]. The blue shading of the stimulated RIXS and REXS intensities reveals a nonlinear increase in transmission. Since the RIXS and XAS intensities differ in practice by about six to seven orders of magnitude, the visibility of a RIXS signal reveals a large increase upon stimulation. As expected, the feature is absent when the incident pulse contains no photons at position α as in the bottom row of the figure.

Both stimulated REXS and RIXS spectral enhancements, however, are distorted by the presence of a third channel, seen as feature β. It is assigned to intra-valence band electron redistribution caused by secondary inelastic scattering of photo- and Auger electrons. This channel has previously been observed by detailed lower fluence XAS and X-ray magnetic circular dichroism studies[29]. In a solid, especially a metal, electron reshuffling around the Fermi energy, E_F, may occur through electron excitations from below to above the Fermi energy (electron hole pairs). Upon deposition of sufficient energy by incident X-rays, such electron redistribution mimics a very high temperature Fermi-Dirac distribution over energies of 2 eV from the Fermi level[29]. Because of electron conservation, the decrease in electron population below E_F is accompanied by an increase in electron occupation above E_F. This adds to the stimulated REXS and RIXS channels in opposite ways.

Stimulated REXS and increased electron population above E_F both reduce resonant absorption and increase transmission (blue shading). In stimulated REXS, the core electron excited into empty $3d$ states above E_F is driven back into the core hole by stimulating photons, leading to a net loss of absorption[15,22]. Similarly, when valence electrons are excited across the Fermi level into empty $3d$ states through electron scattering, the absorption to these states is quenched. Both effects contribute similarly to the nonlinear response.

On the other hand, stimulated RIXS is due to $3d$ valence electrons from filled states below E_F that are driven into core holes by stimulating photons. This makes the RIXS intensity observable through stimulation in the forward direction as a transmission increase. In the presence of electron excitations to states above E_F, their loss in the filled states below E_F quenches stimulated RIXS from this energy region. Hence the two effects partially compensate each other. This explains previous difficulties of observing stimulated RIXS in solids.

Quantitative model for the observed effects. The observed nonlinear effects can be accounted for by treating transition between core and valence states by a simple rigid density of states band model. Such a treatment is possible because of the local character of core hole excitations on Co atoms in the Co layers. The most important valence electrons in the nonlinear REXS/RIXS processes involve the Co $3d$ valence electrons owing to the dominance of atom-specific $2p_{3/2} \leftrightarrow 3d$ transitions. In equilibrium, the $3d$ band is filled with electrons below the Fermi level E_F while states above E_F are empty. In analogy to the description of molecular orbitals[35], we shall denote filled electron states as $3d$ and empty states or holes as $3d^*$.

When Co atoms are excited through X-ray absorption, the final XAS core hole state is the intermediate state in REXS/RIXS. In our rigid band model the XAS process corresponds to $2p_{3/2} \rightarrow 3d^*$ transitions. In the REXS process, the excited electron transiently resides in the $3d^*$ states before it decays back into the core hole. The spontaneous REXS process is incoherent since the decay is stochastically driven by the quantum mechanical zero point (ZP) field. The stimulated REXS process, in contrast, consists of a coherent up-down process driven by the concerted action of two or more photons between the initial and final states, which are the same. The RIXS process also starts with a $2p_{3/2} \rightarrow 3d^*$ XAS excitation to empty $3d^*$ states. It is then followed by a $3d \rightarrow 2p_{3/2}$ decay from filled valence states. The spontaneous RIXS decay is again driven by the ZP field while stimulated RIXS is driven by real photons and can therefore be enhanced.

The average lifetime of the intermediate Co core hole state is known to be $\tau_\Gamma \simeq 1.5$ fs corresponding to a natural emission line width (FHHM) of $\Gamma = \Gamma_X + \Gamma_A = \hbar/\tau_\Gamma = 0.43$ eV[36]. In contrast to optical transitions, the X-ray emission line width Γ is not determined by the dipolar width Γ_X alone but contains a "ghost" contribution Γ_A due to Auger decays. In the low fluence limit, the Auger decay process in Co atoms has a much larger probability, expressed by the small X-ray fluorescence yield $Y_f \simeq \Gamma_X/\Gamma_A$ which is only 8×10^{-3} [7]. This leads to the small spontaneous RIXS cross section relative to the XAS cross section as expressed by (1).

During an X-ray pulse of low incident fluence, the excitation of a specific Co atom in Co/Pd is not influenced by possible excitations of other Co atoms owing to the low probability of two or more Co atoms getting excited during the duration of a pulse. At high incident fluence, a significant fraction of all Co atoms in the sample gets excited during a pulse and for our impulsive stimulation geometry the broad energy bandwidth SASE pulses themselves can stimulate REXS and RIXS decays into the core holes. In addition, ASE can occur along the propagation path[17–21]. For our thin film samples, the ASE effect is quite weak in the forward direction because of the small Co thickness of 25 nm.

While ASE is expected to be weak for a thin film, another stronger indirect non-linear process can exist. It is triggered by primary photoelectrons and Auger electrons that multiply by inelastic scattering in random directions in the sample. At high

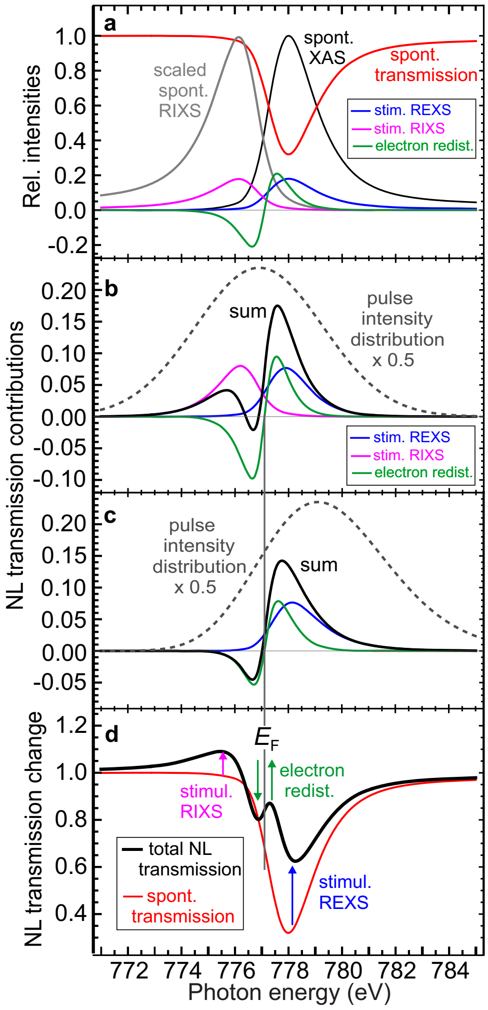

Fig. 3 Model of nonlinear X-ray spectra. Here, spont. stands for spontaneous, stim./stimul. stand for stimulated, redist. stands for redistribution, rel. stands for relative, NL stands for nonlinear and E_F is the Fermi energy. **a** Model Co L_3 spontaneous Resonant Inelastic X-ray Scattering (RIXS, gray), X-Ray Absorption Spectrum (XAS, black) and transmission (red) spectra, and three assumed non-linear contributions, stimulated RIXS (magenta), electron redistribution (green) and stimulated Resonant Elastic X-ray Scattering (REXS, blue). The sizes of the nonlinear contributions are referenced to the unit value of the XAS peak. **b** Assumed incident pulse reference distribution (dashed), which allows all three nonlinear channels to contribute to the sum shown in black. **c** Shifted pulse reference distribution (dashed) which eliminates the stimulated RIXS contribution. The remaining two add up the sum shown in black. **d** Change of the spontaneous transmission spectrum (red) taken from (**a**), to the total nonlinear transmission one (black) for a wide incident energy distribution. The black curve is the red curve plus the the sum of all three nonlinear contributions. Colored arrows indicate nonlinear transmission gain (up arrows) and loss (down arrows) caused by the respective nonlinear channels.

incident fluence, the amplifying cascading effect is strong enough to create significant electron-hole excitations in the Co/Pd valence band. Whether this effect is observed depends on the relative timescale of the valence electron redistribution and the temporal width of the X-ray pulse. In Co/Pd the transfer of energy from the primary photo- and Auger-electrons to the entire valence electron sea proceeds in a cascade that ends up in an electron redistribution within a time of ≈10 fs[29]. Since this time is comparable to our pulse lengths such effects are expected to play a role. In addition, since the hot electron reservoir has not yet equilibrated with the lattice, an electron rearrangement has an extended energy range of about 2 eV around the Fermi level[29].

Our identification of three dominant non-linear effects, namely stimulated REXS and RIXS and electron redistribution, may be used to quantitatively simulate the experimentally observed nonlinear transmission effects. We utilize the same procedure used to derive the experimental nonlinear spectra shown in Fig. 2. We can reference the assumed size and shape of the three nonlinear channels to the resonant X-ray absorption cross section which determines the sample transmission according to Eq. 2. The measured nonlinear transmission spectrum is then simply given by the change of the spontaneous transmission spectrum by the three nonlinear contributions.

In Fig. 3a we show the assumed spontaneous RIXS (gray), XAS (black) and transmission (red) spectra. The RIXS spectrum has been arbitrarily scaled to unit peak height. Also shown are the relative energy distributions and sizes of the three nonlinear contributions, assumed to represent those at the highest incident fluences in Fig. 2. We assume that the stimulated RIXS (magenta) and REXS (blue) contributions have the shape of the spontaneous spectra in (a) and have the same size of 18% of the resonant XAS peak value and area. The electron redistribution (green) is modeled by the difference of two Fermi-Dirac distributions that mimics previous experimental results[29]. It has a peak value of 20% of the resonant XAS value and 8% of the integrated XAS area.

Depending on the energy distribution of the incident pulse, the three nonlinear contributions will contribute with different shapes and intensities. This is shown for two pulse distributions in Fig. 3b, c, modelled to reflect the two 25 fs high-fluence cases in Fig. 2f and h. When the incident distribution covers both the REXS and RIXS regions, all three nonlinear channels contribute and the resulting nonlinear transmission change is shown as a black line in Fig. 3b. When the RIXS energy region is inadequately covered, only the other two nonlinear channels contribute, as shown in Fig. 3c. Finally, we show in Fig. 3d the change of the spontaneous transmission spectrum in (a), shown again in red, by adding to it the three nonlinear contributions in Fig. 3b. The total nonlinear transmission spectrum (black) exhibits strong nonlinear effects whose spectral distortions are indicated by arrows.

Of particular interest is that now the stimulated RIXS spectrum, although, partly obscured by electron redistribution, appears on the same scale as the XAS effect. This arises from a stimulated amplification by a factor of order 10^6 relative to the spontaneous RIXS intensity (see sections Comparison of Experiment with Maxwell-Bloch RIXS Simulations and Comparison of Experiment with Kramers-Heisenberg-Dirac RIXS Theory). The close quantitative agreement of our simulations with experimental results for corresponding incident pulse distributions is underscored by their direct comparison on the same vertical scales in Fig. 4.

The good quantitative agreement of theory and experiment allows us to determine the increase in stimulated over spontaneous RIXS for an incident intensity of about 300 mJ per cm^2 per fs. At this value, the size of the stimulated RIXS intensity has a value of 18% of the spontaneous XAS intensity. We also find that the stimulated RIXS and REXS intensities are the same in our model. In the following we compare these values with calculations for the stimulated RIXS rate.

Comparison of experiment with Maxwell-Bloch RIXS Simulations. In Fig. 5a we show the two RIXS intensities for the highest fluence 5 fs and 25 fs pulses, deduced from the experimental data

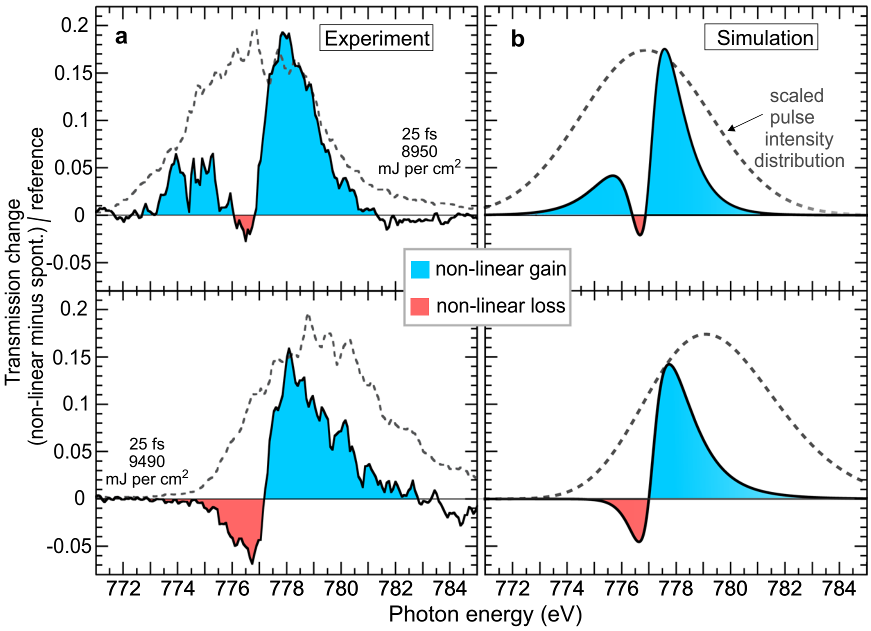

Fig. 4 Comparison of nonlinear spectra model to experiment. Here, spont. stands for spontaneous. **a** Experimental high-fluence non-linear effects for 25 fs pulses taken from Fig. 2f, h. **b** Simulated results with our model for similar incident intensity distributions, plotted on the same scale. The shown simulated curves are the black curves in Fig. 3b, c.

with help of our simulation model, in a logarithmic intensity versus fluence plot. The measured RIXS intensities, indicated by magenta (5 fs) and green (25 fs) filled circles, are referenced to the spontaneously absorbed intensity indicated by a black horizontal line of unit value. Another horizontal line indicates the fluorescence yield of $Y_\mathrm{f} = 8 \times 10^{-3}$ [7], which corresponds to the spontaneous RIXS signal emitted into 4π, most of which is not seen by the detector.

As indicated by the horizontal gray line through the data points, the stimulated RIXS intensity is about 20% of the absorbed intensity, corresponding to a factor of about 20 increase in decay probability relative to the fluorescence yield, as indicated. More importantly, we also show a shaded gray band at the bottom that indicates the small fraction of the spontaneous RIXS signal typically seen by a detector with an angular acceptance of order 10^{-5}–10^{-4} [8]. The gain advantage of stimulated RIXS predominantly arises from the solid angle enhancement rather than the factor 20 increase in decay probability. In fact, the stimulated decay probability will saturate at a maximum increase of a factor of 50 relative to fluorescence yield when at higher incident fluence absorption and emission equilibrate.

Also shown in Fig. 5a as magenta and green lines are the stimulated RIXS intensity increases predicted by the Maxwell-Bloch (MB) theory[16] in conjunction with a statistical description of the SASE XFEL pulses[37,38], discussed in Methods below. The statistical approach, which complicates data analysis, has typically been employed for the description of non-linear phenomena studied with SASE based XFELS[39]. The stimulated RIXS rate is again normalized to the spontaneous absorption rate, so that the theory reveals the expected linear increase with the number of stimulating photons per created core hole. At the highest fluence, the MB rate reveals a deviation from linearity due to saturated absorption. The theory is seen to underestimate the experimentally observed values by a factor of about 5.

In Fig. 5b we have recast the experimental results shown in (a) in terms of incident intensity, given by the fluence divided by the pulse length. The experimental data points then nearly merge and for an incident intensity of ≃300 mJ per cm^2 per fs we find a stimulated RIXS intensity of about 20%, indicated by the horizontal gray line. This value corresponds to the total stimulated RIXS contribution shown as a magenta distribution curve in Fig. 3a. It is difficult to extract from the experimental data, alone, since it is partially hidden by the electron rearrangement intensity.

The additional blue line in Fig. 5b represents the description of stimulated RIXS by the KHD approximation given by (1) in conjunction with a simple model of the SASE pulses which we discuss next.

Comparison of experiment with Kramers-Heisenberg-Dirac RIXS Theory. In the RIXS literature which covers experiments ranging from molecules, polymers and chemisorption systems to solids with weak and strong valence correlations and solids in high pressure environments, the RIXS process is typically described in the KHD second order perturbation formalism[1–4]. It is outlined in Methods with emphasis on its simplification leading to (1). The essence of this "two-step" or "direct RIXS" simplification is the neglect of interference effects in the intermediate core hole state. This is typically a good approximation for solids[1,4] while for free molecules, interference paths through vibrational intermediate states need to be included, leading mostly to relative intensity changes of the vibrational peaks[1,40]. The KHD perturbation approach is valid only as long as the stimulated rate increases linearly with $n_{\mathbf{pk}}$ and does not saturate. This condition is fulfilled over most of the fluence range as shown by the MB curves in Fig. 5a, with small changes due to saturation appearing only at the highest fluences.

The complete KHD theory expressed by Eq. 6 in Methods, distinguishes between exciting and stimulating photons. This distinction is absent in (1) since we normalize the RIXS to the XAS cross section, i.e. the system has already been "pumped" through absorption. The number of photons $n_{\mathbf{pk}}$ in (1) refers to those available in the mode $\mathbf{pk}$ to "dump" excited electrons back into the core hole through stimulation. Photons in the same mode are coherent and contained in the mode volume $V_{\mathbf{pk}} = \lambda^3 \hbar\omega / \Delta_{\mathbf{pk}}$, composed of the minimum lateral coherence area $A = \lambda^2$ and longitudinal coherence length $\ell = \lambda\, \hbar\omega / \Delta_{\mathbf{pk}}$[10]. Since XFEL pulses

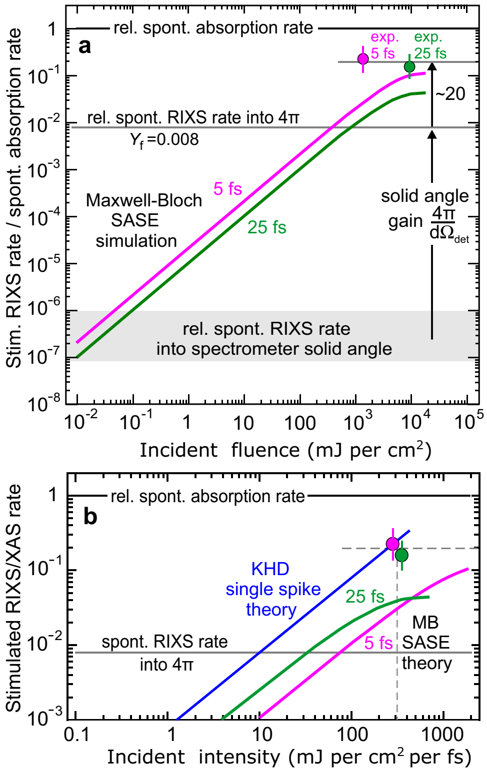

Fig. 5 Experimental and simulated dependence of stimulated Resonant Inelastic X-ray Scattering (RIXS) amplification on X-ray fluence and X-ray intensity. Here, rel. stands for relative, spont. stands for spontaneous, stim. stands for stimulated, XAS stands for X-ray absorption spectrum, Y_f is the fluorescence yield and Ω_{det} is the solid angle of acceptance of the spectrometer. **a** Dependence of stimulated RIXS amplification on fluence and pulse duration. The magenta and green circles are the experimentally determined stimulated RIXS intensities for 5 fs and 25 fs pulses relative to the spontaneous absorption rate. The error bars estimate the standard error in the absence of nonlinear effects. Also indicated as a horizontal line is the spontaneous RIXS rate emitted into 4π, i.e. the fluorescence yield $Y_{\mathrm{f}} = 8\times10^{-3}$ [7]. The correspondingly colored curves represent RIXS rates for L$_3$ excitation of Co atoms, relative to the spontaneous absorption rate, calculated by use of a statistical Self-Amplified Spontaneous Emission (SASE) pulse description combined with a three level Maxwell-Bloch (MB) theory. The gray shaded region at the bottom indicates the fraction of the spontaneous RIXS signal typically seen by a detector with an angular acceptance of order $10^{-5}-10^{-4}$. Vertical arrows indicate the two contributions to the observed stimulated RIXS relative to the absorbed rate. **b** The data in **a** are plotted as a function of incident intensity and comparison with the Kramers-Heisenberg-Dirac (KHD, blue) and MB (magenta and green) theories.

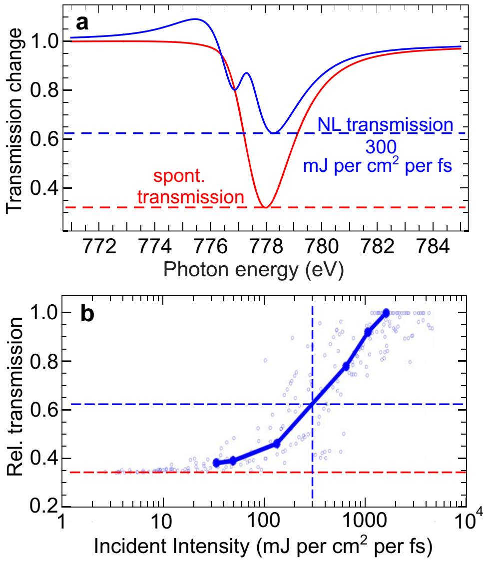

Fig. 6 Experimental and simulated dependence of X-ray transmission on X-ray intensity. Here, rel. stands for relative. **a** Spontaneous (spont.) and nonlinear (NL) transmission spectra taken from Fig. 3d, with horizontal dashed lines indicating the relative peak transmission values. **b** Reproduced with permission Fig. 3a of Chen et al.[23]. Light blue open circles represent the transmission response simulated by statistical modelling of the Self-Amplified Spontaneous Emission (SASE) pulses in conjunctions with the two-level optical Bloch equations. The thick solid blue line links experimental data points, averaged over multiple shots, for the same Co/Pd multilayer samples used here.

are laterally coherent, only the longitudinal or temporal coherence is important in the present study.

Our impulsive stimulation geometry and the small energy separation $\mathcal{E}_b - \mathcal{E}_a \simeq 2\,\mathrm{eV}$ allows us to adopt a particular convenient description of the incident SASE pulses which circumvents statistical modelling. Both pump and dump photons may be viewed as being contained in individual coherent and therefore transform limited spikes of temporal FWHM $\tau = 0.5-1\,\mathrm{fs}$ within the SASE pulses. When transformed into the energy domain, a flat-top temporal spike is converted into a sinc^2 shaped energy distribution with the FWHM of the distributions related by $\tau\Delta_{\mathrm{pk}} = 0.886h$, where $h = 4.14\,\mathrm{fs\,eV}$ is Planck's constant. Because of the large energy width of several eV, REXS and RIXS can then be described by the average number of photons in individual temporal spikes which each cover a broad energy range that contains the absorption and emission regions. This allows us to express n_{pk} in terms of the average spike intensity I_{pk} which may be approximated as the incident fluence divided by the total temporal pulse length. This leads to the relation,

$$n_{\mathrm{pk}} = \frac{1}{c}\frac{\lambda^3}{\Delta_{\mathrm{pk}}} I_{\mathrm{pk}} \tag{3}$$

For our geometry, the incident photons propagate into the forward direction so that the RIXS cross section per atom measured by the detector may be written as,

$$\sigma_{\mathrm{RIXS}} = \underbrace{\frac{d\Omega_{\mathrm{det}}}{4\pi} Y_{\mathrm{f}}\,\sigma_{\mathrm{XAS}}}_{\text{spontaneous}} + \underbrace{n_{\mathrm{pk}}\, Y_{\mathrm{f}}\,\sigma_{\mathrm{XAS}}}_{\text{stimulated}} \tag{4}$$

This formulation clearly shows the advantage of stimulated RIXS. The absence of the factor $d\,\Omega_{\mathrm{det}}/4\pi$ in the stimulated case allows the finite-acceptance-angle detector to see a gain as soon as $n_{\mathrm{pk}} > d\,\Omega_{\mathrm{det}}/4\pi$. This fact is expressed in Fig. 5a by the stimulated gain exceeding the shaded gray region representing the relative spontaneous detection rate.

The stimulated gain calculated with the KHD theory assuming $\Delta_{\mathrm{pk}} = 8\,\mathrm{eV}$ in (3) is shown as a function of incident intensity by a blue line in Fig. 5b. There is agreement with the experimental data. The agreement may be more realistically understood as follows. Equation 4 tacitly assumes that the RIXS response of all atoms in the sample is the same. It does not account for the actual attenuation of the incident intensity as it propagates through the sample. In a proper treatment, the stimulated response of a sample of finite thickness d should be described by the propagation of the stimulated linear response of thin slices of thicknesses much less than one X-ray absorption length (about 20 nm in our case). Since the incident intensity falls by a total factor of about 3 through our total Co thickness of 25 nm, our neglect of propagation overestimates the stimulated response by about a factor of 2. One may more realistically understand the good agreement of the blue line in Fig. 5b with experiment by an effective energy width $\Delta_{p\mathbf{k}} = 4$ eV or half of the assumed value. This increases $n_{p\mathbf{k}}$ according to (3) by a factor of 2 which is compensated a factor of 2 due to the neglected reduction of pulse propagation.

The stimulated REXS channel. Our modelling of the experimental results in Fig. 3 also provided information on the stimulated REXS channel, which at an incident intensity of ≃300 mJ per cm^2 per fs was found to have the same intensity as the stimulated RIXS contribution according to Fig. 3a. The reason for the same contributions of stimulated REXS and RIXS in our case is derived in Methods. There we also discuss different formulations of stimulated REXS, in particular, the semi-classical existence of a coherent enhancement factor introduced in[15]. The equivalence of our present fully quantum mechanical treatment with the semi-classical one used in Chen et al.[23] for the same Co/Pd samples is illustrated in Fig. 6.

In Fig. 6a we have replotted the simulated transmission spectrum of Fig. 3d corresponding to an incident intensity of ≃300 mJ per cm^2 per fs, with the spontaneous and nonlinear peak transmissions indicated by dashed red and blue horizontal lines. Their values agree with those given in Fig. 3a of Chen et al.[23] which is reproduced in Fig. 6b. In both cases, the spontaneous transmission of 32% is found to change to about 62% through nonlinear effects.

Conclusions

Our studies show that both REXS and RIXS channels may be significantly enhanced by stimulation, also in solids. The most important enhancement comes from the direction-preserving nature of stimulated decays. This leads to angular enhancement factors for stimulated over spontaneous RIXS of order 10^4–10^5 due to the small acceptance angle of typical spectrometer. Relative to this number, the gain in stimulation-enhanced decay probability over the spontaneous fluorescence yield is relatively small. For the case of the Co L_3 resonance, we observe about a 20 fold gain in the photon driven decay probability. This compares to the maximum possible enhancement of a factor of about 50, limited by saturation or equilibration of the absorption and emission channels.

As pointed out previously[39], present RIXS experiments are complicated by the statistical SASE structure of XFEL pulses. Our statistical modelling of the pulses in conjunction with the Maxwell-Bloch theory underestimates the observed stimulated RIXS intensity by about a factor of 5. Statistical modelling is expected to yield better average fluence values for longer SASE pulses than used here, because of the greater number of coherent spikes. We also carried out MB calculations in the extreme two color limit, where for each pump photon at the absorption resonance, suitable dump photons at the emission energy were available. For the same incident X-ray intensity, this predicted a stimulated RIXS curve for the 25 fs SASE pulses that was more than a factor of five higher than the MB curve shown in Fig. 5.

The results of the simpler Kramers-Heisenberg-Dirac theory in conjunction with the assumption that the RIXS process is driven by individual SASE spikes whose short temporal duration provides the required bandwidth to cover both absorption and emission energies, was found to give good agreement with experiment. Since the energy losses probed with RIXS in solids are typically limited to a few eV, a beam consisting of a single few hundred attosecond spike[26,41] may be a convenient source for future RIXS studies.

Our results have substantial implications for future RIXS and nonlinear X-ray investigations of solids because of the identified third nonlinear channel, caused by inelastic scattering of photo- and Auger electrons. The resulting valence electron redistribution effects distort the stimulated REXS and RIXS spectra due to overlapping spectral changes. For stimulated RIXS to become a robust technique for the study of low lying excitations in solids, future studies must find a way to mitigate this deleterious effect.

Methods

Adjustment and determination of X-ray fluence. The X-ray fluence at the Co/Pd multilayers was adjusted by changing the attenuation of a nitrogen gas attenuator[42] before the Co/Pd multilayers as well as changing the spot size at the Co/Pd multilayers. The pulse energy at the Co/Pd multilayers was determined from the X-ray pulse energy measured with a gas detector[42]. The X-ray transmission efficiency from the gas detectors to the Co/Pd multilayers was estimated to be 10 percent. The X-ray spot size at the Co/Pd multilayers was measured through pinhole scans, giving a size of either 15 by 15 µm, or 20 by 150 µm, depending on the setting of the X-ray focusing mirrors.

Characterization of X-ray pulse duration. The average duration of X-ray pulses produced by LCLS in different modes was estimated using two different methods. The methods are complementary in that the first sets an upper limit on average pulse duration while the second sets a lower limit. In the first method, an X-band Transverse Deflecting Cavity measured the energy and temporal distribution of electrons in electron bunches after those bunches were used in the production of X-rays. The intensity profile of X-ray pulses was then derived from the time-resolved energy changes due to the XFEL lasing on the measured electron bunch[43]. This confirmed the 25 fs FWHM duration of the longer pulses and set an upper limit of 10 fs on the duration of the shorter pulses. In the second method, averaged pulse durations were estimated from the statistical correlation of X-ray spectra[44,45]. For the same operating modes as used for collecting data on the Co/Pd multilayers, we recorded spectra using the spectrometer of the Soft X-Ray Materials Science beamline[46]. For robustness of this analysis method, we limited the analysis to X-ray pulses where the central electron energy of the electron bunch generating the X-ray pulse was within the middle 10 percent of observed values. This gave a lower limit of 4.7 fs on the duration of the shorter pulses and 8.5 fs on that of the longer pulses.

Retrieval of X-ray spectra. Spectra were obtained from spectrometer CCD images by selecting the relevant region on the imaging detector and projecting along the axis of photon energy dispersion. The photon energy was calibrated by adjusting the coefficients of a linear relationship between spectrometer pixel position and photon energy such that a low fluence absorption spectrum measured at LCLS agreed with that measured on the same sample at beamline 13.3 at the Stanford Synchrotron Radiation Lightsource.

Kramers-Heisenberg-Dirac theory of RIXS. The KHD expression (1) arises in second order perturbation theory which gives the double differential resonant scattering rate as,

$$\frac{\mathcal{W}^{\rm scat}_{a\to b}}{d\Omega_2\, d(\hbar\omega_2)} = \underbrace{\frac{c\, n_{p_1\mathbf{k}_1}}{V_{p_1\mathbf{k}_1}}}_{\Phi_1} \frac{d\sigma^{\rm scat}_{a\to b}}{d\Omega_2\, d(\hbar\omega_2)} \tag{5}$$

where Φ_1 is the incident photon flux expressed by the photon degeneracy parameter, defined as the number of photons $n_{p_1\mathbf{k}_1}$ that are emitted from the mode volume $V_{p_1\mathbf{k}_1} = \lambda^3\hbar\omega_1/\Delta_{p_1\mathbf{k}_1}$ with the speed of light c. In the dipole and rotating wave approximations, the double differential RIXS resonant cross section is expressed by[1],

$$\begin{aligned}\frac{d\sigma^{\rm RIXS}_{a\to b}}{d\Omega_2\, d(\hbar\omega_2)} = &\frac{4\pi^2\hbar\omega_1\hbar\omega_2\,\alpha_{\rm f}^2}{\lambda_2^2}\,\mathcal{R}^4\left(n_{p_2\mathbf{k}_2}+1\right)\\ &\times\sum_b^{\omega_2\le\omega_1}\left|\sum_c\frac{\langle b|\hat{\mathbf{r}}\cdot\epsilon^*_{p_2}|c\rangle\langle c|\hat{\mathbf{r}}\cdot\epsilon_{p_1}|a\rangle}{\hbar\omega_1-\mathcal{E}_{ca}+{\rm i}\Gamma_c/2}\right|^2\\ &\times L(\hbar\omega_1-\hbar\omega_2-\mathcal{E}_{ba})\end{aligned} \tag{6}$$

where $\mathcal{E}_{ij} = \mathcal{E}_i - \mathcal{E}_j$ denotes the energy difference between two electronic states i and j, and

$$L(\hbar\omega_1-\hbar\omega_2-\mathcal{E}_{ba}) = \frac{2}{\pi\Gamma_b}\frac{\Gamma_b^2/4}{\left(\hbar\omega_1-\hbar\omega_2-\mathcal{E}_{ba}\right)^2+\Gamma_b^2/4} \tag{7}$$

describes the final state Lorentzian energy distribution of unit integrated area and FWHM Γ_b. Its argument $\hbar\omega_1 - \hbar\omega_2 - \mathcal{E}_{ba}$ links it to the Raman effect in optical spectroscopy. This expression is valid for negligible instrumental linewidth contributions.

In (6), $\alpha_f \simeq 1/137$ is the fine structure constant and $\mathcal{R}$ the radial $2p \rightarrow 3d$ dipole matrix element, which is assumed to be the same for all transitions linking the core and valence manifolds. The remaining polarization dependent transition double matrix element depends on the angular momentum degeneracy of the core and valence states. The state $|a\rangle$ is the initial electronic ground state of energy $\mathcal{E}_a$ and the states $|c\rangle$ are the intermediate core hole states through which the system passes to the final state $|b\rangle$ of energy $\mathcal{E}_b$. In RIXS, $|b\rangle$ is another excited electronic state lying above the ground state by a relatively small energy separation $\mathcal{E}_{ba} = \mathcal{E}_b - \mathcal{E}_a$. This energy difference extends from meV for vibrationally excited states to several eV for electronic excited states. The normalized Lorentzian of unit integrated area assures strict energy conservation between the initial state $|a\rangle$ and final state $|b\rangle$ which does not involve the intermediate states $|c\rangle$.

The direct RIXS differential cross section is obtained by eliminating intermediate state interference effects by taking the sum over intermediate states c out of the squared absolute value in (6) and rewriting the expression in the three state RIXS form,

$$
\begin{aligned}
\frac{d\sigma^{\mathrm{dir}}_{\mathrm{RIXS}}}{d\Omega_2\, d(\hbar\omega_2)} &= \frac{\lambda_1^2}{2\pi^3}\left(n_{p_2\mathbf{k}_2}+1\right)\sum_b\sum_c \\
&\times \underbrace{\frac{8\pi^2\hbar\omega_1\alpha_{\mathrm{f}}}{\lambda_1^2}\mathcal{R}^2|\langle c|\Big(\hat{\mathbf{r}}\cdot\epsilon_{p_1}|a\rangle|^2}_{\text{absorption: }\Gamma^{p_1}_{ac}} \frac{1}{\Gamma_c^2}\frac{(\Gamma_c/2)^2}{(\hbar\omega_1-\mathcal{E}_{ca})^2+(\Gamma_c/2)^2} \\
&\times \underbrace{\frac{8\pi^2\hbar\omega_2\alpha_{\mathrm{f}}}{\lambda_2^2}\mathcal{R}^2\left|\langle b|(\hat{\mathbf{r}}\cdot\epsilon^*_{p_2})|c\rangle\right|^2}_{\text{emission: }\Gamma^{p_2}_{cb}} \frac{1}{\Gamma_b}\frac{(\Gamma_b/2)^2}{(\hbar\omega_2-\mathcal{E}_{cb})^2+(\Gamma_b/2)^2}
\end{aligned}
\tag{8}
$$

where the underbrackets define dipolar transition energy widths of the excitation ($\Gamma^{p_1}_{ac}$) and decay ($\Gamma^{p_2}_{cb}$) processes, specified below.

The direct double differential RIXS cross section contains two decay lifetime widths, those of the core hole intermediate state Γ_c and that of the final state Γ_b. The intermediate state width is given by $\Gamma_c = \Gamma = \Gamma^{\mathrm{X}} + \Gamma^{\mathrm{A}}$ in (1). We can eliminate the final state width by integrating over all emission energies $\hbar\omega_2$ to obtain the compact expression,

$$
\frac{d\sigma^{\mathrm{dir}}_{\mathrm{RIXS}}}{d\Omega_2} = \frac{1}{4\pi}(1+n_{p\mathbf{k}})\frac{\Gamma^{p_2}_{cb}}{\Gamma}\underbrace{\frac{\lambda_1^2}{\pi}\frac{\Gamma^{p_1}_{ac}}{\Gamma}\frac{(\Gamma/2)^2}{(\hbar\omega_1-\mathcal{E}_{ca})^2+(\Gamma/2)^2}}_{\sigma^{p_1}_{\mathrm{XAS}}}
\tag{9}
$$

If we average the emission rate over polarization, we obtain $\Gamma^{\mathrm{X}} = \langle\Gamma^{p_2}_{cb}\rangle = \frac{1}{3}\sum_{p_2}\Gamma^{p_2}_{cb}$ which is the radiative emission width that determines the fluorescence yield Y_{f}. If we similarly replace the XAS cross section by its polarization averaged value $\sigma_{\mathrm{XAS}} = \frac{1}{3}\sum_{p_1}\sigma^{p_1}_{\mathrm{XAS}}$, we obtain our desired expression (1) or

$$
\frac{d\sigma^{\mathrm{dir}}_{\mathrm{RIXS}}}{d\Omega_2} = \frac{1}{4\pi}\frac{\Gamma^{X}}{\Gamma}(1+n_{p\mathbf{k}})\,\sigma_{\mathrm{XAS}}
\tag{10}
$$

When the spontaneous ($n_{p\mathbf{k}} = 0$) RIXS cross section is integrated over emission energies and angles, we see that it becomes the absorption cross section times the fluorescence yield, as required by energy conservation.

For the Co L edge the absorption and emission widths $\Gamma^{p_1}_{ac}$ and $\Gamma^{p_2}_{cb}$ in (8), averaged over polarization, need to be evaluated by considering the angular momentum degeneracies of the ground state $|a\rangle$ and final (XAS) or intermediate (RIXS) state $|c\rangle$. This consists of counting the electron and hole states per spin that contribute to a given transition, since the dipole operator conserves spin. Denoting the angular momenta for the core states as c and valence states as L, in Co metal there are $N_{\mathrm{h}} = 2.53d^*$ holes in the $2(2L+1) = 10$ total states and $N_{\mathrm{e}} = 7.5$ electrons[6]. The XAS and RIXS dipole transition widths are then obtained by taking the common prefactor in (8) to be

$$
A = \frac{8\pi^2\hbar\omega\,\alpha_{\mathrm{f}}}{\lambda^2}\,\mathcal{R}^2 = 10\,\mathrm{meV}
\tag{11}
$$

This yields for the $L = 2 \rightarrow c = 1$ emission dipole matrix element

$$
\Gamma^{X} = A\,\frac{LN_{\mathrm{e}}}{3(2L+1)(2c+1)} = 3.3\,\mathrm{meV}
\tag{12}
$$

and with the value $\Gamma = 430$ meV[36] gives the literature fluorescence yield of[7]

$$
Y_{\mathrm{f}} = \frac{\Gamma^{X}}{\Gamma} = 7.7\times 10^{-3}
\tag{13}
$$

Similarly we obtain for the $c = 1 \rightarrow L = 2$ absorption matrix element

$$
\Gamma_{\mathrm{XAS}} = A\,\frac{LN_{\mathrm{h}}}{3(2L+1)} = 3.3\,\mathrm{meV}
\tag{14}
$$

which happens to be same as Γ^{X} since the difference in the angular momentum and electron/hole occupation factors cancel each other. The absorption matrix element for the L_3 transition, only, is a factor of 2/3 smaller. The so obtained value, which is self consistent with the literature values of Γ and Y_{f}, is about a factor of 2 larger than that obtained by curve-fitting of the L_3 XAS resonance in Stöhr and Scherz[15].

Kramers-Heisenberg-Dirac theory of REXS. Expression (6) also describes REXS with $|b\rangle = |a\rangle$ and $\hbar\omega = \hbar\omega_1 = \hbar\omega_2$. Since the final state is the ground state with infinitely long lifetime or infinitely narrow linewidth, the Lorentzian is replaced by a Dirac δ-function of the same unit integrated area, which accounts for energy conservation. While in spontaneous REXS, photons are emitted into random directions, stimulated REXS preserves the direction and polarization, $\mathbf{k} = \mathbf{k}_1 = \mathbf{k}_2$ and $p = p_1 = p_2$, so that

$$
\begin{aligned}
\frac{\sigma^{\mathrm{stim}}_{\mathrm{REXS}}}{d\Omega} &= \frac{4\pi^2(\hbar\omega)^2\,\alpha_{\mathrm{f}}^2}{\lambda^2}\,\mathcal{R}^4\,n_{p\mathbf{k}} \\
&\times\left|\sum_c\frac{|\langle c|\hat{\mathbf{r}}\cdot\epsilon_p|a\rangle|^2}{\hbar\omega-\mathcal{E}_{ca}+\mathrm{i}\Gamma_c/2}\right|^2\delta(\hbar\omega-\mathcal{E}_{ca})
\end{aligned}
\tag{15}
$$

For a single intermediate state the stimulated REXS cross section is related to the XAS cross section according to,

$$
\begin{aligned}
\frac{\sigma^{\mathrm{stim}}_{\mathrm{REXS}}}{d\Omega} &= \frac{n_{p\mathbf{k}}}{4\pi\Gamma}\underbrace{\frac{8\pi^2\,\hbar\omega\,\alpha_{\mathrm{f}}}{\lambda^2}\,\mathcal{R}^2\,|\langle a|\hat{\mathbf{r}}\cdot\epsilon_p|c\rangle|^2}_{\Gamma^{p}_{ca}} \\
&\times\underbrace{4\pi\hbar\omega\,\alpha_{\mathrm{f}}\,\mathcal{R}^2|\langle c|\hat{\mathbf{r}}\cdot\epsilon_p|a\rangle|^2\frac{\Gamma/2}{(\hbar\omega-\mathcal{E}_{ca})^2+\Gamma^2/4}}_{\sigma^{p}_{\mathrm{XAS}}}
\end{aligned}
\tag{16}
$$

where $\Gamma^{p}_{ca} = \Gamma^{p}_{ac} = \Gamma_{\mathrm{XAS}}$ expresses a coherent up-down process determined by the XAS matrix element (14). We therefore have,

$$
\Gamma^{\mathrm{stim}}_{\mathrm{REXS}} = \Gamma_{\mathrm{XAS}} = \Gamma_{\mathrm{RIXS}}
\tag{17}
$$

This accounts for the same stimulated RIXS and REXS contributions in our model in Fig. 3 (a).

Finally, we need to comment on the agreement between the change of the nonlinear transmission shown in Fig. 6a and b. Our present formulation of the stimulated REXS cross section (16) leads to the intensity change in Fig. 6a. It is calculated by use of the matrix element for the Co L_3 resonance $\Gamma_{\mathrm{XAS}} = (2/3)\times 3.3 = 2.2$ meV. This corresponds to the assumption that the Co L_3 XAS cross section written in the theoretical atomic form of (9) as

$$
\sigma_{\mathrm{XAS}} = \frac{\lambda^2}{\pi}\frac{\Gamma_{\mathrm{XAS}}}{\Gamma}\frac{(\Gamma/2)^2}{(\hbar\omega-\mathcal{E}_{ca})^2+(\Gamma/2)^2}
\tag{18}
$$

has a peak value of $\lambda^2\Gamma_{\mathrm{XAS}}/(\pi\Gamma) = 41.7$ Mb per atom, concentrated within the natural linewidth of $\Gamma = 430$ meV. In contrast, the intensity change in Fig. 6b, adopted from Chen et al.[23], was calculated in a solid state model, where the peak cross section was taken as the experimental Co metal value of 6.25 Mb, which is smaller due to broadening of the $3d$ valence orbitals by band-structure effects[15]. In the solid state model, the lower peak cross section is compensated by an increased collective atomic response, expressed by a forward scattering coherence factor $G_{\mathrm{coh}} = \lambda^2 N_{\mathrm{a}}/(4\pi A)$[15]. The two formulations give similar results and are linked according to,

$$
n_{pk}\Gamma^{\mathrm{atom}}_{\mathrm{XAS}} \simeq n_{\Gamma}\,G_{\mathrm{coh}}\Gamma^{\mathrm{solid}}_{\mathrm{XAS}}
\tag{19}
$$

Here n_{pk} is the degeneracy parameter or number of photons in the mode coherence volume $V_{p\mathbf{k}} = \lambda^3\hbar\omega/\Delta_{p\mathbf{k}}$, while n_{Γ} is the number of photons in an atom specific volume, defined through the natural decay linewidth Γ as $V_{\Gamma} = \lambda^3\hbar\omega/(2\pi^2\Gamma)$. The photon numbers are just renormalized to different volumes as $n_{\Gamma}\hbar\omega/V_{\Gamma} = n_{pk}\hbar\omega/V_{p\mathbf{k}}$[15]. This may be viewed as an atomic conversion of the incident photons of mode bandwidth $\Delta_{p\mathbf{k}}$, into photons emitted with the natural decay linewidth $\Gamma = \Delta_{p\mathbf{k}}/(2\pi^2)$.

Three-Level Maxwell-Bloch theory. We used a one-dimensional three level Maxwell-Bloch model to estimate the strength of stimulated resonant inelastic X-ray scattering (see[16] for an overview of this and related models). Multilevel Maxwell-Bloch models have been successfully used to describe the propagation of light through a variety of media that can be adequately treated as discrete, few-level systems, including the propagation of strong resonant X-ray pulses through atomic and molecular gases[25,47].

We follow[16] for our calculations. We write the amplitudes of the X-ray electric field as the real part of a slowly varying envelope, $\mathcal{E}(z,t)$ times a rapidly oscillating phase factor (Eq. 21.3 of[16]),

$$
E(z,t) = \mathrm{Re}\left[\mathcal{E}(z,t)e^{i(kz-\omega t)}\right],
\tag{20}
$$

where Re $[x]$ denotes the real part of x, k is the X-ray wavenumber, z is propagation distance, ω is the X-ray angular frequency and t is time. The material polarization (which is determined from the material state, as described below) is written in the same manner

$$
P(z,t) = \mathrm{Re}\left[\mathcal{P}(z,t)e^{i(kz-\omega t)}\right],
\tag{21}
$$

where $\mathcal{P}(z,t)$ is the polarization envelope. Making the slowly varying envelope approximation and the change of variables

$$
Z = z,\quad T = t - z/v
\tag{22}
$$

gives an equation for the evolution of the envelope of the X-ray electric field[16]

$$\frac{\partial}{\partial Z}\mathcal{E}(Z,T) = i\frac{\omega}{2c\epsilon_0}\mathcal{P}(Z,T). \tag{23}$$

Assuming the material polarization does not depend strongly on Z, we can integrate this equation to get an approximate expression for the field of the X-ray pulse exiting the sample (where the sample extends from $Z = 0$ to l),

$$\mathcal{E}(l,T) = \mathcal{E}(0,T) + i\frac{\omega l}{2c\epsilon_0}\mathcal{P}(0,T). \tag{24}$$

As our sample has only a thickness of about one x-ray absorption length at the peak of the Co L_3 absorption resonance, this approximation will be good to within a factor of 2.

Now we describe how we calculate the evolution of the Co/Pd material state. For this, we model the Co/Pd as a slab of discrete three-level atoms. The slab has the same thickness as our samples and the same density of three-level atoms as density of Co atoms in the actual samples. The three levels represent a ground state with energy $E_1 = 0$ eV, a core-excited state with energy $E_2 = 778$ eV (coinciding with the peak of the Co L_3 resonance) and a valence-excited state with energy $E_3 = 2$ eV (coinciding with a typical 3d excitation energy). The dipolar coupling between the ground state and the core-excited state is d_{12}. The dipolar coupling between the core-excited state and the valence-excited state is d_{23}. We chose the dipolar couplings in accordance with the linear X-ray absorption cross sections of our samples, as described at the end of this section. We let $\rho_{nm}(t)$ denote the element in the nth row and mth column of the density matrix in the basis of eigenstates of the three-level atom in the absence of an applied X-ray field. From Equation 16.107 of[16], we define a rotating coordinate representation of the density matrix through

$$\rho_{nm}(t) = s_{nm}(t)e^{i\xi_m(t)-\xi_n(t)}. \tag{25}$$

Here, $\xi_i(t)$ are arbitrary phase factors chosen to be convenient for the problem to be solved. We choose these according to Eq. 13.14 of[16] with a single X-ray pulse acting to both excite and stimulate decay,

$$\hbar\xi_1(t) = 0,\ \hbar\xi_2(t) = \omega t,\ \hbar\xi_3(t) = 0, \tag{26}$$

where ω is the angular frequency of the applied X-ray field and $\hbar$ is Planck's constant divided by 2π. From Eqs. 13.8, 13.27 and 13.29 of[16], we have a matrix which describes the time evolution of the system,

$$W = \frac{1}{2}\begin{bmatrix} 0 & \Omega_P^* & 0 \\ \Omega_P & 2\Delta_P & \Omega_S \\ 0 & \Omega_S^* & 2\Delta_R \end{bmatrix}, \tag{27}$$

with the complex, time-dependent Rabi frequencies defined as

$$\Omega_P = -d_{12}\mathcal{E}/\hbar, \tag{28}$$

and

$$\Omega_S = -d_{23}\mathcal{E}/\hbar. \tag{29}$$

The detunings are

$$\Delta_P = E_2 - E_1 - \hbar\omega = 0, \tag{30}$$

and

$$\Delta_R = E_3 - E_1. \tag{31}$$

The evolution of the density matrix elements is given by Eq. 16.116 of[16],

$$\begin{aligned}\frac{d}{dt}s_{m'm} = &-i\sum_n\left[W_{m'n}(t)s_{nm}(t) - s_{m'n}(t)W_{nm}(t)\right]\\ &-\sum_{nn'}\Gamma_{m'mn'n}s_{n'n}(t),\end{aligned} \tag{32}$$

where Γ is a tensor chosen to phenomenologically model Auger decay. The entries of Γ are

$$\Gamma_{2222} = -\Gamma_{1122} = \Gamma_A, \tag{33}$$

$$\Gamma_{1212} = \Gamma_{2121} = \Gamma_{2323} = \Gamma_{3232} = \frac{\Gamma_A}{2}, \tag{34}$$

and zero otherwise. Once we have calculated $s(t)$ for a particular time, we calculate the envelope of the material polarization for that time from Eq. (21.94) of[16]

$$\mathcal{P}(t) = 2N\left(d_{12}s_{21}(t) + d_{32}s_{23}(t)\right). \tag{35}$$

We note that our choice of Γ_A is a bit different from earlier gas phase modeling[47]. In our model, each atom is returned to the ground state after Auger decay instead of being transferred to a different state that interacts with X-rays differently. This reflects the fact that the energy of a core hole is rapidly transferred to valence electrons over a wide spatial range in our system and most electrons remain in the sample[29]. The impact of the valence electron changes are beyond the scope of our model, however.

We chose the dipole matrix element to correspond to the peak atomic L_3 XAS cross section of $\sigma_{XAS} = 41.7$ Mb per atom as used for the KHD case. Using Eqs. (2.9.8) and (2.5.18) of[14], along with the definition of the absorption cross section as the extinction coefficient divided by the atomic density, we obtain a formula for the absorption cross section at the peak of the resonance,

$$\sigma(\omega_0) = \frac{2\pi c^2\gamma_{sp}}{\omega_0^2\gamma}, \tag{36}$$

where c is the speed of light, ω_0 is the angular frequency at the center of the resonance, $\gamma = \Gamma/(2\hbar)$ is half of the angular frequency FWHM of the absorption resonance, and γ_{sp} is a parameter proportional to the square of the dipole matrix element. In particular, γ_{sp} is given by Eq. (2.5.11) of[14] as

$$\gamma_{sp} = \frac{e^2\omega_0^3 d_{12}^2}{6\pi\epsilon_0\hbar c^3}, \tag{37}$$

where ϵ_0 is the permittivity of free space, and e is the charge of an electron. Combining these gives

$$d_{12} = \sqrt{\frac{3\sigma(\omega_0)\gamma\epsilon_0\hbar c}{\omega_0 e^2}} = 6.1\times 10^{-12}\text{m}. \tag{38}$$

The dipole matrix element between the model core and valence excited states was set to $d_{23} = d_{12}$ as discussed earlier.

We now have the necessary equations to solve for the field of an X-ray pulse exiting a sample. We used the method of[38] to generate simulated SASE pulses with 4 eV bandwidth and either 5 or 25 fs pulse durations. For each pulse duration, we simulated the interaction of the X-ray pulses with 20 different randomly generated SASE pulses and averaged the results. We assume the sample starts in the ground state,

$$s(0) = \begin{bmatrix} 1 & 0 & 0 \\ 0 & 0 & 0 \\ 0 & 0 & 0 \end{bmatrix}. \tag{39}$$

Next, we use Eq. (32) to solve for the evolution of the sample, then Eq. (35) to calculate the polarization as a function of time. Finally, we calculate the X-ray field exiting the sample from Eq. (24). The spectra of X-rays incident and exiting a sample is obtained from these time domain quantities by taking a Fourier transform. From these spectra, we extracted the stimulated inelastic scattering efficiencies shown in Fig. 5.

Data availability

The datasets generated and analysed during the current study are available from the corresponding authors on reasonable request.

Code availability

The code used for simulations and analysis are available from the corresponding authors on reasonable request.

Received: 25 July 2021; Accepted: 1 March 2022;

References

1. Gel'mukhanov, F., Odelius, M., Polyutov, S. P., Föhlisch, A. & Kimberg, V. Dynamics of resonant x-ray and auger scattering. *Rev. Mod. Phys.* **93**, 035001 (2021).
2. Nilsson, A. & Pettersson, L. G. M. Chemical bonding on surfaces probed by x-ray emission spectroscopy and density functional theory. *Surf. Sci. Rep.* **55**, 49 (2004).
3. Rueff, J. P. & Shukla, A. Inelastic x-ray scattering by electronic excitations under high pressure. *Rev. Mod. Phys.* **82**, 847–896 (2010).
4. Ament, L. J. P., van Veenendaal, M., Devereaux, T. P., Hill, J. P. & van den Brink, J. Resonant inelastic x-ray scattering studies of elementary excitations. *Rev. Mod. Phys.* **83**, 705–767 (2011).
5. Jacobsen, C. *X-Ray Microscopy*. (Cambridge University Press, Cambridge, 2020).
6. Stöhr, J. & Siegmann, H. C. *Magnetism: from fundamentals to nanoscale dynamics*. (Springer: Heidelberg, 2006).
7. Krause, M. O. Atomic radiative and radiationless yields for k and l shells. *Journal of physical and chemical reference data* **8**, 307–327 (1979).
8. Qiao, R. et al. High-efficiency in situ resonant inelastic x-ray scattering (irixs) endstation at the advanced light source. *Rev. Sci. Instrum.* **88**, 033106 (2017).
9. Ghiringhelli, G. & Braicovich, L. Magnetic excitations of layered cuprates studied by rixs at cu l3 edge. *J. Electron Spectrosc. Relat. Phenom.* **188**, 26–31 (2013).
10. Stöhr, J. Overcoming the diffraction limit by multi-photon interference: a tutorial. *Adv. Optics and Photonics* **11**, 215 (2019).

11. Bostedt, C. et al. Linac coherent light source: the first five years. *Rev. Mod. Phys.* **88**, 015007 (2016).
12. Dirac, P. A. M. The quantum theory of dispersion. *Proc. Roy. Soc. London A* **114**, 710 (1927).
13. Einstein, A. Zur quantentheorie der strahlung. *Phys. Z.* **18**, 121 (1917).
14. Loudon, R. The quantum theory of light (Oxford University Press, 2000).
15. Stöhr, J. & Scherz, A. Creation of x-ray transparency of matter by stimulated elastic forward scattering. *Phys. Rev. Lett.* **115**, 107402 (2015).
16. Shore, B. W. Manipulating quantum structures using laser pulses (Cambridge University Press, 2011).
17. Rohringer, N. et al. Atomic inner-shell x-ray laser at 1.46 nanometres pumped by an x-ray free-electron laser. *Nature* **481**, 488 (2012).
18. Beye, M. et al. Stimulated x-ray emission for materials science. *Nature* **501**, 191 (2013).
19. Yoneda, H. et al. Atomic inner-shell laser at 1.5-ångström wavelength pumped by an x-ray free-electron laser. *Nature* **524**, 446 (2015).
20. Kroll, T. et al. Stimulated x-ray emission spectroscopy in transition metal complexes. *Phys. Rev. Lett.* **120**, 133203 (2018).
21. Kroll, T. et al. Observation of seeded mn k β stimulated x-ray emission using two-color x-ray free-electron laser pulses. *Phys. Rev. Lett.* **125**, 037404 (2020).
22. Wu, B. et al. Elimination of x-ray diffraction through stimulated x-ray transmission. *Phys. Rev. Lett.* **117**, 027401 (2016).
23. Chen, Z. et al. Ultrafast self-induced x-ray transparency and loss of magnetic diffraction. *Phys. Rev. Lett.* **121**, 137403 (2018).
24. Weninger, C. et al. Stimulated electronic x-ray raman scattering. *Phys. Rev. Lett.* **111**, 233902 (2013).
25. Kimberg, V. et al. Stimulated x-ray raman scattering–a critical assessment of the building block of nonlinear x-ray spectroscopy. *Faraday Discuss.* **194**, 305–324 (2016).
26. O'Neal, J. T. et al. Electronic population transfer via impulsive stimulated x-ray raman scattering with attosecond soft-x-ray pulses. *Phys. Rev. Lett.* **125**, 073203 (2020).
27. Eichmann, U. et al. Photon-recoil imaging: Expanding the view of nonlinear x-ray physics. *Science* **369**, 1630–1633 (2020).
28. Schreck, S. et al. Reabsorption of soft x-ray emission at high x-ray free-electron laser fluences. *Phys. Rev. Lett.* **113**, 153002 (2014).
29. Higley, D. J. et al. Femtosecond x-ray induced changes of the electronic and magnetic response of solids from electron redistribution. *Nat. Commun.* **10**, 5289 (2019).
30. Ferguson, K. R. et al. The atomic, molecular and optical science instrument at the linac coherent light source. *J. Synchrotron Radiat.* **22**, 492–497 (2015).
31. Berrah, N. et al. Two mirror x-ray pulse split and delay instrument for femtosecond time resolved investigations at the lcls free electron laser facility. *Opt. Express* **24**, 11768–11781 (2016).
32. Hellwig, O., Denbeaux, G., Kortright, J. & Fullerton, E. E. X-ray studies of aligned magnetic stripe domains in perpendicular multilayers. *Physica (Amsterdam)* **336B**, 136–144 (2003).
33. Nilsson, A. et al. Determination of the electronic density of states near buried interfaces: Application to co/cu multilayers. *Phys. Rev. B* **54**, 2917 (1996).
34. Sanchez-Gonzalez, A. et al. Accurate prediction of x-ray pulse properties from a free-electron laser using machine learning. *Nat. Commun.* **8**, 15461 (2017).
35. Stöhr, J *NEXAFS Spectroscopy*. Springer: Heidelberg, 1992.
36. Krause, M. O. & Oliver, J. Natural widths of atomic k and l levels, k α x-ray lines and several kll auger lines. *Journal of Physical and Chemical Reference Data* **8**, 329–338 (1979).
37. Saldin, E. L., Schneidmiller, E. A. & Yurkov, M. V. Statistical and coherence properties of radiation from x-ray free-electron lasers. *New J. Phys.* **12**, 035010 (2010).
38. Pfeifer, T., Jiang, Y., Düsterer, S., Moshammer, R. & Ullrich, J. Partial-coherence method to model experimental free-electron laser pulse statistics. *Opt. Lett.* **35**, 3441–3443 (2010).
39. Rohringer, N. X-ray raman scattering: a building block for nonlinear spectroscopy. *Philos. Trans. R. Soc. A* **377**, 20170471 (2019).
40. Kjellsson, L. et al. Resonant inelastic x-ray scattering at the $n_2\pi^*$ resonance: Lifetime-vibrational interference, radiative electron rearrangement, and wave-function imaging. *Phys. Rev. A* **103**, 022812 (2021).
41. Duris, J. et al. Tunable isolated attosecond x-ray pulses with gigawatt peak power from a free-electron laser. *Nat. Photonics* **14**, 30–36 (2020).
42. Moeller, S. et al. Photon beamlines and diagnostics at lcls. *Nucl. Instrum. Methods Phys. Res. A* **635**, S6–S11 (2011).
43. Behrens, C. et al. Few-femtosecond time-resolved measurements of x-ray free-electron lasers. *Nat. Commun.* **5**, 3762 (2014).
44. Lutman, A. et al. Femtosecond x-ray free electron laser pulse duration measurement from spectral correlation function. *Phys. Rev. Spec. Top. Accel. Beams* **15**, 030705 (2012).
45. Engel, R., Düsterer, S., Brenner, G. & Teubner, U. Quasi-real-time photon pulse duration measurement by analysis of fel radiation spectra. *J. Synchrotron Radiat.* **23**, 118–122 (2016).
46. Schlotter, W. et al. The soft x-ray instrument for materials studies at the linac coherent light source x-ray free-electron laser. *Review of Scientific Instruments* **83**, 043107 (2012).
47. Weninger, C. & Rohringer, N. Stimulated resonant x-ray raman scattering with incoherent radiation. *Phys. Rev. A* **88**, 053421 (2013).

Acknowledgements

We acknowledge C. D. Pemmaraju and D. A. Reis for valuable discussions and M. Swiggers, and J. Aldrich for technical assistance. One of us (J. S.) would like to especially thank Faris Gel'mukhanov for elucidating discussions. Use of the Linac Coherent Light Source, SLAC National Accelerator Laboratory, is supported by the U.S. Department of Energy, Office of Science, Office of Basic Energy Sciences under Contract No. DE-AC02-76SF00515.

Author contributions

D.J.H., Z.C., M. Beye, M.H., A.H.R., G.L.D., A.M., S.B., M. Bucher, S.C., T.C., E.J., R.K., T.L., H.A.D., W.F.S. and J.S. performed experiments. V.M., O.H., D.J.H. and Z.C. prepared samples. D.J.H., Z.C., M.H. and J.S. analyzed nonlinear X-ray data. R.Y.E. characterized X-ray pulse duration from X-ray spectra. T.M. and Y.D. analyzed X-band Transverse Deflecting Cavity data. D.J.H. performed Maxwell-Bloch simulations. J.S. performed Kramers-Heisenberg-Dirac simulations. J.S. conceived the experiment. J.S. and D.J.H. wrote the manuscript with input form all authors. A.F., H.A.D., W.F.S. and J.S. supervised the project.

Competing interests

The authors declare no competing interests.

Additional information

Correspondence and requests for materials should be addressed to Daniel J. Higley or Joachim Stöhr.

Peer review information *Communications Physics* thanks Cristian Svetina, Yao Wang and the other, anonymous, reviewer(s) for their contribution to the peer review of this work.

Reprints and permission information is available at http://www.nature.com/reprints

Chapter 6

XUV-Optical Wave mixing

The non-linearity observed in the monochromatic absorption study presented in chapter 4 was largely non-parametric, i.e. the non-linearity of the interaction was caused by the electronic changes induced during the X-ray pulse, not by coherent multi-photon interactions. The broadband absorption study presented in chapter 5 observed the same effects, but additionally demonstrated the wave-mixing process of SRIXS, wherein stimulated emission removes the largest part of the core-excitation energy from the sample. However, the buildup of valence excitations over the duration of the pulse is still problematic in two ways: First, the signal of the thermalizing valence electron distribution overlaps with and thus distorts the measured SRIXS spectra. Second, the studied material is excited into (and at least partially probed in) a state of warm-dense matter, which severely limits the efficacy of this implementation of SRIXS for any material science questions that call for measurements at low temperatures. These problems can in principle be avoided by moving to fully parametric wave-mixing processes, which inherently return the material to the ground state. Prime candidates are the third-order processes (four-wave-mixing) as the lowest-order class of processes that do not vanish due to symmetry reasons in inversion-symmetric materials.

As discussed in chapter 2, parametric wave-mixing like SFG and DFG can, depending on the pulse-sequence and phase matching conditions, deliver spectroscopic information about virtually all types of material excitations, and perhaps equally important, they can be used to unravel the coupling strength between them, and in turn their colocalization, i.e. the overlap of their wave-functions. The theorized method of XCRS, which I introduced in section 2.5.6, impressively demonstrates this use-case, but requires three independent core-resonant waves, which is still beyond current technical capabilities.

An attractive and more easily realizable alternative is therefore the sum- and difference-frequency between one core-resonant XFEL photon and two lower-energy photons produced by conventional lasers. This process is experimentally demonstrated for the first time by us, as presented in the publication below. In this case, we find that the third-order non-linear susceptibility is enhanced due to the colocalization of the resonant $1s2p$ core-excitation with the $1s2s$ core-excitation.
Overall, we demonstrate a background-free experiment (signal separation in photon energy) that delivers on two of the major promised capabilities of core-resonant FWM techniques: Firstly to probe the colocalization of excited states around the resonant

atom, and secondly the sensitivity to "dark" excited states, as the $1s2s$ Li$^+$ configuration cannot be reached from the $(1s)^2$ ground-state through single-photon absorption due to dipole selection rules.

The following publication is reproduced from [7], in accordance with the Creative Commons Attribution-NonCommercial license under which the article is published.

PHYSICS

Probing electron and hole colocalization by resonant four-wave mixing spectroscopy in the extreme ultraviolet

Horst Rottke[1]*, Robin Y. Engel[2,3], Daniel Schick[1], Jan O. Schunck[2,3], Piter S. Miedema[2], Martin C. Borchert[1], Marion Kuhlmann[2], Nagitha Ekanayake[2], Siarhei Dziarzhytski[2], Günter Brenner[2], Ulrich Eichmann[1], Clemens von Korff Schmising[1], Martin Beye[2,3], Stefan Eisebitt[1,4]*

Extending nonlinear spectroscopic techniques into the x-ray domain promises unique insight into photoexcited charge dynamics, which are of fundamental and applied interest. We report on the observation of a third-order nonlinear process in lithium fluoride (LiF) at a free-electron laser. Exploring the yield of four-wave mixing (FWM) in resonance with transitions to strongly localized core exciton states versus delocalized Bloch states, we find resonant FWM to be a sensitive probe for the degree of charge localization: Substantial sum- and difference-frequency generation is observed exclusively when in a one- or three-photon resonance with a LiF core exciton, with a dipole forbidden transition affecting details of the nonlinear response. Our reflective geometry–based approach to detect FWM signals enables the study of a wide variety of condensed matter sample systems, provides atomic selectivity via resonant transitions, and can be easily scaled to shorter wavelengths at free-electron x-ray lasers.

INTRODUCTION

Nonlinear wave mixing in the optical spectral range is a cornerstone of nonlinear optics. It has been used extensively for the generation of coherent light at otherwise inaccessible wavelengths, for the analysis of optical properties of materials, and, using ultrashort light pulses, to explore the evolution of optical excitations in time. Free-electron lasers (FELs) have opened the opportunity to apply these nonlinear techniques in the extreme ultraviolet (XUV) up to the x-ray spectral ranges. One promise of these approaches is that at sufficiently short wavelengths and pulse duration, electronic excitations may be followed on an atomic length and time scale. Moreover, XUV radiation makes it possible operate in resonance with core levels, providing element specificity and spectroscopic information with little lifetime broadening.

So far, however, there have been few studies on nonlinear processes in solids involving XUV or x-ray beams. Parametric down conversion, a second-order nonlinear process, aimed at probing valence-electron charge densities and the optical response of crystals with atomic resolution (*1*–*3*). With similar aims, second-order x-ray and optical sum-frequency mixing, essentially being optically modulated x-ray diffraction, has first been observed using FEL and long-wavelength optical laser radiation (*4*). Proof-of-principle experiments demonstrating second harmonic generation of x-rays in solids and interface sensitivity of second-order nonlinear processes in centrosymmetric crystals in the soft x-ray range have also been reported (*5*, *6*).

In contrast, four-wave mixing (FWM), as a third-order nonlinear process, is able to address the bulk properties of any material, irrespective of its symmetry. Here, first experimental investigations based on transient gratings induced by XUV FEL pulses and probed either by optical or even XUV laser pulses have been reported (*7*–*12*). Very recently, FWM in NaCl at the Na^+ $L_{2,3}$ edge near 33.5 eV, using laser-generated attosecond XUV and near-infrared (NIR) laser pulses, revealed the presence of dark excited states, i.e., states not dipole coupled to the electronic ground state of the material (*13*).

We report on the observation of a complementary FWM process driven in a solid, namely, sum- and difference-frequency generation (SFG and DFG, respectively) involving one XUV (ω_X) and two NIR photons (ω_I) with resulting beams at frequencies $\omega_{FWM} = \omega_X \pm 2\omega_I$, i.e., different from the radiation driving the process, which, to our knowledge, has not been observed yet. We study lithium fluoride (LiF), a prototypical ionic crystal with centrosymmetry. In particular, we investigate the effect of electronic excitations with a high degree of electron-hole correlation on these processes, using the presence of both strongly localized core excitons and delocalized Bloch states in LiF as a model to probe the degree of colocalization of the excited electron and hole.

Exploiting the wavelength tunability of the FEL source, we are able to chart the FWM conversion efficiency. We find significant SFG and DFG in LiF when in either one- or three-photon resonance with the core exciton that is linked with the Li^+ 1s2p excited electron configuration. An energetically near exciton, linked with the Li^+ 1s2s electron configuration and suspected to be present from linear absorption experiments, is seen—via comparison to theory—to affect the frequency conversion processes via two-photon resonance and a near-resonant one-NIR-photon coupling of both excitonic states. In contrast, we do not observe any FWM when exclusively in resonance with transitions to delocalized Bloch states in the experiment. This indicates that FWM in the XUV and soft x-ray spectral range is a sensitive probe of charge colocalization and charge separation. Given that the separation of holes and electrons and the localization of charge at particular atomic sites are key steps in (photo)chemical reactions, light harvesting, and the elementary steps of photovoltaics, we expect this sensitivity to be instrumental in the study of phenomena in materials science, physics, and chemistry in the future.

---

[1] Max-Born-Institut für Nichtlineare Optik und Kurzzeitspektroskopie, Max-Born-Straße 2A, 12489 Berlin, Germany. [2] Deutsches Elektronen-Synchrotron DESY, Notkestr. 85, 22607 Hamburg, Germany. [3] Department of Physics, Universität Hamburg, Luruper Chaussee 149, 22761 Hamburg, Germany. [4] Technische Universität Berlin, Institut für Optik und Atomare Physik, Straße des 17. Juni 135, 10623 Berlin, Germany.
*Corresponding author. Email: rottke@mbi-berlin.de (H.R.); eisebitt@mbi-berlin.de (S.E.)

RESULTS

The frequency mixing processes studied, one- and three-photon resonant with a LiF core exciton, are schematically illustrated in Fig. 1A. The core exciton of interest here is formed by the promotion of one of the strongly localized 1s core electrons of a Li^+ ion in LiF to an excited state equally localized on the same ion and linked with the Li^+ electronic configuration 1s2p. It gives rise to a dipole allowed transition with a characteristic narrow absorption structure in linear spectroscopy (*14*). We will refer to this final state as p-type exciton. The prominent, narrow resonance enhancement of the LiF reflectivity at 62.3-eV photon energy in Fig. 1B is attributable to this core exciton. The 1s2s excited electron configuration of the Li^+ ion is energetically close by but not dipole coupled to the $(1s)^2$ ground state configuration in a perfect cubic LiF crystal. We will refer to this 1s2s Li^+ electron configuration as s-type exciton. In linear absorption spectroscopy (*14*) and in the LiF linear reflectivity shown in Fig. 1B, a small low-energy shoulder of the p-type exciton feature, located at ≈61 eV, is suspected to be due to this s-type exciton, becoming weakly visible via dipole coupling to the $(1s)^2$ configuration through inversion symmetry breaking (*15*). In contrast, transitions into delocalized band states are responsible for the spectral features at higher photon energies in Fig. 1B (*16*–*19*).

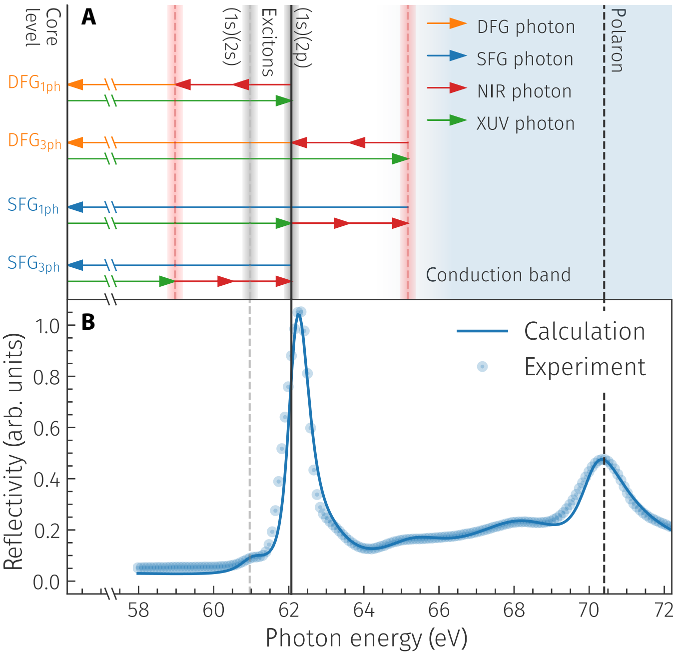

Fig. 1. FWM schemes and the LiF linear reflectivity. (**A**) Schematic view of the LiF level structure relevant to the experiment with the horizontal arrows representing SFG and DFG in one- and three-photon resonance with the p-type LiF core exciton at 62.07-eV photon energy, just below the conduction band edge. The green and red arrows depict the driving XUV and NIR photons, respectively. The blue and orange ones represent the generated sum- and difference-frequency photons, respectively. The shaded regions indicate the spectral bandwidth of the FEL. (**B**) The schematic level structure of (A) showing up in the linear reflectivity of LiF in the photon energy range relevant to the experiment. The blue dots represent the measured reflectivity. The line is the calculated reflectivity based on the model for the linear dielectric constant ϵ as outlined in the Supplementary Materials. The narrow reflectivity peak visible at 62.3 eV is due to the LiF p-type core exciton resonance located at 62.07 eV (vertical line) with one of the Li^+ $(1s)^2$ core electrons excited. Conduction band absorption is generally assumed to start at photon energies to the right of this resonance. arb. units, arbitrary units.

We study FWM at the sum and difference frequencies $\omega_X \pm 2\omega_I$ by detecting the generated radiation emitted by a LiF single crystal toward the vacuum side, from where the process driving XUV and NIR laser beams are impinging. The scheme of the setup in Fig. 2 visualizes this detection approach; the experimental parameters are detailed in Materials and Methods. Note that an aluminum filter directly upstream of the detector not only blocks NIR radiation but also absorbs XUV with photon energies exceeding 72.7 eV.

In Fig. 3, we show our main experimental result, the dependence of the sum- and difference-frequency conversion yields on the setting of the FEL photon energy in a range covering the LiF core exciton and part of the conduction band. The density plot in Fig. 3A reveals the energy offset of the radiation generated by wave mixing with respect to the corresponding setting of the FEL photon energy. As directly evident from the experimental data, it amounts to $\pm 2\hbar\omega_I = \pm 3.1$ eV, i.e., two times the fixed NIR photon energy, for the generated sum and difference frequency with narrow spectral distributions. This spectral spacing is indicative of the wave mixing nature of the signals observed. Figure 3B presents individually the total number of sum- and difference-frequency photons generated in each FEL pulse train during XUV and NIR temporal overlap as a function of the photon energy of the process driving XUV radiation. On average, $(5.3 \pm 0.1) \times 10^{11}$ XUV photons per pulse train were impinging from the FEL on the LiF sample for the data shown in Fig. 3 (A and B). The direction of polarization of both, the FEL and NIR laser pulses, is in the common plane of incidence on the sample, and both pulses arrive simultaneously except for a statistically distributed relative arrival time jitter. The entire measurement is performed at a fixed NIR pulse intensity on the LiF crystal. As is obvious in Fig. 3 (A and B), we observe a significant yield of frequency conversion only when in resonance with the p-type core exciton located at $\hbar\omega_{exc} = 62.07$ eV. This can either be a one-photon resonance with the FEL photon energy tuned to resonance ($\omega_X \approx \omega_{exc}$) or a three-photon resonance satisfying $\omega_X \pm 2\omega_I \approx \omega_{exc}$. In both cases, SFG and

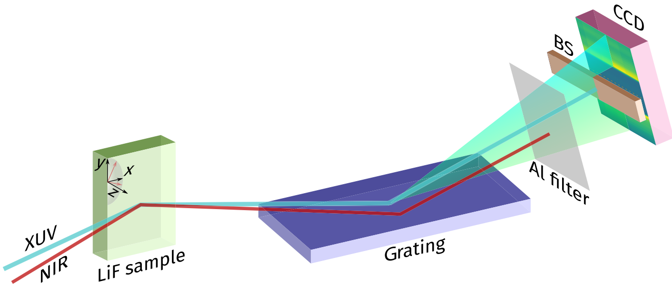

Fig. 2. Schematic view of the experimental setup. The FEL (blue), NIR (red), and the generated sum- and difference-frequency beams reflected off the LiF to vacuum interface are dispersed by a reflection grating. Subsequently, the NIR beam is blocked by an aluminum foil and the FEL beam by a separate beam stop (BS) directly in front of a charge-coupled device (CCD) camera that detects the generated sum- and difference-frequency beams. The XUV and NIR beams propagate in a common plane of incidence toward the LiF sample that we choose to be the *xz* plane of a suitably chosen Cartesian coordinate system with the *z* axis normal to the LiF surface and parallel to one of the LiF cubic crystal axes (see the axis system indicated on the LiF crystal surface). The two in-plane axes of the LiF crystal (red axes) were rotated by (22.5 ± 2.5)° with respect to the *x* and *y* axes of this coordinate system in the LiF surface plane.

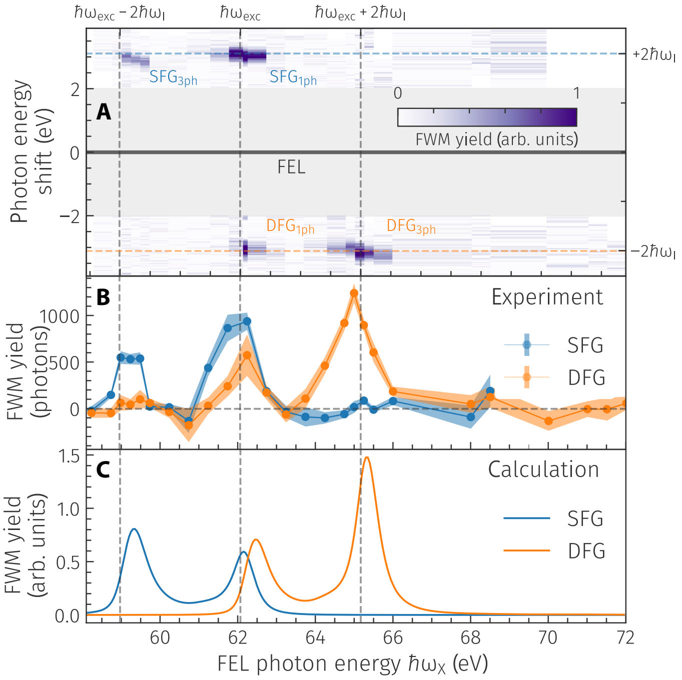

Fig. 3. Measured and calculated frequency conversion yields. (**A**) Density plot of the experimental spectral distributions of the generated sum- and difference-frequency photons (vertical axis) for the different FEL photon energy settings (horizontal axis). The spectral distributions are shown relative to the respective FEL photon energy settings. They thus appear at an offset of $\pm 2\hbar\omega_I = \pm 3.1$ eV with respect to the respective FEL photon energy (horizontal line at zero). (**B**) The generated number of sum- (blue) and difference-frequency (orange) photons plotted over the process driving FEL photon energy $\hbar\omega_X$. Shown is the total number of generated photons per FEL pulse train at zero FEL-NIR pulse delay summed over the whole spectral distribution of the generated radiation. Sizable frequency conversion is observed only with the incident FEL and NIR radiation in one- or three-photon resonance with the p-type core exciton of LiF. (**C**) Calculated sum- and difference-frequency yields plotted as functions of the process driving FEL photon energy. The NIR photon energy is fixed at 1.55 eV. The plot is based on our basic model of the LiF third-order nonlinear susceptibility tensor in this photon energy range and corresponds to the parameter $R = 0.112$ in Fig. 5. Shaded areas in (B) connect 95% confidence intervals of the data.

DFG are observed as sketched in Fig. 1A. Aside from these settings, no FWM frequency conversion was detectable above the residual background level of FEL stray light.

Further corroboration of the FWM nature of the signals shown in Fig. 3 comes from a detailed analysis of (i) the direction of propagation and divergence of the individual beams observed and (ii) their spectral and (iii) temporal behavior. Details of these characteristics of the generated radiation beams are shown in Fig. 4, exemplified for DFG in three-photon resonance with the LiF p-type core exciton, obeying ($\omega_X - 2\omega_I = \omega_{exc}$).

Regarding (i): We treat an FWM process, where the driving radiation impinges (Fig. 2) from the vacuum side. In this case, the emission direction of sum- and difference-frequency beams emitted by the medium toward the vacuum side is fixed through boundary conditions given by the driving FEL and NIR fields at the crystal interface to vacuum, via the induced nonlinear polarization in the medium. Fundamentally, this amounts to momentum conservation at the vacuum-medium interface, with the components of the driving fields' wave vectors along the interface on the vacuum side being the relevant quantities. In the experiment, the angle enclosed between the FEL and NIR beams is rather small ($|\theta_X - \theta_I| = 0.75°$), resulting in a practically collinear geometry, and moreover, $\omega_X \gg \omega_I$. Therefore, the nonlinear reflection is expected closely along the reflected FEL beam with an estimated offset angle α of $|\alpha| < 0.04°$ (see the Supplementary Materials for more details). This angle is much smaller than the radial divergence of the FEL beam, which can be determined to be 0.12° using the characteristics of the focusing x-ray optics. The beam directions observed are thus in line with momentum conservation and the presence of an FWM process in our geometry. This shows that the generated signal keeps the typical directional characteristics of an FWM signal in contrast to, e.g., a fluorescence emission channel. To discriminate the beams, the experimental geometry requires a spectral separation of the FEL beam and the nonlinear reflection rather than a spatial separation (see Fig. 2). An example for a difference-frequency beam profile on the charge-coupled device (CCD) camera as projected on the direction perpendicular to the dispersion direction of the grating is shown in Fig. 4A. The full width of this beam amounts to ≈4 mm at half maximum (FWHM), corresponding to a far-field radial beam divergence of ≈0.09°. As expected, the nonlinear emission cone is limited by the divergence of the focused XUV and NIR laser beams that drive the nonlinear processes.

Regarding (ii): In Fig. 4D, we show the spectral distribution of the frequency conversion yield over the relative delay of the FEL and NIR pulses. A cut through this density plot along a line at zero delay, i.e., the detailed spectral distribution of the $\omega_X - 2\omega_I$ difference-frequency photon yield, is displayed in Fig. 4B. The distribution is centered at 62.05 eV, which is in close agreement with the expectation according to energy conservation requiring $\hbar\omega = \hbar\omega_X - 2\hbar\omega_I = 62.15$ eV. The bandwidth of the FEL varies between 500 and 600 meV FWHM, depending on photon energy, while the bandwidth of the NIR pulses is close to 100 meV. Thus, observing the bandwidth of the SFG and DFG signals with an FWHM of 351 meV suggests that the wave mixing process is limited by the natural linewidth of the excitonic lithium *K*-edge resonance.

Regarding (iii): The dependence of the difference-frequency yield on the time delay between the FEL and NIR pulses in Fig. 4C indicates that the nonlinear conversion process requires temporal overlap of the pulses. This is expected for a nonlinear wave mixing process for which the induced nonlinear polarization decays on a time scale faster than the widths of the driving laser pulses. The observed temporal profile represents the cross-correlation of the FEL and NIR pulses including the relative timing jitter of the pulses on the LiF sample. A Gaussian fit to the yield indicates an FWHM of this cross-correlation of the pulses of (180 ± 22) fs. Because the NIR laser pulse width was 21 fs and the FEL pulse width was set to be less than 100 fs, a substantial contribution of ≈140 fs to the width of the cross-correlation curve is actually due to the relative arrival time jitter of the pulses on the LiF sample.

DISCUSSION

Having firmly established that the signals that we observe are due to FWM, we now turn our attention to the pronounced variation of the photon yield of the $\omega_X \pm 2\omega_I$ wave mixing processes as a function of the driving FEL photon energy seen in Fig. 3B. How does the nature of the resonances involved influence this yield? Obviously, significant frequency conversion is present only in close one- or three-photon

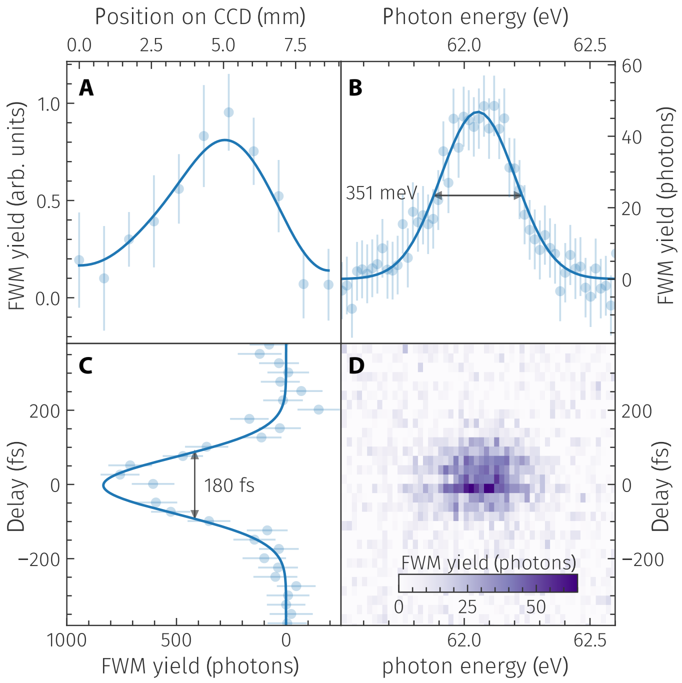

Fig. 4. Characteristic details of the radiation generated in the nonlinear processes. As a characteristic example, we present details for the difference-frequency beam with the FEL tuned to three-photon resonance with the LiF core exciton at $\hbar\omega_X = 65.25$ eV. (**A**) Sample profile of the generated difference-frequency beam on the CCD camera perpendicular to the dispersion direction of the grating. The blue curve is intended to guide the eye. (**B**) Spectral distribution of the difference-frequency photon yield with the FEL-NIR pulse delay set to zero, i.e., a cut through the density plot in (**D**) along a line at zero delay. (**C**) The total amount of generated difference-frequency photons plotted over the FEL-NIR pulse delay, i.e., a projection of the density plot in (D) on the delay axis. Blue curves in (B) and (C) represent Gaussian fits to the data, and arrows indicate their FWHM. Error bars represent the SD. The maximum of the Gaussian fit in (C) is shown in Fig. 3B as the DFG yield at $\hbar\omega_X = 65.25$ eV. (D) Density plot of the dependence of the spectral distribution of the difference-frequency photon yield on the FEL-NIR pulse delay.

resonance with the p-type core exciton, giving rise to the characteristic two-peak structure in both the $\omega_X + 2\omega_I$ and $\omega_X - 2\omega_I$ photon yields, separated by approximately $2\omega_I$ in Fig. 3B. In contrast, one- or three-photon resonance exclusively with conduction band states does not give rise to detectable frequency conversion, i.e., no FWM yield was observed with an FEL photon energy setting higher than ≈64 and ≈67 eV for sum- and difference-frequency mixing, respectively.

The influence of electronic correlation and, in particular, the formation of a core exciton next to the Li^+ *K*-edge absorption have been studied in the past (*14*), and first-principles calculations indicate that strong correlation effects between the core hole and the electrons are restricted to the first few electron volts of the XUV absorption starting at ≈60 eV (*20*). The nature of the electronic states involved in linear absorption and correspondingly in the linear reflectivity of LiF in Fig. 1B can explain what we observe in FWM. In the initial state, the active electron is well localized on a Li atom in the crystal. This also is true for the p-type core exciton, where the excited electron remains localized in the vicinity of that same Li atom (*15*). The corresponding overlap of the wave function with other localized states of the lithium atom enhances the respective transition matrix elements, i.e., the probability that a suitable photon may drive a transition between colocalized states. In other words, a colocalization of excited states strongly enhances the third-order nonlinear susceptibility $\chi^{(3)}$ of LiF, which is the quantity responsible for the FWM processes that we study. In contrast, the higher-energy conduction band electronic states can be described by delocalized Bloch states with the excited electron being able to move freely in the crystal. The lack of colocalization in this case can, in turn, give rise to a strongly suppressed $\chi^{(3)}$. This difference in electron-hole colocalization is reflected in the observed frequency conversion yield in Fig. 3B.

Specifically, we note that we observe no significant DFG when tuning the FEL photon energy to the 70.5-eV feature in the linear reflectivity spectrum Fig. 1B. The corresponding feature in the LiF near *K*-edge absorption fine-structure spectrum has been debated to be due to correlation effects, namely, an electron polaron (*21*, *22*). Furthermore, it has been speculated that this electron polaron is bound to the Li 1s core hole (*21*). While this debate is about half a century old, ab initio electronic structure calculations, to this day, have not been able to address this question. Our experiment can address this question experimentally: In the hypothesized case of a bound polaron, an increase of the nonlinear susceptibility and hence the FWM yield would be expected in one- and three-photon resonance with the 70.5-eV feature. However, no significant FWM yield was observed either in the three-photon resonant sum-frequency yield (Fig. 3B, blue curve around 67.4 eV) nor in the one-photon resonant difference-frequency yield (Fig. 3B, orange curve around 70.5 eV). This indicates the absence of colocalization of the active electron and core hole of the same order of magnitude as it is present for the core p-type exciton at 62.07 eV.

Next, we strive to obtain a basic understanding of the pronounced sum- and difference-frequency conversion yield when in resonance with the p-type core exciton. Given the strong localization and hence roughly atomic character of the core exciton, we model the third-order nonlinear susceptibility tensor $\chi^{(3)}$, which is not known for LiF in the relevant photon energy range, by involving Li^+ionic states, namely, the $(1s)^2$ ground state and excited states corresponding to the p-type and to the s-type exciton. This approach is in analogy to the early efforts to understand the linear absorption spectrum (*23*). The details of the model are presented in Materials and Methods and in the Supplementary Materials.

On the basis of this $\chi^{(3)}$ model in conjunction with the experimental parameters, we obtain the conversion yields for the generated reflected sum- and difference-frequency beams as functions of the driving FEL photon energy as shown in Fig. 5. It is assumed that the polarization of both the FEL and NIR radiation is in their common plane of incidence on the LiF crystal and their angle of incidence is 52° with respect to the crystal normal as it was in the experiment. In Fig. 5B, we present the dependence of the difference-frequency yield on the applied FEL photon energy. Here, the ratio *R* of the radial parts of the Li^+ dipole matrix elements for the (1s2s) − (1s2p) (d_2) and $(1s)^2$ − (1s2p) (d_1) transitions $R = d_2/d_1$ serves as a parameter to characterize the relative influence of the states on $\chi^{(3)}$ and thus on the nonlinear polarization of the medium. The electric field strengths of the incident XUV and NIR radiation are assumed as constant. In Fig. 5A, we show the corresponding results for SFG.

At $R = 0$, the LiF s-type core exciton does not influence the frequency conversion at all. The resonance structure found thus exclusively originates from the driving laser radiation being either

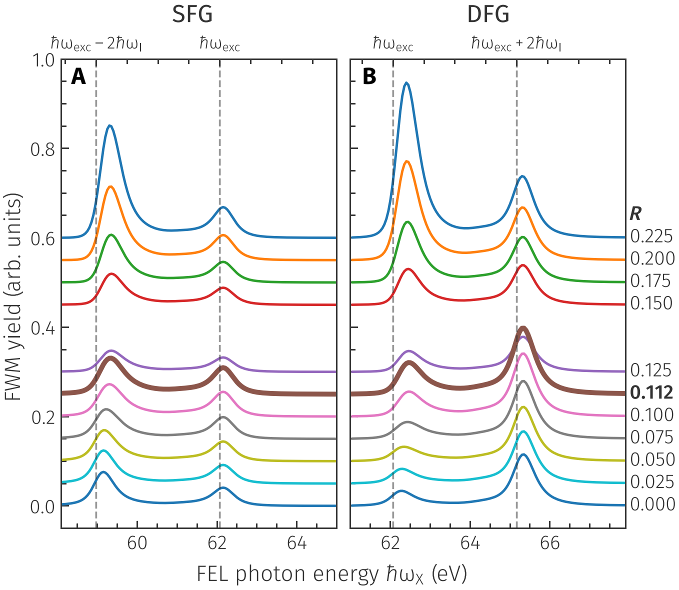

Fig. 5. Calculated frequency conversion efficiencies. Sum- (**A**) and difference-frequency mixing (**B**) yields calculated for the beams emitted from the LiF sample toward the vacuum side (reflection geometry; see Fig. 2). Shown are the dependencies of the efficiencies on the photon energy $\hbar\omega_X$ of the incident FEL radiation when scanned over the LiF p-type core exciton at $\hbar\omega_{exc} = 62.07$ eV for a set of values of the parameter R starting at zero up to $R = 0.225$. R quantifies the dipole coupling strength of the LiF p-type to the s-type core exciton, the latter being separated in energy from the former by 1.1 eV, i.e., somewhat less than one NIR photon energy $\hbar\omega_I = 1.55$ eV. For comparison purposes, the conversion efficiency scales in (A) and (B) are chosen to be identical. Compared to the lower group of curves, the calculated efficiencies for the upper group have been scaled by a factor of 0.5. In both panels, we highlighted the efficiency curves for $R = 0.112$, which most closely reproduce the conversion yield structures found in the experiment (thick brown lines; see also Fig. 3C).

in one-photon ($\omega_X \approx \omega_{exc}$) or three-photon ($\omega_X \pm 2\omega_I \approx \omega_{exc}$) resonance with the p-type core exciton. The slight offset of the frequency conversion maxima toward a higher FEL photon energy as compared with the p-type exciton position ($\omega_{exc} = 62.07$ eV, table S1 and indicated by vertical lines in Fig. 5) can be attributed to the strong variation of the linear dielectric constant over the p-type exciton (fig. S2) accompanied by strong absorption of either the driving or generated radiation on resonance. For DFG, a shifting of the conversion maximum at $\omega_X \approx \omega_{exc}$ toward a higher FEL photon energy is predicted with increasing R (Fig. 5B), whereas the maximum at $\omega_X \approx \omega_{exc} + 2\omega_I$ does not shift. Moreover, the conversion efficiency peak at $\omega_X \approx \omega_{exc}$ gains strongly in amplitude with rising R. The underlying reason is a rising contribution of two-photon resonance with the s-type exciton relative to one–XUV photon resonance ($\omega_X \approx \omega_{exc}$) with the p-type exciton. Two-photon resonance with the s-type exciton would occur at $\omega_X = 62.52$ eV, compared to one–XUV photon resonance with the p-type exciton at $\omega_X = 62.07$ eV. A rising value of R represents a stronger coupling between s- and p-type core excitations. Thus, the rising conversion efficiency and shift are a consequence of the s-type exciton providing an intermediate two-photon resonance in the three-photon DFG process, as the 1.55-eV NIR photons are not far off resonance with the energy difference of 1.1 eV between s- and p-type excitons. In contrast, at three-photon resonance with the p-type exciton ($\omega_X \approx \omega_{exc} + 2\omega_I$), the frequency difference $\omega_X - \omega_I$ is well off the two-photon resonance with the s-type exciton. This results in a negligible effect of two-photon resonance on the corresponding difference-frequency conversion yield and on the position of the yield maximum.

A similar interpretation holds for the changes observable in the sum-frequency conversion yield with rising values of the parameter R in Fig. 5A. However, in this case, the conversion yield maximum at $\omega_X \approx \omega_{exc} - 2\omega_I$, originating from three-photon resonance with the p-type exciton, is affected by two-photon resonance with the s-type exciton, whereas the $\omega_X \approx \omega_{exc}$ conversion maximum, representing one–XUV photon resonance with the p-type exciton, is not. Combined, the model particularly predicts the difference-frequency conversion yield maximum at $\omega_X \approx \omega_{exc}$ appearing at a slightly higher FEL photon energy than the corresponding sum-frequency yield maximum and links it to the NIR photons being able to cause a coupling between s- and p-type excitons for $R > 0$.

Comparing the outcome of our model (Fig. 5) with the resonance structure observed in the experiment leads to an estimated R of approximately 0.112 when basing the comparison on the relative strengths of the frequency conversion yield maxima. For the purpose of direct comparison with the experiment, we show this calculated result in Fig. 3C for both SFG and DFG. To illustrate the precision of this estimate, a transition moment ratio of $R = 0.225$ changes the resonance behavior of the frequency conversion processes completely in a way that is significantly different from the experimental result. Similarly, $R = 0$ is not compatible with the experiment. In the model, $R \approx 0.112$ already results in a clear offset of the calculated difference-frequency conversion yield maximum at $\omega_X \approx \omega_{exc}$ to a higher FEL photon energy as compared to the corresponding sum-frequency yield maximum (Fig. 3C). A hint at such a shift can also be found in the experimental data in Fig. 3B at $\omega_X \approx \omega_{exc} \approx 62$ eV.

Within the limitations of our simple $\chi^{(3)}$ model, we are able to understand the experimental observations quantitatively, particularly the energy positions and relative yields of the FWM processes in LiF when in resonance with Li^+ 1s core excitations, including the significance of a dipole coupling of the p-type to the s-type exciton in the nonlinear response. The model calculation reproduces the significant sum- and difference-frequency conversion yield when close to one- and three-photon resonance with the p-type core exciton. While being in resonance with the p-type exciton is key for efficient frequency mixing, a two-photon resonance with the s-type exciton does affect the frequency conversion because a close to one-photon resonant, dipole allowed, coupling of the s- and p-type core excitons is present, mediated by the NIR laser pulses. Thus, our findings further corroborate the assignment of the low-energy shoulder of the linear reflection maximum observable at 61 eV in Fig. 1B due to an s-type exciton (*15*, *18*).

For NaCl, the observation of a complementary FWM process has recently been reported in a purely laser-based experiment, involving excitons related to the excited Na^+ 3s state with a hole in its closed 2p shell (*13*). This experiment revealed the presence of dark excited states that appear only in nonlinear spectroscopy besides bright excitonic excitations observable in linear absorption. A potential coherent lifetime of the nonlinear polarization induced in LiF as it was reported for NaCl on a time scale of 10 fs in (*13*) is too short to be detectable with our present temporal resolution. With recent advances of pushing x-ray–optical relative pulse jitter at FELs to below 25 fs (*24*) and the availability of both x-ray and optical pulses in the few femtoseconds or even attosecond domain (*25*, *26*), we expect that such information for processes involving core excitations may also become accessible by our FEL-based approach and extendable to suitable resonances in the multi–kilo–electron volt photon energy range.

From an experimental point of view, we note that the third-order nonlinear process studied in this work, i.e., SFG and DFG, allows for easy spectroscopic discrimination of the nonlinear signal from the incident XUV or x-ray radiation, which is particularly important when mixing harder x-rays with laser pulses in the optical spectral range due to the challenge posed by an increasingly small angular separation. Furthermore, we note that the observation of a nonlinear process in reflection from a solid sample–vacuum interface is convenient in particular in the XUV spectral range (*27*, *28*), because, due to strong absorption, only very thin samples can typically be used to detect the generated radiation propagating through the nonlinear medium, e.g., a sample of 50-nm thickness was used in (*13*). We expect both these aspects as demonstrated here to be of relevance for the application of nonlinear x-ray spectroscopy in materials science, where tailoring the samples under study to experiments is only viable to a limited extent. Nevertheless, detecting transmitted radiation may be advantageous in selected cases where phase matching ($k_z - \widetilde{k}_z = 0$ in eq. S11) can be exploited, provided that the propagation lengths of the FEL and optical and generated radiation in the sample can be made long enough before efficient absorption limiting the detectable signal. At interfaces of centrosymmetric crystals to vacuum or to other materials, a loss of inversion symmetry is commonly used to obtain surface or interface sensitivity via observation of second harmonic generation in the optical regime. As we have demonstrated, third-order nonlinear signals can now be detected in one- and three-photon resonance with specific inner shell excitations. Looking ahead, the combination of second- and third-order nonlinear frequency conversion involving x-rays will allow one to differentiate between bulk- and surface-specific contributions to the nonlinear polarization of a material.

Our work demonstrates that FWM under resonant conditions is a sensitive probe of charge localization, allowing for atomic specificity even when using wavelengths substantially larger than the unit cell of the system of interest. While scalable to hard x-rays, we note that even when carried out with soft x-rays, our approach can complement the atomic scale information on the valence charge distribution obtainable with wavelengths comparable to the interatomic spacing (*4*) and mesoscale information with a length scale defined by a transient grating period (*7*–*9*). Nonlinear spectroscopy with few-femtosecond x-rays gives access to otherwise forbidden, dark transitions and hence information beyond the linear spectroscopy dominating current x-ray spectroscopy. We note that our approach of exploiting core-hole resonances differs from some studies based on nonresonant hard x-ray wave mixing (*29*–*31*): The nonresonant methods can be understood as a wave mixing probe, which is scattering from an electronic system that was modified by one or more optical pump pulses. In contrast, our approach probes the coupling between core-excited states following an x-ray pump. As core holes are generally strongly localized, we gain selective spectroscopic information on optically "dark" states local to targeted sites in the probed system. We did not observe nonresonant wave mixing because LiF in its ground state is transparent for the 1.55-eV NIR pulses due to its large bandgap. The charge density remained mostly unperturbed by the optical laser alone. With the dynamics of transient localization and delocalization of charge at different atomic species being of fundamental importance for a multitude of processes not only in physics, chemistry, and biology but also in materials design, e.g., for light harvesting applications, we expect wave mixing processes in resonance with inner shell excitations to become a particularly fruitful approach for future time domain studies at FELs.

MATERIALS AND METHODS

Experiment

The experiment was carried out on the beamline FL24 of the FLASH2 FEL using the MUSIX (multidimensional spectroscopy and inelastic x-ray scattering) end station (*32*). A schematic view of the setup is shown in Fig. 2. The FEL delivered pulses in bunch trains with 40 laser pulses per train at a train repetition rate of 10 Hz. The pulse separation within each train was 10 μs, i.e., a pulse repetition rate of 100 kHz. The FEL beam was attenuated using a gas attenuator filled with 1.1×10^{-2} mbar of neon and a silicon attenuator foil of 411-nm thickness. The beam path was constrained by five beam diameters limiting irises: the first three with a diameter of 7.5 mm, and the latter two with a diameter of 10.0 and 10.5 mm, respectively. A focusing Kirkpatrick-Baez active optics system (KAOS) was used to focus the beam on the LiF sample (*33*). The spot size on the LiF crystal is estimated to be 150 μm FWHM in diameter as gauged with an yttrium aluminum garnet (YAG) scintillation screen. While the duration of the FEL pulses was not measured during the experiment, it was tuned to be less than 100 fs. The spectral bandwidth of the FEL pulses was determined from the measurements used for spectrometer calibration and varied between 0.5 and 0.6 eV, depending on photon energy. The angle of incidence of the beam on the LiF sample with respect to its surface normal was 52°. The energy of individual FEL pulses on the sample was (130 ± 25) nJ. This energy and the corresponding number of photons impinging on the LiF sample per pulse were determined by using an x-ray gas monitor detector upstream of the FEL beam and multiplying these data by an estimated beamline transmission up to the sample (*34*). The Supplementary Materials provides further details on the transmission estimates of the beamline.

The optical laser system was based on optical parametric chirped pulse amplification (OPCPA) synchronized to the FEL pulses and operated at a fixed photon energy of 1.55 eV. It delivered pulse trains identical in structure to those of the FEL with pulses of 21 fs in width (FWHM). The NIR laser beam was focused on the LiF sample using a lens pair with −250- and 750-mm focal lengths, respectively. After passing through a λ/2-wave plate and polarizer for adjusting the pulse energy and a second half-wave plate for turning its polarization, the linearly polarized NIR beam was aligned nearly collinear with the FEL beam path by reflecting it off a flat 90° silver-coated turning mirror that passed the FEL beam through a center hole (5-mm diameter). Thereby, the NIR laser beam enclosed a small angle of (0.75 ± 0.03)° with the FEL beam, propagating in the plane of incidence spanned by the FEL beam and the LiF surface normal, which coincided with one of the LiF crystal axes. This plane of incidence is assumed to be spanned by the x and z axes of a suitably chosen coordinate system as shown in Fig. 2. The two LiF crystal axes in the interface plane to vacuum, i.e., the two red axes in Fig. 2, enclosed an angle of (22.5 ± 2.5)° with the x and y axes of this coordinate system, respectively. The polarization vectors of the FEL and NIR pulses were located in the plane of incidence. The NIR laser pulse energy on the LiF target was (68.0 ± 1.5) μJ with the spots of the FEL and NIR beams spatially overlapping.

The LiF sample was a single, (100) cut crystal with the crystal surface polished. With a thickness of 3 mm, it was transparent to the NIR laser beam, whereas the FEL beam was practically absorbed within ≈100 nm into the crystal, thus limiting the SFG and DFG to a narrow stretch below the crystal surface. The NIR, FEL, and generated sum- and difference-frequency beams reflected off the LiF sample were dispersed by a reflection grating and directed to a CCD camera positioned behind an aluminum filter (200-nm thickness), which not only blocked the NIR beam and stray light but also inhibited the detection of FWM signals beyond the aluminum *K*-edge at 72.7 eV. The specular reflection of the FEL beam was blocked by a narrow beam stop placed directly in front of the CCD camera (see Fig. 2).

The dispersion grating with spherical shape and varied line spacing was used to separate the FEL radiation from the generated sum- and difference-frequency radiation (*32*). It was operated at grazing incidence (2.1° grazing angle) and imaged the radiation spectrum onto the CCD camera. Because of the large radius of curvature of the grating (≈13.9 m), it had little influence on the divergence of the sum- and difference-frequency beams on their way from the LiF sample to the camera along the direction orthogonal to the dispersion direction of the grating. The length of the spectrometer setup, i.e., the separation of the LiF sample from the camera via the grating, was 1.33 m.

The back-illuminated CCD camera (Greateyes model GE-VAC 2048 2048) used to detect the XUV radiation was mounted in the vacuum chamber (*32*). Its detector consisted of 2048 by 2048 square pixels of 13.5 μm in size (*32*). For the experiment, 4 detector pixels were binned along the direction of dispersion of the spectrometer grating and 64 along the orthogonal direction to optimize the camera sensitivity. To speed up the readout rate, only 11 binned pixels perpendicular to the dispersion direction of the grating were read out. Thus, each stored camera image consisted of 512 × 11 image points. The detector accumulated the light of individual pulse trains, i.e., of 40 laser pulses before being read out. Limited by the detector readout speed, a frame rate of 5 Hz was achieved, meaning that the sum- and difference-frequency light generated by every second FEL pulse train was captured.

In the experimental runs, the FEL photon energy was tuned in steps in the range between approximately 58 and 72 eV. The FWM yields shown in Fig. 3 (A and B) were measured over the course of about 100 hours with individual datasets recorded for about 30 to 60 min on each single spot on the LiF sample at each FEL photon energy setting as a precaution against potential sample damage. We did, however, not observe systematic changes to the FWM yield measured in the first and last minutes of measurement on a given spot. At each energy setting, the delay between the XUV and NIR pulses was scanned within a 1- to 2-ps interval around the time overlap. This allowed to account for slow drifting of the XUV pulses' arrival time relative to that of the NIR pulses, which would have affected the FWM efficiency. The CCD camera recorded the radiation generated by FWM spectrally dispersed by the spectrometer grating. The recorded spectra were scaled to estimate the absolute number of photons actually generated by FWM in the LiF sample (see the Supplementary Materials for details). Fluctuations in optical stray light, generating a varying offset to each spectrum, were compensated by subtracting the average signal recorded in the FEL beam block shadow from each spectrum. Intensity fluctuations in the FEL beam were mitigated by normalizing the spectra such that the FEL stray light level of each spectrum equals the ensemble average. From these spectral distributions, a mean stray light spectrum was determined by averaging overall spectra recorded at FEL-NIR pulse delays larger than ±250 fs, leaving only the FWM signal together with a small, however fluctuating, residual background level. These spectra were then sorted by the XUV-NIR delay into delay-time bins of 25 fs with an average FWM spectrum computed for each bin. The result is a two-dimensional map of the FWM signal over the XUV-NIR delay and the energy distribution of the spectrally dispersed generated photons, as shown in Fig. 4D. While the average spectrum was calculated by the simple mean for each photon energy, an estimate of the uncertainty of this mean was computed as the SD of the averaged photon yields divided by the square root of the number of spectra in the respective bin, resulting in spectra such as shown in Fig. 4B for each delay bin. To derive the FWM yield shown in Fig. 3B, these delay-dependent spectra were integrated within ±500 meV of the expected photon energy of the FWM signal to form a delay trace as shown in Fig. 4C, which was then fitted by a Gaussian using the Levenberg-Marquardt algorithm. This fit was weighed with the inverse square uncertainty of the spectra. The maximum of this Gaussian represents the FWM yield at time overlap that is depicted in Fig. 3B. The error bars are derived from the fit and represent the SD of the fit result. Conversely, the FWM yield shown as a spectrally resolved colormap in Fig. 3A is an integration of FWM yields measured within ±250 fs of the expected time overlap.

The linear reflection of LiF shown in Fig. 1B was measured separately at the PM3 beamline of the BESSY II facility (*35*) using tunable synchrotron radiation linearly polarized in the plane of incidence of the beam. The angle of incidence on the LiF single crystal was 50° with respect to the surface normal of the sample.

Theoretical modeling of third-order FWM

The nonlinear reflection off a medium with a plane boundary to vacuum in the *xy* plane of a suitably chosen coordinate system (see Fig. 2) is connected with the generated electric field on the vacuum side. In the monochromatic, plane wave limit, this electric field can be represented by

$$\mathbf{E}_r = \mathbf{A}_r \exp\,(i\,\mathbf{k}_r\mathbf{x} - i\omega t) \tag{1}$$

where $\mathbf{A}_r$ is the amplitude and $\mathbf{k}_r = (k_x, 0, k_{rz})$ is the wave vector on the vacuum side ($k_{rz} > 0$) satisfying the dispersion relation $\mathbf{k}_r^2 = k_x^2 + k_{\mathrm{rz}}^2 = (\omega/c)^2$ (c, the speed of light). The amplitude $\mathbf{A}_r$ can be found to be (for the derivation, see the Supplementary Materials)

$$\boldsymbol{A}_r = \frac{4\pi}{\tilde{k}_z + k_z}\left(\frac{(\tilde{k}_z P_x + k_x P_z)}{\tilde{k}_z - \epsilon\, k_{rz}}\begin{bmatrix} k_{rz} \\ 0 \\ -k_x \end{bmatrix} - \left(\frac{\omega}{c}\right)^2 \frac{P_y}{\tilde{k}_z - k_{rz}}\begin{bmatrix} 0 \\ 1 \\ 0 \end{bmatrix}\right) \tag{2}$$

This expression presumes a monochromatic, plane nonlinear polarization wave $\mathbf{P}\exp\,(i\mathbf{k}\mathbf{x} - i\omega t)$ propagating into the medium that is assumed to be located in the half-space $z < 0$ with frequency ω and wave vector $\mathbf{k} = (k_x, 0, k_z)$ chosen to be located in the *xz* plane (see Fig. 2). The real and the imaginary parts of k_z are negative numbers, representing propagation of the nonlinear polarization into the medium and absorption of the fields driving it. $\tilde{\mathbf{k}} = (k_x, 0, \tilde{k}_z)$ in Eq. 2 is the wave vector of the generated electric field at frequency ω propagating in the nonlinear medium. It satisfies the dispersion relation $\tilde{\mathbf{k}}^2 = k_x^2 + \tilde{k}_z^2 = (\omega/c)^2 \epsilon(\omega)$, where $\epsilon(\omega)$ is the dielectric constant of the medium at the frequency ω of the generated field. In the medium, it propagates with the nonlinear polarization and experiences linear absorption, meaning that the real and the imaginary parts of $\tilde{k}_z$ are negative numbers. k_x—the wave number component in the plane of the surface of the nonlinear medium, which appears in the expressions for $\mathbf{k}_r$, $\mathbf{k}$, and $\tilde{\mathbf{k}}$—is a real number and is fixed by boundary conditions for the FEL and NIR fields, which drive the nonlinear polarization, at the interface of the medium with vacuum.

The components of the wave vector $\mathbf{k}$ of the nonlinear polarization wave and its frequency ω are fixed by the frequencies and wave vectors of the fields driving the nonlinear polarization and by the specific nonlinear process, i.e., in our case, third-order sum- and difference-frequency mixing, respectively. Provided that ω_X, $\mathbf{k}_X$ and ω_I, $\mathbf{k}_I$ are the frequencies and wave vectors of the driving FEL and NIR laser fields in the medium, respectively, ω and $\mathbf{k}$ are defined as

$$\omega = \omega_X \pm 2\omega_I$$

$$\mathbf{k} = \mathbf{k}_X \pm 2\mathbf{k}_I$$

This assumes that one FEL photon and two NIR photons are involved in the mixing process as was the case in the experiment.

The amplitude $\mathbf{P}$ of the nonlinear polarization wave in Eq. 2 is set by the third-order nonlinear susceptibility tensor $\chi^{(3)}$ of LiF governing the experimentally studied SFG and DFG. For the cubic LiF crystal structure, only few of the Cartesian components of $\chi^{(3)}$ are different from zero and independent of each other (*36*). In a coordinate system aligned with the crystal axes, a set of independent nonzero components is $\chi^{(3)}_{xxxx}, \chi^{(3)}_{xyyx}, \chi^{(3)}_{xyxy}, \chi^{(3)}_{xxyy}$. We use atomic transition matrix elements among Li^+ states for the purpose of a basic approximation of $\chi^{(3)}$. Therefore, full rotational symmetry prevails for the tensor elements, not just cubic symmetry. This adds an additional constraint to the tensor components, namely, $\chi^{(3)}_{xxxx} = \chi^{(3)}_{xyyx} + \chi^{(3)}_{xyxy} + \chi^{(3)}_{xxyy}$ (*36*). This extended model symmetry and the fact that the LiF dielectric constant is a scalar quantity also mean that the Cartesian coordinate system tied to the experimental plane of incidence in Fig. 2 is equivalent to the coordinate system spanned by the cubic crystal axes. Then, independent of the direction of polarization of the NIR laser beam, the nonlinear polarization component P_y in Eq. 2 is equal to zero, meaning that the field generated is always polarized in the plane of incidence.

The p-type core exciton of LiF at 62.07 eV observed in linear absorption spectra has been attributed to derive from Li^+ dipole allowed transitions from the $(1s)^2$ ground state to excited states (1s2p, $m_l = 0, \pm 1$). A second, much smaller resonance structure on the low-energy side of this p-type resonance has been tentatively associated with a $(1s)^2 - (1s2s)$ Li^+ transition (s-type exciton), not dipole allowed in the free ion (*15*, *17*). A potentially sizable dipole allowed transition matrix element between the (1s2p, $m_l = 0, \pm 1$) and (1s2s) states may, however, influence the third-order nonlinear susceptibility $\chi^{(3)}$ substantially. We thus model $\chi^{(3)}$ of the LiF crystal using just these Li^+ ionic states, ignoring any potential contribution of conduction band states. Our simple model is intended to qualitatively represent the experimentally observed dependence of the reflected sum- and difference-frequency yields on the FEL photon energy (Fig. 3B). Thus, only the ratio of the dipole matrix elements for the Li^+ transitions (1s2s) − (1s2p, $m_l = 0, \pm 1$) and $(1s)^2$ − (1s2p, $m_l = 0, \pm 1$) will be relevant for the characterization of $\chi^{(3)}$. Moreover, we will retain the full atomic rotational symmetry for the dipole matrix elements, ignoring crystal field effects. This reduces the number of adjustable parameters in an expression for $\chi^{(3)}$ to the ratio R of the radial parts of these dipole matrix elements. The excitation energies of the p- and s-type core excitons and their widths, assumed to be homogeneous widths, are extracted from the linear reflection data in Fig. 1B. The data used to determine the components of the third-order nonlinear susceptibility are summarized in the Supplementary Materials, and the expression used for our model nonlinear susceptibility is taken from page 93 of (*36*).

A more sophisticated theoretical treatment of the third-order nonlinear susceptibility tensor of LiF in this photon energy range is beyond the scope of this work. It will have to consider a potential influence of conduction band states, account for the excitonic structure more precisely, and take into account the lower cubic crystal symmetry that we replaced by full rotational symmetry in our model. We note that the lower symmetry may have an influence on the relative strengths of the frequency conversion yields, because, in that case, the angle enclosed by the plane of incidence of the laser beams with the LiF crystal axes in the surface plane of the crystal matters (see the Supplementary Materials). Also, we have used a monochromatic approach, whereas the laser pulses have a short pulse duration and possibly a substantial phase modulation accompanied by a corresponding spectral bandwidth that is of the order of the widths of the relevant LiF resonance structures.

SUPPLEMENTARY MATERIALS

Supplementary material for this article is available at https://science.org/doi/10.1126/sciadv.abn5127

REFERENCES AND NOTES

1. H. Danino, I. Freund, Parametric down conversion of x rays into the extreme ultraviolet. *Phys. Rev. Lett.* **46**, 1127–1130 (1981).
2. K. Tamasaku, K. Sawada, E. Nishibori, T. Ishikawa, Visualizing the local optical response to extreme-ultraviolet radiation with a resolution of λ/380. *Nat. Phys.* **7**, 705–708 (2011).
3. A. Schori, C. Bömer, D. Borodin, S. P. Collins, B. Detlefs, M. Moretti Sala, S. Yudovich, S. Shwartz, Parametric down-conversion of x rays into the optical regime. *Phys. Rev. Lett.* **119**, 253902 (2017).
4. T. E. Glover, D. M. Fritz, M. Cammarata, T. K. Allison, S. Coh, J. M. Feldkamp, H. Lemke, D. Zhu, Y. Feng, R. N. Coffee, M. Fuchs, S. Ghimire, J. Chen, S. Shwartz, D. A. Reis, S. E. Harris, J. B. Hastings, X-ray and optical wave mixing. *Nature* **488**, 603–608 (2012).
5. S. Shwartz, M. Fuchs, J. B. Hastings, Y. Inubushi, T. Ishikawa, T. Katayama, D. A. Reis, T. Sato, K. Tono, M. Yabashi, S. Yudovich, S. E. Harris, X-ray second harmonic generation. *Phys. Rev. Lett.* **112**, 163901 (2014).
6. R. K. Lam, S. L. Raj, T. A. Pascal, C. D. Pemmaraju, L. Foglia, A. Simoncig, N. Fabris, P. Miotti, C. J. Hull, A. M. Rizzuto, J. W. Smith, R. Mincigrucci, C. Masciovecchio, A. Gessini, E. Allaria, G. De Ninno, B. Diviacco, E. Roussel, S. Spampinati, G. Penco, S. Di Mitri, M. Trovò, M. Danailov, S. T. Christensen, D. Sokaras, T.-C. Weng, M. Coreno, L. Poletto, W. S. Drisdell, D. Prendergast, L. Giannessi, E. Principi, D. Nordlund, R. J. Saykally, C. P. Schwartz, Soft x-ray second harmonic generation as an interfacial probe. *Phys. Rev. Lett.* **120**, 023901 (2018).
7. F. Bencivenga, R. Cucini, F. Capotondi, A. Battistoni, R. Mincigrucci, E. Giangrisostomi, A. Gessini, M. Manfredda, I. P. Nikolov, E. Pedersoli, E. Principi, C. Svetina, P. Parisse, F. Casolari, M. B. Danailov, M. Kiskinova, C. Masciovecchio, Four-wave mixing experiments with extreme ultraviolet transient gratings. *Nature* **520**, 205–208 (2015).
8. L. Foglia, F. Capotondi, R. Mincigrucci, D. Naumenko, E. Pedersoli, A. Simoncig, G. Kurdi, A. Calvi, M. Manfredda, L. Raimondi, N. Mahne, M. Zangrando, C. Masciovecchio, F. Bencivenga, First evidence of purely extreme-ultraviolet four-wave mixing. *Phys. Rev. Lett.* **120**, 263901 (2018).
9. F. Bencivenga, R. Mincigrucci, F. Capotondi, L. Foglia, D. Naumenko, A. A. Maznev, E. Pedersoli, A. Simoncig, F. Caporaletti, V. Chiloyan, R. Cucini, F. Dallari, R. A. Duncan, T. D. Frazer, G. Gaio, A. Gessini, L. Giannessi, S. Huberman, H. Kapteyn, J. Knobloch,

G. Kurdi, N. Mahne, M. Manfredda, A. Martinelli, M. Murnane, E. Principi, L. Raimondi, S. Spampinati, C. Spezzani, M. Trovò, M. Zangrando, G. Chen, G. Monaco, K. A. Nelson, C. Masciovecchio, Nanoscale transient gratings excited and probed by extreme ultraviolet femtosecond pulses. *Sci. Adv.* **5**, eaaw5805 (2019).

10. E. Shwartz, S. Shwartz, Difference-frequency generation of optical radiation from two-color x-ray pulses. *Opt. Express* **23**, 7471–7480 (2015).
11. C. P. Schwartz, S. L. Raj, S. Jamnuch, C. J. Hull, P. Miotti, R. K. Lam, D. Nordlund, C. B. Uzundal, C. Das Pemmaraju, R. Mincigrucci, L. Foglia, A. Simoncig, M. Coreno, C. Masciovecchio, L. Giannessi, L. Poletto, E. Principi, M. Zuerch, T. A. Pascal, W. S. Drisdell, R. J. Saykally, Angstrom-resolved interfacial structure in buried organic-inorganic junctions. *Phys. Rev. Lett.* **127**, 096801 (2021).
12. J. R. Rouxel, D. Fainozzi, R. Mankowsky, B. Rösner, G. Seniutinas, R. Mincigrucci, S. Catalini, L. Foglia, R. Cucini, F. Döring, A. Kubec, F. Koch, F. Bencivenga, A. A. Haddad, A. Gessini, A. A. Maznev, C. Cirelli, S. Gerber, B. Pedrini, G. F. Mancini, E. Razzoli, M. Burian, H. Ueda, G. Pamfilidis, E. Ferrari, Y. Deng, A. Mozzanica, P. J. M. Johnson, D. Ozerov, M. G. Izzo, C. Bottari, C. Arrell, E. J. Divall, S. Zerdane, M. Sander, G. Knopp, P. Beaud, H. T. Lemke, C. J. Milne, C. David, R. Torre, M. Chergui, K. A. Nelson, C. Masciovecchio, U. Staub, L. Patthey, C. Svetina, Hard x-ray transient grating spectroscopy on bismuth germanate. *Nat. Photonics* **15**, 499–503 (2021).
13. J. D. Gaynor, A. P. Fidler, Y.-C. Lin, H.-T. Chang, M. Zuerch, D. M. Neumark, S. R. Leone, Solid state core-exciton dynamics in NaCl observed by tabletop attosecond four-wave mixing spectroscopy. *Phys. Rev. B* **103**, 245140 (2021).
14. R. Haensel, C. Kunz, B. Sonntag, Measurement of photoabsorption of the lithium halides near the lithium *K* edge. *Phys. Rev. Lett.* **20**, 262–264 (1968).
15. W. Olovsson, I. Tanaka, P. Puschnig, C. Ambrosch-Draxl, Near-edge structures from first principles all-electron Bethe-Salpeter equation calculations. *J. Phys. Condens. Matter* **21**, 104205 (2009).
16. S. T. Pantelides, Electronic excitation energies and the soft-x-ray absorption spectra of alkali halides. *Phys. Rev. B* **11**, 2391–2411 (1975).
17. J. R. Fields, P. C. Gibbons, S. E. Schnatterly, Electronic excitations in LiF: 10-70 eV. *Phys. Rev. Lett.* **38**, 430–434 (1977).
18. E. L. Shirley, Li 1s near-edge spectra in six lithium halides. *J. Electron Spectros. Relat. Phenomena* **137-140**, 579–584 (2004).
19. W. Olovsson, I. Tanaka, T. Mizoguchi, P. Puschnig, C. Ambrosch-Draxl, All-electron Bethe-Salpeter calculations for shallow-core x-ray absorption near-edge structures. *Phys. Rev. B* **79**, 041102 (2009).
20. A. B. Kunz, J. C. Boisvert, T. O. Woodruff, Li *K*-edge soft-x-ray absorption in LiF. *Phys. Rev. B* **30**, 2158–2162 (1984).
21. A. B. Kunz, J. T. Devreese, T. Collins, The role of the electronic polaron in the soft X-ray absorption of the lithium halides. *J. Phys. C Solid State Phys.* **5**, 3259–3263 (1972).
22. B. F. Sonntag, Observations of "forbidden" soft-x-ray transitions: Li *K* absorption in LiF. *Phys. Rev. B* **9**, 3601–3602 (1974).
23. W. Gudat, C. Kunz, H. Petersen, Core exciton and band structure in LiF. *Phys. Rev. Lett.* **32**, 1370–1373 (1974).
24. T. Sato, R. Letrun, H. J. Kirkwood, J. Liu, P. Vagovič, G. Mills, Y. Kim, C. M. S. Takem, M. Planas, M. Emons, T. Jezynski, G. Palmer, M. Lederer, S. Schulz, J. Mueller, H. Schlarb, A. Silenzi, G. Giovanetti, A. Parenti, M. Bergemann, T. Michelat, J. Szuba, J. Grünert, H. N. Chapman, A. P. Mancuso, Femtosecond timing synchronization at megahertz repetition rates for an X-ray free-electron laser. *Optica* **7**, 716 (2020).
25. S. Schulz, I. Grguraš, C. Behrens, H. Bromberger, J. T. Costello, M. K. Czwalinna, M. Felber, M. C. Hoffmann, M. Ilchen, H. Y. Liu, T. Mazza, M. Meyer, S. Pfeiffer, P. Prędki, S. Schefer, C. Schmidt, U. Wegner, H. Schlarb, A. L. Cavalieri, Femtosecond all-optical synchronization of an X-ray free-electron laser. *Nat. Commun.* **6**, 5938 (2015).
26. J. Duris, S. Li, T. Driver, E. G. Champenois, J. P. MacArthur, A. A. Lutman, Z. Zhang, P. Rosenberger, J. W. Aldrich, R. Coffee, G. Coslovich, F.-J. Decker, J. M. Glownia, G. Hartmann, W. Helml, A. Kamalov, J. Knurr, J. Krzywinski, M.-F. Lin, J. P. Marangos, M. Nantel, A. Natan, J. T. O'Neal, N. Shivaram, P. Walter, A. L. Wang, J. J. Welch, T. J. A. Wolf, J. Z. Xu, M. F. Kling, P. H. Bucksbaum, A. Zholents, Z. Huang, J. P. Cryan, A. Marinelli, Tunable isolated attosecond X-ray pulses with gigawatt peak power from a free-electron laser. *Nat. Photonics* **14**, 30–36 (2020).
27. A. A. Maznev, R. Mincigrucci, F. Bencivenga, V. Unikandanunni, F. Capotondi, G. Chen, Z. Ding, R. A. Duncan, L. Foglia, M. G. Izzo, C. Masciovecchio, A. Martinelli, G. Monaco, E. Pedersoli, S. Bonetti, K. A. Nelson, Generation and detection of 50 GHz surface acoustic waves by extreme ultraviolet pulses. *Appl. Phys. Lett.* **119**, 044102 (2021).
28. E. Berger, S. Jamnuch, C. B. Uzundal, C. Woodahl, H. Padmanabhan, A. Amado, P. Manset, Y. Hirata, Y. Kubota, S. Owada, K. Tono, M. Yabashi, C. Wang, Y. Shi, V. Gopalan, C. P. Schwartz, W. S. Drisdell, I. Matsuda, J. W. Freeland, T. A. Pascal, M. Zuerch, Extreme ultraviolet second harmonic generation spectroscopy in a polar metal. *Nano Lett.* **21**, 6095–6101 (2021).
29. D. Popova-Gorelova, D. A. Reis, R. Santra, Theory of X-ray scattering from laser-driven electronic systems. *Phys. Rev. B* **98**, 224302 (2018).
30. R. Cohen, S. Shwartz, Theory of nonlinear interactions between x rays and optical radiation in crystals. *Phys. Rev. Res.* **1**, 033133 (2019).
31. J. R. Rouxel, M. Kowalewski, K. Bennett, S. Mukamel, X-ray sum frequency diffraction for direct imaging of ultrafast electron dynamics. *Phys. Rev. Lett.* **120**, 243902 (2018).
32. M. Beye, R. Y. Engel, J. O. Schunck, S. Dziarzhytski, G. Brenner, P. S. Miedema, Non-linear soft x-ray methods on solids with MUSIX–the multi-dimensional spectroscopy and inelastic X-ray scattering endstation. *J. Phys. Condens. Matter* **31**, 014003 (2019).
33. L. Raimondi, C. Svetina, N. Mahne, D. Cocco, A. Abrami, M. De Marco, C. Fava, S. Gerusina, R. Gobessi, F. Capotondi, E. Pedersoli, M. Kiskinova, G. De Ninno, P. Zeitoun, G. Dovillaire, G. Lambert, W. Boutu, H. Merdji, A. Gonzalez, D. Gauthier, M. Zangrando, Microfocusing of the FERMI@Elettra FEL beam with a K–B active optics system: Spot size predictions by application of the WISE code. *Nucl. Instrum. Methods Phys. Res. Sect. A Accel. Spectrometers Detect. Assoc. Equip.* **710**, 131–138 (2013).
34. A. A. Sorokin, Y. Bican, S. Bonfigt, M. Brachmanski, M. Braune, U. F. Jastrow, A. Gottwald, H. Kaser, M. Richter, K. Tiedtke, An X-ray gas monitor for free-electron lasers. *J. Synchrotron Radiat.* **26**, 1092–1100 (2019).
35. T. Kachel, The PM3 beamline at BESSY II. *J. large-scale Res. Facil. JLSRF* **2**, A48 (2016).
36. P. N. Butcher, D. Cotter, *The Elements of Nonlinear Optics* (Cambridge Univ. Press, 1990).
37. A. Milgram, M. P. Givens, Extreme ultraviolet absorption by lithium fluoride. *Phys. Rev.* **125**, 1506–1509 (1962).
38. J. D. Jackson, *Classical Electrodynamics* (John Wiley & Sons Inc., ed. 3, 1998).
39. M. Braune, J. Buck, M. Kuhlmann, S. Grunewald, S. Düsterer, J. Viefhaus, K. Tiedtke, Non-invasive online wavelength measurements at FLASH2 and present benchmark. *J. Synchrotron Radiat.* **25**, 3–15 (2018).
40. B. L. Henke, E. M. Gullikson, J. C. Davis, *X-Ray Interactions With Matter* (U.S. Department of Energy, 1993).
41. B. Henke, E. Gullikson, J. Davis, X-ray interactions: Photoabsorption, scattering, transmission, and reflection at E = 50-30,000 eV, Z = 1-92. *At. Data Nucl. Data Tables* **54**, 181–342 (1993).

Acknowledgments: We acknowledge DESY (Hamburg, Germany), a member of the Helmholtz Association HGF, for the provision of experimental facilities. Parts of this research were carried out at FLASH, beamline FL24, using the MUSIX end station. Beamtime was allocated for proposal F-20181181. Other parts of the research were carried out at the PM3 beamline at the BESSY II electron storage ring operated by the Helmholtz-Zentrum Berlin für Materialien und Energie. **Funding:** This work was supported by Helmholtz foundation grant VH-NG-1105 (to R.Y.E, J.O.S., P.S.M., and M.B.) **Author contributions:** Conceptualization: H.R., S.E., and M.B. Experiment: H.R., R.Y.E., J.O.S., P.S.M., M.C.B., M.K., N.E., S.D., G.B., U.E., D.S., and C.v.K.S. Data analysis: R.Y.E. and H.R. Theoretical model and calculations: H.R. Visualization: H.R., R.Y.E, and D.S. Interpretation: H.R., S.E., R.Y.E., and M.B. Writing—original draft: H.R., D.S., and S.E. (with input from all authors). Writing—revision and reply: H.R., R.Y.E., D.S., and S.E. **Competing interests:** The authors declare that they have no competing interests. **Data and materials availability:** All data needed to evaluate the conclusions in the paper are present in the paper and/or the Supplementary Materials. In addition, we provide the presented data within the following repository: 10.5281/zenodo.5723994.

Submitted 13 December 2021
Accepted 5 April 2022
Published 20 May 2022
10.1126/sciadv.abn5127

Science Advances
AAAS

Supplementary Materials for

Probing electron and hole colocalization by resonant four-wave mixing spectroscopy in the extreme ultraviolet

Horst Rottke*, Robin Y. Engel, Daniel Schick, Jan O. Schunck, Piter S. Miedema,
Martin C. Borchert, Marion Kuhlmann, Nagitha Ekanayake, Siarhei Dziarzhytski,
Günter Brenner, Ulrich Eichmann, Clemens von Korff Schmising, Martin Beye, Stefan Eisebitt*

*Corresponding author. Email: rottke@mbi-berlin.de (H.R.); eisebitt@mbi-berlin.de (S.E.)

Published 20 May 2022, *Sci. Adv.* **8**, eabn5127 (2022)
DOI: 10.1126/sciadv.abn5127

This PDF file includes:

Frequency conversion: monochromatic plane wave limit Throughout the following derivation we will employ the cgs system of units. The corresponding geometry is sketched in Fig. S1. The Maxwell equations in the frequency domain used to determine the propagation of the nonlinearly generated electromagnetic waves in the LiF crystal while applying intense driving radiation fields are:

$$\nabla \times \mathbf{E}_\omega(\mathbf{x}) = i\frac{\omega}{c}\mathbf{B}_\omega(\mathbf{x}) \qquad \nabla \mathbf{B}_\omega(\mathbf{x}) = 0 \tag{S1}$$

$$\nabla \times \mathbf{B}_\omega(\mathbf{x}) = -i\frac{\omega}{c}\mathbf{D}_\omega(\mathbf{x}) \qquad \nabla \mathbf{D}_\omega(\mathbf{x}) = 0. \tag{S2}$$

ω represents the frequency of the generated electromagnetic wave, $\mathbf{E}_\omega(\mathbf{x})$ its electric field, $\mathbf{B}_\omega(\mathbf{x})$ the corresponding magnetic induction, $\mathbf{D}_\omega(\mathbf{x})$ the dielectric displacement, and c is the speed of light. The equations above assume the magnetic permeability of the nonlinear medium to be equal to 1. The dielectric displacement is linked to the electric field strength via:

$$\mathbf{D}_\omega(\mathbf{x}) = \epsilon(\omega)\,\mathbf{E}_\omega(\mathbf{x}) + 4\pi\mathbf{P}_\omega(\mathbf{x}) \tag{S3}$$

with $\epsilon(\omega)$ the linear dielectric constant of the medium at the frequency ω of the generated electromagnetic wave and $\mathbf{P}_\omega(\mathbf{x})$ the nonlinear contribution to the polarization of the medium at that frequency. The polaritation wave, in our case, is driven by the propagation of the FEL and NIR laser fields in the LiF crystal. We assume $\epsilon(\omega)$ to be a scalar quantity since the LiF crystal is of cubic symmetry. Absorption of LiF at the frequency of the generated wave renders $\epsilon(\omega)$ a complex quantity with its imaginary part being positive. On the vacuum side from where the FEL and NIR laser beams enter the crystal the same Maxwell equations above apply with $\epsilon(\omega) = 1$ and $\mathbf{P}_\omega(\mathbf{x}) = 0$.

The Maxwell equations together with relation (S3) for the dielectric displacement can be combined into an inhomogeneous wave equation for the electric field $\mathbf{E}_\omega(\mathbf{x})$:

$$\Delta\mathbf{E}_\omega + \epsilon(\omega)\left(\frac{\omega}{c}\right)^2\mathbf{E}_\omega = -4\pi\left[\left(\frac{\omega}{c}\right)^2\mathbf{P} - \frac{1}{\epsilon(\omega)}\mathbf{k}\left(\mathbf{k}\mathbf{P}\right)\right]\exp\left(i\mathbf{k}\mathbf{x}\right), \tag{S4}$$

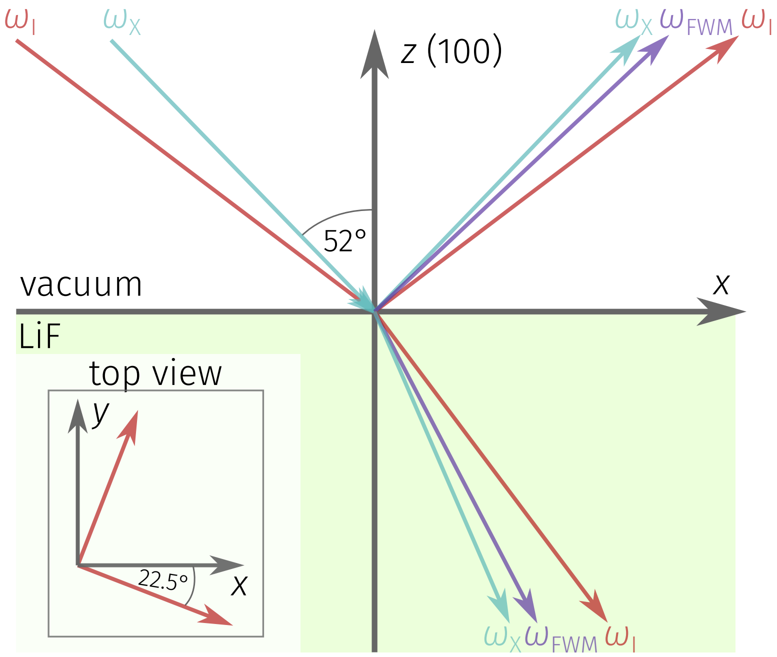

Figure S1: **The geometry used to measure the FWM signal in refection off a polished (100)-cut LiF interface to vacuum.** The blue arrows represent the FEL (X), the red the NIR (I) laser beam, and the purple ones the generated sum-/difference-frequency beams (FWM). They propagated in a common plane of incidence which we choose to be the x-z-plane of a suitably chosen Cartesian coordinate system with the z-axis normal to the LiF surface and parallel to one of the LiF cubic crystal axes. The x-y-axes of this coordinate system in the LiF surface plane were rotated by $22.5 \pm 2.5°$ with respect to the two in plane crystal axes of the LiF crystal used as shown in the inset.

with solutions subject to the additional restriction:

$$\nabla \mathbf{E}_\omega = -\frac{4\pi i}{\epsilon(\omega)} \mathbf{k}\mathbf{P} \exp{(i\mathbf{k}\mathbf{x})}. \tag{S5}$$

Relations (S4) and (S5) assume $\mathbf{P}_\omega(\mathbf{x})$ to be a plane wave $\mathbf{P}_\omega(\mathbf{x}) = \mathbf{P}\exp{(i\mathbf{k}\mathbf{x})}$, implying the driving FEL and NIR laser fields are plane waves. The wave vector $\mathbf{k}$ of the polarization wave is fixed by the specific nonlinear conversion process and by the wave vectors of the driving laser fields in the medium. We further assume the polarization wave to propagate in the (x, z)-plane of a suitably chosen coordinate system with $\mathbf{k} = (k_x, 0, k_z)$ determined by the common plane of incidence of the FEL and NIR radiation on the LiF crystal. $\mathbf{P}$ represents the constant amplitude of the polarization wave. We do not account for any potential nonlinear polarization of the medium bound to the vacuum-material interface.

The Maxwell equations (S1) and (S2) imply specific boundary conditions at the vacuum-medium interface (the x, y-plane). Namely, the magnetic induction has to be continuous across the boundary. Also the x- and y-components of the electric field (i.e. the components parallel to the interface) and the z-component of the dielectric displacement (i.e. the component perpendicular to the interface) have to be continuous across the interface. In the medium the generated electromagnetic wave propagates with the polarization wave $\mathbf{P}_\omega(\mathbf{x})$ into the medium, i.e. towards $z = -\infty$. The generated wave on the vacuum side propagates towards $z = +\infty$. There is no wave on the vacuum side propagating towards the interface at $z = 0$ at the frequency ω. Since the wave vector of the polarization wave $\mathbf{k} = (k_x, 0, k_z)$ has zero y-component so the wave vectors of the generated waves in vacuum and in the medium have a zero y-component. The electric field of the generated wave on the vacuum side can thus be represented by $\mathbf{E}_r(\mathbf{x}) = \mathbf{A}_r \exp{(i\mathbf{k}_r\mathbf{x})}$ with $\mathbf{k}_r = (k_{rx}, 0, k_{rz})$, transverse electric field amplitude $\mathbf{A}_r$ ($\mathbf{k}_r\mathbf{A}_r = 0$) and $k_{rz} > 0$. The dispersion relation $\mathbf{k}_r^2 = (\omega/c)^2$ ties the x- and z-components of the wave vector together.

The inhomogeneous wave equation (S4) in the medium for this geometry is solved with the Ansatz

$$\mathbf{E}_M(\mathbf{x}) = \tilde{\mathbf{E}}\,(z)\exp{(i\tilde{k}_x x)}. \tag{S6}$$

It results in an inhomogeneous ordinary second order differential equation for the amplitude $\tilde{\mathbf{E}}\,(z)$

$$\frac{\mathrm{d}^2\tilde{\mathbf{E}}\,(z)}{\mathrm{d}z^2} + \tilde{k}_z^2\tilde{\mathbf{E}}\,(z) = \frac{4\pi}{\epsilon(\omega)}\left[\mathbf{k}\,(\mathbf{kP}) - \epsilon(\omega)\left(\frac{\omega}{c}\right)^2\mathbf{P}\right]\exp{(ik_z z)}. \tag{S7}$$

$\tilde{k}_z$ used in Eq. (S7) is set via the dispersion relation $\tilde{k}_z^2 = \epsilon(\omega)\,(\omega/c)^2 - \tilde{k}_x^2$ with the real and imaginary parts of $\tilde{k}_z$ chosen to be negative in order to make sure the generated electric field in the nonlinear medium propagates with the polarization wave towards $z = -\infty$ and force absorption in the medium. With these restrictions the general solution of Eq. (S7) reads

$$\tilde{\mathbf{E}}\,(z) = \tilde{\mathbf{A}}\exp{(i\tilde{k}_z z)} + \frac{\mathbf{H}}{\tilde{k}_z^2 - k_z^2}\exp{(ik_z z)}, \tag{S8}$$

with

$$\mathbf{H} = \frac{4\pi}{\epsilon(\omega)}\left[\mathbf{k}\,(\mathbf{kP}) - \epsilon(\omega)\left(\frac{\omega}{c}\right)^2\mathbf{P}\right]. \tag{S9}$$

The amplitude vectors $\mathbf{A}_r$ of the electric field on the vacuum side [Eq. (1) of the main text] and $\tilde{\mathbf{A}}$ are still free constants. They are fixed by the boundary conditions at the vacuum-medium interface, by Eq. (S5) in the medium, and by the fundamental condition that the electric field vector on the vacuum side must be transverse to the propagation direction of the wave. The boundary conditions can only be satisfied provided the still free wave vector components $\tilde{k}_x$ and k_{rx} satisfy the condition $\tilde{k}_x = k_{rx} = k_x$, i.e. they have to be equal to the x-component of the wave vector of the nonlinear polarization wave. Via the dispersion relations on the vacuum side and in the medium then also the z-components $\tilde{k}_z$ and k_{rz} are fixed subject to the constraints $k_{rz} > 0$ and the real and imaginary parts of $\tilde{k}_z$ have to be negative.

Involving these constraints results in the explicit form for the electric field amplitude $\mathbf{A}_r$ on the vacuum side given in Eq. (2) of the main text and in

$$\begin{aligned}\tilde{\mathbf{A}} =& \frac{4\pi}{\epsilon(\omega)\left[\tilde{k}_z - \epsilon(\omega)\, k_{rz}\right]}\left\{P_x + (k_z - \epsilon(\omega)\, k_{rz})\,\frac{[\mathbf{k}\times\mathbf{P}]_y}{\tilde{k}_z^2 - k_z^2}\right\}\begin{bmatrix}\tilde{k}_z\\ 0\\ -k_x\end{bmatrix} + \\ & 4\pi\left(\frac{\omega}{c}\right)^2 \frac{k_z - k_{rz}}{\tilde{k}_z - k_{rz}}\,\frac{P_y}{\tilde{k}_z^2 - k_z^2}\begin{bmatrix}0\\ 1\\ 0\end{bmatrix}\end{aligned} \qquad \text{(S10)}$$

The result Eq. (S8) for the dependence of the electric field in the medium on the z-coordinate may be rewritten in the form

$$\tilde{\mathbf{E}}\,(z) = \left[\tilde{\mathbf{A}} + \frac{\mathbf{H}}{\tilde{k}_z^2 - k_z^2} + \mathbf{H}\frac{\exp[i(k_z - \tilde{k}_z)z] - 1}{\tilde{k}_z^2 - k_z^2}\right]\exp\left(i\tilde{k}_z z\right) \qquad \text{(S11)}$$

to emphasize the role of phase matching in the nonlinear process provided the wave vectors $\mathbf{k}$ of the nonlinear polarization wave in the medium and $\tilde{\mathbf{k}}$ of the generated wave become equal [meaning $\tilde{k}_z = k_z$ in Eq. (S11)]. In the limit of phase matching the z independent term in square brackets in Eq. (S11), namely $\tilde{\mathbf{A}} + \mathbf{H}/(\tilde{k}_z^2 - k_z^2)$, does not become singular. This can be seen when explicitly evaluating it using the expressions for $\mathbf{H}$ and $\tilde{\mathbf{A}}$ given above. Phase matching means the z dependent term in square brackets in Eq. (S11), i.e. the amplitude of the electric field of the generated wave in the medium grows in proportion to the propagation length z in the medium. However, one has to keep in mind that absorption in the medium will counteract the buildup of the electric field. Absorption enters via the imaginary part of $\tilde{k}_z$ in $\exp\left(i\tilde{k}_z z\right)$ in the expression for the electric field in Eq. (S11). After a certain propagation length absorption will always win over the linear buildup in z of the wave's amplitude.

The directions of emission of the sum- and difference-frequency beams on the vacuum side In the plane wave approximation used here the wave vector components of the XUV and NIR beams impinging on the LiF crystal in the surface plane of the crystal determine the corresponding component of the wave vector of the polarization wave in the crystal. We represent these wave vectors by $\mathbf{k}^{v\mathrm{X}} = (k_x^{v\mathrm{X}}, 0, k_z^{v\mathrm{X}})$ and $\mathbf{k}^{v\mathrm{I}} = (k_x^{v\mathrm{I}}, 0, k_z^{v\mathrm{I}})$ for the XUV and NIR beams, respectively, using the coordinate system defined in Fig. S1. Boundary conditions for the electromagnetic fields imply that the x-components of the wave vectors of the XUV and NIR beams (in plane components), which drive the nonlinear processes, do not change when passing into the LiF crystal. Then the x-components of the wave vectors of the polarization waves in the medium are $k_x = k_x^{v\mathrm{X}} \pm 2k_x^{v\mathrm{I}}$, respectively. According to the previous section k_x, in turn, equals the x-component of the wave vectors of the generated electromagnetic fields on the vacuum side ($k_{rx} = k_x$). Based on the dispersion relation for the sum- and difference-frequency fields on the vacuum side they thus propagate along the wave vector $\mathbf{k}_r = \left(k_x, 0, \sqrt{(\omega/c)^2 - k_x^2}\right)$. Nonlinear reflection thus occurs at an angle $\theta = \arcsin(ck_x/\omega)$ relative to the LiF surface normal.

The nonlinear polarization amplitude P For the particular nonlinear processes of four-wave mixing relevant to our experiment, namely sum- and difference-frequency mixing, the amplitude $\mathbf{P}$ of the nonlinear polarization of the medium is linked to the specific third order nonlinear susceptibility tensors $\chi^{(3)}\left(-\omega_\mathrm{X} - 2\omega_\mathrm{I}; \omega_\mathrm{X}, \omega_\mathrm{I}, \omega_\mathrm{I}\right)$ and $\chi^{(3)}\left(-\omega_\mathrm{X} + 2\omega_\mathrm{I}; \omega_\mathrm{X}, -\omega_\mathrm{I}, -\omega_\mathrm{I}\right)$, respectively. Based on the cubic symmetry of the LiF crystal (space group $m\overline{3}m$) these tensors have 27 elements which are different from zero with only four of them being independent (*36*). Skipping the dependence on the frequencies for convenience, one complete set of independent, non-zero elements is $\chi^{(3)}_{x,x,x,x}$, $\chi^{(3)}_{x,x,y,y}$, $\chi^{(3)}_{x,y,x,y}$ and $\chi^{(3)}_{x,y,y,x}$ in a Cartesian frame of reference with axes coinciding with the crystal axes (*36*).

According to the experimental situation, the LiF crystal's z-axis is chosen to coincide with the z-axis of the plane of incidence of the FEL and NIR laser beams, whereas the crystal's x-axis enclosed an angle φ with the x-axis of the plane of incidence (see Fig. 2 of the main text and Fig. S1). The components of the electric field amplitudes of the FEL and NIR plane waves in the nonlinear medium may be written $\mathbf{E}_{\mathrm{X}} = (E_{\mathrm{X},x}, 0, E_{\mathrm{X},z})$ and $\mathbf{E}_{\mathrm{I}} = (E_{\mathrm{I},x}, 0, E_{\mathrm{I},z})$. This representation uses as the frame of reference the x- and z-axes of the plane of incidence together with the corresponding orthogonal y-axis (see Fig. S1). The y-components of the amplitudes are both set to zero, assuming the waves are polarized in the plane of incidence, just as the setting in the experiment. With these assumptions the components of the induced nonlinear polarization (P_x, P_y, P_z) in the same reference frame can be written as

$$\begin{aligned}
P_x =& \chi^{(3)}_{x,x,x,x} E_{\mathrm{X},x} E^2_{\mathrm{I},x} \left(\sin^4\varphi + \cos^4\varphi\right) + \chi^{(3)}_{x,x,y,y} E_{\mathrm{X},x} E^2_{\mathrm{I},z} + \left(\chi^{(3)}_{x,y,x,y} + \chi^{(3)}_{x,y,y,x}\right) E_{\mathrm{X},z} E_{\mathrm{I},x} E_{\mathrm{I},z} \\
&+ \frac{1}{2}\left(\chi^{(3)}_{x,x,y,y} + \chi^{(3)}_{x,y,x,y} + \chi^{(3)}_{x,y,y,x}\right) E_{\mathrm{X},x} E^2_{\mathrm{I},x} \sin^2 2\varphi \qquad \text{(S12)} \\
P_y =& \frac{1}{4}\left(\chi^{(3)}_{x,x,y,y} + \chi^{(3)}_{x,y,x,y} + \chi^{(3)}_{x,y,y,x} - \chi^{(3)}_{x,x,x,x}\right) E_{\mathrm{X},x} E^2_{\mathrm{I},x} \sin 4\varphi \qquad \text{(S13)} \\
P_z =& \chi^{(3)}_{x,x,x,x} E_{\mathrm{X},z} E^2_{\mathrm{I},z} + \chi^{(3)}_{x,x,y,y} E_{\mathrm{X},z} E^2_{\mathrm{I},x} + \left(\chi^{(3)}_{x,y,x,y} + \chi^{(3)}_{x,x,y,y}\right) E_{\mathrm{X},x} E_{\mathrm{I},x} E_{\mathrm{I},z} \qquad \text{(S14)}
\end{aligned}$$

This relation supposes the nonlinear process of sum-frequency mixing. For difference-frequency mixing one has to use the complex conjugate NIR electric field strength components in the equations for the amplitude components of the nonlinear polarization above.

In our model for $\chi^{(3)}(-\omega_{\mathrm{X}} - 2\omega_{\mathrm{I}}; \omega_{\mathrm{X}}, \omega_{\mathrm{I}}, \omega_{\mathrm{I}})$ and $\chi^{(3)}(-\omega_{\mathrm{X}} + 2\omega_{\mathrm{I}}; \omega_{\mathrm{X}}, -\omega_{\mathrm{I}}, -\omega_{\mathrm{I}})$ we simplify the LiF crystal symmetry by assuming the medium to be invariant under the full rotation group. This introduces an additional constraint for the independent elements of the nonlinear susceptibility tensor above. Only three of the four elements remain independent (*36*)

$$\chi^{(3)}_{x,x,y,y} + \chi^{(3)}_{x,y,x,y} + \chi^{(3)}_{x,y,y,x} - \chi^{(3)}_{x,x,x,x} = 0\,. \qquad \text{(S15)}$$

As one may already expect, this relation eliminates any dependence of the induced nonlinear polarization $\mathbf{P}$ above on the angle φ.

The model for the linear and 3rd order susceptibilities Computing the amplitude of the electric field [Eq. (2), main text] of the reflected sum- and difference-frequency waves requires the knowledge of the linear dielectric constant $\epsilon(\omega)$ of LiF in the relevant photon energy range. We constructed $\epsilon(\omega)$ using the measured linear reflection off LiF in Fig. 1(B). As a model a set of seven discrete, homogeneously broadened resonances was chosen to simulate the structures found in the reflection curve by suitably choosing their positions, widths and oscillator strengths. Since the measurement did not determine the reflection coefficient but only represents the intensity of the reflected light the absolute scale for the dielectric constant had to be set using a reported LiF absorption coefficient at a certain photon energy. We utilized the measured absorption coefficient at 70 eV photon energy reported in (*37*).

The relation

$$\alpha\left(\omega\right)=\sum_{j}\frac{f_j}{\omega_j^2-\omega^2-i\gamma_j\omega} \tag{S16}$$

for the microscopic reaction of LiF to an applied electric field in the frequency range of interest is employed to determine the dielectric constant. It is based on molecular polarizability (see (*38*)). The adjustable parameters ω_j, γ_j and $f_j > 0$ are chosen so as to simulate the measured LiF reflection in Fig. 1B. The Clausius-Massotti equation

$$\alpha\left(\omega\right)=3\frac{\epsilon\left(\omega\right)-1}{\epsilon\left(\omega\right)+2} \tag{S17}$$

links the microscopic reaction to the dielectric constant ϵ (*38*). The parameters ω_j, γ_j and $f_j > 0$ which result in a reasonable fit of the experimental linear reflection off LiF (see Fig. 1(B), the blue line) are gathered in Table S1. The real and imaginary parts of the dielectric constant ϵ corresponding to this choice of parameters are shown in Fig. S2. The main, p-type LiF core exciton resonance is responsible for the maximum of the imaginary part of $\epsilon(\omega)$ at 62 eV while its low energy shoulder represents the suspected s-type core exciton.

The calculation of the third order nonlinear susceptibility tensor is based on the expression for its components given in reference (*36*) (page 93). Since in the experiment a detectable, resonance like enhancement of sum- and difference-frequency mixing was observed when the

j	1	2 (1s)(2s)	3 (1s)(2p)	4	5	6	7
ω_j / eV	49.82	60.97	62.07	63.12	65.0	67.55	69.92
γ_j / eV	50.0	1.1	0.79	1.3	2.4	4.3	1.45
f_j / eV^2	42.0	0.59	1.54	0.17	0.92	2.77	0.75

Table S1: The parameters entering Eq. (S16) for the linear microscopic reaction of LiF to an applied electromagnetic wave in the photon energy range between $\approx 58\,\mathrm{eV}$ and $\approx 72\,\mathrm{eV}$ which is relevant to the experiment. The dielectric constant based on this choice of the parameters allows to reasonably reproduce the experimental LiF reflectivity as shown in Fig. 1(B) of the main text.

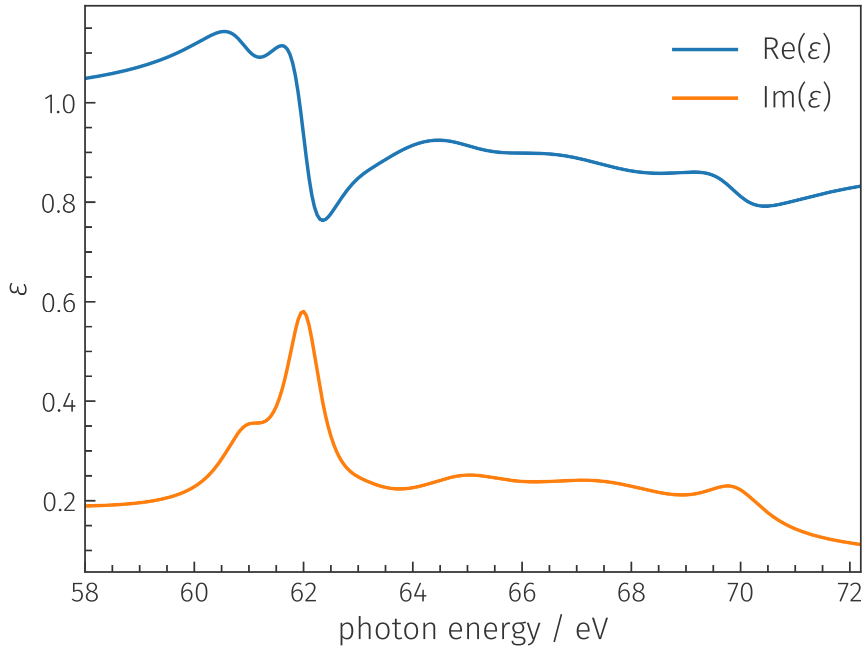

Figure S2: **The calculated linear dielectric constant $\epsilon(\omega)$ in the photon energy range between 58 eV and 72 eV.** The blue line shows the real and the orange one the imaginary part of ϵ.

LiF p-type exciton was involved, we only take this resonance into account together with the suspected s-type excitonic resonance in determining the dependence of $\chi^{(3)}$ on the driving FEL photon energy. In the expression for $\chi^{(3)}$ we therefore only employ the resonance positions ω_j and widths γ_j in Table S1 with $j = 2, 3$ which correspond to these resonances. For the nonlinear susceptibility we neglect a dipole coupling of the s-type exciton to the ground electronic state. However, we take into account a potential, dipole allowed coupling of this s- to the p-type main exciton. We use this simplification since we think the main influence on sum- and difference-frequency generation by the suspected s-type exciton is through its coupling to the p-type exciton which is driven by the applied NIR laser field. The NIR photon energy of $1.55\,\mathrm{eV}$ does not much exceed the separation in energy of these two excitons ($\omega_3 - \omega_2 = 1.1\,\mathrm{eV}$ according to Table S1).

With this simplification, only two dipole matrix elements are relevant in the expression for $\chi^{(3)}$: one for the dipole coupling of the p-type exciton to the ground state and one for the coupling of the s- and p-type excitons. For lack of information on the details of the electronic states involved we use one-electron atomic dipole matrix elements and assume the ground state is represented by a state with angular momentum $l = 0$ (s-state) and the excited states involved by $l = 0$ and $l = 1$ with magnetic quantum numbers $m_l = 0, \pm 1$. This approach reduces the number of free parameters in the expression for $\chi^{(3)}$ to two radial dipole matrix elements and modifies the symmetry of the LiF crystal from cubic to full rotational symmetry. Based on this simplified model we calculate the independent components of $\chi^{(3)}$ which in turn provide the amplitude of the third order nonlinear polarization amplitude $\mathbf{P}$ needed for the determination of the sum- and difference-frequency yields for comparison with the experimental result.

Calibration of the MUSIX spectrometer Incidence angles on the sample surface were determined in situ with a photodiode on the diffractometer. The sample's crystal axes were determined *ex situ* through Laue diffraction and the sample orientation was transferred by mounting the sample on a holder with an azimuthal Vernier scale.

For every setting of the spectrometer grating, a calibration measurement was performed by varying the undulator gap of the FEL. This generated a discrete series of different FEL photon energies reflected off the LiF sample via the grating onto the CCD camera, bypassing the installed beam-block. To prevent saturation of the CCD, two 295 nm thick zirconium attenuator foils were placed in the FEL beam path. This allowed calibrating the MUSIX spectrometer against the wavelength measurement implemented in the beamline (*39*). In addition, the overall consistency of the various estimated parameters used in the MUSIX spectrometer transmission calculations described below was verified by asserting an agreement between the number of photons measured by an x-ray gas-monitor-detector (XGMD) (*34*) in the FEL beamline and by the MUSIX spectrometer's CCD at different wavelengths. As no linear reflectivity spectrum of the sample was acquired with the MUSIX spectrometer, a flat sample reflectivity of 0.05 % was used in this consistency check.

Estimation of the total number of photons generated in the FWM processes The read out CCD camera counts were converted to an estimated number of incident photons assuming 50 % of these photons (a conservative estimate of the CCD's quantum efficiency) were converted into electron-hole-pairs in the silicon chip with a bandgap of 3.1 eV. Each electron created one digital count in the analog-to-digital converter of the CCD, according to the manufacturer information for the readout frequency employed in the experimental runs. On the way from the LiF sample to the CCD the photons have been reflected off the MUSIX spectrometer gating and passed an aluminum filter foil. For the grating a 15 % diffraction efficiency in first order is assumed. The aluminum filter transmission (thickness 200 nm) is retrieved from tabulated data (*40, 41*). We also accounted for an estimated 12.5 nm aluminum-oxide layer on each side of the filter.

In a similar way, the total number of FEL photons impinging on the LiF sample per pulse was derived from pulse energy measurements using an XGMD upstream (*34*). Following the XGMD the FEL beam passed a silicon filter, three beamline mirrors, beam width limiting apertures and the incoupling mirror for the NIR laser beam which all reduced the FEL pulse energy before reaching the sample. The number of photons per pulse was determined from the total pulse energy measured by the XGMD, assuming 7 % of the measured pulse energy was due to FEL harmonics that were absorbed by the downstream 411 nm thick silicon filter. Its transmission for the fundamental FEL beam was calculated from tabulated transmission data assuming a 12.5 nm thick silicon oxide layer on each side (*40, 41*). Likewise, based on tabulated data (*40, 41*), the reflectivities of the three beamline mirrors (2° grazing angle of incidence and coated with nickel, gold and platinum, respectively) were taken into account. Wavefront-sensor measurements during beamline-alignment further suggested 25 % transmission through the beamline apertures and the incoupling mirror for the IR laser beam due to clipping.

Comparing the photon flux on the CCD to that measurd by the XGMD in the calibration measurements described above lends some credence to the transmission estimates made here. However, a significant uncertainty of the scaling factors involved remains. Therefore, we refer to the total number of FEL photons arriving on the LiF sample and photons generated in the FWM processes, which we show in Figs. 3 and 4 of the main text, as estimates only.

The experimental dependence of the frequency conversion on the NIR laser pulse energy

To further support the nature of the observed nonlinear processes we determined the dependence of the frequency conversion yield on the pulse energy of the NIR laser pulses. In the regime of low conversion, as was the case in the experiment, the dependence is expected to be quadratic. This is just what the experiment indicates as Fig. S3 shows. The measurement was done with the FEL photon energy set to 59.25 eV. The nonlinear process involved was sum-frequency mixing

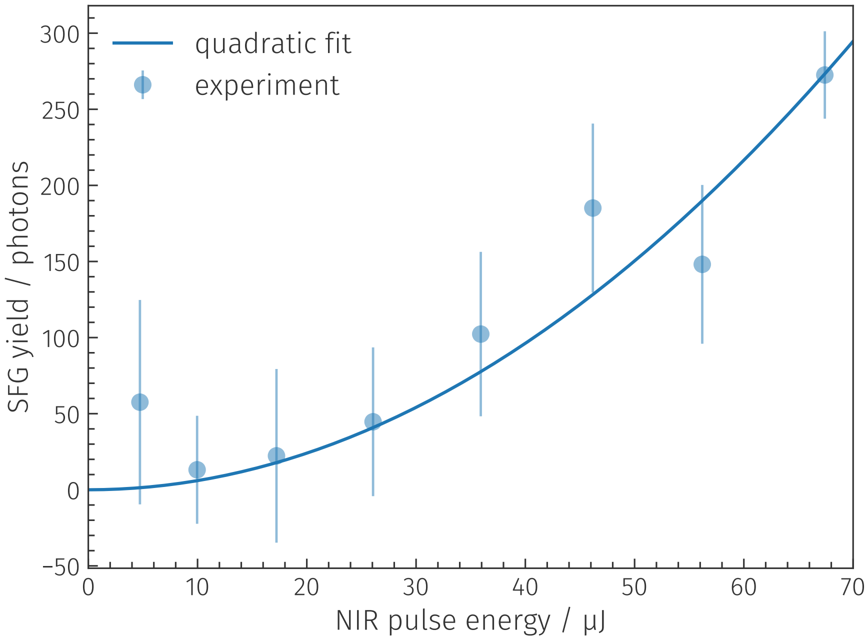

Figure S3: **Dependence of the number of sum-frequency photons generated on the NIR laser pulse energy arriving on the LiF crystal.** The FEL laser photon energy was set to 59.25 eV, i.e. 3-photon resonant with the LiF exciton resonance ($\omega_{\text{exc}} = \omega_{\text{X}} + 2\omega_{\text{I}}$). The blue line represents a fit to the data points using a quadratic polynomial in the NIR pulse energy.

three-photon resonant with the LiF exciton resonance ($\omega_{\text{exc}} = \omega_{\text{X}} + 2\omega_{\text{I}}$). The data points allow fitting a quadratic dependence of the sum-frequency photon yield on the NIR laser pulse energy (blue line in Fig. S3).

REFERENCES AND NOTES

1. H. Danino, I. Freund, Parametric down conversion of x rays into the extreme ultraviolet. *Phys. Rev. Lett.* **46**, 1127–1130 (1981).

2. K. Tamasaku, K. Sawada, E. Nishibori, T. Ishikawa, Visualizing the local optical response to extreme-ultraviolet radiation with a resolution of λ/380. *Nat. Phys.* **7**, 705–708 (2011).

3. A. Schori, C. Bömer, D. Borodin, S. P. Collins, B. Detlefs, M. Moretti Sala, S. Yudovich, S. Shwartz, Parametric down-conversion of x rays into the optical regime. *Phys. Rev. Lett.* **119**, 253902 (2017).

4. T. E. Glover, D. M. Fritz, M. Cammarata, T. K. Allison, S. Coh, J. M. Feldkamp, H. Lemke, D. Zhu, Y. Feng, R. N. Coffee, M. Fuchs, S. Ghimire, J. Chen, S. Shwartz, D. A. Reis, S. E. Harris, J. B. Hastings, X-ray and optical wave mixing. *Nature* **488**, 603–608 (2012).

5. S. Shwartz, M. Fuchs, J. B. Hastings, Y. Inubushi, T. Ishikawa, T. Katayama, D. A. Reis, T. Sato, K. Tono, M. Yabashi, S. Yudovich, S. E. Harris, X-ray second harmonic generation. *Phys. Rev. Lett.* **112**, 163901 (2014).

6. R. K. Lam, S. L. Raj, T. A. Pascal, C. D. Pemmaraju, L. Foglia, A. Simoncig, N. Fabris, P. Miotti, C. J. Hull, A. M. Rizzuto, J. W. Smith, R. Mincigrucci, C. Masciovecchio, A. Gessini, E. Allaria, G. De Ninno, B. Diviacco, E. Roussel, S. Spampinati, G. Penco, S. Di Mitri, M. Trovò, M. Danailov, S. T. Christensen, D. Sokaras, T.-C. Weng, M. Coreno, L. Poletto, W. S. Drisdell, D. Prendergast, L. Giannessi, E. Principi, D. Nordlund, R. J. Saykally, C. P. Schwartz, Soft x-ray second harmonic generation as an interfacial probe. *Phys. Rev. Lett.* **120**, 023901 (2018).

7. F. Bencivenga, R. Cucini, F. Capotondi, A. Battistoni, R. Mincigrucci, E. Giangrisostomi, A. Gessini, M. Manfredda, I. P. Nikolov, E. Pedersoli, E. Principi, C. Svetina, P. Parisse, F. Casolari, M. B. Danailov, M. Kiskinova, C. Masciovecchio, Four-wave mixing experiments with extreme ultraviolet transient gratings. *Nature* **520**, 205–208 (2015).

8. L. Foglia, F. Capotondi, R. Mincigrucci, D. Naumenko, E. Pedersoli, A. Simoncig, G. Kurdi, A. Calvi, M. Manfredda, L. Raimondi, N. Mahne, M. Zangrando, C. Masciovecchio, F. Bencivenga, First evidence of purely extreme-ultraviolet four-wave mixing. *Phys. Rev. Lett.* **120**, 263901 (2018).

9. F. Bencivenga, R. Mincigrucci, F. Capotondi, L. Foglia, D. Naumenko, A. A. Maznev, E. Pedersoli, A. Simoncig, F. Caporaletti, V. Chiloyan, R. Cucini, F. Dallari, R. A. Duncan, T. D. Frazer, G. Gaio, A. Gessini, L. Giannessi, S. Huberman, H. Kapteyn, J. Knobloch, G. Kurdi, N. Mahne, M. Manfredda, A. Martinelli, M. Murnane, E. Principi, L. Raimondi, S. Spampinati, C. Spezzani, M. Trovò, M. Zangrando, G. Chen, G. Monaco, K. A. Nelson, C. Masciovecchio, Nanoscale transient gratings excited and probed by extreme ultraviolet femtosecond pulses. *Sci. Adv.* **5**, eaaw5805 (2019).

10. E. Shwartz, S. Shwartz, Difference-frequency generation of optical radiation from two-color x-ray pulses. *Opt. Express* **23**, 7471–7480 (2015).

11. C. P. Schwartz, S. L. Raj, S. Jamnuch, C. J. Hull, P. Miotti, R. K. Lam, D. Nordlund, C. B. Uzundal, C. Das Pemmaraju, R. Mincigrucci, L. Foglia, A. Simoncig, M. Coreno, C. Masciovecchio, L. Giannessi, L. Poletto, E. Principi, M. Zuerch, T. A. Pascal, W. S. Drisdell, R. J. Saykally, Angstrom-resolved interfacial structure in buried organic-inorganic junctions. *Phys. Rev. Lett.* **127**, 096801 (2021).

12. J. R. Rouxel, D. Fainozzi, R. Mankowsky, B. Rösner, G. Seniutinas, R. Mincigrucci, S. Catalini, L. Foglia, R. Cucini, F. Döring, A. Kubec, F. Koch, F. Bencivenga, A. A. Haddad, A. Gessini, A. A. Maznev, C. Cirelli, S. Gerber, B. Pedrini, G. F. Mancini, E. Razzoli, M. Burian, H. Ueda, G. Pamfilidis, E. Ferrari, Y. Deng, A. Mozzanica, P. J. M. Johnson, D. Ozerov, M. G. Izzo, C. Bottari, C. Arrell, E. J. Divall, S. Zerdane, M. Sander, G. Knopp, P. Beaud, H. T. Lemke, C. J. Milne, C. David, R. Torre, M. Chergui, K. A. Nelson, C. Masciovecchio, U. Staub, L. Patthey, C. Svetina, Hard x-ray transient grating spectroscopy on bismuth germanate. *Nat. Photonics* **15**, 499–503 (2021).

13. J. D. Gaynor, A. P. Fidler, Y.-C. Lin, H.-T. Chang, M. Zuerch, D. M. Neumark, S. R. Leone, Solid state core-exciton dynamics in NaCl observed by tabletop attosecond four-wave mixing spectroscopy. *Phys. Rev. B* **103**, 245140 (2021).

14. R. Haensel, C. Kunz, B. Sonntag, Measurement of photoabsorption of the lithium halides near the lithium *K* edge. *Phys. Rev. Lett.* **20**, 262–264 (1968).

15. W. Olovsson, I. Tanaka, P. Puschnig, C. Ambrosch-Draxl, Near-edge structures from first principles all-electron Bethe-Salpeter equation calculations. *J. Phys. Condens. Matter* **21**, 104205 (2009).

16. S. T. Pantelides, Electronic excitation energies and the soft-x-ray absorption spectra of alkali halides. *Phys. Rev. B* **11**, 2391–2411 (1975).

17. J. R. Fields, P. C. Gibbons, S. E. Schnatterly, Electronic excitations in LiF: 10-70 eV. *Phys. Rev. Lett.* **38**, 430–434 (1977).

18. E. L. Shirley, Li 1s near-edge spectra in six lithium halides. *J. Electron Spectros. Relat. Phenomena* **137-140**, 579–584 (2004).

19. W. Olovsson, I. Tanaka, T. Mizoguchi, P. Puschnig, C. Ambrosch-Draxl, All-electron Bethe-Salpeter calculations for shallow-core x-ray absorption near-edge structures. *Phys. Rev. B* **79**, 041102 (2009).

20. A. B. Kunz, J. C. Boisvert, T. O. Woodruff, Li *K*-edge soft-x-ray absorption in LiF. *Phys. Rev. B* **30**, 2158–2162 (1984).

21. A. B. Kunz, J. T. Devreese, T. Collins, The role of the electronic polaron in the soft X-ray absorption of the lithium halides. *J. Phys. C Solid State Phys.* **5**, 3259–3263 (1972).

22. B. F. Sonntag, Observations of “forbidden” soft-x-ray transitions: Li *K* absorption in LiF. *Phys. Rev. B* **9**, 3601–3602 (1974).

23. W. Gudat, C. Kunz, H. Petersen, Core exciton and band structure in LiF. *Phys. Rev. Lett.* **32**, 1370–1373 (1974).

24. T. Sato, R. Letrun, H. J. Kirkwood, J. Liu, P. Vagovič, G. Mills, Y. Kim, C. M. S. Takem, M. Planas, M. Emons, T. Jezynski, G. Palmer, M. Lederer, S. Schulz, J. Mueller, H. Schlarb, A. Silenzi, G. Giovanetti, A. Parenti, M. Bergemann, T. Michelat, J. Szuba, J. Grünert, H. N. Chapman, A. P. Mancuso, Femtosecond timing synchronization at megahertz repetition rates for an X-ray free-electron laser. *Optica* **7**, 716 (2020).

25. S. Schulz, I. Grguraš, C. Behrens, H. Bromberger, J. T. Costello, M. K. Czwalinna, M. Felber, M. C. Hoffmann, M. Ilchen, H. Y. Liu, T. Mazza, M. Meyer, S. Pfeiffer, P. Prędki, S. Schefer, C. Schmidt, U. Wegner, H. Schlarb, A. L. Cavalieri, Femtosecond all-optical synchronization of an X-ray free-electron laser. *Nat. Commun.* **6**, 5938 (2015).

26. J. Duris, S. Li, T. Driver, E. G. Champenois, J. P. MacArthur, A. A. Lutman, Z. Zhang, P. Rosenberger, J. W. Aldrich, R. Coffee, G. Coslovich, F.-J. Decker, J. M. Glownia, G. Hartmann, W. Helml, A. Kamalov, J. Knurr, J. Krzywinski, M.-F. Lin, J. P. Marangos, M. Nantel, A. Natan, J. T. O'Neal, N. Shivaram, P. Walter, A. L. Wang, J. J. Welch, T. J. A. Wolf, J. Z. Xu, M. F. Kling, P. H. Bucksbaum, A. Zholents, Z. Huang, J. P. Cryan, A. Marinelli, Tunable isolated attosecond X-ray pulses with gigawatt peak power from a free-electron laser. *Nat. Photonics* **14**, 30–36 (2020).

27. A. A. Maznev, R. Mincigrucci, F. Bencivenga, V. Unikandanunni, F. Capotondi, G. Chen, Z. Ding, R. A. Duncan, L. Foglia, M. G. Izzo, C. Masciovecchio, A. Martinelli, G. Monaco, E. Pedersoli, S. Bonetti, K. A. Nelson, Generation and detection of 50 GHz surface acoustic waves by extreme ultraviolet pulses. *Appl. Phys. Lett.* **119**, 044102 (2021).

28. E. Berger, S. Jamnuch, C. B. Uzundal, C. Woodahl, H. Padmanabhan, A. Amado, P. Manset, Y. Hirata, Y. Kubota, S. Owada, K. Tono, M. Yabashi, C. Wang, Y. Shi, V. Gopalan, C. P. Schwartz, W. S. Drisdell, I. Matsuda, J. W. Freeland, T. A. Pascal, M. Zuerch, Extreme ultraviolet second harmonic generation spectroscopy in a polar metal. *Nano Lett.* **21**, 6095–6101 (2021).

29. D. Popova-Gorelova, D. A. Reis, R. Santra, Theory of X-ray scattering from laser-driven electronic systems. *Phys. Rev. B* **98**, 224302 (2018).

30. R. Cohen, S. Shwartz, Theory of nonlinear interactions between x rays and optical radiation in crystals. *Phys. Rev. Res.* **1**, 033133 (2019).

31. J. R. Rouxel, M. Kowalewski, K. Bennett, S. Mukamel, X-ray sum frequency diffraction for direct imaging of ultrafast electron dynamics. *Phys. Rev. Lett.* **120**, 243902 (2018).

32. M. Beye, R. Y. Engel, J. O. Schunck, S. Dziarzhytski, G. Brenner, P. S. Miedema, Non-linear soft x-ray methods on solids with MUSIX–the multi-dimensional spectroscopy and inelastic X-ray scattering endstation. *J. Phys. Condens. Matter* **31**, 014003 (2019).

33. L. Raimondi, C. Svetina, N. Mahne, D. Cocco, A. Abrami, M. De Marco, C. Fava, S. Gerusina, R. Gobessi, F. Capotondi, E. Pedersoli, M. Kiskinova, G. De Ninno, P. Zeitoun, G. Dovillaire, G. Lambert, W. Boutu, H. Merdji, A. Gonzalez, D. Gauthier, M. Zangrando, Microfocusing of the FERMI@Elettra FEL beam with a K–B active optics system: Spot size predictions by application of the WISE code. *Nucl. Instrum. Methods Phys. Res. Sect. A Accel. Spectrometers Detect. Assoc. Equip.* **710**, 131–138 (2013).

34. A. A. Sorokin, Y. Bican, S. Bonfigt, M. Brachmanski, M. Braune, U. F. Jastrow, A. Gottwald, H. Kaser, M. Richter, K. Tiedtke, An X-ray gas monitor for free-electron lasers. *J. Synchrotron Radiat.* **26**, 1092–1100 (2019).

35. T. Kachel, The PM3 beamline at BESSY II. *J. large-scale Res. Facil. JLSRF* **2**, A48 (2016).

36. P. N. Butcher, D. Cotter, *The Elements of Nonlinear Optics* (Cambridge Univ. Press, 1990).

37. A. Milgram, M. P. Givens, Extreme ultraviolet absorption by lithium fluoride. *Phys. Rev.* **125**, 1506–1509 (1962).

38. J. D. Jackson, *Classical Electrodynamics* (John Wiley & Sons Inc., ed. 3, 1998).

39. M. Braune, J. Buck, M. Kuhlmann, S. Grunewald, S. Düsterer, J. Viefhaus, K. Tiedtke, Non-invasive online wavelength measurements at FLASH2 and present benchmark. *J. Synchrotron Radiat.* **25**, 3–15 (2018).

40. B. L. Henke, E. M. Gullikson, J. C. Davis, *X-Ray Interactions With Matter* (U.S. Department of Energy, 1993).

41. B. Henke, E. Gullikson, J. Davis, X-ray interactions: Photoabsorption, scattering, transmission, and reflection at E = 50-30,000 eV, Z = 1-92. *At. Data Nucl. Data Tables* **54**, 181–342 (1993).

6.2 The Next Steps

The above publication has reached some milestones for FWM-techniques, namely the background-free measurement of SFG and DFG signals, separated in energy, and the characterization of the coupling strength between different excitations. However, the experiment was still limited in several important ways that point to open opportunities for upcoming studies.

Perhaps the most straightforward next step from this experiment is to move to a non-collinear geometry with a near-90°-angle between FEL and IR laser. Due to momentum conservation, this would allow detecting the SFG and DFG signals not only separated in photon energy but also in emission angle. This way, the signal background (which was given through the tails of the SASE spectrum) can be suppressed even further to allow a far better signal-to-noise ratio.
Current improvement efforts at the beamline that aim to decrease the timing jitter and increase long-term arrival-time stability between XFEL and IR-laser are expected to further increase the signal-to-noise ratio.[1]

In principle, as this experiment was performed in reflection from the LiF crystal, phase-matching effects beyond momentum conservation should not be relevant, even in a non-collinear geometry. To me, this prediction not only calls for confirmation but also offers an opportunity for a direct comparison with the corresponding experiment performed in transmission in order to map out the relevance and stringency of phase-matching conditions around a core resonance.

Moving to the more demanding improvements, one cannot help but notice that this experiment observes a fully coherent wave-mixing process, but does so with longitudinally incoherent SASE-radiation. Moving to a seeded XFEL source, ideally with a very short pulse duration and control or knowledge of the relative phases between the XUV and IR waves, would allow full control of the wave-mixing process, which would e.g. allow a measurement of dephasing time (as well as the population lifetime) of the excited states.

The suggestions above regard further studies of the already measured signal, which was enhanced through the coupling between the $1s2p$ and $1s2s$ core-excited states. A critical reader of our experimental report may object that the coupling between two core excitons is not particularly insightful knowledge for common material science, which is mostly concerned with low-energy excitations. They might find the coupling between a core exciton and a valence excitation far more interesting, as it would hold information about the (time-dependent) localization of that valence excitation. Thus, I want to close the core of this thesis with an encouragement to stay curious for the next experiments, as the expected improvement in background suppression by moving to a non-collinear geometry already gives a hopeful outlook to observing such a process.

---

[1] In this experiment, occasional long-term timing drifts made it necessary to constantly scan over several picoseconds in relative delay in order to ensure that the perfect time-overlap is included in the scanned range. Thus, a more reliable arrival time stability will directly increase the effective measurement time at the time-overlap.

Chapter 7

Conclusion

As F. Bencivenga remarks [102], the concepts needed to understand non-linear optics were already in the hands of Maxwell and Lorentz in the late 19th century, and the relevant equations might have been formulated by them if they had deemed it necessary to include anharmonic terms in the oscillator model of the atom and expanded the field equations using a power series. But the experimental methods of the time did not enable research in this direction, until the development of the laser in 1960 [16], which was promptly followed by the observation of second harmonic generation one year later [17]. Similarly, non-linear methods in the XUV and X-ray regimes have been largely ignored until the advent of XFELs was foreseeable to provide for the first time the high X-ray fluences required to realize non-linear X-ray spectroscopy methods [102].

With XFELs having been available for user operation for just over a decade, we finally see a rapid development of non-linear X-ray methods. Nevertheless, there were and are significant experimental hurdles to overcome, three of which this thesis addressed in the following order:

First, the spectral intensity fluctuation of SASE-FEL-radiation requires adequate normalization to enable spectroscopic transmission studies with high sensitivity. Second, as non-linear X-ray studies involve the absorption of high-fluences, a practical understanding of non-linear absorption needs to be established; this means studying the interplay of high levels of X-ray absorption with the processes of core-hole-decay, electronic scattering, and thermalization. Third, wave-mixing processes between different colors of X-rays as well as between X-rays/XUV and optical/IR photons must be demonstrated experimentally.

Consequently, this thesis first presents a scheme for sensitive linear transmission measurements at SASE-XFELs, namely the split-beam normalization technique; different implementations of this scheme were discussed, two of them in dedicated technical publications[1, 2]:[1] One uses a monochromator upstream of the sample; the other, foregoing monochromatization, exposes the sample to the full SASE-bandwidth and uses a spectrometer downstream to analyze both beams. Using the latter setup, a pump-probe study on the antiferromagnetic response of nickel oxide to sub-gap optical excitation was shown as an application example, revealing a strong coupling of the sub-bandgap excitation to the magnetic spin system, in particular the 1 THz magnon mode.

---

[1] The third setup used in [4] is partly discussed therein, and a full technical publication is available for the successor of this setup after further development [8], but is not printed in this thesis.

Next, a split-beam normalization scheme was utilized to measure the non-linearities emerging in the X-ray absorption of nickel at high X-ray fluences, and a rate model was developed in order to understand the electron population dynamics within the pulse duration, in particular around a core-resonance [4]. Remarkably, the model accurately describes a large part of the non-linear effects, although it operates on a picture of independent electrons and no time-dependent changes to the density of states are considered [5]. Together, the experiment and model reveal that electronic scattering cascades are a major driver in both thermal and non-thermal redistribution of valence electrons.

Furthermore, a conceptually very similar study is presented, but using broadband excitation of the sample (this time a Co/Pt multilayer) [6]. We find that due to the broadband excitation, significant stimulated X-ray emission is observed in addition to the processes observed in the monochromatic study on nickel, although inhibited partly by the aforementioned electron redistribution processes. Nevertheless, the study represents the first spectroscopic implementation of externally stimulated RIXS in a solid, and with that a big step towards the realization of wave-mixing techniques for material science.

Lastly, we demonstrated the first SFG and DFG between two IR and one XUV photon in a solid [7]. The results of the study emphasize the utility of material resonances, in particular those of excitonic character, to enhance the non-linear susceptibility in spectroscopic experiments. In addition to the background-free detection of SFG and DFG signals, the study demonstrates a sensitivity to the coupling strength between excited states, which constitutes one of the core promises of wave-mixing studies.

In summary, I believe that the work presented in this thesis contributes significantly to the development of non-linear X-ray spectroscopy on various fronts, from the development of suitable normalization schemes [1, 2, 8] over the understanding of the relevant mechanisms in non-linear X-ray absorption around resonances [4, 5] to the exploitation of stimulated emission [6] and finally XUV-IR-wave-mixing [7]. Nevertheless, further experimental developments will be needed to establish that X-ray-wave-mixing techniques can deliver the significant scientific advancement in molecular and solid-state dynamics that they promise [80, 94–96].

Chapter 8

Outlook

This thesis has discussed, and to a modest degree contributed to, some of the significant advances in XFEL-based non-linear spectroscopies in the last decade. These have included the demonstration of most of the relevant non-linear processes, ranging from saturated [67] to multi-photon [25] absorption, second harmonic [85] and sum/difference-frequency generation [87], amplified spontaneous X-ray emission [82], externally stimulated X-ray emission in gases [83] and solids [6], as well as FWM using transient gratings [101], as well direct FWM between XUV and IR photons [7, 110].

Nevertheless, current experiments are still severely limited in directly translating more complex non-linear wave-mixing schemes from the optical regime [51, 92, 93, 178, 201–203]. Overall, many of these demonstrations were done without explicit control over the relative phases of the pulses involved. This is because, in contrast to the extremely well-established technology at longer wavelengths, even modern XFEL-facilities are still limited in regard to the control over temporal coherence, multi-color-operation, and phase-stability in relation to optical pump lasers.

Now, the ongoing challenge is on the one hand to further develop X-ray sources for increasingly short, coherent, and well-defined pulses, ideally combining several colors, and on the other hand to develop experimental schemes which work within the confines of the available sources. With the accelerating pace of advances, the field is making steady progress towards unlocking FWM techniques such as for example XCRS, to measure coherent wave-packet dynamics between targeted scattering centers through various kinds of excitations - from nuclear modes like phonons, structural relaxation, and heat diffusion, over electronic excitations like excitons and plasmons to mixed degrees of freedom like polarons and polaritons - with increasingly higher photon energies [102].
Together, the coming improvements on light-sources, experiments and theoretical understanding will doubtlessly translate the recently demonstrated X-ray wave-mixing processes into increasingly wider application and deeper scientific insights.

The broader X-ray community [. . .] only recently has ventured into the exploration of effects outside the conventional first-order description of light. [. . .] It is envisioned that the exploration of higher-order coherence in the X-ray regime may reveal new aspects of the complex nature of light, and it may well become a new paradigm for obtaining unprecedented structural resolution. - J. Stöhr [204]

Bibliography

1. Engel, R. Y. *et al.* Shot noise limited soft X-ray absorption spectroscopy in solution at a SASE-FEL using a transmission grating beam splitter. *Structural Dynamics* **8,** 014303. `https://doi.org/10.1063/4.0000049` (Jan. 2021).
2. Engel, R. Y. *et al.* Parallel Broadband Femtosecond Reflection Spectroscopy at a Soft X-ray Free-Electron Laser. *Applied Sciences* **10,** 6947. ISSN: 2076-3417. `https://www.doi.org/10.3390/app10196947` (Oct. 2020).
3. Wang, X. *et al.* Ultrafast manipulation of the NiO antiferromagnetic order via sub-gap optical excitation. *Faraday Discussions* **237,** 300–316. `https://doi.org/10.1039/D2FD00005A` (Feb. 2022).
4. Engel, R. Y. *et al.* Electron Dynamics at High-Energy Densities in Nickel from Non-linear Resonant X-ray Absorption Spectra. *arXiv,* 2211.17008. `https://arxiv.org/abs/2211.17008` (Nov. 2022).
5. Engel, R. Y., Scholz, M., Schunck, J. O. & Beye, M. A Rate Model of Electron Populations for Non-linear High-Fluence X-ray Absorption Near-Edge Spectra. *arXiv,* 2211.17144. `https://arxiv.org/abs/2211.17144` (Nov. 2022).
6. Higley, D. J. *et al.* Stimulated resonant inelastic X-ray scattering in a solid. *Communications Physics* **5,** 83. `https://doi.org/10.1038/s42005-022-00857-8` (Apr. 2022).
7. Rottke, H. *et al.* Probing electron and hole colocalization by resonant four-wave mixing spectroscopy in the extreme ultraviolet. *Science Advances* **8,** eabn5127. `https://doi.org/10.1126/sciadv.abn5127` (May 2022).
8. Guyader, L. L. *et al.* Photon-shot-noise-limited transient absorption soft X-ray spectroscopy at the European XFEL. *Journal of Synchrotron Radiation* **30,** 284–300. `https://doi.org/10.1107/S1600577523000619` (Jan. 2023).
9. Beye, M. *et al.* Non-linear soft X-ray methods on solids with MUSIX — the multidimensional spectroscopy and inelastic X-ray scattering endstation. *Journal of Physics: Condensed Matter* **31,** 014003. `https://doi.org/10.1088/1361-648X/aaedf3` (Jan. 2019).
10. Dziarzhytski, S. *et al.* The TRIXS end-station for femtosecond time-resolved resonant inelastic X-ray scattering experiments at the soft X-ray free-electron laser FLASH. *Structural Dynamics* **7,** 054301. `https://doi.org/10.1063/4.0000029` (Sept. 2020).
11. Lojewski, T. *et al.* The interplay of local electron correlations and ultrafast spin dynamics in fcc Ni. *arXiv,* 2210.13162. `http://arxiv.org/abs/2210.13162` (Oct. 2022).

12. Grånäs, O. *et al.* Ultrafast modification of the electronic structure of a correlated insulator. *Physical Review Research* **4,** L032030. `https://doi.org/10.1103/PhysRevResearch.4.L032030` (3 Aug. 2022).

13. Thielemann-Kühn, N. *et al.* Optical control of 4f orbital state in rare-earth metals. *arXiv,* 2106.09999. eprint: `2106.09999`. `http://arxiv.org/abs/2106.09999` (June 2021).

14. Schunck, J. O. *et al.* Soft X-ray imaging spectroscopy with micrometer resolution. *Optica* **8,** 156. `https://doi.org/10.1364/OPTICA.405977` (Feb. 2021).

15. Schunck, J. O. *et al.* Microstructure effects on the phase transition behavior of a prototypical quantum material. *Scientific Reports* **12,** 10464. `https://doi.org/10.1038/s41598-022-13872-0` (Dec. 2022).

16. Maiman, T. H. Stimulated optical radiation in ruby. *Nature* **187,** 493–494. `https://doi.org/10.1038/187493a0` (Aug. 1960).

17. Franken, P. A., Hill, A. E., Peters, C. W. & Weinreich, G. Generation of Optical Harmonics. *Physical Review Letters* **7,** 118–119. `https://doi.org/10.1103/PhysRevLett.7.118` (4 Aug. 1961).

18. Tiedtke, K., Treusch, R., Ploenjes-Palm, E., Beye, M. & Schreiber, S. FLASH2020+ Conceptual Design Report. *Deutsches Elektronen-Synchrotron.* `https://doi.org/10.3204/PUBDB-2020-00465` (Mar. 2020).

19. Schroer, C. *et al.* PETRA IV Conceptual Design Report. *Deutsches Elektronen Synchrotron.* `https://doi.org/10.3204/PUBDB-2019-03613` (Nov. 2019).

20. Bostedt, C. *et al.* Linac Coherent Light Source: The first five years. *Rev. Mod. Phys.* **88,** 015007. `https://doi.org/10.1103/RevModPhys.88.015007` (1 Mar. 2016).

21. Rossbach, J., Schneider, J. R. & Wurth, W. 10 years of pioneering X-ray science at the Free-Electron Laser FLASH at DESY. *Physics Reports* **808,** 1–74. ISSN: 0370-1573. `https://doi.org/10.1016/j.physrep.2019.02.002` (May 2019).

22. Zastrau, U. *et al.* Bremsstrahlung and line spectroscopy of warm dense aluminum plasma heated by XUV free-electron-laser radiation. *Physical Review E* **78,** 066406. `https://doi.org/10.1103/PhysRevE.78.066406` (6 Dec. 2008).

23. Humphries, O. S. *et al.* Probing the Electronic Structure of Warm Dense Nickel via Resonant Inelastic X-ray Scattering. *Physical Review Letters* **125,** 195001. ISSN: 10797114. arXiv: `2001.05813`. `https://doi.org/10.1103/PhysRevLett.125.195001` (Nov. 2020).

24. Wirok-Stoletow, S. *et al.* Nonsequential two-photon absorption in solid Ge irradiated by an intense X-ray free-electron-laser pulse. *Physical Review A* **106,** 023118. ISSN: 2469-9926. `https://doi.org/10.1103/PhysRevA.106.023118` (Aug. 2022).

25. Tamasaku, K. *et al.* X-ray two-photon absorption competing against single and sequential multiphoton processes. *Nature Photonics* **8,** 313–316. ISSN: 1749-4885. `https://doi.org/10.1038/nphoton.2014.10` (Apr. 2014).

26. Vinko, S. M. *et al.* Time-Resolved XUV Opacity Measurements of Warm Dense Aluminum. *Physical Review Letters* **124,** 225002. ISSN: 10797114. eprint: `2001.06639`. `https://doi.org/10.1103/PhysRevLett.124.225002` (June 2020).

27. Kang, G. & Cho, B. I. Investigation of warm dense matter using time-resolved X-ray absorption spectroscopy with third- and fourth-generation light sources. *Current Applied Physics* **30,** 58–68. ISSN: 15671739. `https://doi.org/10.1016/j.cap.2021.05.006` (Oct. 2021).

28. García Saiz, E. *et al.* Probing warm dense lithium by inelastic X-ray scattering. *Nature Physics* **4,** 940–944. ISSN: 17452481. `https://doi.org/10.1038/nphys1103` (Oct. 2008).

29. Vinko, S. M. *et al.* Electronic Structure of an XUV Photogenerated Solid-Density Aluminum Plasma. *Physical Review Letters* **104,** 225001. `https://doi.org/10.1103/PhysRevLett.104.225001` (22 June 2010).

30. Vinko, S. M. *et al.* Creation and diagnosis of a solid-density plasma with an X-ray free-electron laser. *Nature* **482,** 59–62. ISSN: 0028-0836. `https://doi.org/10.1038/nature10746` (Feb. 2012).

31. Cho, B. I. *et al.* Resonant Kα Spectroscopy of Solid-Density Aluminum Plasmas. *Physical Review Letters* **109,** 245003. ISSN: 0031-9007. `https://doi.org/10.1103/PhysRevLett.109.245003` (Dec. 2012).

32. Vinko, S. M. X-ray free-electron laser studies of dense plasmas. *Journal of Plasma Physics* **81,** 365810501. ISSN: 0022-3778. `https://doi.org/10.1017/S0022377815000902` (Oct. 2015).

33. Bailey, J. E. *et al.* A higher-than-predicted measurement of iron opacity at solar interior temperatures. *Nature* **517,** 56–59. ISSN: 14764687. `https://doi.org/10.1038/nature14048` (Jan. 2015).

34. Preston, T. R. *et al.* Measurements of the K-Shell Opacity of a Solid-Density Magnesium Plasma Heated by an X-Ray Free-Electron Laser. *Physical Review Letters* **119,** 1–5. ISSN: 10797114. `https://doi.org/10.1103/PhysRevLett.119.085001` (Aug. 2017).

35. Hollebon, P. *et al.* Ab initio simulations and measurements of the free-free opacity in aluminum. *Physical Review E* **100,** 043207. ISSN: 2470-0045. arXiv: `1806.02726`. `https://doi.org/10.1103/PhysRevE.100.043207` (Oct. 2019).

36. Pietzsch, A. *et al.* Towards time resolved core level photoelectron spectroscopy with femtosecond X-ray free-electron lasers. *New Journal of Physics* **10,** 033004. ISSN: 1367-2630. `https://doi.org/10.1088/1367-2630/10/3/033004` (Mar. 2008).

37. Fognini, A. *et al.* Ultrafast reduction of the total magnetization in iron. *Applied Physics Letters* **104,** 032402. ISSN: 0003-6951. `https://doi.org/10.1063/1.4862476` (Jan. 2014).

38. Först, M. *et al.* Melting of Charge Stripes in Vibrationally Driven $La_{1.875}Ba_{0.125}CuO_4$. *Physical Review Letters* **112,** 157002. ISSN: 0031-9007. `https://doi.org/10.1103/PhysRevLett.112.157002` (Apr. 2014).

39. Staub, U. *et al.* Persistence of magnetic order in a highly excited Cu^{2+} state in CuO. *Physical Review B* **89,** 220401. ISSN: 1098-0121. `https://doi.org/10.1103/PhysRevB.89.220401` (June 2014).

40. Gutt, C. *et al.* Resonant magnetic scattering with soft X-ray pulses from a free-electron laser operating at 1.59 nm. *Physical Review B* **79,** 212406. ISSN: 1098-0121. `https://doi.org/10.1103/PhysRevB.79.212406` (June 2009).

41. Beye, M., Sorgenfrei, F., Schlotter, W. F., Wurth, W. & Föhlisch, A. The liquid-liquid phase transition in silicon revealed by snapshots of valence electrons. *Proceedings of the National Academy of Sciences* **107,** 16772–16776. ISSN: 0027-8424. `https://doi.org/10.1073/pnas.1006499107` (Sept. 2010).

42. Pontius, N. *et al.* Time-resolved resonant soft X-ray diffraction with free-electron lasers: Femtosecond dynamics across the Verwey transition in magnetite. *Applied Physics Letters* **98,** 182504. ISSN: 0003-6951. `https://doi.org/10.1063/1.3584855` (May 2011).

43. Pfau, B. *et al.* Ultrafast optical demagnetization manipulates nanoscale spin structure in domain walls. *Nature Communications* **3,** 1100. ISSN: 2041-1723. `https://doi.org/10.1038/ncomms2108` (Jan. 2012).

44. Wang, T. *et al.* Femtosecond Single-Shot Imaging of Nanoscale Ferromagnetic Order in Co/Pt Multilayers Using Resonant X-ray Holography. *Physical Review Letters* **108,** 267403. ISSN: 0031-9007. `https://doi.org/10.1103/PhysRevLett.108.267403` (June 2012).

45. Dell'Angela, M. *et al.* Real-Time Observation of Surface Bond Breaking with an X-ray Laser. *Science* **339,** 1302–1305. ISSN: 0036-8075. `https://doi.org/10.1126/science.1231711` (Mar. 2013).

46. Johnson, S. L. *et al.* Femtosecond Dynamics of the Collinear-to-Spiral Antiferromagnetic Phase Transition in CuO. *Physical Review Letters* **108,** 037203. ISSN: 0031-9007. arXiv: `1106.6128`. `https://doi.org/10.1103/PhysRevLett.108.037203` (Jan. 2012).

47. Zhang, W. *et al.* Tracking excited-state charge and spin dynamics in iron coordination complexes. *Nature* **509,** 345–348. ISSN: 0028-0836. `https://doi.org/10.1038/nature13252` (May 2014).

48. Shablaev, S. I. & Pisarev, R. V. Giant nonlinear absorption in the NiO antiferromagnet. *Physics of the Solid State* **45,** 1742–1745. ISSN: 1063-7834. `https://doi.org/10.1134/1.1611243` (Sept. 2003).

49. Tamasaku, K. *et al.* Nonlinear Spectroscopy with X-ray Two-Photon Absorption in Metallic Copper. *Physical Review Letters* **121,** 083901. ISSN: 0031-9007. `https://doi.org/10.1103/PhysRevLett.121.083901` (Aug. 2018).

50. Straub, M. *et al.* Differential Measurement of Electron Ejection after Two-Photon Two-Electron Excitation of Helium. *Physical Review Letters* **129,** 183204. `https://doi.org/10.1103/PhysRevLett.129.183204` (18 Oct. 2022).

51. Boyd, R. W. *Nonlinear optics* 3rd edition. ISBN: 0123694701. `https://dl.acm.org/doi/abs/10.5555/1817101` (Academic press, 2008).

52. *WavemiX: EUV and soft to hard X-ray non-linear science network* `https://www.elettra.eu/Prj/WAVEMIX/`.

53. Young, L. *et al.* Femtosecond electronic response of atoms to ultra-intense X-rays. *Nature* **466,** 56–61. ISSN: 00280836. `https://doi.org/10.1038/nature09177` (July 2010).

54. Rudek, B. *et al.* Ultra-efficient ionization of heavy atoms by intense X-ray free-electron laser pulses. *Nature Photonics* **6,** 858–865. ISSN: 17494885. `https://doi.org/10.1038/nphoton.2012.261` (Sept. 2012).

55. Hoener, M. *et al.* Ultraintense X-ray induced ionization, dissociation, and frustrated absorption in molecular nitrogen. *Physical Review Letters* **104,** 253002. ISSN: 00319007. `https://doi.org/10.1103/PhysRevLett.104.253002` (June 2010).

56. Fang, L. *et al.* Multiphoton ionization as a clock to reveal molecular dynamics with intense short X-ray free electron laser pulses. *Physical Review Letters* **109,** 263001. ISSN: 00319007. `https://doi.org/10.1103/PhysRevLett.109.263001` (Dec. 2012).

57. Berrah, N. *et al.* Multiphoton ionization and fragmentation of molecules with the LCLS X-ray FEL. *Journal of Electron Spectroscopy and Related Phenomena* **196,** 34–37. ISSN: 03682048. `http://dx.doi.org/10.1016/j.elspec.2013.10.009` (Oct. 2014).

58. Schorb, S. *et al.* Size-dependent ultrafast ionization dynamics of nanoscale samples in intense femtosecond X-ray free-electron-laser pulses. *Physical Review Letters* **108,** 233401. ISSN: 00319007. `https://doi.org/10.1103/PhysRevLett.108.233401` (June 2012).

59. Thomas, H. *et al.* Explosions of xenon clusters in ultraintense femtosecond X-ray pulses from the LCLS free electron laser. *Physical Review Letters* **108,** 133401. ISSN: 00319007. `https://doi.org/10.1103/PhysRevLett.108.133401` (Mar. 2012).

60. Gorkhover, T. *et al.* Nanoplasma dynamics of single large xenon clusters irradiated with superintense X-ray pulses from the linac coherent light source free-electron laser. *Physical Review Letters* **108,** 245005. ISSN: 00319007. `https://doi.org/10.1103/PhysRevLett.108.245005` (June 2012).

61. Zhou, X. *et al.* Space charge effect and mirror charge effect in photoemission spectroscopy. *Journal of Electron Spectroscopy and Related Phenomena* **142,** 27–38. ISSN: 0368-2048. `https://doi.org/10.1016/j.elspec.2004.08.004` (Jan. 2005).

62. Schönhense, B. *et al.* Multidimensional photoemission spectroscopy—the space-charge limit. *New Journal of Physics* **20,** 033004. `https://doi.org/10.1088/1367-2630/aaa262` (Mar. 2018).

63. Nagler, B. *et al.* Turning solid aluminium transparent by intense soft X-ray photoionization. *Nature Physics* **5,** 693–696. `https://doi.org/10.1038/nphys1341` (July 2009).

64. Hoffmann, L. *et al.* Saturable Absorption of Free-Electron Laser Radiation by Graphite near the Carbon K-Edge. *Journal of Physical Chemistry Letters* **13,** 8963–8970. ISSN: 19487185. `https://doi.org/10.1021/acs.jpclett.2c01020` (Oct. 2022).

65. Recoules, V. & Mazevet, S. Temperature and density dependence of XANES spectra in warm dense aluminum plasmas. *Physical Review B* **80,** 064110. ISSN: 1098-0121. `https://doi.org/10.1103/PhysRevB.80.064110` (Aug. 2009).

66. Di Cicco, A. *et al.* Interplay of electron heating and saturable absorption in ultrafast extreme ultraviolet transmission of condensed matter. *Physical Review B* **90,** 220303. `https://doi.org/10.1103/PhysRevB.90.220303` (22 Dec. 2014).

67. Yoneda, H. *et al.* Saturable absorption of intense hard X-rays in iron. *Nature Communications* **5,** 5080. `https://doi.org/10.1038/ncomms6080` (Oct. 2014).

68. Rackstraw, D. S. *et al.* Saturable Absorption of an X-ray Free-Electron-Laser Heated Solid-Density Aluminum Plasma. *Physical Review Letters* **114,** 015003. `https://doi.org/10.1103/PhysRevLett.114.015003` (1 Jan. 2015).

69. Principi, E. *et al.* Free electron laser-driven ultrafast rearrangement of the electronic structure in Ti. *Structural Dynamics* **3,** 023604. `https://doi.org/10.1063/1.4935687` (Mar. 2016).

70. Chen, Z. *et al.* Ultrafast Self-Induced X-Ray Transparency and Loss of Magnetic Diffraction. *Physical Review Letters* **121,** 137403. ISSN: 0031-9007. `https://doi.org/10.1103/PhysRevLett.121.137403` (Sept. 2018).

71. Bernstein, D. P. *et al.* Near edge X-ray absorption fine structure spectroscopy with X-ray free-electron lasers. *Applied Physics Letters* **95,** 10–13. ISSN: 00036951. `https://doi.org/10.1063/1.3236540` (Sept. 2009).

72. Higley, D. J. *et al.* Femtosecond X-ray induced changes of the electronic and magnetic response of solids from electron redistribution. *Nature Communications* **10,** 5289. `https://doi.org/10.1038/s41467-019-13272-5` (Nov. 2019).

73. Brenner, G. *et al.* Normalized single-shot X-ray absorption spectroscopy at a free-electron laser. *Optics Letters* **44,** 2157. ISSN: 0146-9592. `https://doi.org/10.1364/OL.44.002157` (Apr. 2019).

74. Schreck, S. *et al.* Reabsorption of Soft X-ray Emission at High X-ray Free-Electron Laser Fluences. *Physical Review Letters* **113,** 153002. ISSN: 0031-9007. `https://doi.org/10.1103/PhysRevLett.113.153002` (Oct. 2014).

75. Hatada, K. & Di Cicco, A. Modeling saturable absorption for ultra short X-ray pulses. *Journal of Electron Spectroscopy and Related Phenomena* **196,** 177–180. ISSN: 0368-2048. `https://doi.org/10.1016/j.elspec.2014.02.012` (Oct. 2014).

76. Hantschmann, M. & Föhlisch, A. A rate model approach for FEL pulse induced transmissions changes, saturable absorption, X-ray transparency and stimulated emission. *Journal of Electron Spectroscopy and Related Phenomena* **256,** 147139. ISSN: 0368-2048. `https://doi.org/10.1016/j.elspec.2021.147139` (Apr. 2022).

77. Medvedev, N., Tkachenko, V., Lipp, V., Li, Z. & Ziaja, B. Various damage mechanisms in carbon and silicon materials under femtosecond X-ray irradiation. *4open* **1,** 3. `https://doi.org/10.1051/fopen/2018003` (Aug. 2018).

78. Lipp, V. *et al.* Density functional tight binding approach utilized to study X-ray-induced transitions in solid materials. *Scientific Reports* **12,** 1551. `https://doi.org/10.1038/s41598-022-04775-1` (Jan. 2022).

79. Gel'mukhanov, F. & Ågren, H. Resonant X-ray Raman scattering. *Physics Reports* **312,** 87–330. ISSN: 03701573. `https://doi.org/10.1016/S0370-1573(99)00003-4` (May 1999).

80. Patterson, B. D. Resource Letter on Stimulated Inelastic X-ray Scattering at an XFEL. *Slac-Tn* **026.** `https://doi.org/10.2172/992898` (Sept. 2010).

81. Gel'mukhanov, F., Odelius, M., Polyutov, S. P., Föhlisch, A. & Kimberg, V. Dynamics of resonant X-ray and Auger scattering. *Reviews of Modern Physics* **93,** 035001. ISSN: 0034-6861. `https://doi.org/10.1103/RevModPhys.93.035001` (July 2021).

82. Beye, M. *et al.* Stimulated X-ray emission for materials science. *Nature* **501,** 191–194. `https://doi.org/10.1038/nature12449` (Aug. 2013).

83. Weninger, C. *et al.* Stimulated Electronic X-ray Raman Scattering. *Physical Review Letters* **111,** 233902. `https://doi.org/10.1103/PhysRevLett.111.233902` (23 Dec. 2013).

84. Schreck, S., Beye, M. & Föhlisch, A. Implications of stimulated resonant X-ray scattering for spectroscopy, imaging, and diffraction in the regime from soft to hard X-rays. *Journal of Modern Optics* **62,** S34–S45. `https://doi.org/10.1080/09500340.2015.1052028` (July 2015).

85. Shwartz, S. *et al.* X-ray Second Harmonic Generation. *Physical Review Letters* **112,** 163901. ISSN: 0031-9007. `https://doi.org/10.1103/PhysRevLett.112.163901` (Apr. 2014).

86. Lam, R. K. *et al.* Soft X-ray Second Harmonic Generation as an Interfacial Probe. *Physical Review Letters* **120,** 023901. ISSN: 10797114. `https://doi.org/10.1103/PhysRevLett.120.023901` (Jan. 2018).

87. Glover, T. E. *et al.* X-ray and optical wave mixing. *Nature* **488,** 603–608. ISSN: 00280836. `https://doi.org/10.1038/nature11340` (Aug. 2012).

88. Boyer, V., Marino, A. M., Pooser, R. C. & Lett, P. D. Entangled images from four-wave mixing. *Science* **321,** 544–547. ISSN: 00368075. `https://doi.org/10.1126/science.1158275` (July 2008).

89. Foster, M. A. *et al.* Broad-band optical parametric gain on a silicon photonic chip. *Nature* **441,** 960–963. ISSN: 14764687. `https://doi.org/10.1038/nature04932` (June 2006).

90. Chen, P. Y. & Alù, A. Subwavelength imaging using phase-conjugating nonlinear nanoantenna arrays. *Nano Letters* **11,** 5514–5518. ISSN: 15306984. `https://doi.org/10.1021/nl203354b` (Nov. 2011).

91. Strauss, C. E. M. & Funk, D. J. Broadly tunable difference-frequency generation of VUV using two-photon resonances in H_2 and Kr. *Optics Letters* **16,** 1192. ISSN: 0146-9592. `https://doi.org/10.1364/ol.16.001192` (Aug. 1991).

92. Brixner, T. *et al.* Two-dimensional spectroscopy of electronic couplings in photosynthesis. *Nature* **434,** 625–628. ISSN: 0028-0836. `https://doi.org/10.1038/nature03429` (Mar. 2005).

93. Cheng, J.-X. & Xie, X. S. Coherent Anti-Stokes Raman Scattering Microscopy: Instrumentation, Theory, and Applications. *The Journal of Physical Chemistry B* **108,** 827–840. ISSN: 1520-6106. `https://doi.org/10.1021/jp035693v` (Jan. 2004).

94. Tanaka, S. & Mukamel, S. Coherent X-ray Raman Spectroscopy: A Nonlinear Local Probe for Electronic Excitations. *Physical Review Letters* **89,** 4–7. ISSN: 10797114. `https://doi.org/10.1103/PhysRevLett.89.043001` (July 2002).

95. Mukamel, S. Multiple core-hole coherence in X-ray four-wave-mixing spectroscopies. *Physical Review B* **72,** 235110. `https://doi.org/10.1103/PhysRevB.72.235110` (23 Dec. 2005).

96. Mukamel, S., Healion, D., Zhang, Y. & Biggs, J. D. Multidimensional attosecond resonant X-ray spectroscopy of molecules: Lessons from the optical regime. *Annual Review of Physical Chemistry* **64,** 101–127. ISSN: 0066426X. `https://doi.org/10.1146/annurev-physchem-040412-110021` (Dec. 2013).

97. Kowalewski, M., Fingerhut, B. P., Dorfman, K. E., Bennett, K. & Mukamel, S. Simulating Coherent Multidimensional Spectroscopy of Nonadiabatic Molecular Processes: From the Infrared to the X-ray Regime. *Chemical Reviews* **117,** 12165–12226. ISSN: 15206890. `https://doi.org/10.1021/acs.chemrev.7b00081` (Sept. 2017).

98. Kroll, T. *et al.* Stimulated X-ray Emission Spectroscopy in Transition Metal Complexes. *Physical Review Letters* **120,** 133203. ISSN: 10797114. `https://doi.org/10.1103/PhysRevLett.120.133203` (Mar. 2018).

99. Young, L. *et al.* Roadmap of ultrafast X-ray atomic and molecular physics. *Journal of Physics B: Atomic, Molecular and Optical Physics* **51,** 032003. `https://dx.doi.org/10.1088/1361-6455/aa9735` (Jan. 2018).

100. Rouxel, J. R. *et al.* Hard X-ray transient grating spectroscopy on bismuth germanate. *Nature Photonics* **15,** 499–503. ISSN: 1749-4885. `http://doi.org/10.1038/s41566-021-00797-9` (July 2021).

101. Bencivenga, F. *et al.* Four-wave mixing experiments with extreme ultraviolet transient gratings. *Nature* **520,** 205–208. ISSN: 0028-0836. `https://doi.org/10.1038/nature14341` (Apr. 2015).

102. Bencivenga, F. *et al.* Nonlinear optics with coherent free electron lasers. *Physica Scripta* **2016,** 014003. ISSN: 02811847. `https://doi.org/10.1088/0031-8949/T169/1/014003` (Aug. 2016).

103. Svetina, C. *et al.* Towards X-ray transient grating spectroscopy. *Optics Letters* **44,** 574. ISSN: 0146-9592. `https://doi.org/10.1364/ol.44.000574` (Jan. 2019).

104. Bencivenga, F. *et al.* Nanoscale transient gratings excited and probed by extreme ultraviolet femtosecond pulses. *Science Advances* **5,** 3–10. ISSN: 23752548. `https://doi.org/10.1126/sciadv.aaw5805` (July 2019).

105. Lutman, A. A. *et al.* Experimental demonstration of femtosecond two-color X-ray free-electron lasers. *Physical Review Letters* **110,** 134801. ISSN: 00319007. `https://doi.org/10.1103/PhysRevLett.110.134801` (Mar. 2013).

106. Lutman, A. A. *et al.* Demonstration of single-crystal self-seeded two-color X-ray free-electron lasers. *Physical Review Letters* **113,** 254801. ISSN: 10797114. `https://doi.org/10.1103/PhysRevLett.113.254801` (Dec. 2014).

107. Lutman, A. A. *et al.* Fresh-slice multicolour X-ray free-electron lasers. *Nature Photonics* **10,** 745–750. ISSN: 17494893. `https://doi.org/10.1038/nphoton.2016.201` (Oct. 2016).

108. Bencivenga, F. *et al.* Multi-colour pulses from seeded free-electron-lasers: Towards the development of non-linear core-level coherent spectroscopies. *Faraday Discussions* **171,** 487–503. ISSN: 13645498. `https://doi.org/10.1039/c4fd00100a` (May 2014).

109. Bencivenga, F. *et al. An approach for realizing four-wave-mixing experiments stimulated by two-color extreme ultraviolet pulses* in *International Conference on X-ray Lasers 2020* (ed Bleiner, D.) **11886** (SPIE, 2021), 118860E. `https://doi.org/10.1117/12.2593345`.

110. Gaynor, J. D. *et al.* Solid state core-exciton dynamics in NaCl observed by tabletop attosecond four-wave mixing spectroscopy. *Physical Review B* **103,** 245140. ISSN: 2469-9950. arXiv: `2103.14590`. `https://doi.org/10.1103/PhysRevB.103.245140` (June 2021).

111. Robinson, I., Gruebel, G. & Mochrie, S. Focus on X-ray Beams with High Coherence. *New Journal of Physics* **12,** 035002. `https://dx.doi.org/10.1088/1367-2630/12/3/035002` (Mar. 2010).

112. Shintake, T. *Review of the worldwide SASE FEL development* in *2007 IEEE Particle Accelerator Conference (PAC)* (July 2007), 89–93. `https://ieeexplore.ieee.org/document/4440331`.

113. Rupp, K. *50 years of microprocessor trend data* `https://github.com/karlrupp/microprocessor-trend-data`. 2022.

114. Margaritondo, G. & Rebernik Ribič, P. A simplified description of X-ray free-electron lasers. *Journal of Synchrotron Radiation* **18,** 101–108. `https://doi.org/10.1107/S090904951004896X` (Mar. 2011).

115. Wille, K. *Physik der Teilchenbeschleuniger und Synchrotronstrahlungsquellen: Eine Einführung* ISBN: 978-3-663-11039-2 (Springer-Verlag, 2013).

116. Attwood, D. *Soft X-rays and Extreme Ultraviolet Radiation* ISBN: 9780521652148. `https://doi.org/10.1017/CBO9781139164429` (Cambridge University Press, Aug. 1999).

117. Martins, M. *Lecture: Röntgenphysik - Insertion Devices* University, Hamburg. 2018.

118. Saldin, E. L., Schneidmiller, E. A. & Yurkov, M. *The Physics of Free Electron Lasers* ISBN: 9783540662662 (Springer, 1999).

119. Saldin, E., Schneidmiller, E. & Yurkov, M. Statistical properties of radiation from VUV and X-ray free electron laser. *Optics Communications* **148,** 383–403. ISSN: 0030-4018. `https://doi.org/10.1016/S0030-4018(97)00670-6` (Mar. 1998).

120. Saldin, E., Schneidmiller, E. & Yurkov, M. Statistical properties of the radiation from VUV FEL at DESY operating at 30nm wavelength in the femtosecond regime. *Nuclear Instruments and Methods in Physics Research Section A: Accelerators, Spectrometers, Detectors and Associated Equipment* **562,** 472–486. ISSN: 0168-9002. `https://doi.org/10.1016/j.nima.2006.02.166` (June 2006).

121. Feng, C. *et al.* Coherent extreme ultraviolet free-electron laser with echo-enabled harmonic generation. *Physical Review Accelerators and Beams* **22,** 050703. ISSN: 2469-9888. `https://doi.org/10.1103/PhysRevAccelBeams.22.050703` (May 2019).

122. Rebernik Ribič, P. *et al.* Coherent soft X-ray pulses from an echo-enabled harmonic generation free-electron laser. *Nature Photonics* **13,** 555–561. ISSN: 17494893. `http://dx.doi.org/10.1038/s41566-019-0427-1` (May 2019).

123. Paraskaki, G. *et al.* Study of a seeded oscillator-amplifier. *Proceedings of the 39th International Free-Electron Laser Conference, FEL 2019,* 234–237. `https://doi.org/10.18429/JACoW-FEL2019-TUP077` (Aug. 2019).

124. Serkez, S. Self-Seeding XFELs: Operation Principle and Challenges. *Synchrotron Radiation News* **29,** 10–14. ISSN: 19317344. `https://doi.org/10.1080/08940886.2016.1174037` (May 2016).

125. Bödewadt, J. *et al.* Recent results from FEL seeding at FLASH. *6th International Particle Accelerator Conference, IPAC 2015,* 1366–1369. `https://doi.org/10.18429/JACoW-IPAC2015-TUBC3` (May 2015).

126. Pfeifer, T., Jiang, Y., Düsterer, S., Moshammer, R. & Ullrich, J. Partial-coherence method to model experimental free-electron laser pulse statistics. *Optics Letters* **35,** 3441–3443. `https://doi.org/10.1364/OL.35.003441` (Oct. 2010).

127. Krinsky, S. & Gluckstern, R. L. Analysis of statistical correlations and intensity spiking in the self-amplified spontaneous-emission free-electron laser. *Physical Review Accelerators and Beams* **6,** 050701. `https://doi.org/10.1103/PhysRevSTAB.6.050701` (5 May 2003).

128. Düsterer, S. *et al.* Development of experimental techniques for the characterization of ultrashort photon pulses of extreme ultraviolet free-electron lasers. *Physical Review Accelerators and Beams* **17,** 120702. `https://doi.org/10.1103/PhysRevSTAB.17.120702` (12 Dec. 2014).

129. Serkez, S. *Analysis of statistical properties of FLASH radiation in spectral domain to characterize pulse duration* Master's Thesis. Ivan Franko Lviv National University / Deutsches Electronen Synchrotron. 2012.

130. Engel, R. *Real Time Analysis of FEL Radiation Spectra for the Estimation of Photon Pulse Duration* Bachelor's Thesis. Universität Oldenburg / Deutsches Electronen Synchrotron (DESY). 2015. `https://oops.uni-oldenburg.de/id/eprint/2203`.

131. Engel, R., Düsterer, S., Brenner, G. & Teubner, U. Quasi-real-time photon pulse duration measurement by analysis of FEL radiation spectra. *Journal of Synchrotron Radiation* **23,** 118–122. `https://doi.org/10.1107/S1600577515022997` (Jan. 2016).

132. Henke, B., Gullikson, E. & Davis, J. X-ray interactions: photoabsorption, scattering, transmission, and reflection at E= 50-30,000 eV, Z= 1-92. *Atomic Data and Nuclear Data Tables* **54,** 181–342. ISSN: 0092-640X. `https://doi.org/10.1006/adnd.1993.1013` (May 1993).

133. Watts, B. Calculation of the Kramers-Kronig transform of X-ray spectra by a piecewise Laurent polynomial method. *Optics Express* **22,** 23628. ISSN: 10944087. `https://doi.org/10.1364/oe.22.023628` (Sept. 2014).

134. Welton, T. A. Some Observable Effects of the Quantum-Mechanical Fluctuations of the Electromagnetic Field. *Physical Review* **74,** 1157–1167. `https://link.aps.org/doi/10.1103/PhysRev.74.1157` (9 Nov. 1948).

135. Krause, M. O. Atomic radiative and radiationless yields for K and L shells. *Journal of Physical and Chemical Reference Data* **8,** 307–327. `https://doi.org/10.1063/1.555594` (Oct. 1979).

136. Krause, M. O. & Oliver, J. Natural widths of atomic K and L levels, K α X-ray lines and several KLL Auger lines. *Journal of Physical and Chemical Reference Data* **8,** 329–338. `https://doi.org/10.1063/1.555595` (Oct. 1979).

137. Einstein, A. *Strahlungs-Emission und -Absorption nach der Quantentheorie* in *The collected papers of Albert Einstein* (July 1916), 363. `https://cds.cern.ch/record/632330`.

138. Hilborn, R. C. Einstein coefficients, cross sections, f values, dipole moments, and all that. *arXiv preprint physics/0202029.* `https://arxiv.org/abs/physics/0202029` (Feb. 2002).

139. Stöhr, J. *NEXAFS spectroscopy* `https://doi.org/10.1007/978-3-662-02853-7` (Springer Science & Business Media, 1992).

140. Dirac, P. A. M. On the theory of quantum mechanics. *Proceedings of the Royal Society of London. Series A, Containing Papers of a Mathematical and Physical Character* **112,** 661–677. ISSN: 0950-1207. `https://doi.org/10.1098/rspa.1926.0133` (Oct. 1926).

141. Campillo, I. *et al.* First-principles calculations of hot-electron lifetimes in metals. *Physical Review B* **61,** 13484–13492. `https://doi.org/10.1103/PhysRevB.61.13484` (20 May 2000).

142. Ziaja, B., London, R. A. & Hajdu, J. Ionization by impact electrons in solids: Electron mean free path fitted over a wide energy range. *Journal of Applied Physics* **99,** 033514. ISSN: 00218979. `https://doi.org/10.1063/1.2161821` (Feb. 2006).

143. Bethe, H. Zur Theorie des Durchgangs schneller Korpuskularstrahlen durch Materie. *Annalen der Physik* **397,** 325–400. ISSN: 15213889. `https://doi.org/10.1002/andp.19303970303` (Mar. 1930).

144. Sommerfeld, A. Zur Elektronentheorie der Metalle auf Grund der Fermischen Statistik. *Zeitschrift für Physik* **47,** 1–32. ISSN: 1434-6001. `https://doi.org/10.1007/BF01391052` (Jan. 1928).

145. Tanuma, S., Powell, C. J. & Penn, D. R. Calculations of electron inelastic mean free paths for 31 materials. *Surface and Interface Analysis* **11,** 577–589. ISSN: 10969918. `https://doi.org/10.1002/sia.740111107` (Apr. 1988).

146. Ashley, J. C. Energy loss rate and inelastic mean free path of low-energy electrons and positrons in condensed matter. *Journal of Electron Spectroscopy and Related Phenomena* **50,** 323–334. ISSN: 03682048. `https://doi.org/10.1016/0368-2048(90)87075-Y` (Oct. 1990).

147. Powell, C. J. & Jablonski, A. Consistency of calculated and measured electron inelastic mean free paths. *Journal of Vacuum Science & Technology A: Vacuum, Surfaces, and Films* **17,** 1122–1126. ISSN: 0734-2101. `https://doi.org/10.1116/1.581784` (July 1999).

148. Anisimov, S., Kapeliovich, B. L. & Perel'man, T. L. Electron emission from metal surfaces exposed to ultrashort laser pulses. *Sov. Phys. JETP* **39,** 375–377. `http://www.jetp.ras.ru/cgi-bin/dn/e_039_02_0375.pdf` (Feb. 1973).

149. Ibrahim, W. M., Elsayed-Ali, H. E., Bonner, C. E. & Shinn, M. Ultrafast investigation of electron dynamics in multi-layer metals. *International Journal of Heat and Mass Transfer* **47,** 2261–2268. ISSN: 00179310. `https://doi.org/10.1016/j.ijheatmasstransfer.2003.11.029` (May 2004).

150. Chen, J., Tzou, D. & Beraun, J. A semiclassical two-temperature model for ultrafast laser heating. *International Journal of Heat and Mass Transfer* **49,** 307–316. ISSN: 0017-9310. `https://doi.org/10.1016/j.ijheatmasstransfer.2005.06.022` (Jan. 2006).

151. Beye, M. *Ultrafast Dynamics in Solids Studied with Soft X-rays* PhD thesis (Universität Hamburg, 2010). ISBN: 978-3-86853-603-4. `https://www.dr.hut-verlag.de/978-3-86853-603-4.html`.

152. Reinert, F. & Hüfner, S. Photoemission spectroscopy—from early days to recent applications. *New Journal of Physics* **7,** 97. ISSN: 1367-2630. `https://doi.org/10.1088/1367-2630/7/1/097` (Apr. 2005).

153. Von Barth, U. & Grossmann, G. Dynamical effects in X-ray spectra and the final-state rule. *Physical Review B* **25,** 5150–5179. ISSN: 0163-1829. `https://link.aps.org/doi/10.1103/PhysRevB.25.5150` (Apr. 1982).

154. Miedema, P. S., Beye, M., Könnecke, R., Schiwietz, G. & Föhlisch, A. Thermal evolution of the band edges of 6H-SiC: X-ray methods compared to the optical band gap. *Journal of Electron Spectroscopy and Related Phenomena* **197,** 37–42. ISSN: 03682048. `http://dx.doi.org/10.1016/j.elspec.2014.08.003` (Dec. 2014).
155. Mårtensson, N. *et al.* On the relation between X-ray photoelectron spectroscopy and XAFS. *Journal of Physics: Conference Series* **430,** 012131. ISSN: 17426596. `https://doi.org/10.1088/1742-6596/430/1/012131` (July 2013).
156. Beye, M. *et al.* Measurement of the predicted asymmetric closing behaviour of the band gap of silicon using X-ray absorption and emission spectroscopy. *New Journal of Physics* **12,** 043011. ISSN: 13672630. `https://doi.org/10.1088/1367-2630/12/4/043011` (Apr. 2010).
157. Teo, B. K. *EXAFS: Basic principles and data analysis* ISBN: 978-3-642-50031-2. `https://doi.org/10.1007/978-3-642-50031-2` (Springer Science & Business Media, Dec. 2012).
158. Stöhr, J. Exploring the microscopic origin of magnetic anisotropies with X-ray magnetic circular dichroism (XMCD) spectroscopy. *Journal of Magnetism and Magnetic Materials* **200,** 470–497. ISSN: 0304-8853. `https://doi.org/10.1016/S0304-8853(99)00407-2` (Oct. 1999).
159. Stöhr, J. & Siegmann, H. C. in *Springer series in solid-state sciences* 1st ed. (Aug. 2006). ISBN: 978-3-540-30283-4. `https://doi.org/10.1007/978-3-540-30283-4`.
160. Smolentsev, G. *et al.* X-ray Emission Spectroscopy To Study Ligand Valence Orbitals in Mn Coordination Complexes. *Journal of the American Chemical Society* **131,** 13161–13167. ISSN: 0002-7863. `https://doi.org/10.1021/ja808526m` (Sept. 2009).
161. De Groot, F. High-resolution X-ray Emission and X-ray absorption spectroscopy. *Chemical Reviews* **101,** 1779–1808. ISSN: 0009-2665. `https://doi.org/10.1021/cr9900681` (June 2001).
162. Kramers, H. A. & Heisenberg, W. Über die Streuung von Strahlung durch Atome. *Zeitschrift für Physik* **31,** 681–708. ISSN: 0044-3328. `http://doi.org/10.1007/BF02980624` (Feb. 1925).
163. Dirac, P. A. M. The quantum theory of the emission and absorption of radiation. *Proceedings of the Royal Society of London. Series A, Containing Papers of a Mathematical and Physical Character* **114,** 243–265. ISSN: 0950-1207. `https://doi.org/10.1098/rspa.1927.0039` (Mar. 1927).
164. Ament, L. J., Van Veenendaal, M., Devereaux, T. P., Hill, J. P. & Van Den Brink, J. Resonant inelastic X-ray scattering studies of elementary excitations. *Reviews of Modern Physics* **83,** 705–767. ISSN: 00346861. arXiv: `1009.3630`. `https://doi.org/10.1103/RevModPhys.83.705` (June 2011).
165. Liu, J. C., Sun, Y. P., Wang, C. K., Ågren, H. & Gel'Mukhanov, F. Auger effect in the presence of strong X-ray pulses. *Physical Review A - Atomic, Molecular, and Optical Physics* **81,** 043412. ISSN: 10502947. `https://doi.org/10.1103/PhysRevA.81.043412` (Apr. 2010).
166. Rohringer, N. *et al.* Atomic inner-shell X-ray laser at 1.46 nanometres pumped by an X-ray free-electron laser. *Nature* **481,** 488–491. ISSN: 00280836. `https://doi.org/10.1038/nature10721` (Jan. 2012).

167. Kimberg, V. & Rohringer, N. Amplified X-ray Emission from Core-Ionized Diatomic Molecules. *Physical Review Letters* **110,** 043901. ISSN: 0031-9007. `https://doi.org/10.1103/PhysRevLett.110.043901` (Jan. 2013).

168. Sun, Y. P., Liu, J. C. & Gel'Mukhanov, F. The propagation of a strong X-ray pulse followed by pulse slowdown and compression, amplified spontaneous emission and lasing without inversion. *Journal of Physics B: Atomic, Molecular and Optical Physics* **42,** 201001. ISSN: 09534075. `https://doi.org/10.1088/0953-4075/42/20/201001` (Oct. 2009).

169. Sun, Y. P., Liu, J. C. & Gel'Mukhanov, F. Slowdown and compression of a strong X-ray free-electron pulse propagating through the Mg vapors. *Epl* **87,** 64002. ISSN: 12864854. `https://doi.org/10.1209/0295-5075/87/64002` (Oct. 2009).

170. Kimberg, V. & Rohringer, N. Stochastic stimulated electronic X-ray Raman spectroscopy. *Structural Dynamics* **3,** 034101. ISSN: 2329-7778. arXiv: `1511.00481`. `http://doi.org/10.1063/1.4940916` (May 2016).

171. Kimberg, V. *et al.* Stimulated X-ray Raman scattering – a critical assessment of the building block of nonlinear X-ray spectroscopy. *Faraday Discussions* **194,** 305–324. ISSN: 1359-6640. `http://doi.org/10.1039/C6FD00103C` (June 2016).

172. Freund, I. & Levine, B. F. Optically modulated X-ray diffraction. *Physical Review Letters* **25,** 1241–1245. ISSN: 00319007. `https://doi.org/10.1103/PhysRevLett.25.1241` (Nov. 1970).

173. Levine, B. & Freund, I. Parametric down conversion of X-rays. *Optics Communications* **1,** 419–422. ISSN: 00304018. `https://doi.org/10.1016/0030-4018(70)90168-9` (Apr. 1970).

174. Eisenberger, P. M. & McCall, S. L. Mixing of X-ray and optical photons. *Physical Review A* **3,** 1145–1151. ISSN: 10502947. `https://doi.org/10.1103/PhysRevA.3.1145` (Mar. 1971).

175. Krebs, D. & Rohringer, N. Theory of parametric X-ray optical wavemixing processes. *arXiv,* 2104.05838. arXiv: `2104.05838`. `http://arxiv.org/abs/2104.05838` (Apr. 2021).

176. Boemer, C. *et al.* Towards novel probes for valence charges via X-ray optical wave mixing. *Faraday Discuss.* **228,** 451–469. `http://dx.doi.org/10.1039/D0FD00130A` (0 Jan. 2021).

177. Tanaka, S. & Mukamel, S. X-ray four-wave mixing in molecules. *Journal of Chemical Physics* **116,** 1877–1891. ISSN: 00219606. `https://doi.org/10.1063/1.1429950` (Sept. 2002).

178. Cao, W., Warrick, E. R., Fidler, A., Leone, S. R. & Neumark, D. M. Excited-state vibronic wave-packet dynamics in H_2 probed by XUV transient four-wave mixing. *Physical Review A* **97,** 023401. ISSN: 2469-9926. `https://doi.org/10.1103/PhysRevA.97.023401` (Feb. 2018).

179. Fresnel, A.-J. On the calculation of the tints that polarization develops in crystalline plates, & postscript. Version 3. *Zenodo* (ed Putland, G. R.) 4561712. `https://doi.org/10.5281/zenodo.4561712` (Feb. 2021).

180. Andreeva, M. & Baulin, R. Reflectivity spectra as absorption resonant spectra: is it correct? *Journal of Applied Crystallography* **55,** 1196–1204. `https://doi.org/10.1107/s160057672200783x` (Aug. 2022).

181. Lengeler, B. X-Ray Reflection, A New Tool for Investigating Layered Structures and Interfaces. *Advances in X-ray analysis* **35,** 127–135. `https://doi.org/10.1154/S0376030800008752` (Mar. 1991).

182. Becker, R. S., Golovchenko, J. A. & Patel, J. R. X-ray evanescent-wave absorption and emission. *Physical Review Letters* **50,** 153–156. ISSN: 00319007. `https://doi.org/10.1103/PhysRevLett.50.153` (Jan. 1983).

183. *The X-ray standing wave technique: Principles and applications* (eds Zegenhagen, J. & Kazimirov, A.) 1–556. ISBN: 9789812779014. `https://doi.org/10.1142/6666` (Apr. 2013).

184. De Groot, F. M. F. Dips and peaks in fluorescence yield X-ray absorption are due to state-dependent decay. *Nature Chemistry* **4,** 766–767. ISSN: 1755-4330. `http://doi.org/10.1038/nchem.1431` (Oct. 2012).

185. Miedema, P. S. & Beye, M. Total 3s Emission Yield as Bulk-Sensitive Probe for a True Soft X-ray Absorption Spectrum? *Journal of Physical Chemistry Letters* **9,** 2579–2583. ISSN: 19487185. `https://doi.org/10.1021/acs.jpclett.8b00720` (May 2018).

186. Sorokin, A. A. *et al.* An X-ray gas monitor for free-electron lasers. *Journal of Synchrotron Radiation* **26,** 1092–1100. ISSN: 16005775. `https://doi.org/10.1107/S1600577519005174` (July 2019).

187. Tiedtke, K. *et al.* Gas detectors for X-ray lasers. *Journal of Applied Physics* **103,** 094511. ISSN: 00218979. `https://doi.org/10.1063/1.2913328` (May 2008).

188. Berrah, N. *et al.* Two mirror X-ray pulse split and delay instrument for femtosecond time resolved investigations at the LCLS free electron laser facility. *Optics Express* **24,** 11768. ISSN: 1094-4087. `https://opg.optica.org/abstract.cfm?URI=oe-24-11-11768` (May 2016).

189. Sorgenfrei, F. *et al.* The extreme ultraviolet split and femtosecond delay unit at the plane grating monochromator beamline PG2 at FLASH. *Review of Scientific Instruments* **81,** 043107. ISSN: 0034-6748. `http://aip.scitation.org/doi/10.1063/1.3374166` (Apr. 2010).

190. Roling, S. *et al. A soft X-ray split-and-delay unit for FLASH II* in *Advances in X-ray Free-Electron Lasers Instrumentation IV* (eds Tschentscher, T. & Patthey, L.) **1023712** (June 2017), 10237. `https://doi.org/10.1117/12.2265708`.

191. Roling, S. *et al. Design of an X-ray split- and delay-unit for the European XFEL* in *X-Ray Free-Electron Lasers: Beam Diagnostics, Beamline Instrumentation, and Applications* (eds Moeller, S. P., Yabashi, M. & Hau-Riege, S. P.) **8504** (SPIE, Oct. 2012), 850407. `https://doi.org/10.1117/12.965547`.

192. Wöstmann, M. *et al.* The XUV split-and-delay unit at beamline BL2 at FLASH. *Journal of Physics B: Atomic, Molecular and Optical Physics* **46,** 164005. ISSN: 09534075. `https://doi.org/10.1088/0953-4075/46/16/164005` (Aug. 2013).

193. Roling, S. & Zacharias, H. in *Synchrotron Light Sources and Free-Electron Lasers: Accelerator Physics, Instrumentation and Science Applications* (eds Jaeschke, E. J., Khan, S., Schneider, J. R. & Hastings, J. B.) 1057–1091 (Springer Cham, May 2020). ISBN: 9783030232016. `https://doi.org/10.1007/978-3-030-23201-6_24`.

194. Simoncig, A. *et al.* AC/DC: The FERMI FEL split and delay optical device for ultrafast X-ray science. *Photonics* **9,** 314. ISSN: 23046732. `https://doi.org/10.3390/photonics9050314` (Apr. 2022).

195. Doring, F. *et al.* 1D-Full Field Microscopy of Elastic and Inelastic Scattering with Transmission off-axis Fresnel Zone Plates. *Microscopy and Microanalysis* **24,** 182–183. `https://doi.org/10.1017/S1431927618013260` (Aug. 2018).

196. Döring, F. *et al.* Multifocus off-axis zone plates for X-ray free-electron laser experiments. *Optica* **7,** 1007. ISSN: 23342536. `https://doi.org/10.1364/optica.398022` (Aug. 2020).

197. Schlotter, W. F. *et al.* Balanced Detection in Femtosecond X-ray Absorption Spectroscopy to Reach the Ultimate Sensitivity Limit. *arXiv,* 2006.13968. arXiv: `2006.13968`. `http://arxiv.org/abs/2006.13968` (June 2020).

198. Wellhoefer, M. *The Monochromator Beamline at the Free Electron Laser in Hamburg: (FLASH); Assembly, Characterization, and First Experiments* PhD thesis (Hamburg University, July 2007). ISBN: 9783899635850.

199. Schwickert, D. *et al.* Electronic quantum coherence in glycine molecules probed with ultrashort X-ray pulses in real time. *Science Advances* **8,** eabn6848. ISSN: 23752548. `https://doi.org/10.1126/sciadv.abn6848` (June 2022).

200. Shore, B. W. *Manipulating Quantum Structures Using Laser Pulses* 1st, 572. ISBN: 9781139157469 (Cambridge University Press, 2011).

201. West, B. A., Womick, J. M. & Moran, A. M. Probing ultrafast dynamics in adenine with mid-UV four-wave mixing spectroscopies. *Journal of Physical Chemistry A* **115,** 8630–8637. ISSN: 10895639. `https://doi.org/10.1021/jp204416m` (July 2011).

202. Consani, C., Aubock, G., van Mourik, F. & Chergui, M. Ultrafast Tryptophan-to-Heme Electron Transfer in Myoglobins Revealed by UV 2D Spectroscopy. *Science* **339,** 1586–1589. ISSN: 0036-8075. `https://doi.org/10.1126/science.1230758` (Feb. 2013).

203. Mewes, L., Wang, M., Ingle, R. A., Börjesson, K. & Chergui, M. Energy relaxation pathways between light-matter states revealed by coherent two-dimensional spectroscopy. *Communications Physics* **3,** 157. ISSN: 2399-3650. `https://doi.org/10.1038/s42005-020-00424-z` (Sept. 2020).

204. Stöhr, J. Overcoming the diffraction limit by multi-photon interference: a tutorial. *Advances in Optics and Photonics* **11,** 215. ISSN: 1943-8206. `https://doi.org/10.1364/AOP.11.000215` (Mar. 2019).

List of Acronyms

AAB	4-AminoAzoBenzene	53
CCD	Charge Coupled Device	41
CI	Confidence Interval	54
DFG	Difference-Frequency Generation	5
EXAFS	Extended X-ray Absorption Fine Structure	30
EXFEL	European X-ray Free Electron Laser	41
FLASH	Free-electron LASer in Hamburg	3
FEL	Free-Electron Laser	3
FVU	Fraction of Variance Unexplained	53
FWHM	Full Width Half Maximum	17
FWM	Four-Wave Mixing	5
GMD	Gas Monitor Detector	40
IR	Infrared	5
laser	Light Amplification by Stimulated Emission of Radiation	1
LCLS	Linac Coherent Light Source	3
MUSIX	MUlti-dimensional Spectroscopy and Inelastic X-ray scattering	42
NEXAFS	Near-Edge X-ray Absorption Fine Structure	30
PEY	Partial Electron Yield	38
PG	Plane Grating Monochromator	40
PFY	Partial Fluorescence Yield	38
SASE	Self Amplified Spontaneous Emission	3
REXS	Resonant Elastic X-ray Scattering	29

RF	Radio Frequency	8
RIXS	Resonant Inelastic X-ray Scattering	iii
SCS	Spectroscopy and Coherent Scattering	41
SDU	Split-and-Delay-Unit	41
SFG	Sum-Frequency Generation	5
SNR	Signal-to-Noise Ratio	38
SRIXS	Stimulated Resonant Inelastic X-ray Scattering	28
TEY	Total Electron Yield	39
TFY	Total Fluorescence Yield	39
XANES	X-ray Absorption Near-Edge Spectroscopy	3
XAS	X-ray Absorption Spectroscopy	29
XCRS	X-ray Coherent Raman Scattering	34
XES	X-ray Emission Spectroscopy	28
XFEL	X-ray Free Electron Laser	iii
XMCD	X-ray Magnetic Circular Dichroism	30
XMLD	X-ray Magnetic Linear Dichroism	30
XUV	Extreme Ultraviolet	5

Eidesstattliche Versicherung

Hiermit versichere ich an Eides statt, die vorliegende Dissertationsschrift selbst verfasst und keine anderen als die angegebenen Hilfsmittel und Quellen benutzt zu haben.

Datum:	Unterschrift:
15.03.2023	R.G. Engel

Diese zur Publikation bestimmte Version der Dissertationsschrift enthält redaktionelle Änderungen im Vergleich zur Prüfungsversion.